Postbuckling Analysis of Isotropic and Anisotropic Plate Assemblies Under Combined Loading

Thesis submitted in fulfilment of the requirement for the degree of

Doctor of Philosophy

By

Chi Zhang

September 2018

School of Engineering

Cardiff University

I dedicate this thesis to my wife and my parents

Declaration and Statements

DECLARATION

This work has not been submitted in substance for any other degree or award at this or any other university or place of learning, nor is being submitted concurrently in candidature for any degree or other award.

Signed ……(Chi Zhang) Date……

STATEMENT 1

This thesis is being submitted in partial fulfillment of the requirements for the degree of Doctor of Philosophy (PhD).

Signed ……(Chi Zhang) Date ……

STATEMENT 2

This thesis is the result of my own independent work/investigation, except where otherwise stated, and the thesis has not been edited by a third party beyond what is permitted by Cardiff University's Policy on the Use of Third Party Editors by Research Degree Students. Other sources are acknowledged by explicit references. The views expressed are my own.

Signed …… (Chi Zhang) Date ……

STATEMENT 3

I hereby give consent for my thesis, if accepted, to be available online in the University's Open Access repository and for inter-library loan, and for the title and summary to be made available to outside organisations.

Signed …… (Chi Zhang) Date ……

Abstract

Plated structures are used extensively in aerospace structures to reduce mass, while maintaining a high degree of stiffness. In many cases, such structures exhibit stable postbuckling behaviour and can carry loads far in excess of their critical buckling load. However, postbuckling behaviour is often complex and computationally expensive to determine particularly when anisotropic composite material is utilised.

In aerostructure design, engineers require fast yet reliable software to extend the design envelope as far as possible into the postbuckling region. The exact finite strip computer program VICONOPT is a powerful tool for analysis and optimisation of prismatic plate assemblies but has some limitations particularly in conducting postbuckling analysis. For example, it gives conservative postbuckling results for structures subject to combined shear and compression because it assumes the mode shape varies sinusoidally in the longitudinal direction. Also, it unable to predict correct postbucked stress distribution patterns. This work is motivated by the need to address these limitations.

A new postbuckling analysis procedure is proposed for analysis of isotropic and anisotropic plates under combined loading. This approach is based on a geometrical relationship between the postbuckling axial stiffnesses calculated from the actual mode shapes and those calculated under the sinusoidal assumption. This enables comparison studies to be conducted to correct the previous conservative postbuckling analysis.

An 'Improved' method is also proposed to obtain an accurate stress distribution during the postbuckling analysis. Enhanced trigonometric functions are developed to that the in-plane displacement field can be represented more adequately. The in-plane governing equilibrium equations are derived and solved analytically for both isotropic and general anisotropic plates.

This Improved method is further extended to handle more complex problems, including stiffened panels for which some adjustments to the equilibrium equations are made. Each proposed method is presented alongside appropriate practical examples and numerical results, and a commercial finite element package is used to validate the results obtained.

Acknowledgements

In the journey towards submitting this thesis, I am indebted to many intelligent, patient and encouraging people who have helped me through the course of my PhD study. I would like to take this opportunity to appreciate their supports.

I would like to express my deepest gratitude to my supervisors Prof David Kennedy and Prof Carol Featherston for their continuous guidance, patience, encouragement and wisdom, and for being the friendliest supervisors I have ever met. Their valuable feedbacks and constructive comments helped me in all my time of research and writing of this thesis.

I would like to thank China Scholarship Council and Cardiff University who fund my PhD project. I am also quite thankful to my colleagues and friends whom I have worked with in the office W1.33, in Queen's Building over the years for their kind suggestions and accompany. Special thanks to my friends Chao Guo and Yulin Luo, who kindly gave me valuable advice and offered me warm support during my life in the UK.

I wish to thank my wife, Yang Zheng, for her immense and endless emotional supports throughout my PhD study. Without her love and care, it would have been much more stressful during difficult times. Finally, I would like to dedicate this thesis to my parents, Weimin Luan and Xiaoqing Zhang, for their consistent encouragement and unconditional support. It was their great love and sacrifice that made the completion of this thesis possible.

Contents

List of figures

List of tables

Nomenclature

$\boldsymbol{A}, \boldsymbol{B}, \boldsymbol{C}$	membrane, bending-membrane and flexural stiffness matrices
a	length of plate
b_s	width of strip
$\boldsymbol{D}$	displacement vector
f	eigenparameter
f^*	trial value of f
J	number of eigenvalues below f^*
J_0	number of fixed end eigenvalues below f^*
J_m	number of fixed end eigenvalues of member m below f^*
$\boldsymbol{K_m}$	member stiffness matrix
$\boldsymbol{K}(\boldsymbol{f})$	global stiffness matrix
n	number of strips
N_x, N_y, N_{xy}	stress resultants
P	Axial load
$s\{\boldsymbol{K}(\boldsymbol{f})\}$	sign count of $\boldsymbol{K}(\boldsymbol{f})$
u, v	in-plane displacements
V_x, V_y, V_{xy}	work done by applied loads
w, ψ	out-of-plane displacements and rotations
x, y, z	longitudinal, transverse and lateral directions
$\varepsilon_x, \varepsilon_y, \varepsilon_{xy}$	middle surface strain
$\kappa_x, \kappa_y, \kappa_{xy}$	curvatures
λ	longitudinal half-wavelength

Publications from this thesis

Zhang C, Kennedy D, Featherston CA. Initial Postbuckling of Composite Stiffened Panels in Combined Shear and Compression. *Proceedings of 12th World Congress on Computational Mechanics (WCCM XII), MS010D-2 (2016)*

Zhang C, Kennedy D, Featherston CA. Improved Exact Strip Analysis of Initial Postbuckling Behaviour of Isotropic and Anisotropic Plate. *Proceedings of 13th World Congress on Computational Mechanics (WCCM XIII), MS1010-4 (2018)*

Zhang C, Kennedy D, Featherston CA. Initial Postbuckling of Anisotropic plates using improved exact strip analysis. 'Submitted to Computers and Structures, 2018.'

Chapter 1

Introduction

1.1 General introduction

The aerospace industry is characterised by highly complex design, manufacture and integration processes, all of which are both scientifically and technically challenging. International Air Transport Association (IATA) adopted a set of strategic targets to mitigate CO2 emissions from air transport which include improving aircraft fuel efficiency by 1.5% per year from 2009 to 2020 and reduce the net aviation CO_2 emissions of 50% by 2050, relative to 2005 levels (International Air Transport Association 2018). Achieving such goals requires continuous exploration of the possibilities for significant weight reduction of primary aerostructure components without compromising performance. A possible step towards minimising structural weight is to utilise composite materials, such as carbon fibre reinforced plastic (CFRP), which consists of many unidirectional (UD) plies stacked upon each other allowing advantageous anisotropic mechanical properties to be achieved. Owing to its high strength-weight ratio and better resistance to corrosion (Gibson 2011), an increasing number of primary structures in the wings and fuselage are manufactured from the CFRP (examples shown in Figure 1.1).

From a structural engineering point of view, high-performance aerospace structures can be inherently categorised as thin-walled because of their relatively low thickness in comparison with other dimensions of the structure (Chajes 1974). These thin plate

components in the primary loading-carrying structures are often subjected to destabilising loads and therefore are susceptible to instability failures. Hence, the design of aerospace structures is often driven by the need to prevent or mitigate buckling phenomena (Megson 2012). On the other hand, it is well known that these thin plate structures can often carry load in excess of their critical buckling load and have a considerable postbuckling reserve of strength. Therefore, the prospect of allowing composite aerostructures to operate in a post-buckled state, between the design limit and ultimate loads, and thus to extend the safety design envelope, can potentially lead to them becoming significantly lighter and more efficient (Bisagni 2008).

a b

Figure 1.1: Photograph showing the use of composite material in primary aeronautical structures: (a) Airbus A-350 lower wing cover and the largest single composite part in commercial aviation (Airbus 2012) and (b) Airbus A-350 advanced composite fuselage (Airbus 2016).

In terms of practical design, analytical and numerical analyses of nonlinear composite plate postbuckling using algebraic expressions are simply too complicated to conduct manually. Engineers use a range of computer aided engineering (CAE) software to model the nonlinear postbuckling behaviour of composite plates in aerostructure design (Jenkinson 1999). The CAE software used can range from bespoke programmes to state-of-art finite element packages, with different software packages complementing each

other and suitable for different stages of the design process. Bespoke design software is most useful at the preliminary stage where design options are fluid and structural idealisation has been used to represent potentially complex structures as comprised of relatively simple prismatic beams, plates and shells. Engineers and researchers are always seeking fast and reliable computational tools to analyse an excessive number of structural configurations so that the most promising design can be identified. Detailed finite element analyses (FEA) then focus on either the interactions between structural members or overall structural performance to gain more accurate numerical information to arrive at a final design.

The computer program VICONOPT (VIpasa with CONstraints and OPTimization) is a powerful tool for accurate analysis of buckling and post-buckling of prismatic plate assemblies in the preliminary design stage. The analysis is based on the exact finite strip method (exact-FSM) and the Wittrick–Williams (W-W) algorithm, which provide an alternative numerical approach to the more established traditional one of using the FEA in the preliminary design stage.

Although FEA is more widely used with the help of cheap computing power and increased development of computational tools, there remains a need for aerospace designers and researchers to understand alternative numerical methods like exact-FSM. Such alternatives not only lead to fast and reliable design solutions but can also be used to assess the credibility of FEA and other numerical solutions. VICONOPT has been proved to provide adequate accuracy compared with experimental and finite element analysis and has been used for analysis and design of the preliminary design phase, in both industry and academia, for nearly three decades.

However, while VICONOPT can analyse and design prismatic structural components, it has some limitations particularly in conducting postbuckling analyses. For example,

VICONOPT gives conservative postbuckling results for structures subject to combined shear and compression. Also, it unable to predict correct postbuckled stress distribution patterns. All of these limitations can be used as a starting point for researchers to further develop this software. In this thesis, new numerical approaches are proposed based on existing applications of the exact-FSM, and some enhancements have been made to the current exact-FSM assumptions to further improve the postbuckling analysis capabilities of VICONOPT.

1.2 Thesis scope

This thesis addresses some of the inaccuracies identified in the VICONOPT software in relation to its prediction of the postbuckling behaviour. Two types of inaccuracy are considered in this work:

Firstly, in the simplest VIPASA (vibration and instability of plate assemblies including shear and anisotropy) form of analysis, some initial buckling results, notably in the conditions of combined loading or with material anisotropy, have been found to be quite conservative (Stroud et al. 1984). VIPASA analysis has previously been extended by the use of Lagrangian multipliers to incorporate a set of constraints to form VICON (VIPASA with constraints) analysis, which is efficient in overcoming this inaccuracy but this is currently limited to initial buckling analysis (F. W. Williams and Anderson 1983). A new approach taking advantage of VICON features while retaining the VIPASA postbuckling capacity is desirable for further development of VICONOPT and is presented in this thesis.

Secondly, VICONOPT is a highly efficient tool for investigating plate buckling and postbuckling problems. However, precisely because VICONOPT is both specialised and efficient, several conservative assumptions have been made. For example, the software

assumes that the stresses in each strip are longitudinally invariant (Anderson and Kennedy 2008). Such an assumption is appropriate for initial buckling analysis but reduces the accuracy of the subsequent post-buckling analysis. An improved assumption concentrating on improving the postbuckling predictions of stress and strain distributions is introduced in this thesis, where specialised trigonometric series functions are introduced to enrich the nodal line to accurately capture the in-plane displacements along the plate.

1.3 Thesis aims and objectives

The main aim of this study is to investigate the postbuckling behaviours of plate structure in the context of exact strip analysis so that the postbuckling analysis capabilities of the computer program VICONOPT can be improved. To begin with, several objectives have been set for this thesis to fulfil this goal:

1. To study the analysis features of the VICONOPT software and to identify the causes of the conservative results under shear and anisotropy.
2. To develop a fast, yet reliable approach to allow VICON features to be used in postbuckling analysis.
3. To propose an improved approach to address the stress invariant issue present in VIPASA analysis.
4. To develop a finite element model to validate the improved method with special focus on the stress field developed during the postbuckling analysis.
5. To further modify the improved analysis so as to apply the proposed method to complex prismatic structures such as stiffened panels.

1.4 Thesis overview

This section provides an overview of each Chapter and its content, as a reference to help guide the reader towards areas of specific interest.

Chapter 2: Literature Review

This chapter provides a review of the relevant work conducted in the field of prismatic plate postbuckling behaviours. Classical Plate Theory (CPT) and its formulation in plate buckling and postbuckling are briefly covered, intending to explain the difference between buckling and postbuckling analyses. Research work showing the development of non-linear structural stability analysis is also summarised. More recent research work concerning postbuckling behaviour of plate structures is critically reviewed and evaluated.

Chapter 3: Exact finite strip method and applications

This chapter reviews some related numerical methods including the finite element method (FEM), the finite strip method (FSM) and the exact finite strip method (exact-FSM), focusing on comparing the differences between these numerical approaches. This chapter also describes the main features of VICONOPT with an emphasis on the details of the Wittrick-Williams algorithm. The analysis packages of VICONOPT, VIPASA and VICON, are compared in detail to fulfil Objective 1.

Chapter 4: Simulated VICON Analysis

A simulated VICON analysis based on investigating the difference in postbuckling stiffness between VIPASA and VICON analyses is developed for the first time to carry out postbuckling analysis of a prismatic plate. The proposed method focuses on tracing the equilibrium path of a plate under combined shear and compression which intends to fulfil Objective 2. Finite element models are constructed and used to verify the simulated

VICON analysis. The Simulated VICON analysis presented in this chapter is programmed using Matlab 2016.

Chapter 5: Improved VIPASA analysis

An improved exact strip method is proposed for the analysis of the initial postbuckling behaviour of prismatic plate structures in this chapter. Enhanced trigonometric functions inspired by Stein's assumptions (1983; 1985) are developed to represent longitudinal and transverse in-plane displacements, which help to derive and solve the governing in-plane equilibrium equation analytically. This improved analysis enables accurate stress distributions to be found at each stage of the postbuckling analysis, which fulfil Objective 3. The Improved VIPASA analysis proposed in this chapter is implemented in a Maple programme environment.

Chapter 6: Validation of the Improved VIPASA analysis

This chapter presents the process for validating the Improved VIPASA analysis and compares the results given by the proposed method with analytical results and finite element (FE) benchmark results. The main outputs of the Improved VIPASA analysis, namely, in-plane displacements (u and v), strains (ε_x and ε_y) and stress resultants (N_x and N_y), are all compared in this chapter. This chapter offers valuable insight into the mechanisms of the Improved VIPASA analysis, exploring its advantages as well as the its weaknesses to fulfil Objective 4. The graphs and curves shown in this chapter are produced by using Matlab 2016.

Chapter 7: Further development

This chapter attempts to expand the Improved VIPASA analysis to predict the postbuckling behaviours of stiffened panels to fulfil Objective 5. Two models with increasingly complex geometry and equilibrium set-ups are analysed using Improved VIPASA analysis to assess its suitability for more practical situations. Each model is

presented alongside appropriate results that highlight the important adjustments made to the Improved VIPASA analysis to enable it to model such structures and their effects on the postbuckling response of the corresponding model. The examples presented in this section are also coded in a Maple programme environment.

Chapter 8 Contributions, conclusions and future work

This final chapter concludes the thesis and summarises contributions made to the research area. It also provides suggestions for future work.

Chapter 2

Background theory and general literature review

There have been extensive studies carried out in the field of thin-walled structures and buckling and postbuckling behaviour. These studies focused on developing predictive methods to ensure these thin-wall structural components can be utilised safely and efficiently. The numerous literatures associated with these studies involve complex structural stability theory and sophisticated numerical theory. This chapter gives a general literature review of the relevant previous work conducted in this field, which includes an outline of basic structural stability theory and classical plate theory in order to aid understanding of the following general literature review. Thus, this chapter is organised as follow: Section 2.1 reviews earlier buckling analysis conducted by Euler and outlines some basic concepts in structural stability. Section 2.2 lists some important formulations used in plate buckling analysis. Section 2.3 introduces the plate postbuckling features, focusing on explaining the cause of plate stable postbuckling behaviour. Section 2.4 lists some of the fundamental equations derived for investigating the isotropic and anisotropic plate postbuckling problems. Section 2.5 gives a general postbuckling literature survey of some of the important work in the development of plate postbuckling analysis to set the scene for this research. More literature specifically related to this project will be reviewed in Chapter 3.

2.1 Buckling of members under compression

Thin metallic structural components are expected to fail in two distinct ways: one is a material failure which depends on the tensile, compressive or shear strength, or on von Mises or an alternative stress failure criteria if they are under multi-axial loading. The other is a set of more complex failure mechanisms which occur under compression, often referred to as buckling phenomenon. Buckling is triggered by a specific critical load at which the structural member suddenly bows out sideways. This geometric instability gives rise to large deformations, which in turn cause the member to collapse.

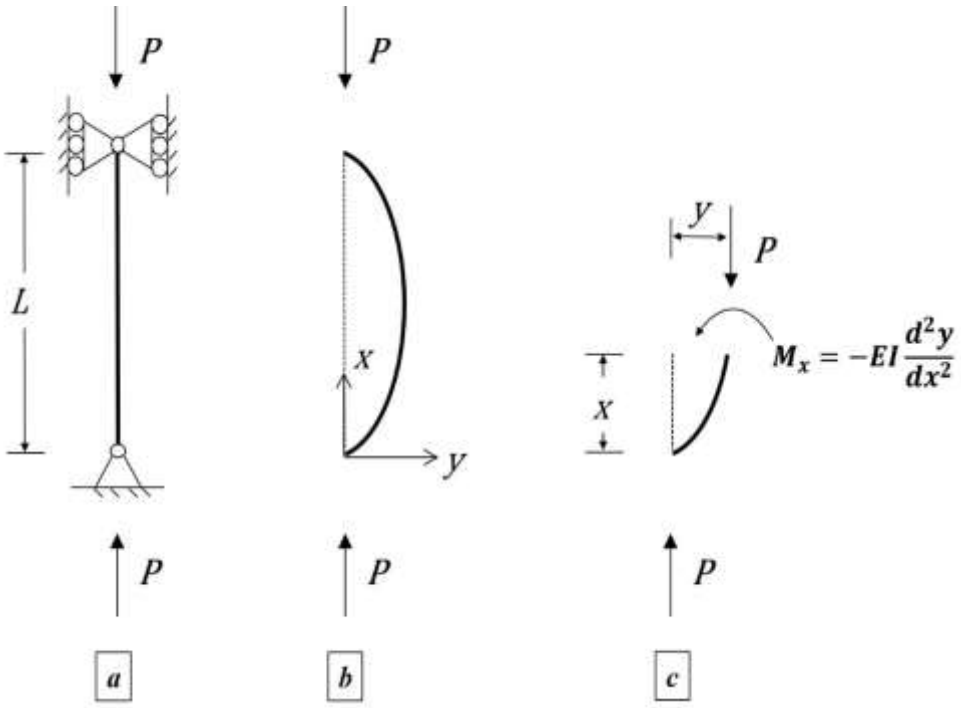

Figure 2.1 A structural member under axial compression P: (a) An idealized Euler column; (b) the slightly bent configuration of the Euler column and (c) the free body diagram of the bent column. (Adapted from (Chajes 1974))

The foremost piece of work in the field of buckling was conducted by Euler (Euler 1759) who used a new mathematical method at that time, the calculus of variations, to formulate the mechanics of an axially-loaded pin-ended incompressible thin strut, as represented in Figure2.1a. Geometrically, buckling is a form of instability which leads to structural

failure. Mathematically, the buckling of the strut is caused by a bifurcation in the solution to the equilibrium equations which can be illustrated by Figure 2.2. With an increasing load P from the unloaded state, the column initially remains straight and undergoes only axial compression and sustains a stable equilibrium state, shown as the fundamental path. When the critical value P_{cr} is reached, the column loses its stability and switches to a laterally deformed state shown as the post-buckling path.

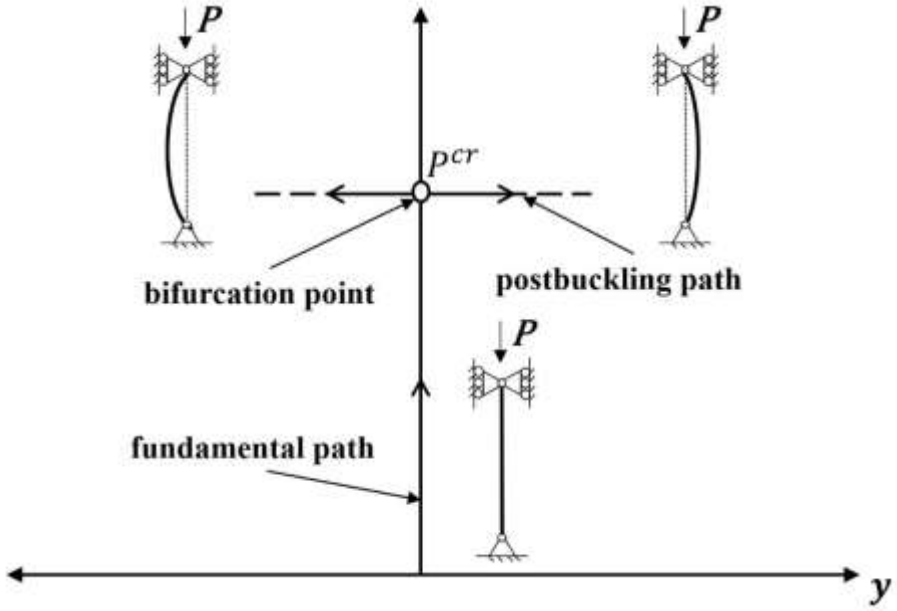

Figure 2.2 Simplified equilibrium path of a simply supported strut. The critical load P_{cr} is the bifurcation point; P is the axial load and y is the amplitude of the buckling deflection. (Adapted from (Thompson and Hunt 1984))

The most straightforward strut equilibrium equation can be expressed as

$$\frac{d^2y}{dx^2} + \frac{P}{EI}y = 0 \tag{2.1}$$

where y is the lateral deformation of the strut along the x coordinate in Figure 2.1, EI is the flexural rigidity of the strut and P is the applied axial load. The general solution of equation 2.1 can be written in the form:

$$w(x) = A\sin kx + B\cos kx \tag{2.2}$$

where k is defined as

$$k^2 = \frac{P}{EI} \tag{2.3}$$

The coefficients A and B can be determined by making use of the boundary conditions

$$\begin{aligned} y &= 0 \quad at\ x = 0 \\ y &= 0 \quad at\ x = L \end{aligned} \tag{2.4}$$

Hence, the non-trivial solutions of Equation (2.1) and the corresponding deflection shapes y can be solved:

$$P_n = \frac{n^2\pi^2 EI}{L^2} \tag{2.5}$$

$$y = A \sin\frac{n\pi x}{L} \tag{2.6}$$

where n is an integer and A is the amplitude of the deflection. The lowest P_n is called the Euler critical load (P_E) which can be gained by setting $n = 1$, thus:

$$P_E = \frac{\pi^2 EI}{L^2} \tag{2.7}$$

Short columns may fail inelastically (Engesser 1891; Shanley 1947; Duberg 1950), whereas the failure load of a slender column is closely associated with the Euler critical load. Both experience and experiments have shown that the column collapses as soon as the critical load is reached, and therefore the critical load of the column is also its failure load. Thus, columns exhibit an unstable postbuckling behaviour and have no reserve of strength after buckling.

2.2 Formulation of plate buckling

Thin isotropic plates, which can be regarded as sheets of material whose thickness is small compared with their other dimensions, but which are capable of resisting bending as well as in-plane forces, are widely used as engineering structural components. Buckling of thin plates is another classical structural stability problem, which is complicated by the fact that the element possesses curvature in both xz and yz planes, shown in Figure 2.3.

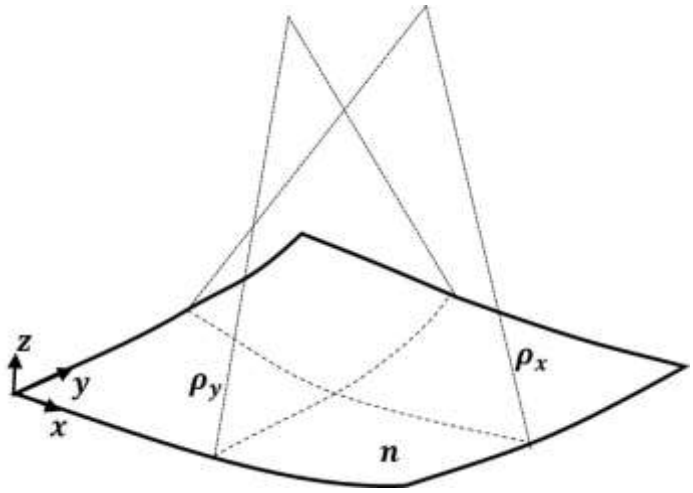

Figure 2.3 ρ_x in the xz plane and ρ_y in the yz plane are the radii of curvature of the neutral plane n, respectively. (Adapted from (Megson 2012))

The investigation of the stability of a simply supported, axially compressed plate can be dated back to the late 19th century when Bryan (1890) presented the derivation and solutions to the problem. At the beginning of the twentieth century, more loading cases and various boundary conditions were considered by Timoshenko (1936) and presented in his classic textbook on stability. According to the small deflection theory of thin plates (Timoshenko 1936), an element of a laterally bent plate is acted on by two sets of forces, in-plane forces (shown in Figure 2.4a) equal to the externally applied loads and moments

and shear forces (shown in Figure 2.4b) that result from the transverse bending of the plate. The thin plate buckling governing equation, which can be developed by considering

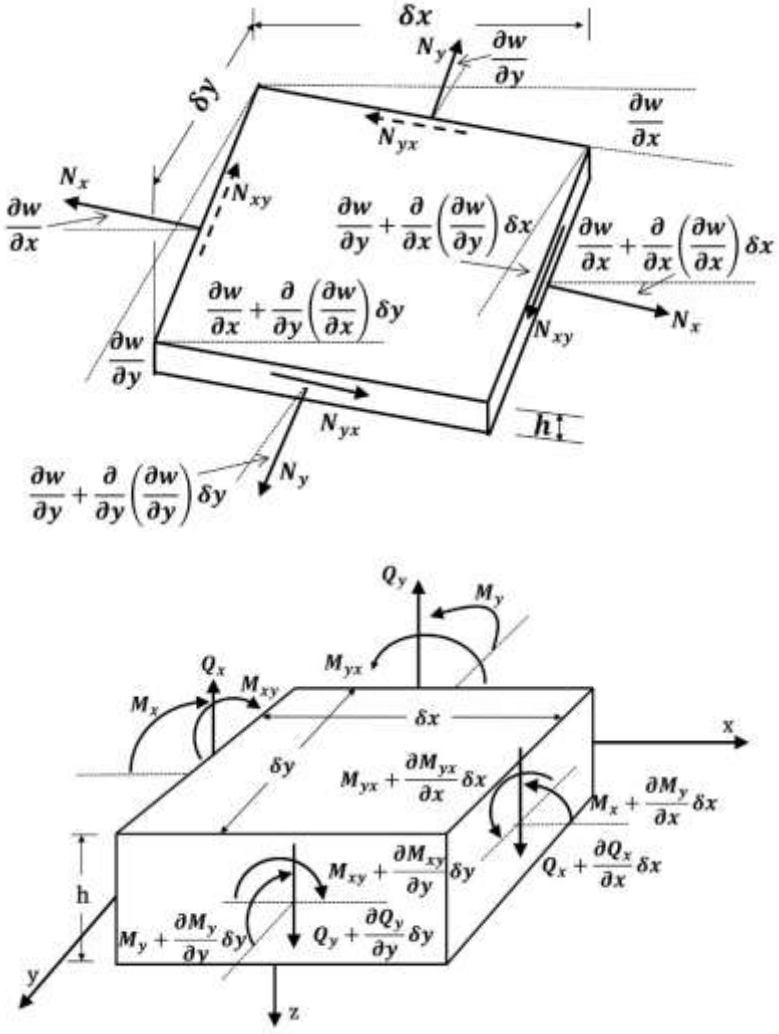

Figure 2.4 Free body diagram of an element of a laterally bent plate: (a) in-plane force (N_x, N_y, N_{xy}) on plate element and (b) bending moment (M_x, M_y), twisting moment (M_{xy}), and shear (Q_x, Q_y) on a plate element. (Adapted from (Megson 2012; Chajes 1974))

these two sets of forces separately and combining the results through their effect on the vertical equilibrium of the plate, is of the form.

$$\frac{\partial^2 M_x}{\partial x^2} - 2\frac{\partial^2 M_{xy}}{\partial x \partial y} + \frac{\partial^2 M_y}{\partial y^2} + N_x\frac{\partial^2 w}{\partial x^2} + N_y\frac{\partial^2 w}{\partial y^2} + 2N_{xy}\frac{\partial^2 w}{\partial x \partial y} = 0 \qquad (2.8)$$

where the bending and twisting moments M_x, M_y, M_{xy} can be expressed in term of out-of-plane displacement w. (The detailed derivation of Equations 2.8 and 2.9 can be found

in Appendix A from Equation A1 to Equation A36) Hence the differential equation of plate buckling can be expressed as:

$$D\left(\frac{\partial^4 w}{\partial x^4}+2\frac{\partial^4 w}{\partial x^2\partial y^2}+\frac{\partial^4 w}{\partial y^4}\right)=N_x\frac{\partial^2 w}{\partial x^2}+N_y\frac{\partial^2 w}{\partial y^2}+2N_{xy}\frac{\partial^2 w}{\partial x\partial y} \tag{2.9}$$

The quantity $D=\frac{Eh^3}{12(1-\nu^2)}$ is the flexural rigidity per unit width of a plate which corresponds to the bending stiffness EI of a beam. Compared with beam rigidity, a strip of a plate is stiffer than a beam of similar width and depth by a factor of $\frac{1}{1-\nu^2}$. The difference in stiffness exists because the beam is free to deform laterally, whereas the plate strip is constrained from deforming in this manner by the adjacent material.

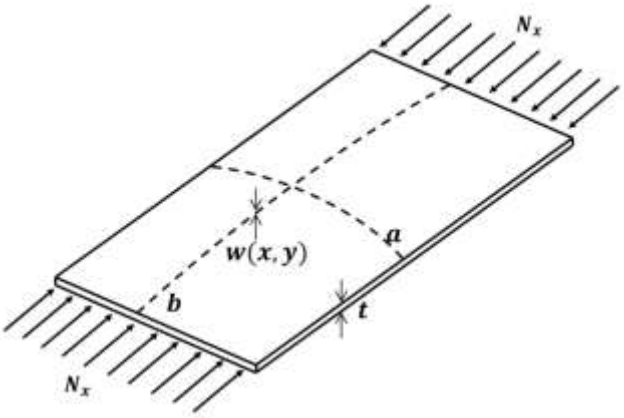

Figure 2.5 Axially loaded, simply supported plate undergoing elastic buckling with displacement $w(x,y)$. Note that all edges have zero lateral deflection. (Adapted from (Timoshenko and Woinowsky-Krieger 1959)

The out-of-plane displacement function of a simply supported, axially loaded plate (shown in Figure 2.5) can be represented by a series of trigonometrical functions

$$w=\sum_{m=1}^{\infty}\sum_{n=1}^{\infty}A_{mn}\sin\frac{m\pi x}{a}\sin\frac{n\pi y}{b} \tag{2.10}$$

Substituting the first term of Equation 2.10 into Equation 2.9, and combining with appropriate boundary conditions, the critical stress resultant can be achieved

$$N_x = \frac{kD\pi^2}{b^2} \tag{2.11}$$

$$k = \left(\frac{mb}{a} + \frac{n^2 a}{mb}\right)^2 \tag{2.12}$$

where k is the plate buckling coefficient, which depends on the aspect ratio a/b and on n and m, the number of half-waves that the plate buckles into x and y direction, respectively. In general, $n = 1$ and $m = a/b$, where m must be an integer, gives the critical value of N_x.

2.3 Postbuckling phenomenon

Small Deflection Theory should suffice for determining the critical buckling load of a plate; however, plates can often continue to carry increasing load after reaching the critical load and Small Deflection Theory can lead to considerable underestimation of the load carrying capacity. Hence, it is necessary to employ Large Deflection Theory to analyse postbuckling behaviours. The principal difference between small and large deflection theory is that small deflection theory assumes loads to be carried by bending action alone, whereas the Large Deflection Theory takes account of membrane forces that develop as a result of deflections.

The physical explanation of one plate membrane effect under large deflections can be represented by the plane grid analogy shown in Figure 2.6. The rigid plane grid is made up of 6 members (Figure 2.6a), and a point load P is applied at the central point O. It is noted that the vertical reactions at the roller-supported corner points A, B, C and D are $P/4$, and the horizontal reactions are zero (Figure 2.6b).

Initially, for small loads, the load is carried by bending of the diagonals. The four edge members make no significant contribution, and the load is roughly proportional to the deflection. As the load and deflection increase, the large deflections make the four diagonal members pull-in at the corners putting themselves into tension and the four edge members into compression. This represents membrane action but does not require

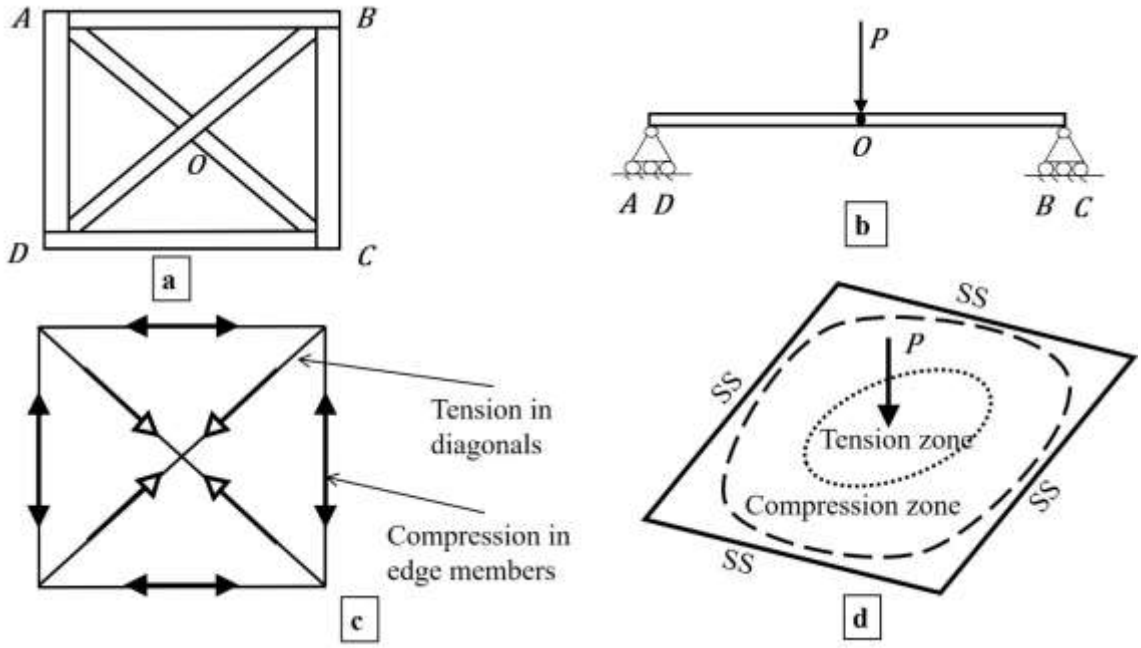

Figure 2.6 The plane rigid grid model is subjected to a point load *P*: (a) a plan view of the grid; (b) an elevation view of the grid; (c) the load carrying mechanism of the plane grid and (d) the central tensile zone and outer compressive ring. (Adapted from (Reddy 2006))

heavy external supports to achieve because the membrane forces are in self-equilibrium (Figure 2.6c).

The behaviour of a continuous plate, with simply supported edges, is very similar to the plate grid. At lower loads, the load is carried primarily by plate bending. For higher loads, large deflections occur, and a central tension zone is formed which is similar to that in the diagonals with a compressive ring which is similar to the edge members (Figure 2.6d). By analogy to a point loaded plate, the axial loaded plate also exhibits the stress redistribution phenomenon in the postbuckling stage. Prior to buckling, the stress

distribution is uniform across the plate, beyond buckling, the stress distribution across a simply supported plate varies from a minimum at the centre to a maximum near the edge. Von Kármán (1932) simplified this phenomenon and presented the concept of effective width which assumed that the majority of the edge stress acts uniformly over two strips at the edges of the plate, and the central region remained unstressed (as shown in Figure 2.7).

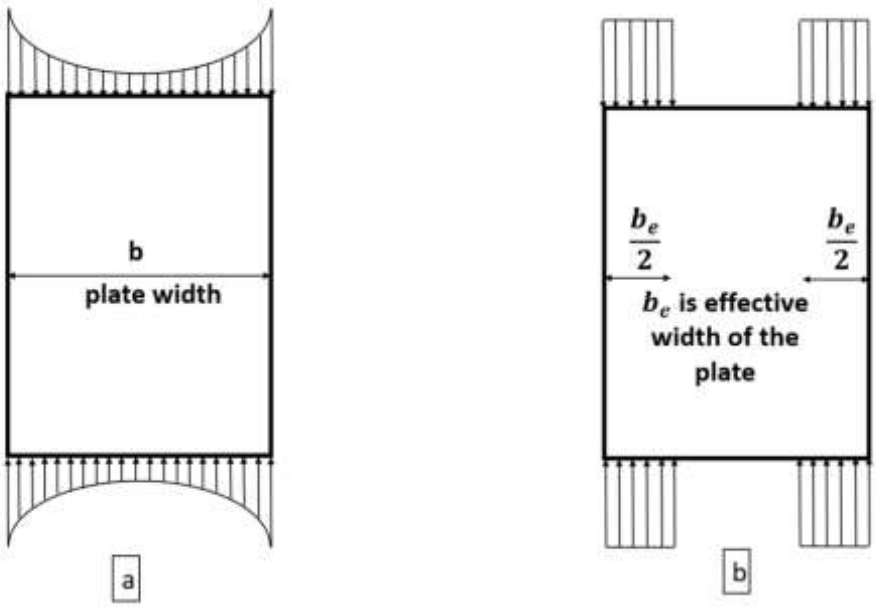

Figure 2.7 Von Kármán's effective width concept: (a) non-uniform distribution of axial stress in the postbuckling stage and (b) assumed uniform stress distribution over an effective width b_e

2.4 Formulation of plate postbuckling

In going from small to large deformations, a significant change occurs in the nature of the in-plane forces N_x, N_y and N_{xy}. Comparing Figure 2.4a and Figure 2.8a for large deflections, there are in-plane forces due to membrane action in addition to the forces applied along the edges of the plate (marked within the black boxes in Figure 2.8) which implies that the middle surface becomes stressed under large deflections.

By considering the components of these in-plane forces in the x and y directions, the two in-plane equilibrium equations are achieved:

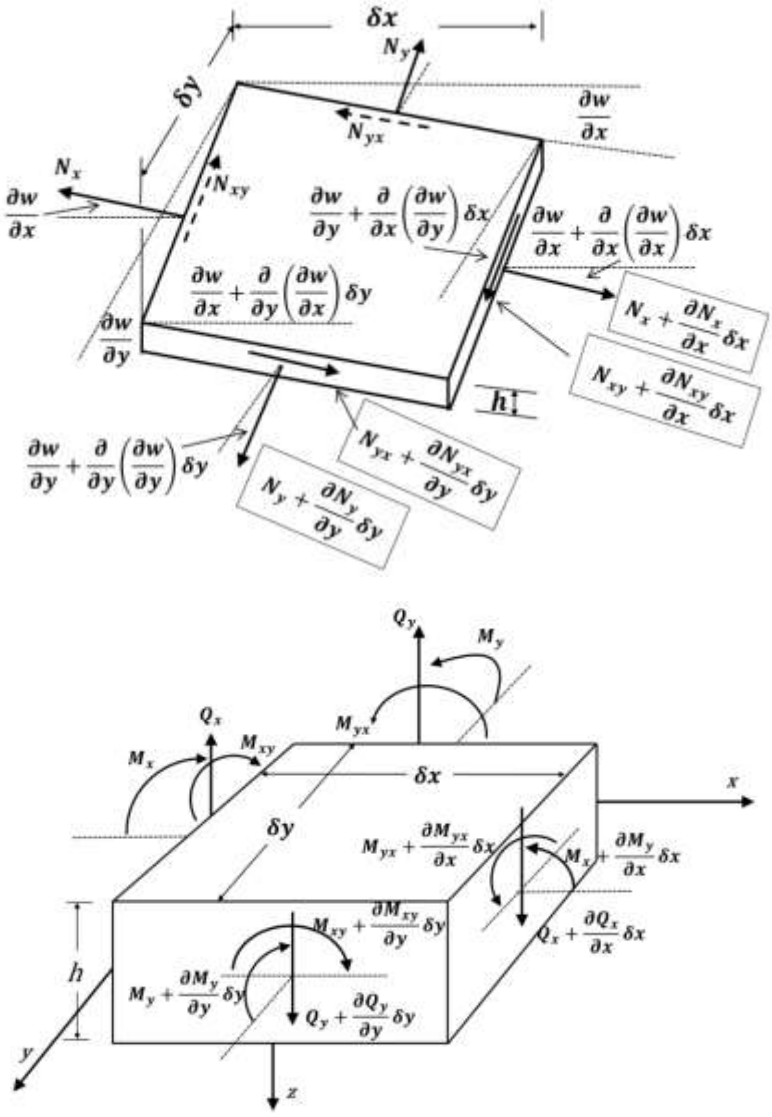

Figure 2.8 Free body diagram of an element of a laterally bent plate: (a) in-plane force (N_x, N_y, N_{xy}) on plate element and (b) bending moment (M_x, M_y), twisting moment (M_{xy}), and shear (Q_x, Q_y) on a plate element. (Adapted from (Megson 2012; Chajes 1974))

$$\frac{\partial N_x}{\partial x} + \frac{\partial N_{xy}}{\partial y} = 0 \tag{2.13}$$

$$\frac{\partial N_y}{\partial y} + \frac{\partial N_{xy}}{\partial x} = 0 \tag{2.14}$$

On the other hand, there are no changes to the bending moments, twisting moments, and transverse shears under large deflections, and so the out-of-plane equilibrium described in Appendix A from Equation A1 to Equation A36 can again be used to derive Equation 2.15

$$D\left(\frac{\partial^4 w}{\partial x^4}+2\frac{\partial^4 w}{\partial x^2 \partial y^2}+\frac{\partial^4 w}{\partial y^4}\right)=N_x\frac{\partial^2 w}{\partial x^2}+N_y\frac{\partial^2 w}{\partial y^2}+2N_{xy}\frac{\partial^2 w}{\partial x \partial y} \tag{2.15}$$

There is a fundamental difference between the Equation 2.15 and Equation 2.9, however, they appear to be identical. Equation 2.9 is a linear differential equation as it has only one dependent variable (w) and constant coefficients N_x, N_y and N_{xy} representing the constant edge forces under buckling. In contrast to Equation 2.9, Equation 2.15 is a nonlinear differential equation containing four dependent variables, w and the three in-plane forces N_x, N_y and N_{xy} are now unknown functions of x and y (Chajes 1974). Hence, the equilibrium equations (Equations 2.13-2.15) must be supplemented by compatibility equations.

Von Kármán (1910) first pointed out that the key difference between small and large deflection theory lay in the compatibility equations. He introduced the second order terms of the deflection derivatives into the strain expression which implied that the middle surface strain under large deflection is comprised of two components-bending and stretching due to the out-of-plane deflections (Chajes 1974; Jaeger 2013). Thus, the total strains in the x and y directions for an element on the mid surface is:

$$\varepsilon_x=\frac{\partial u}{\partial x}+\frac{1}{2}\left(\frac{\partial w}{\partial x}\right)^2 \tag{2.16}$$

$$\varepsilon_y=\frac{\partial v}{\partial y}+\frac{1}{2}\left(\frac{\partial w}{\partial y}\right)^2 \tag{2.17}$$

Similarly, the total shear strain for an element on the mid surface is:

$$\gamma_{xy} = \frac{\partial u}{\partial y} + \frac{\partial v}{\partial x} + \frac{\partial w}{\partial x}\frac{\partial w}{\partial y} \tag{2.18}$$

A detailed derivation of the compatibility equations can be found in Appendix B (from Equation B1 to Equation B13).

For elastic behaviour, the middle surface strain can also be expressed in term of the mid surface forces:

$$\varepsilon_x = \frac{1}{Et}\left(N_x - \nu N_y\right) \tag{2.19}$$

$$\varepsilon_y = \frac{1}{Et}\left(N_y - \nu N_x\right) \tag{2.20}$$

$$\gamma_{xy} = \frac{2(1+\nu)}{Et} N_{xy} \tag{2.21}$$

The elasticity relations (Equations 2.19-2.21), the strain displacement relations (Equations 2.16-2.18), and the equilibrium relations (Equations 2.13-2.15), comprise a set of nine equations with nine unknowns. These equations describe the postbuckling behaviour of the plate and can be used to solve for all unknown forces and displacements. These nine equations can be simplified into two equations by introducing the Airy stress function Φ, where $N_x = t\frac{\partial^2 \Phi}{\partial y^2}$, $N_y = t\frac{\partial^2 \Phi}{\partial x^2}$, and $N_{xy} = -h\frac{\partial^2 \Phi}{\partial x \partial y}$, giving,

$$\frac{\partial^4 \Phi}{\partial x^4} + 2\frac{\partial^4 \Phi}{\partial x^2 \partial y^2} + \frac{\partial^4 \Phi}{\partial y^4} = E\left[\left(\frac{\partial^2 w}{\partial x \partial y}\right)^2 - \frac{\partial^2 w}{\partial x^2}\frac{\partial^2 w}{\partial y^2}\right] \tag{2.22}$$

$$D\left(\frac{\partial^4 w}{\partial x^4} + 2\frac{\partial^4 w}{\partial x^2 \partial y^2} + \frac{\partial^4 w}{\partial y^4}\right) = t\left(\frac{\partial^2 \Phi}{\partial y^2}\frac{\partial^2 w}{\partial x^2} + \frac{\partial^2 \Phi}{\partial x^2}\frac{\partial^2 w}{\partial y^2} + 2\frac{\partial^2 \Phi}{\partial x \partial y}\frac{\partial^2 w}{\partial x \partial y}\right) \tag{2.23}$$

Equations 2.22 and 2.23 are referred as the Von Kármán large deflection plate equations. The von Kármán large equations were particularly useful when computers were unavailable as they reduced the computational cost significantly. These equations

compactly represent the interaction between in-plane (membrane) effects and out-of-plane (flexural) effects using only two equations. Instead of solving nine equations, the von Kármán equations can be solved exclusively if both in-plane and out-of-plane boundary conditions are assumed.

If laminated composite material is considered, the relationships between force and moment resultants and mid-surface strains and curvature can be expressed in matrix form:

$$\begin{bmatrix} N_x \\ N_y \\ N_{xy} \\ M_x \\ M_y \\ M_{xy} \end{bmatrix} = \begin{bmatrix} A_{11} & A_{12} & A_{16} & B_{11} & B_{12} & B_{16} \\ A_{12} & A_{22} & A_{26} & B_{12} & B_{22} & B_{26} \\ A_{16} & A_{26} & A_{66} & B_{16} & B_{26} & B_{66} \\ B_{11} & B_{12} & B_{16} & D_{11} & D_{12} & D_{16} \\ B_{12} & B_{22} & B_{26} & D_{12} & D_{22} & D_{26} \\ B_{16} & B_{26} & B_{66} & D_{16} & D_{26} & D_{66} \end{bmatrix} \begin{bmatrix} \varepsilon_x \\ \varepsilon_y \\ \varepsilon_{xy} \\ \kappa_x \\ \kappa_y \\ \kappa_{xy} \end{bmatrix} \tag{2.24}$$

where A_{ij}, B_{ij} and D_{ij} are stiffness coefficients arising from integrals of the following forms:

$$A_{ij} = \int_{-\frac{t}{2}}^{\frac{t}{2}} C_{ij}\, dz \qquad B_{ij} = \int_{-\frac{t}{2}}^{\frac{t}{2}} C_{ij}\, z dz \qquad D_{ij} = \int_{-\frac{t}{2}}^{\frac{t}{2}} C_{ij}\, z^2 dz \tag{2.25}$$

with C_{ij} being the stiffness coefficient used in general Hooke's Law, which change from layer to layer during the integration.

For orthotropic plates, the postbuckling Equations (2.23) then become

$$\begin{aligned} D_{11}\frac{\partial^4 w}{\partial x^4} + 2(D_{12} + 2D_{66})\frac{\partial^4 w}{\partial x^2 \partial y^2} + D_{22}\frac{\partial^4 w}{\partial y^4} \\ = t\left(\frac{\partial^2 \Phi}{\partial y^2}\frac{\partial^2 w}{\partial x^2} + \frac{\partial^2 \Phi}{\partial x^2}\frac{\partial^2 w}{\partial y^2} + 2\frac{\partial^2 \Phi}{\partial x \partial y}\frac{\partial^2 w}{\partial x \partial y}\right) \end{aligned} \tag{2.26}$$

For symmetric anisotropic plates, the postbuckling equations can be written as

$$D_{11}\frac{\partial^4 w}{\partial x^4} + 4D_{16}\frac{\partial^4 w}{\partial x^3 \partial y} + 2(D_{12} + 2D_{66})\frac{\partial^4 w}{\partial x^2 \partial y^2} + 4D_{26}\frac{\partial^4 w}{\partial x \partial y^3} + D_{22}\frac{\partial^4 w}{\partial y^4} = t\left(\frac{\partial^2 \Phi}{\partial y^2}\frac{\partial^2 w}{\partial x^2} + \frac{\partial^2 \Phi}{\partial x^2}\frac{\partial^2 w}{\partial y^2} + 2\frac{\partial^2 \Phi}{\partial x \partial y}\frac{\partial^2 w}{\partial x \partial y}\right) \quad (2.27)$$

For unsymmetric anisotropic plates, the postbuckling equations can be expressed in matrix form

$$\begin{bmatrix} L_{11} & L_{12} & L_{13} \\ L_{21} & L_{22} & L_{23} \\ L_{31} & L_{32} & (L_{33} - F) \end{bmatrix} \begin{bmatrix} u \\ v \\ w \end{bmatrix} = \begin{bmatrix} 0 \\ 0 \\ 0 \end{bmatrix} \quad (2.28)$$

where the L_{ij} are differential operators given by:

$$L_{11} = A_{11}\frac{\partial^2}{\partial x^2} + 2A_{16}\frac{\partial^2}{\partial x \partial y} + A_{66}\frac{\partial^2}{\partial y^2}$$

$$L_{22} = A_{22}\frac{\partial^2}{\partial y^2} + 2A_{26}\frac{\partial^2}{\partial x \partial y} + A_{66}\frac{\partial^2}{\partial x^2}$$

$$L_{33} = D_{11}\frac{\partial^4}{\partial x^4} + 4D_{16}\frac{\partial^4}{\partial x^3 \partial y} + 2(D_{12} + 2D_{66})\frac{\partial^4}{\partial x^2 \partial y^2} + 4D_{26}\frac{\partial^4}{\partial x \partial y^3} + D_{22}\frac{\partial^4}{\partial y^4} \quad (2.29)$$

$$L_{12} = L_{21} = A_{16}\frac{\partial^2}{\partial x^2} + (A_{12} + 2A_{66})\frac{\partial^2}{\partial x \partial y} + A_{26}\frac{\partial^2}{\partial y^2}$$

$$L_{13} = L_{31} = -B_{11}\frac{\partial^3}{\partial x^3} - 3B_{16}\frac{\partial^3}{\partial x^2 \partial y} - (B_{12} + 2B_{66})\frac{\partial^3}{\partial x \partial y^2} - B_{26}\frac{\partial^3}{\partial y^3}$$

$$L_{23} = L_{32} = -B_{16}\frac{\partial^3}{\partial x^3} - (B_{12} + 2B_{66})\frac{\partial^3}{\partial x \partial y^2} - 3B_{26}\frac{\partial^3}{\partial x \partial y^2} - B_{22}\frac{\partial^3}{\partial y^3}$$

and F is a differential operator representing the in-plane loading

$$F = t\left(\frac{\partial^2 \Phi}{\partial y^2}\frac{\partial^2 w}{\partial x^2} + \frac{\partial^2 \Phi}{\partial x^2}\frac{\partial^2 w}{\partial y^2} + 2\frac{\partial^2 \Phi}{\partial x \partial y}\frac{\partial^2 w}{\partial x \partial y}\right) \quad (2.30)$$

2.5 Postbuckling literature survey

Several early approximate solutions to the large deflection equations were proposed by Cox (1933) and Timoshenko (1936) by using the energy method. They assumed simple functions for u, v, and w, expressed the total potential energy of the system in terms of these functions, and then evaluated the arbitrary constants in u, v, and w by minimizing the energy with respect to them. Marguerre and Trefftz (1937) also applied the energy method to solve an improved version of the governing equations in which the initial curvature and imperfection were taken into account. Later, these equations were further expanded by Marguerre (1938) and were used for analysing simply supported infinitely long plates loaded in compression and shear. The energy method requires a minimum amount of numerical work and gives a fairly good prediction of the essential characteristics of the postbuckling process.

The Fourier series method is another widely used approach to approximate the solution of the Von Kármán equations. Levy (1942) assumed double Fourier trigonometric functions for w and F to break up the von Kármán equations into a set of equations that can be solved individually, and then recombined to obtain the solution for the simply supported plate under combined axial and lateral compression. Based on Levy's solution, Coan (1951) further adapted the Fourier series method. His approach was validated by analysing a simply-supported (out-of-plane) and stress-free (in-plane) plate with an initial imperfection under uniform compression. Yamaki (1960) also improved Levy's method and solved the governing equations for rectangular and circular plates subjected to various boundary conditions under combined loading. The advantage of the Fourier series approach is that it can achieve a higher order of accuracy if sufficient terms are

used. On the other hand, it usually involves lengthy computations, and because no explicit relationship among the variables is obtained, it is difficult to generalize the results.

The non-linear response involved in the elastic stability of conservative systems was first examined in general terms by Koiter (1945) in his thesis. In his theory, an asymptotic technique based on a Taylor series expansion around the critical load was used to approximate the equilibrium curve in the postbuckling range. This investigation of stability in the neighbourhood of the bifurcation point allowed the postbuckling behaviour to be classified according to the continuum of the critical load itself. The newly developed theory was applied to investigate the initial buckling and postbuckling of a strut, a plate and a shell. The concept of imperfection sensitivity was also introduced to explain why shell experiments did not act in accordance with Euler's classical theory. Koiter's work showed that shells possess unavoidable small imperfections, deviations from the desired ideal form which have a dramatic influence on their stability. This influence could reduce the ideal theoretical results by a factor of ten, invalidating previous results.

Koiter's theory drew little attention until the beginning of the sixties. Budiansky and Hutchinsion (1966) and Budiansky (1966) modified his theory and derived the general equation needed in order to conduct the asymptotic post-buckling analysis, which was referred to as the Budiansky–Hutchinson notation in a recent textbook (Byskov 2013). They also introduced a time dependant load $\lambda(t)$ and presented a general theory of dynamic buckling of imperfection-sensitive elastic structures. The analytical method developed by Koiter was subsequently applied to several stiffened plate and shell buckling problems, and was further extended to multiple buckling modes and buckling mode interactions; see, for example (Koiter 1976; Van der Neut 1969; Amazigo and

Hutchinson 1967; Byskov and Hutchinson 1977). A more comprehensive review of the development of postbucking analysis in the sixties and seventies can be found in the literature reviews written by Hutchinson and Koiter (1970) and Budiansky (1974).

The exploration of the postbuckling behaviour around a critical point can be regarded as a perturbation application which is only valid for a small post-buckling range around the vicinity of the critical point itself. Various numerical methods were proposed by Cochelin et al. (1994), Vannucci et al (1998) and Steen (1998) to extend the validity of Koiter's method and increase the precision of the asymptotic approximation.

The development of a more general non-linear buckling theory was initiated in the UK at University College London by Chilver (Thompson 1963) in the sixties. Later, Thompson (1969) developed Koiter's theory further by applying total potential energy principles to a discretized system and introducing the static perturbation method for explicit solutions of the postbuckling problem. This method indicated that an elastic system can be discretized into so-called generalized coordinates. In this discretized system, n discrete coordinates Q_n define the system geometry. The total potential energy $V = V(Q_1, Q_2, Q_3, \dots Q_n, p)$ is a function of Q_n and at least one loading parameter p. According to Thompson and Hunt (1973), the following two fundamental axioms in terms of total potential energy need to be applied to obtain the governing equilibrium equations and check the stability of each equilibrium state.

'Axiom 1: *A stationary value of the total potential energy with respect to the generalized coordinates is necessary and sufficient for the equilibrium of the system.*

Axiom 2: *A complete relative minimum of the total potential energy with respect to the generalized coordinates is necessary and sufficient for the stability of an equilibrium*

state.'

These two axioms can be written in mathematical form as follows:

- $\frac{\partial V}{\partial Q_i} = 0$ for any static system to be in an equilibrium state, where Q_i is a generalized coordinate previously defined.
- Considering the second derivatives of V, $\frac{\partial^2 V}{\partial Q_i \partial Q_j}$, the Hessian matrix V_{ij} must be positive-definite for stability. A singular matrix indicates a critical equilibrium state, with higher order terms needing to be derived in this case, to determine the stability of the system.

The status of an elastic system was then expressed in the form of the function V which could be used to determine the equilibrium path of the structure.

At the same time, parallel works by Sewell used similar theory to investigate the elastic stability of structures. Sewell (1965) illustrated the comprehensive steps of the static perturbation technique as applied to the investigation of the local shape of the equilibrium paths bifurcating from an equilibrium point of a general conservative and holonomic system (or structure) with a finite number of degrees of freedom. He showed that discretized systems combined with the static perturbation technique can be applied to structures which exhibit a bifurcation as well as a snap-through buckling. Sewell (1969) later compared Koiter's theory with discrete system theory and suggested that the latter provided a very quick overall view of the relationships between the load factor and the instability amplitudes (i.e. total displacement of a point in the structure) due to its starting assumption and convergence techniques.

The discrete coordinate method has since been used extensively in the field of postbuckling analysis for a variety of structures, for example, Hunt (Hunt et al. 1988) and

Hunt and Wadee (1998) utilized this approach to investigate the postbuckling behaviours of a sandwich plate in which two skins were separated by a relatively soft core. Postbuckling behaviour resulting from the interaction between the global Euler strut mode and the local buckling mode was investigated. The system was first discretized into two generalised coordinates known as the 'sway' (W) and 'tilt' (θ) modes. Another four degrees of freedom accounting for the in-plane displacements (u and v), total end shortening and total transverse shortening were then introduced to formulate the total potential energy equation. This six-degree-of-freedom model was used to trace the equilibrium paths of the system, and an analytical solution based on total potential energy principles showed that postbuckling was initiated by the overall mode of buckling and was rapidly followed by secondary bifurcation into an unstable combination of at least two local modes. The interaction between the first and second modes progressively destabilized the postbuckling response.

It is the modern use of high strength composite material that has made the problem of buckling and postbuckling of thin plate members one of practical importance. Since the von Kármán large deflection equations applied to laminate plates are non-linear partial differential equations which do not have an exact closed-form solution, identification of an appropriate approximate method which could be used to solve these equations was of great interest to researchers. Reissner and Stavsky (1961) provided a general non-linear buckling theory to demonstrate the existence of coupling phenomenon between mid-plane bending and stretching of an unsymmetrically laminated plate. The constitutive relationship between force, moment, stress resultants, strains and curvature in the mid-plane was established and the governing equations for buckling were expressed in terms of out-of-plane displacement (w) and an Airy stress function (Φ). Explicit solutions were

given for specific unsymmetrically laminated plates, for which $B_{11} = B_{12} = B_{22} = B_{66} = 0$, which leaves the B_{16} and B_{26} terms to cause the coupling. Lekhnitskii (1968) comprehensively established the basic theory of classical buckling for homogeneous orthotropic and anisotropic plates. Ambartsumian (1970) conducted a more complex buckling study which included the effect of transverse shear in orthotropic plates.

Whitney and Leissa (1969) further developed the anisotropic laminated plate theory by modifying the von Karman large deflection equation based on the Kirchhoff hypotheses. A closed-form solution to the linearised equations of unsymmetric cross-ply and unsymmetric angle-ply laminates was obtained. Results revealed that the buckling load decreased as the coupling between bending and stretching increased. The size of this reduction depended on the degree of anisotropy of the individual layers and the total number of plies in the laminate.

The extensive study of laminated plate buckling properties paved the way for more complicated postbuckling problems. The postbuckling of orthotropic plates under edge compression was firstly studied by Yusuff (1952). Analytical solutions were achieved by using a three-term deflection series function based on Coan's work. However, early analysis was only applied in the solving of buckling or postbuckling problems of a symmetrical laminate plate.

Prabhakara and Chia (1973) improved Yusuff's work by introducing a double Fourier series for both the transverse deflection and the stress function in order to solve the von Karman large deflection equations. Three types of orthotropic plates made of glass, boron, and graphite fibres was analysed. The study proved that composite plates experience

greater deflection than isotropic ones following the same increase in axial compressive stress beyond the buckling stress.

Turvey and Wittrick (1973), however, found that the differences between the postbuckling stiffness of symmetric and unsymmetric laminate plates is quite trivial despite the appearance of the in-plane and out-of-plane coupling terms B_{ij}. A further study by Harris (Harris 1975) observed that the stiffness change in an unsymmetric laminate plate after buckling is in most cases due to the interactions of different buckling modes. Prabhakara and Chia (1974) presented an analysis for the postbuckling behaviour of unsymmetrically layered rectangular anisotropic plates subjected to axial and biaxial compression under simply supported and clamped boundary conditions. The numerical results obtained showed that the load-displacement behaviours are no longer bifurcational due to the appearance of coupling terms B_{11} and B_{22} causing the bending effect to be present from the beginning of the loading process.

Feng (1983) used an energy approach to study the postbuckling behaviour of a composite plate subject to combined biaxial compression and shear with mixed boundary conditions. A Newton-Raphson iteration technique was used for the minimisation of the total potential energy which was expressed by a system of nonlinear coupled algebraic equations in terms of the in-plane displacements (u and v) and out-of-plane displacement (w). Both an I-beam stiffened panel and a J-beam stiffened panel were tested in combined compression and shear to compare with the analytical results obtained. It turned out that these analyses were unable to sufficiently capture the mode transitions observed in experiments.

The postbuckling behaviour of thin-walled composite structures such as stiffened panels is further complicated by the possibility of sudden changes in buckling mode-shape. The earlier investigation of this secondary instability phenomenon which is commonly referred to as a mode-jumping or a mode switch can be found in the studies conducted by Stein (1959b) and Supple (1970). More recent work dealing with the numerical analysis of mode-jump includes that of Shin (1993) who used an energy method to investigate the postbuckling of laminate plates under uniaxial compression. A truncated Fourier sine series associated with single and double half waves was used to represent the out-of-plane displacement w, so that a buckling mode change was allowed in the postbuckling range. The governing equation was then transferred to a series of trigonometric equations and solved using the principle of minimum potential energy. Several results were obtained to compare with experiments as well as other researchers' work and good agreement was achieved. Falzon and Cerini (2006; 2007) identified that standard nonlinear solution schemes such as the Newton–Raphson method and Riks method are unable to robustly capture mode-jumps. They presented a solution procedure based on the arc-length method, but which did not require restart schemes to capture the mode-jump in the vicinity of instabilities. This automated procedure can be as part of the quasi-static part of the solution or used as a modified explicit dynamic routine implemented in finite element software to quickly assess the possibility of a mode-jump.

Diaconu and Weaver (2005; 2006) derived an approximate closed-form solution for postbuckling of both symmetrically and unsymmetrically laminated infinitely long plates under axial compression. The composite plate postbuckling governing equations were nondimensionalized by using bounded non-dimensional parameters, which reduce the complexity of the formulation so that closed form solutions are achievable. The governing

equations were then solved in conjunction with simply supported boundary conditions by the use of the Galerkin method. Though the analysis of postbuckling for an infinitely long plate is closer to the real panels used in aircraft structures, the solutions did not take into account mode change and mode snap through.

Bisagni (2009) developed analytical formulations for the localised postbuckling behaviours of isotropic and anisotropic plates. Airy stress functions and out of plane displacements approximated by trigonometric shape functions were used to derive the nonlinear governing equation by applying the Ritz method. A creditable solution of the governing equations was then found by using the Newton–Raphson method. This approach was developed to investigate the localised postbuckling problems of symmetric laminate plates and stiffened panels. A fast analysis technique for non-symmetric composite plates was further developed by Vescovini and Bisagni (2016) who combined the use of a semi-analytical approach to study the postbuckling response and genetic algorithms were employed for the optimization of a composite plate.

A modified effective width method was developed by Pevzner and Abramovich (2008) to investigate the postbuckling and collapse load of laminate stiffened curved panels. In this study, the calculation of the ultimate load of the stiffened curved panel was replaced by calculation of the critical load of a column with an equivalent cross-section. The equivalent cross section of a stiffened curved panel carrying postbuckling load was then determined by buckling, bending and torsion geometric relationships. The idealised predictions of collapse load in the postbuckling state compared well with test results and finite element simulations. These efficient idealisation techniques were used as an

additional validation approach for buckling and postbuckling experiments of complex gemmetry such as box sections (Abramovich et al. 2008).

Based on the well-established postbuckling analysis techniques, the postbuckling behaviour of plates made by the novel material or innovative manufacturing approaches, such as functional gradient material (FGM) plates and variable angle tow (VAT) plates, can be analysed. Wu et al. (2008) investigated the post-buckling response of FGM rectangular plate subjected to in-plane edge compressive loading. The governing equation was derived by using on first-order shear deformation theory and solved by applying a second-order polynomial shape functions. The postbuckling of FGM plate including the thermal effect was further studied by Shen et al. (2017) who employed a Koiter-type perturbation technique to determine the buckling loads and the postbuckling equilibrium paths. Wu (2013) and Coburn (2016) recently studied the postbuckling behaviours of variable angle tow (VAT) composite plates and sandwich plate. VAT plates possessing pointwise variable in-plane stiffness properties allow the fibres to be arranged in the direction of load paths to efficiently re-distribute the postbuckling stresses thereby improving the plate structural performance according to design requirements. The postbuckling behaviours of VAT plates were modelled by a mixed variational approach containing a single variational formula to express Airy's stress function and the transverse deflection function. The Rayleigh–Ritz method was subsequently applied to solve the postbuckling problem. Comparison with numerical results showed that the postbuckling stiffness reductions seen in the VAT plates with linear fibre variations were less obvious compared with that in conventional straight-fibre composite plates.

Chapter 3

Exact finite strip method and its applications

This chapter focuses on reviewing related numerical methods and software providing key ideas and platforms that can be used to determine the postbuckling behaviours of a thin plate. The chapter is organised as follows: Section 3.1 gives a general review of the finite element method (FEM) and its applications in plate postbuckling analysis. Sections 3.2-3.4 review the related finite strip method (FSM) work with a focus on the exact strip modification and the special algorithm used to support the application of the exact strip approach. Sections 3.5-3.7 summarise the theory of the exact strip software, VIPASA, VICON and VICONOPT, the platforms which are used in this thesis to generate results and develop improvement work. Section 3.8 discusses the development and analysis features of the plate postbuckling function in the VIPASA software, while Section 3.9 concludes the chapter.

3.1 Finite element method

With the advance of modern computational technology, the finite element method (FEM) is the most widely used numerical method for solving structural stability problems. FEM is conducted by discretising a continuous system into a finite number of elements which are connected at selected node points. Node points are the places where the forces and

displacements are defined, and then individual element stiffness matrices expressing the relationship between these nodal forces and nodal displacements can be established based on the total potential energy principle. The global stiffness matrix showing the relationships for the entire system is obtained by combining the individual element stiffness matrices, and then this system of equations is solved. In finite element analysis, the degrees of freedom the node point possesses, the number of node points within an element and the mesh size over the whole system have a significant effect on the accuracy and computational cost of the solving techniques. More details of FEM can be found in classic textbooks by Przemieniecki (1968), Zienkiewicz and Taylor (2005), and Cook (2007)

There is a large volume of research work on structural stability problems conducted by applying FEM with varying degrees of complexity. Earlier FEM studies used one-dimensional beam-column elements or two-dimensional rectangular elements to solve buckling problems of thin-walled structural members (Barsoum and Gallagher 1970)(Chin et al. 1993). Although efficient and straightforward, these approaches are only capable of predicting the overall member buckling load and will not be sufficient to estimate local buckling modes or postbuckling behaviours. Olsen and Byskov (1982) first formulated Koiter's method in terms of finite elements. A unique discretisation technique was introduced to restructure the standard compatible finite element formulation, which allowed the combination of asymptotic and finite element methods. Later much more complicated three-dimensional higher order elements (Shiau and Wu 1995) were developed and applied to investigate the postbuckling behaviour of a composite laminated plate subjected to edge shortening or in-plane compressive loading.

The finite element method has been implemented in several powerful commercial packages, including ABAQUS (1998), ANSYS (2009) and NASTRAN (1970). ABAQUS has

been used extensively in this thesis to model plate structures and to solve plate buckling and postbuckling problems. A widely used technique for modelling postbuckling within ABAQUS includes two separate steps (Hibbit et al. 2012). A linear eigenvalue buckling analysis is firstly conducted to find and scale the initial buckling modes, and then the appropriate eigenmodes are imported as initial geometric imperfections into a nonlinear Riks analysis (Riks 1979) to find the post-buckling response.

The use of finite element software gives the user the flexibility to decide the complexity of the model according to the physical specimen. However, these flexibilities can lead to various errors, such as modelling errors, discretisation errors and round-off errors. The software sometimes gives unrealistic solutions if these errors are left unchecked. For this reason, whilst there have been a significant number of analyses conducted using FEM, but caution should be exercised when implementing results into designs, and verification with experimental data or analytical methods must be conducted (Lynch et al. 2004).

3.2 Finite strip method

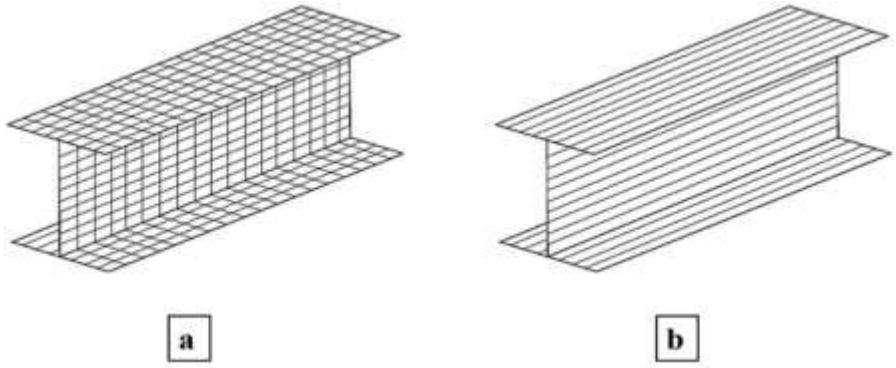

Figure 3.1 Diagrams showing the discretisation used in (a) FE methods and (b) finite strip methods.

An alternative approach to analysing thin-wall structures is the finite strip method (FSM), developed since the 1960s by Cheung (1976). The FSM only divides the structure into a

number of longitudinal strips (Figure 3.1b), in contrast to the FEM which divides the structure into a mesh grid (Figure 3.1a). In the FSM, the longitudinal deformed shape is interpolated by an appropriate series of trigonometric functions or polynomial functions which must satisfy a priori the geometric boundary conditions at the plate ends, and the transverse or out-of-plane deformed shape can also be assumed. The equilibrium equation is then derived by energy methods, and the linear buckling problem can be subsequently expressed in matrix form as

$$\left[\mathbf{K} - \lambda \mathbf{K_g}\right][\mathbf{D}] = \{\mathbf{0}\} \tag{3.1}$$

where $\mathbf{K}$ and $\mathbf{K_g}$ are the stiffness and geometric stiffness matrices respectively, and $\mathbf{D}$ is a vector of nodal displacements. λ is a load factor which can be extracted using various eigenvalue algorithms.

Subsequent to linear buckling, different forms of the FSM were developed by other researchers and applied to various plate buckling and postbuckling analyses. Dawe et al. (1993) used a FSM based on the Classical Plate Theory (CPT) to predict the postbuckling response of prismatic composite plates. A trigonometric function was used to adequately represent the longitudinal displacement so that an enhanced strain-displacement relationship could be achieved. Wang and Dawe (1996) extended the previous FSM in the context of First Order Shear Deformation Theory (SDPT) to enable the method to include the through thickness shear effect during the postbuckling of prismatic plate structures. Various geometric configurations were analysed and compared with FEM, but the mode shape was limited to the overall buckling mode.

Instead of using continuous trigonometric functions, a special finite strip model whose displacement field uses cubic B-splines longitudinally, quadratic crosswise interpolation of the in-plane displacements and cubic crosswise interpolation of the out-of-plane

displacements was developed by Dawe and Wang (1998) and used to analyse the postbuckling behaviour of laminated plates. This spline finite strip more easily satisfies explicitly the kinematic conditions at the plate ends and achieves good agreement with buckling and postbuckling results from FEM. It may be noted that all the FSMs mentioned above can be categorised as semi-analytical FSMs since the longitudinal exact solution of the governing equations is imposed and only the transverse solution is found.

Ovesy and his co-workers (2005; 2006) developed an alternative FSM where the out-of-plane displacement within a strip is the only postulated displacement, and the in-plane displacement is derived based on that. They called this method the semi-energy FSM as opposed to the full-energy FSM in which all displacement fields (i.e. both the in-plane and the out-of-plane displacement) are represented by appropriate shape functions. The developed semi-energy FSM was applied to analyse the initial postbuckling behaviour of thin flat plates (Ovesy et al. 2005), open channel sections (Ovesy et al. 2006) and box section struts (Ovesy et al. 2006).

Ghannadpour and his co-workers further improved the above-mentioned method and developed the so-called full-analytical-FSM. In this theory, each strip was regarded as a plate, and thus the Von-Karman's equilibrium equation is solved exactly to obtain the out-of-plane displacements and buckling mode. This shape function is used to obtain a transcendental stiffness matrix for the corresponding strip based on the principle of minimum potential energy. The transcendental overall stiffness matrix for the whole section is then obtained by assembling the individual strip stiffness matrices and solved by applying various numerical methods. The calculated buckling loads and modes were claimed to be fully analytical since the usual FSM approximations with respect shape functions were avoided. Subsequently, Von-Karman's compatibility equation is solved exactly to obtain the general form of the in-plane displacement fields in the post-buckling

region. This full-analytical-FSM has been applied to analyse the postbuckling behaviour of thin isotropic struts (Ghannadpour and Ovesy 2008) and plates (Ovesy and Ghannadpour 2009), symmetric laminate plates (Ghannadpour and Ovesy 2009) and moderately thick plates (Ghannadpour et al. 2015).

The above literature demonstrates the versatility of the FSM in analysing the buckling and postbuckling behaviour of various structural components. Since the order and bandwidth of the matrix to be solved are considerably reduced compared with the FEM, the method is particularly attractive with regard to its computational efficiency and numerical accuracy. However, the finite strip method is not applicable when dealing with irregular structures which cannot be easily divided into strips.

3.3 Exact finite strip method

Wittrick (1968a; 1968b) proposed the exact strip method for determining the elastic stability of plate assemblies. In this approach, the plate is divided into a series of strips which are rigidly connected at their edges. Having assumed a sinusoidal variation of the buckling mode in the longitudinal direction only, the governing differential equations of each component strip are transformed to transcendental ordinary differential equations according to classical plate theory. The assumption of sinusoidal variation not only leads to a convenient single-term type of analysis, but also satisfies the buckling mode shape and nodal line conditions which are straight and parallel to the ends in the absence of shear and anisotropy. By solving the governing differential equations explicitly, a stiffness matrix containing transcendental coefficients can be assembled.

Wittrick and Curzon (1968) further extended this analysis to account for the presence of in-plane shear loading. With the appearance of shear load, the nodal lines are skewed and

hence there are spatial phase differences across the width of the plates. These differences are addressed by defining the magnitude of displacement and other quantities using complex quantities. In order to satisfy the single sinusoidal term assumptions, the structure is assumed to be much longer than the half-wavelength of the buckling mode, so that the buckling mode can be regarded as local in the context of an infinitely long structure. The exact approach of Wittrick (1968) was extended to incorporate a certain level of anisotropic material behaviour by Viswanathan et al. (1973; 1974) where analyses of flat and curved component plates were conducted.

The exact stiffness method differs from other finite strip methods in the sense that the strip properties are based on the direct solution of the governing differential equations of classical plate theory, rather than on the use of energy or work principles. By solving the governing differential equations for each strip explicitly, a stiffness matrix containing transcendental coefficients can be assembled. Since the transcendental function is highly nonlinear, the standard linear eigenvalue routines cannot be used to extract the buckling load (Williams and Wittrick 1970). To obtain the eigenvalues therefore, the Wittrick-Williams (W-W) algorithm was developed.

3.4 Wittrick-Williams (W-W) algorithm

It is well known that the eigenvalues represent natural frequencies in free vibration problems or critical load factors in buckling problems. The Wittrick-Williams (W-W) algorithm (Wittrick and Williams 1974) is a numerical technique developed to calculate the number of eigenvalues which lie between zero and any trial value, and convergence can be achieved on any required natural frequency or critical load factor to any specific accuracy without determining them explicitly. This algorithm was first introduced by

Wittrick and Williams for determining the natural frequencies of vibration problems (1970), followed by finding the critical buckling load for elastic structures (1973). The procedures of the Wittrick-Williams (W-W) algorithm, though explained and applied by countless papers, is briefly elaborated here for the sake of completeness.

1. The global stiffness matrix $\mathbf{K}$ of the overall structure is first assembled from the member stiffness matrices $\mathbf{K_m}$. The global stiffness $\mathbf{K}$ relates a finite set of displacements D at the nodes of the structure to their corresponding perturbation forces P, by

$$\mathbf{KD} = \mathbf{P} \tag{3.2}$$

2. The critical buckling load of the structure corresponding to the eigenvalues is found by solving

$$\mathbf{KD} = \mathbf{0} \tag{3.3}$$

3. The determinant of the stiffness matrix should equal to zero ($|\boldsymbol{K}| = 0$) to obtain the eigenvalues. Hence, the usual form of Gauss elimination is applied to the global stiffness matrix $\mathbf{K}$, and it is transformed into its upper triangular $\mathbf{K^{\Delta}}$ form.
4. The number of negative terms on the leading diagonal of $\mathbf{K^{\Delta}}$ is now defined as the sign count $s\{K(f)\}$ which forms the fundamental basis of the algorithm. The number of eigenvalues J of a structure lying below a trial value f^* can then be calculated as

$$J = J_0 + s\{K(f^*)\} \tag{3.4}$$

where J_0 is the summation of the number of eigenvalues of all single elements within the structure which are still lower than the trial value (f^*) when their nodes are fully clamped and can be expressed as

$$J_0 = \sum_m J_m \tag{3.5}$$

where J_m is the number of eigenvalues of member m exceeded at the trial value f^* when its ends are fully restrained.

5. Once $s\{K(f^*)\}$ and J_0 are known, standard numerical techniques, for example, the bisection method or parabolic interpolation, can be used to find any critical load factor or natural frequency within any desired accuracy.

3.5 VIPASA

VIPASA is a powerful software developed in the 1970s and incorporating the Wittrick-Williams algorithm to analyse buckling and vibration problems including prismatic plate assemblies. Allowing for general loading and geometry configurations, VIPASA was a preferred preliminary design package at NASA and was proved to be faster than conventional finite element programs, e.g. STAGS (Structural Analysis of General Shells) (Almroth et al. 1981), whilst retaining acceptable accuracy (Stroud et al. 1984).

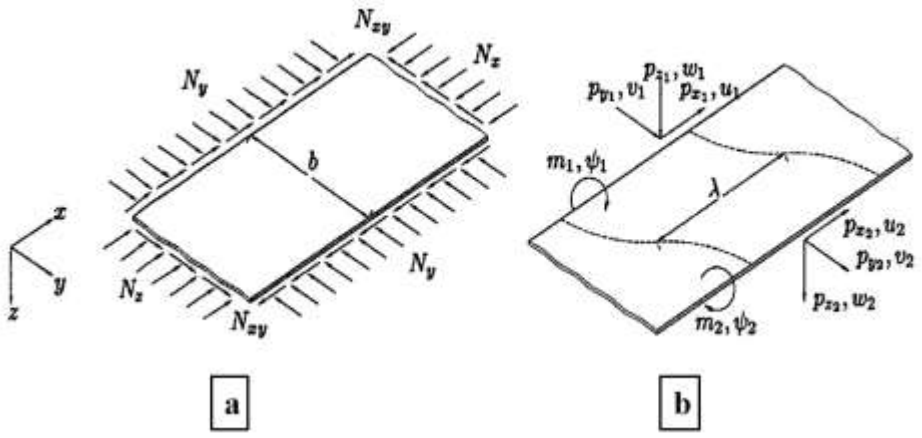

Figure 3.2 The VIPASA component plate: (a) a component plate of width b, subject to in-plane loads per unit width N_x, N_y, N_{xy} together with a reference axis system; (b) the skew model lines resulting from shear or material anisotropy predicted by a VIPASA analysis. Perturbation forces are given by p_j $(j = 1,2)$, displacements u, v, w corresponding to deflections in x, y, z directions and ψ is the rotation about the x-axis.

VIPASA uses the exact stiffness method based on classical thin plate theory while allowing some degrees of anisotropy. VIPASA analysis is fast and accurate for isotropic plates or composites plates where layups are balanced and symmetric implying that coupling between the in-plane shear and extension (A_{16} and A_{26} are zero), and coupling between in-plane membrane and out-of-plane bending (**B** matrix is zero) is not permitted (Wittrick and Williams 1974).

In VIPASA analysis, perturbation force and displacement vectors are defined by

$$\mathbf{P_j} = \{m_j \; p_{zj} \; p_{yj} \; ip_{xj}\} \tag{3.6}$$

$$\mathbf{d_j} = \{\psi_j \; w_j \; v_j \; iu_j\} \tag{3.7}$$

These edge forces need to be multiplied by $\exp(i\pi x/\lambda)$, where complex terms are used to allow for the possible spatial phase differences between edge force and displacement to be taken into account. The stiffness matrices are defined as

$$\mathbf{P}_1 = \mathbf{k}_{11}\mathbf{d}_1 + \mathbf{k}_{12}\mathbf{d}_2 \tag{3.8}$$

$$\mathbf{P}_2 = \mathbf{k}_{21}\mathbf{d}_1 + \mathbf{k}_{22}\mathbf{d}_2 \tag{3.9}$$

which can be combined as

$$\mathbf{p} = \mathbf{kd} \tag{3.10}$$

According to the out-of-plane and in-plane elastic properties of the plate, the stiffness matrix **k** can be expressed explicitly in complex Hermitian form as

$$\mathbf{k_{11}} = \begin{bmatrix} s_{MM} & -s_{MQ} & 0 & 0 \\ \overline{-s_{MQ}} & s_{QQ} & 0 & 0 \\ 0 & 0 & s_{NN} & -s_{NT} \\ 0 & 0 & -s_{NT} & s_{TT} \end{bmatrix} \tag{3.11}$$

$$\mathbf{k_{22}} = \begin{bmatrix} s_{MM} & \overline{s_{MQ}} & 0 & 0 \\ s_{MQ} & s_{QQ} & 0 & 0 \\ 0 & 0 & s_{NN} & s_{NT} \\ 0 & 0 & s_{NT} & s_{TT} \end{bmatrix} \tag{3.12}$$

$$\mathbf{k_{12}} = \overline{\mathbf{k_{21}^t}} = \begin{bmatrix} f_{MM} & f_{MQ} & 0 & 0 \\ -f_{MQ} & -f_{QQ} & 0 & 0 \\ 0 & 0 & -f_{NN} & -f_{NT} \\ 0 & 0 & f_{NT} & f_{TT} \end{bmatrix} \tag{3.13}$$

where a bar denotes the complex conjugate, and superscript t denotes the transpose. Expressions for the individual stiffness coefficients s, f are derived by solving the out-of-plane and in-plane governing equations (Wittrick and Williams 1974). The stiffness is expressed in terms of in-plane displacements u, v and out-of-plane displacement w and rotation ψ, and the overall system equation is assembled in the form

$$\mathbf{KD} = \mathbf{P} \tag{3.14}$$

The eigenvalues of the stiffness matrix are obtained by using the W-W algorithm combined with standard numerical methods.

The advantages of the VIPASA software were addressed by Williams et al. (1991), where the solution time from VIPASA for a composite six-blade stiffened panel under pure compression was 1000 times faster than that from the finite element program STAGS while the error was less than 1%. Faster solution times, effective data preparation and less computer memory usage made VIPASA extremely efficient in the preliminary aircraft design stage especially in the era in which computers were much less powerful than today. However, the requirement that shear load and anisotropy are absent for accurate analysis with simply supported end conditions reduced the versatility and robustness of the software, and hence further development was required.

3.6 VICON

VICON (VIPASA with Constraints), an enhanced version of the VIPASA analysis, was developed in Cardiff University, inheriting all the functionalities and capabilities of VIPASA while addressing its conservative nature under the influence of shear and anisotropy (Anderson et al. 1983). The way in which VICON analysis overcomes the inaccuracy which appeared in VIPASA is to introduce Lagrangian multipliers to incorporate a set of constraints which can be regarded as regularly repeating point supports, so that the plate is set to be infinitely long and the skewed mode is local in nature. The transcendental stiffness matrices can be established by using the total energy principle and solved by the modified Wittrick-Williams algorithm (F W Williams and Anderson 1983). The analysis procedure is briefly summarised below.

i. Since the sinusoidal assumptions can still be valid under shear and anisotropy if the structures are infinitely long, the deflected shape of the infinitely long panel can no longer be appropriately represented by a single term analysis. Hence, a Fourier series which couples the buckling or vibration responses of the panel at different values of half-wavelength is used to interpolate the deflected shape of the infinitely long plate assembly:

$$\mathbf{D_a} = \sum_{m=-\infty}^{\infty} \mathbf{D_m} \exp\left(\frac{i\pi x}{\lambda_m}\right) \tag{3.15}$$

$$\mathbf{P_a} = \sum_{m=-\infty}^{\infty} \mathbf{K_m D_m} \exp\left(\frac{i\pi x}{\lambda_m}\right) \tag{3.16}$$

Equation 3.15 shows that the nodal deflections $\mathbf{D_a}$ of the infinite plate assemblies consist of a series of coupling deflection modes $\mathbf{D_m}$ from the VIPASA analysis. The deflections are then used to obtain forces at each node as shown in Equation 3.16 where $\mathbf{K_m}$ is the VIPASA stiffness matrix for half-wavelength λ_m.

ii. The infinitely long plate assembly is modelled by allowing the elastic point support constraints to repeat at intervals of the actual panel length l, so that the buckling or vibration mode also repeats n times over a length Ml, where M and n are integers. An accurate mode shape is then achieved by coupling different half-wavelengths λ_m together using the expression

$$\lambda_m = \frac{l}{\xi + 2m}\ , (m = 0, \pm 1, \pm 2 \ldots \pm q) \tag{3.17}$$

where m and q are integers, and ξ can be given as $\xi = 2n/M$, $(0 \leq \xi \leq 1)$. The critical load factor can be found by examining all values of ξ or, more practically, a representative set of values in the range 0 to 1. The length over which the mode shape repeats can be represented by

$$L = \frac{2l}{\xi}\ (0 \leq \xi \leq 1) \tag{3.18}$$

iii. The fundamental difference between VICON analysis and VIPASA analysis is the usage of Lagrangian Multipliers which couple the responses of different half-wavelengths λ_m. Applying the Lagrangian Multiplier method involves setting up a target function φ, which represents the total energy function, expressed in terms of the nodal deflection $\mathbf{D_a}$ and the stiffness matrices $\mathbf{K_m}$, plus the product of the Lagrangian Multipliers and the constraints. The target function φ is given by

$$\varphi = \sum_{m=-\infty}^{\infty} \frac{1}{2} \mathbf{D_m^T K_m D_m} + \mathbf{P_L^T} \sum_{m=-\infty}^{\infty} \mathbf{E_m D_m} \tag{3.19}$$

where $\mathbf{P_L}$ is the vector of Lagrangian Multipliers, $\mathbf{E_m}$ are the constraint matrices, and superscript T denotes the transpose of a matrix. A graphical explanation of the use of Lagrangian constraints is presented in Figure 3.3. The Lagrangian multipliers are used to couple the stiffness matrices of component structures to

represent connections between the structures, and physically represent the reaction forces needed to enforce the constraints.

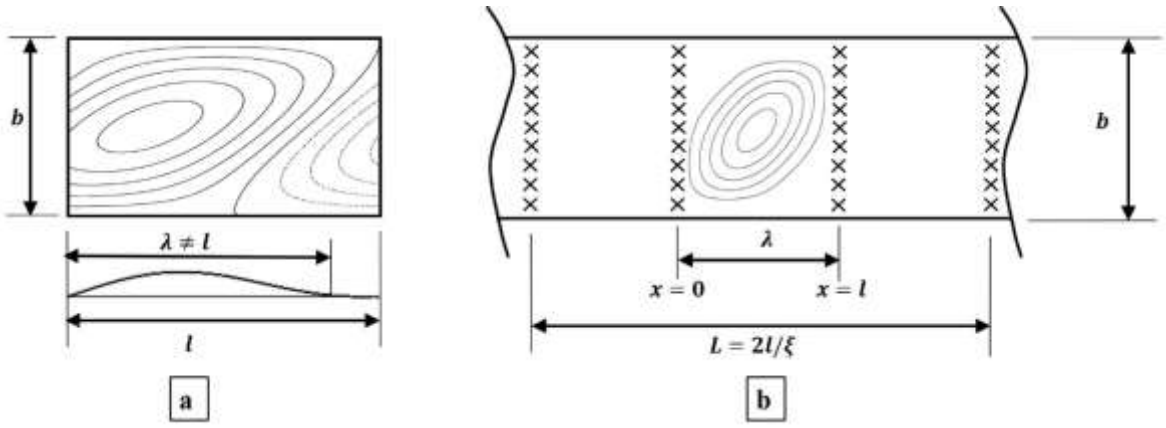

Figure 3.3 Graphical explanation of the use of Lagrangian constraints: (a) a panel with a skew traverse support of a finite length l, and (b) a panel of infinite length which use Lagrangian constraints to provide point supports with point supports (shown as crosses), so that the continuous halfwaves λ in the longitudinal direction can be enforced.

iv. In order to minimise the total energy subjected to the constraints, the partial derivatives of function φ with respect to the elements of the stiffness matrices D_m are equated to zero to find the stationary value of φ, which gives,

$$\mathbf{L K_m D_m + E_m^H P_L = 0} \tag{3.20}$$

$$\sum_{m=-\infty}^{\infty} \mathbf{E_m D_m = 0} \tag{3.21}$$

Then the eigenvalue problem can be written in matrix form by combining Equation 3.20 and Equation 3.21:

$$\begin{bmatrix} LK_0 & & & & & & E_0^t \\ & LK_1 & & & & & E_1^t \\ & & LK_{-1} & & & & E_{-1}^t \\ & & & LK_2 & & & E_2^H \\ & & & & LK_{-2} & & E_{-2}^t \\ & & & & & \ddots & \vdots \\ E_0 & E_1 & E_{-1} & E_2 & E_{-2} & \cdots & 0 \end{bmatrix} \begin{bmatrix} D_0 \\ D_1 \\ D_{-1} \\ D_2 \\ D_{-2} \\ \vdots \\ P_t \end{bmatrix} = 0 \tag{3.22}$$

where $\mathbf{K_m}$ $\mathbf{E_m}$ and $\mathbf{D_m}$ are the corresponding component matrices, and the negative sign in the subscripts indicates the complex conjugates.

v. To solve the resulting complex transcendental matrices, the Wittrick-Williams algorithm has been modified to allow Lagrangian Multipliers to be used. In VICON analysis, the Wittrick-Williams algorithm can be written as,

$$J = \sum_{m} (J_{0m} + s\{K_m\}) + s\{R\} - r \tag{3.23}$$

The first two terms of Equation 3.23 count the number of eigenvalues for the plate assembly for each of the half-wavelengths λ_m, $s\{R\}$ denotes the sign count of the constraint matrix R and r is the number of the constraints. Thus, the number of eigenvalues J between 0 and any trial value can be obtained by summing the above terms, so that eigenvalues can be found by the same bisection or parabolic interpolation method used in VIPASA.

In summary, the VICON analysis was developed to overcome the inaccuracies in VIPASA when shear or anisotropy appeared. VICON analysis uses Lagrangian multipliers to couple VIPASA stiffness matrices for an appropriate set of half-wavelengths, so that the compatibility of an infinitely long plate with repeating rigid and elastic point supports structure is achieved.

VICON analysis has been applied in many other stability problems as well. Wittrick and Horsington (1984) used VICON-type analysis combined with the Rayleigh-Ritz method to deal with folded structures which are joined together by several finite length orthotropic plates under combined shear and compression. Williams and Anderson (1985) developed a related further procedure which does not require the use of Lagrange multipliers but which enforces the compatibility of the structure with diaphragm end supports at a number of discrete points.

3.7 VICONOPT

VICONOPT (VIpasa with CONstraints and OPTimization) is a 50,000-line Fortran 77 computer program which covers both prismatic plate assembly analysis and optimisation in the aerospace structure design process (Williams et al. 1990, 1991). In terms of analysis capability, VICONOPT incorporates the features of both VIPASA and VICON, enabling the calculation of critical buckling load factors, or undamped natural frequencies, and correct mode shapes for any prismatic assembly of anisotropic plates under any combination of compression and shear (Williams et al. 1990). To provide an optimum design capability to VICONOPT, continuous design procedures were introduced by Butler and Williams (1992) based on a sizing strategy with the well-established linear optimiser CONMIN (Vanderplaats 1973) used to converge on a safer design of low mass. Details of the continuous design optimisation process are illustrated in Figure 3.4 and summarised below.

An initial analysis (step 1) is performed to determine the most important constraints in the design, such as critical buckling load. This is followed by an initial stabilisation (step 2) which scales the thickness variables in the initial design configuration to achieve 'a just stable status'. The sizing cycle starts at (step 3), which begins by calculating a set of critical constraints such as critical buckling factors, and their sensitivities. Appropriate lower and upper design variable limits are determined in (step 4) and these limits are passed to the CONMIN optimiser. In the CONMIN optimisation (step 5), the design variables are iteratively changed by applying the method of feasible directions in which the objective function $W(\{X\})$ is minimised under the conditions of $G_m(\{X\}) < 0$ and $\{X_L\} \leq \{X\} \leq \{X_U\}$. $G_m(\{X\})$ is a function that contains the design constraints, and $\{X_U\}$, and $\{X_L\}$ are the upper and lower design limits, respectively. The iteration process is

performed using an approximate analysis based on a first-order Taylor series expansion. Having completed the CONMIN optimisation, another stabilization calculation (step 6) is carried out to verify the feasibility of the new design, which ensures the design is just stable. More CONMIN cycles are performed with intelligent adjustment of the move limits so that the convergence can be accelerated. Then the new configuration is used as a starting point for the next sizing cycle. Once convergence has been obtained for all the CONMIN and sizing cycles (Steps 7 and 8), a final VICONOPT analysis (Step 9) is carried out to verify the buckling results.

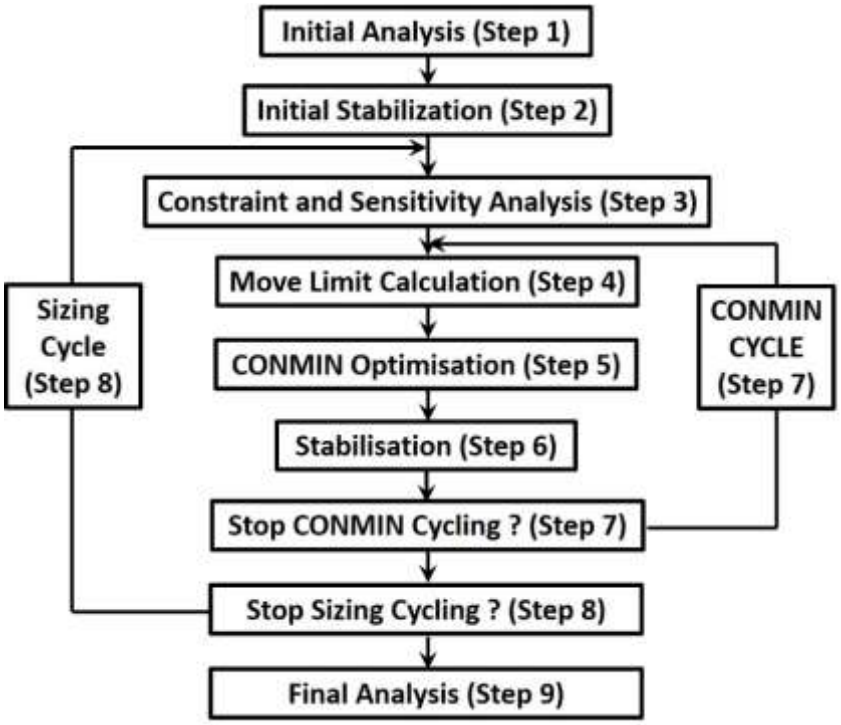

Figure 3.4 The VICONOPT continuous optimisation process.

Apart from the continuous optimisation discussed above, VICONOPT is able to conduct other types of optimisation, such as discrete optimisation, discontinuous cost function optimisation (Kennedy et al. 1999) and vibration constraint optimisation (O'Leary 2000; O'Leary et al. 2001). Fischer et al. (2002) developed an interface for multilevel optimisation called VICONOPT MLO (Multi-Level Optimisation), which connected

VICONOPT with the finite element software MSC/NASTRAN to optimise complex aerospace structures like wing boxes. More recent research conducted by Qu (2011) took postbuckling effects into consideration and created the new multilevel optimisation interface VICONOPT MLOP (VICONOPT MLO with Postbuckling). Although the author has not used these optimum design features in this thesis, it is important to mention that VICONOPT is not only an analysis computer program but has capabilites for design and optimisation purposes.

3.8 VIPASA postbuckling

The exact strip method combined with the Wittrick–Williams algorithm presented in previous sections provide a solid foundation for the postbuckling analysis of prismatic structures to be carried out in the VICONOPT software. The postbuckling analysis capability in VICONOPT was first developed based on the VIPASA type of analysis, which was extended to cover the geometrically non-linear local postbuckling analysis of a longitudinally compressed plate (Powell et al. 1998). The postbuckling analysis started with the VIPASA buckling analysis to efficiently find the critical buckling load and the initial buckling mode. Then a pre-determined increment of the mode amplitude including an imperfection, which was conservatively assumed to have the same mode shape, was added to the buckling mode to calculate the corresponding applied load (P), longitudinal strain (ε_x), and stress resultants (N_x). Next, the Wittrick-Williams algorithm was used to find the correct postbuckling mode shape and amplitude (w) for that given stress distribution.

Calculating the above quantities is defined as a postbuckling cycle and convergence within each cycle is based on finding consistent estimates of P, ε_x, N_x before the

commencement of each new cycle. Once convergence is achieved a new cycle begins with another increment of mode amplitude followed by a similar calculation to that mentioned above, with the postbuckling analysis procedures stopping when a pre-defined number of cycles is reached. Although good agreement has been obtained with previously published results, some problems with regularly spaced stiffeners exhibit slow convergence due to the limited numerical accuracy of the mode shapes, interaction between similar local modes and mode jumping (Watson and Kennedy 2004). This difficulty can be partially avoided by using an infinitely wide model.

An alternative exact strip postbuckling analysis which relies on Newton iteration was developed by Anderson and Kennedy (2008) and has been implemented in the VIPASA analysis option of VICONOPT. In this version of VIPASA postbuckling analysis, each component plate is modelled as a substructure comprising n_s longitudinal strips of equal width b_s shown in Figure 3.5.

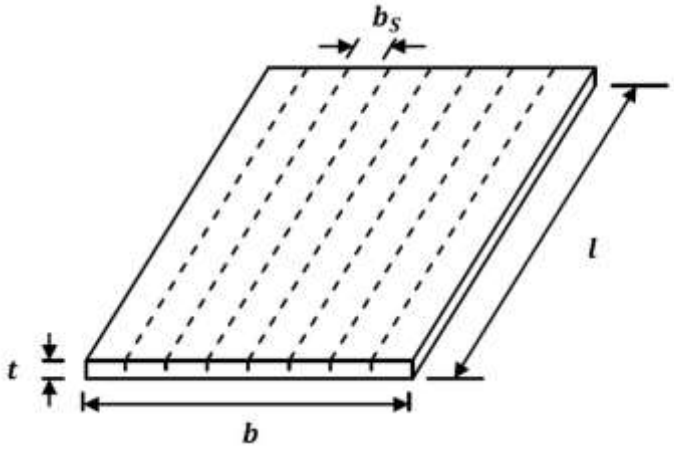

Figure 3.5 Plate of width b, divided into n_s strips of equal width b_s.

This analysis is again controlled through a number of cycles which are defined by pre-determined increments of longitudinal or shear strain. Within each cycle, convergence on several quantities including the total applied load, the variation of stress resultants across

the structure, and the amplitude and shape of the postbuckling mode is required. In order to address the inaccurate mode shape problems mentioned above, a recursive Newton method involving the inverse iteration method is introduced to give accurate convergence on the critical buckling load and associated mode which solve the transcendental eigenproblem;

$$\mathbf{KD} = \mathbf{0} \tag{3.24}$$

where $\boldsymbol{D} = \{D_j; j = 1 \dots n\}$ is the mode vector of the structure, which includes displacements and rotations at the edges of each strip. $\mathbf{K} = \{K_{ij}; i, j = 1 \dots n\}$ is the corresponding exact stiffness matrix containing transcendental function of the stress resultants in each strip. The postbuckling iteration process begins with assuming a trial mode $\mathbf{D}^*$ and searching for an adjustment vector $\mathbf{d}$ which are added together to update the buckling mode vector $\mathbf{D}$:

$$\mathbf{D} = \mathbf{D}^* + \mathbf{d} \tag{3.25}$$

The key feature of this method is that, instead of using the Wittrick-Williams algorithm, Newton iterations are performed which can be expressed in matrix form as:

$$\left(\mathbf{K}^* + \sum_{j=1}^{n} \frac{\partial \mathbf{K}^*}{\partial D_j} d_j\right)(\mathbf{D}^* + \mathbf{d}) = 0 \tag{3.26}$$

where $K^* = K(D^*)$. Neglecting higher order terms Equation3.26 becomes

$$\sum_{j=1}^{n}\left(\mathbf{K}^*_{\mathbf{ij}} + \sum_{k=1}^{n} \frac{\partial \mathbf{K}^*_{\mathbf{ij}}}{\partial D_j} D^*_k\right) d_j = -\sum_{j=1}^{n} \mathbf{K}^*_{\mathbf{ij}} D^*_j \quad (i = 1 \dots n) \tag{3.27}$$

d_j can be obtained by solving Equation 3.27, and a new trial mode vector $\mathbf{D}$ can be expressed by substituting d_j into Equation 3.25, passing $\mathbf{D}^*$ to the next Newton iteration. Finite difference approximations combined with suitably small perturbations about the

trial values D_j^* are used to achieve the derivatives needed in Equation 3.27. It should be noted that when an element D_j is perturbed, the only non-zero derivatives in Equation 3.27 are those of the plates (or for some loading conditions, strips) immediately adjacent to D_j, and this is allowed for in the logic of the computer coding. For anisotropic and shear loaded panels, Equation 3.27 is assembled and solved using complex arithmetic. Convergence on the amplitude and shape of the mode vector **D** implies convergence on the adjustments to the stress resultants due to flexure, and hence the postbuckling stress distribution and total loads on the structure can be calculated.

3.9 Concluding remarks

This chapter presents an overview of some of the important numerical methods that are relevant to the subjects covered in this thesis. The early concepts of FEM were first addressed and then compared with conventional FSM, and some of the most closely related literature was discussed. The chapter focused on the more specialised branch of FSM-the exact strip method, first outlined systematically by researchers such as Wittrick and Williams (1968; 1970), with an important feature of this being the development of the first special algorithm for the solution of transcendental eigen problems. The theory behind and features of the exact strip software VIPASA, VICON and VICONOPT were discussed and summarised. Analysis models and results from exact strip software are used extensively in the remaining chapters of the thesis. Recent works by Powell (1998) and Anderson and Kennedy (2008) have made suggestion regarding recommended directions for further work and this thesis is a development of their research. In the following chapters, an alternative post-buckling approach will be developed using some of the analysis principles in exact strip methods that have previously been discussed in this literature review.

Chapter 4

Simulated VICON analysis

In this chapter, a Simulated VICON analysis based on investigating the difference in postbuckling stiffness between VIPASA and VICON analyses is developed for the first time to carry out postbuckling analysis of a prismatic plate with shear load or anisotropy. The proposed method is applied to focuses on the analysis of a thin plate under combined shear and compression loading. The hypothesis is that the ratio of postbuckling to prebuckling axial stiffness given by VIPASA buckling and post-buckling analysis can be used to work out the corresponding VICON postbuckling stiffness and strain, so that characteristic plate postbuckling features such as load-strain curves can be achieved by an iterative process involving successive increases of the longitudinal strain and total applied load. The chapter is organised as follows: Section 4.1 expands on the differences between VIPASA and VICON theory. Section 4.2 uses a numerical example to illustrate this. Section 4.3 clarifies the motivation behind and objectives of this study in terms of extending VICON capability. Section 4.4 provides the details of the formulation used in the proposed Simulated VICON analysis and Section 4.5 gives the analysis procedures involved in conducting the Simulated VICON analysis. Section 4.6 demonstrates the validation of the Simulated VICON analysis by comparing results with those available in the literature and by using the commercially available FEA software ABAQUS. Section 4.7 concludes the chapter.

4.1 Theoretical basis

In VIPASA analysis, the out-of-plane displacement is given by Equation 4.1 based on the assumption that the initial buckling mode varies sinusoidally in the longitudinal direction with half-wavelength λ.

$$w = f_1(y)\sin\left(\frac{\pi x}{\lambda}\right) + f_2(y)\cos\left(\frac{\pi x}{\lambda}\right) \tag{4.1}$$

Similar expressions are assumed for the in-plane displacements u and v to ensure the connection of the individual plate elements and the continuity of the buckle pattern across the intersection of neighbouring plate elements. Since specified shape functions have been assumed for the buckling displacements in one direction, the governing partial differential equation solution is essentially reduced to a one-dimensional ordinary differential equation solution. The functions $f_1(y)$ and $f_2(y)$ satisfy the differential equations of equilibrium and allow various boundary conditions to be prescribed on the lateral edges of the panel. However, the boundary conditions cannot be prescribed on the ends of the panel because of the specific trigonometric function used, which makes the accuracy of predicting buckling load dependent on the loading conditions (Stroud et al. 1984).

In the absence of applied shear stress and material anisotropy, simply supported end conditions are perfectly satisfied in VIPASA analysis and the half-wavelength λ divides exactly into the plate length, i.e. $\lambda = l, l/2, l/3 \ldots l/m$ where m is an integer and l is the plate length. In this case, the mode shapes result in nodal lines of zero displacement which are straight and parallel to the ends of the panel and perpendicular to its longitudinal axis, and therefore satisfy simply supported boundary conditions at the ends of a finite, rectangular plate (W. H. Wittrick and Williams 1974). Under these circumstances therefore, the VIPASA solution is exact.

For anisotropic plates or plates with shear loading, the mode shapes result in nodal lines of zero displacement which are skewed and not straight. As shown in Figure 4.1a, the out-of-plane displacement contours pass through the boundary indicating that the simply supported conditions are not satisfied. Therefore, the VIPASA solution for loadings involving shear may underestimate the buckling load substantially when λ approaches l, because forcing the nodal lines to coincide with the end edges addes constraints and therefore produces buckling loads that are higher. In summary, VIPASA analysis is accurate only when many half wavelengths form along the panel length making λ considerably smaller than the l, in which case boundary conditions at the ends are not important (Dawe 2002).

The fundamental difference between VICON analysis and VIPASA analysis is the use of Lagrangian Multipliers (F. W. Williams and Anderson 1983). As introduced in the previous chapter, VICON analysis overcomes the inaccuracy in VIPASA under shear loading by using Lagrangian multipliers to couple together VIPASA responses for different half-wavelengths λ to simulate an infinitely long panel subject to periodically repeating rigid or elastic point supports. Thus, VICON analysis matches the simply supported end conditions more effectively than VIPASA for the shear loaded panels shown in Figure 4.1b, whose critical buckling loads can then be found with high accuracy. These repeating rigid supports also account for the continuity over several bays of typical aerospace construction and match closely with real design situations (Williams et al. 1991).

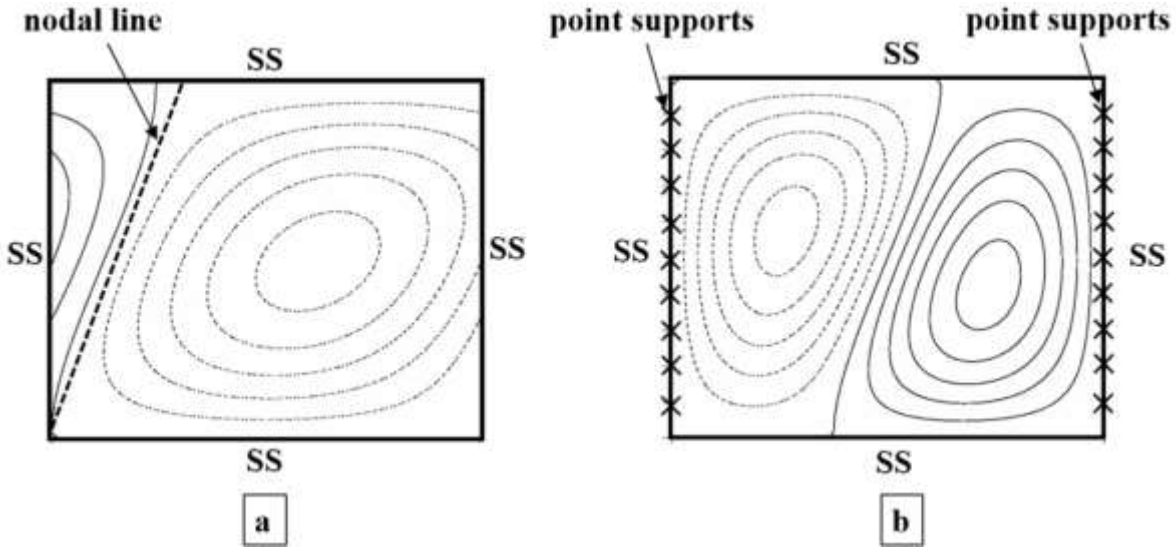

Figure 4.1: The out-of-plane displacement contour plot at critical buckling for a plate loaded in combined shear and compression: (a) VIPASA and (b)VICON

4.2 Numerical Definition

The theoretical differences discussed in the previous section are illustrated by the following numerical example. An isotropic rectangular plate of length $l = 300$ mm, width $b = 250$ mm and thickness $h = 1$mm is modelled using both VIPASA and VICON analyses with Youngs modulus $E = 110$ kNmm^{-2} and Poisson's ratio $v = 0.3$. Based on the exact strip method, the plate is divided into a number of strips, and each strip is subjected to a combination of a longitudinal compressive force N_x and a shearing force N_{xy} per unit width of the strip (i.e. the total forces are bN_x and bN_{xy}). The longitudinal compressive force is distributed between all the strips assuming a uniform strain ε_x. The compressive force is constant with a magnitude of 8000 N/m, while the shear force varies from 0 N/m to 10000 N/m accordingly. Ten sets of loading cases are subsequently generated to investigate the difference between VIPASA and VICON under the increasing levels of shear.

Table 4.1 shows the results obtained from VIPASA and VICON in terms of the values of critical buckling load factor obtained for different load cases, using a range of different

Table 4.1 Critical buckling load factor comparison for VIPASA and VICON analyses under different combined loading cases

Combined loading Cases			*Critical buckling load factor*		*Comparison*
N_{xy}/N_x	N_x (N/m)	N_{xy} (N/m)	VIPASA	VICON	*Difference (%)*
0	8000	0	0.8221	0.8221	0
0.125		1000	0.8142	0.8201	0.72
0.25		2000	0.7921	0.8144	2.74
0.375		3000	0.7601	0.8050	5.58
0.5		4000	0.7228	0.7923	8.77
0.625		5000	0.6836	0.7769	12.01
0.75		6000	0.6450	0.7593	15.05
0.875		7000	0.6082	0.7399	17.79
1		8000	0.5739	0.7194	20.23
1.125		9000	0.5422	0.6982	22.34
1.25		10000	0.5132	0.6767	24.16

magnitudes of shear resultant to illustrate the difference between the two programs. For each load case, the critical buckling mode shape given by VIPASA is associated with $\lambda = l$. It appears from Table 1 that identical load factors are obtainable from VIPASA and VICON under pure compression, which implies that coupling between different half wavelengths λ below l in VICON is unimportant under this circumstance. In terms of the combined loading cases, agreement between the VIPASA and VICON results is 0.72% with 1000 N/m shear loading and 2.74% with 2000 N/m shear loadings, demonstrating that with each increment of shear loading, the differences are much more pronounced. Results for higher compression shear ratios ($N_x/N_{xy} \geq 1$) suggest there is more than a 20% discrepancy between VIPASA analysis and VICON analyses.

These results are plotted in Figure 4.2. The solid curve indicates the VIPASA solution for $\lambda = l$. The dashed curves indicate VICON solutions for coupling of $\lambda = l, l/2, l/3 \ldots l/10$.

Except for the pure compression case, the VICON results are higher than the VIPASA results, indicating that the VIPASA solution for $\lambda = l$ under combined loading is unduly conservative, whereas the results obtained from VICON using Lagrangian multipliers to couple together different half-wavelengths λ are not. This suggests that the 20% discrepancy between the two sets of results can be attributed to the assumption of single half-wavelength and inaccurate representation of the simply supported end. Recognising that practical panels loaded in shear will have adjacent bays that provide a continuity effect, the VICON results are believed to be applicable to actual construction.

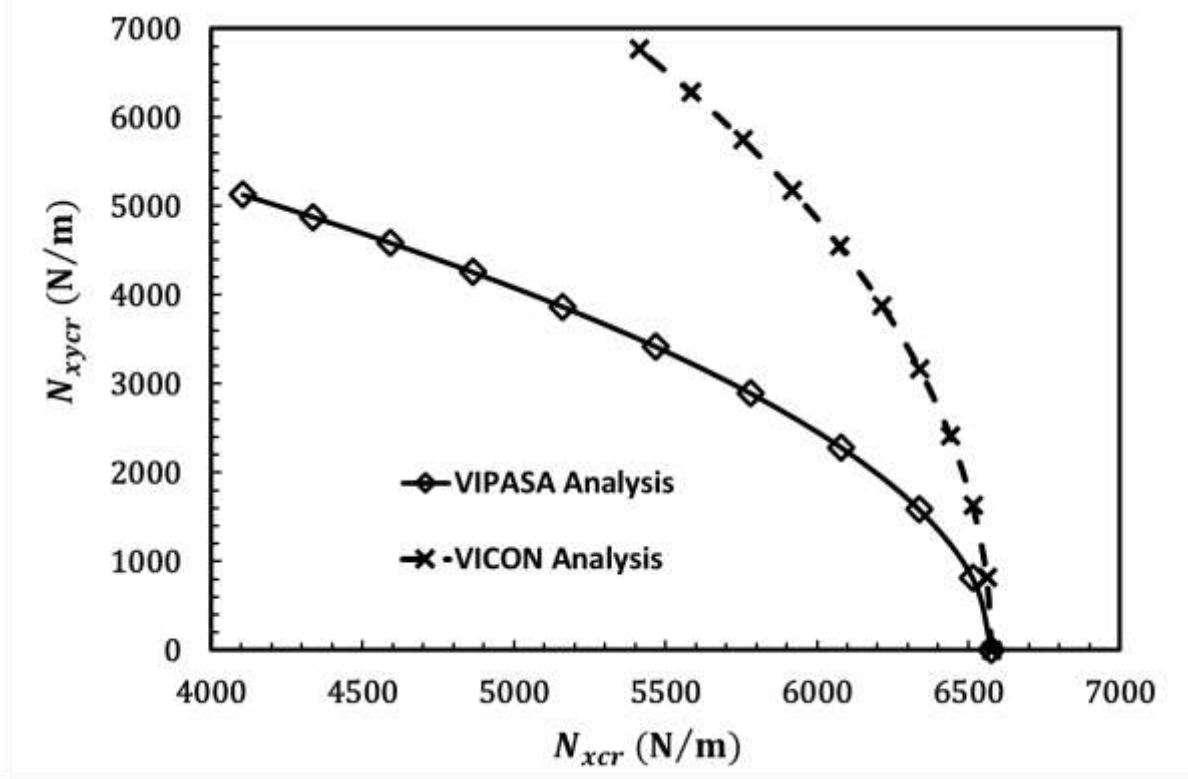

Figure 4.2 The interaction curve for VIPASA and VICON analysis under combined loading

4.3 Extension to postbuckling

The critical buckling load discrepancy between VIPASA and VICON analyses under shear loading has been studied and compared with other analysis methods by many authors including Anderson et al. (1983); Wittrick and Horsington (1984), and Dawe (2002).

Though it is known that VIPASA initial buckling analysis is conservative under combined loading and there will be an increase in predicting critical buckling load, by using VICON analysis under the same circumstances, it is not known how this difference will progress in the postbuckling stage and what discrepancy between these two programs should be assumed during postbuckling analysis. Due to this uncertainty, VIPASA postbuckling analysis cannot be relied upon to give accurate postbuckling predictions with combined loading since VIPASA postbuckling analysis depends heavily on the initial buckling results. Therefore, a wiser choice of analysis scheme in postbuckling is the VICON type of analysis. However, VICON cannot currently be used for conducting postbuckling analysis due to the complex constraint matrices used to couple the different wavelengths. An alternative, yet still practically credible, simulated VICON postbuckling analysis scheme is proposed at the preliminary stage of this postbuckling study and presented in the following sections.

4.4 Simulated VICON analysis formulation

As shown by the previous example, VIPASA and VICON analyses give identical initial buckling results in the absence of shear and material anisotropy. Thus, the relationships between their critical buckling loads, critical strains and pre-buckled stiffnesses K can be expressed as follows,

$$P_{VIPASA}^{cr} = P_{VICON}^{cr} \tag{4.2}$$

$$\varepsilon_{VIPASA}^{cr} = \varepsilon_{VICON}^{cr} \tag{4.3}$$

$$K_{VIPASA} = K_{VICON} = \frac{P_{VIPASA}^{cr}}{\varepsilon_{VIPASA}^{cr}} = \frac{P_{VICON}^{cr}}{\varepsilon_{VICON}^{cr}} \tag{4.4}$$

With the introduction of shear or anisotropy, VIPASA initial buckling results become very conservative when the buckling mode is an overall shear buckling mode and $\lambda = l$, while

VICON results are less conservative and close to reality (shown in Figure 4.3a). Based on this difference, the following relationships can be expressed.

$$P^{cr}_{\mathrm{VICON}} > P^{cr}_{\mathrm{VIPASA}} \tag{4.5}$$

$$\varepsilon^{cr}_{\mathrm{VICON}} > \varepsilon^{cr}_{\mathrm{VIPASA}} \tag{4.6}$$

$$\Delta P^{cr} = P^{cr}_{\mathrm{VICON}} - P^{cr}_{\mathrm{VIPASA}} \tag{4.7}$$

$$\Delta \varepsilon^{cr} = \varepsilon^{cr}_{\mathrm{VICON}} - \varepsilon^{cr}_{\mathrm{VIPASA}} \tag{4.8}$$

In the postbuckling stage with the onset of buckling, the growth of out-of-plane deflections causes radical changes in the stress distributions within the plate, reducing the stiffness of the plate against further compression. According to Marguerre's experiments (Singer et al. 2008), the post-buckled plate stiffness can be expressed as

$$P - P^{cr} = K^{*}_{VIPASA}(\varepsilon - \varepsilon^{cr}) \tag{4.9}$$

where K^{*} is the postbucking stiffness (shown in Figure 4.3b). The VIPASA postbuckling stiffness after n increments in the postbuckling stage can thus be written as

$$K^{*}_{VIPASA} = \frac{P^{n}_{VIPASA} - P^{cr}_{VIPASA}}{\varepsilon^{n}_{VIPASA} - \varepsilon^{cr}_{VIPASA}} \tag{4.10}$$

where P^{n}_{VIPASA} and ε^{n}_{VIPASA} are the applied load and strain at n increments into the postbuckling stage. In order to simulate VICON postbuckling analysis, the corresponding stress resultants from VIPASA postbuckling analysis are then passed to VICON buckling analysis to find P^{n}_{VICON}, however, unlike VIPASA, VICON analysis cannot predict the strain $\varepsilon^{n}_{\mathrm{VICON}}$. Therefore, a strain value in VICON is required to be calculated separately. Since VICON is less conservative under shear load, it predicts a higher load and strain than VIPASA in postbuckling resulting in the following relationships:

$$\Delta P^{n} = P^{n}_{\mathrm{VICON}} - P^{n}_{\mathrm{VIPASA}} \tag{4.11}$$

$$\Delta\varepsilon^n = \varepsilon^n_{VIPASA} - \varepsilon^n_{VICON} \tag{4.12}$$

The strain ε^n_{VICON} can be calculated by determining the strain difference between VICON and VIPASA. To obtain this strain differences ($\Delta\varepsilon^n$), it is assumed in Figure 4.3c that the gradient between point A and point B is same as that between point C and point D. This assumption is valid because the initial buckling slope ($K_{VIPASA} = K_{VICON}$), and the stress redistribution after initial buckling in VIPASA and VICON are the same. So once the gradient (k'_2) and the vertical difference (ΔP^n) between point C and point D are known, the strain differences ($\Delta\varepsilon^n$) is achieved by using the Pythagorean theorem. Thus,

$$K = k'_1 = k'_2 = \frac{\Delta P^{cr}}{\Delta\varepsilon^{cr}} \tag{4.13}$$

and,

$$\Delta\varepsilon^n = \frac{\Delta P^n}{k} = \frac{\Delta P^n \Delta\varepsilon^{cr}}{\Delta P^{cr}} \tag{4.14}$$

Once $\Delta\varepsilon^n$ is known, the postbuckling stiffness of the Simulated VICON analysis can be written as

$$K^*_{VICON} = \frac{P^n_{VICON} - P^{cr}_{VICON}}{\varepsilon^n_{VICON} - \varepsilon^{cr}_{VICON}} \tag{4.15}$$

After m increments,

$$K^*_{VICON} = \frac{P^m_{VICON} - P^{cr}_{VICON}}{\varepsilon^m_{VIPASA} + \frac{(P^m_{\mathrm{VICON}} - P^m_{\mathrm{VIPASA}})\Delta\varepsilon^{cr}}{P^{cr}_{\mathrm{VICON}} - P^{cr}_{\mathrm{VIPASA}}} - \varepsilon^{cr}_{VICON}} \tag{4.16}$$

Once the postbuckling stiffness of VICON analysis is calculated, the equilibrium path can be captured (shown in Figure 4.3d).

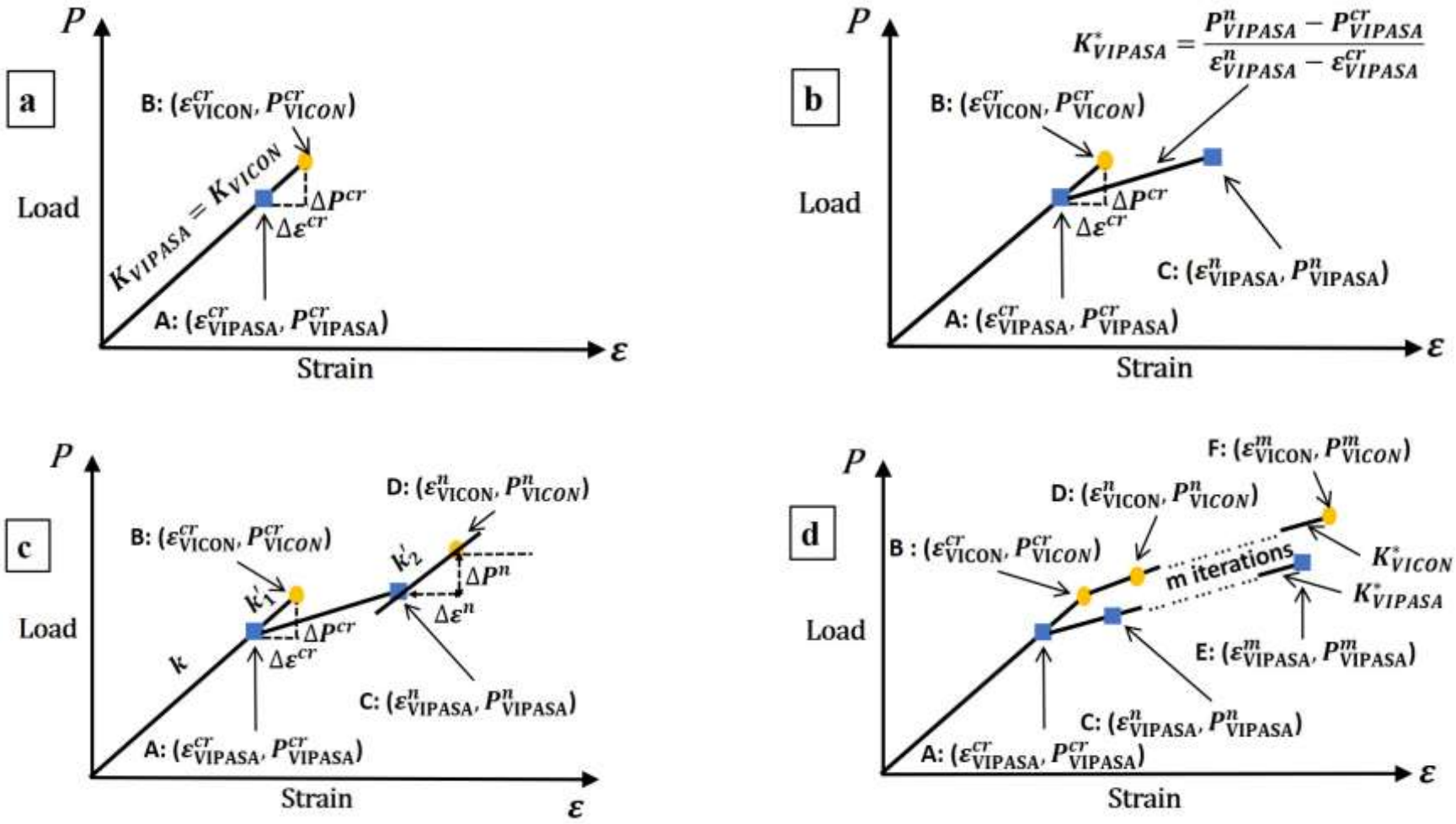

Figure 4.3 The graphic illustration of the formulation of the Simulated VICON analysis: (a) initial buckling difference; (b) the calculation of VIPASA postbuckling stiffness K^*_{VIPASA}; (c) the calculation of $k = k'_1 = k'_2$ and (d) the postbuckling curve given by Simulated VICON analysis

4.5 Simulated VICON analysis procedures

The simulated VICON analysis can be implemented based on the calculations outlined above by following the procedure described below:

i. Run the VIPASA post-buckling analysis and plot the VIPASA post-buckling curve.

   The VIPASA postbuckling analysis comprises m cycles (m is an integer) until it stops, each cycle is defined by a pre-determined increment of longitudinal strain or shear strain.

ii. Extract the stress resultant data from the VIPASA postbuckling analysis.

   In a VIPASA posbuckling analysis, each component plate of width b is divided into a_s longitudinal strips of equal width b_s. Furthermore, each of these strips is subdivided into d_s sub-strips, so that an accurate longitudinal stress (N_x) and shear stress (N_{xy}) variation across the width of the plate can be achieved. The total ($a_s d_s \times m$) stress resultant matrix $\{\boldsymbol{N}\}$ can be extracted from VIPASA.

iii. Transform the data from VIPASA to VICON

   Matlab scripts are written to separate the total stress resultant matrix $\{\boldsymbol{N}\}$ into a number of sub-matrices according to the data formation requirement in VICON buckling analysis.

iv. Perform VICON buckling analysis

   The comparison model constructed in the VICON analysis is divided into $a_s \times d_s$ strips, allowing the stress resultant matrices obtained from VIPASA to be exactly transferred to the VICON analysis. Then, VICON analysis is performed so that a meaningful and practical postbuckling comparison between the two programs can be established.

v. Plot the simulated VICON postbuckling load-strain curve

The conservative VIPASA postbuckling results for each cycle are compared with the corresponding VICON results, respectively. The VICON strain is calculated based on the trigonometric difference between the VIPASA and VICON postbuckling stiffnesses, which are mentioned in the previous section. The percentage difference for a specific cycle in the postbuckling analysis between these two programmes can then be obtained.

4.6 Postbuckling results and discussions

The analysis procedures described above have been converted into a computer program which has been tested in a number of applications by comparing with the numerical results given by FEA, VIPASA analysis and the work of other researchers discussed in this section. Here, single and stiffened panels are modelled with isotropic and anisotropic materials. The details of the material properties and thickness (t) used are listed in Table 4.2. The numerical results given by Simulated VICON analysis, VIPASA and FEA are obtained for a rectangular plate with the aspect ratio 1.5 in Example 1 and Example 2 and a square stiffened plate in Example 3. Schematic drawings showing the loading and overall dimensions for each of these examples are shown in Figure 4.4.

Table 4.2 Properties of materials used in examples

Metal		Graphite-epoxy 1		Graphite-epoxy 2	
$E(N/m^2)$	110×10^9	$E_{11}(N/m^2)$	164.1×10^9	$E_{11}(N/m^2)$	140×10^9
		$E_{22}(N/m^2)$	9.79×10^9	$E_{22}(N/m^2)$	10×10^9
ν_{12}	0.28	$G_{12}(N/m^2)$	4.799×10^9	$G_{12}(N/m^2)$	5×10^9
		ν_{12}	0.28	ν_{12}	0.33
t (mm)	1	t (mm)	5.25	t (mm)	3

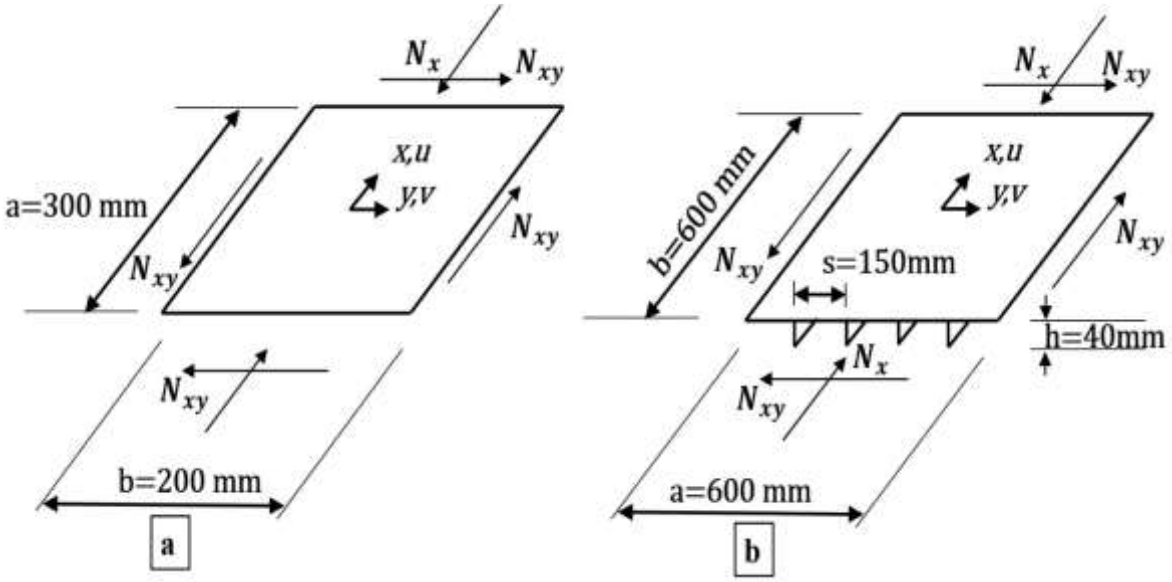

Figure 4.4 The loading and dimension used in examples: (a) single isotropic and anisotropic plate and (b) isotropic and anisotropic stiffened panel

The aspect ratios used were chosen to show the improvement achieved by using the proposed method to analyse finite length plate postbuckling responses under combined loading in which case the VIPASA postbuckling analysis struggles to obtain correct solutions due to the conservative boundary conditions assumed. All of the models chosen also have a relatively large width to thickness ratio ($b/t > 20$), to minimise transverse shear effects.

A finite element isotropic plate model was also created using the commercial code ABAQUS and employing the four-node quadratic shell element S4R and a mesh of 3000 elements. Convergence studies on the mesh size were carried out to determine the suitability of this mesh density. Compressive axial loads were applied to the nodes at the transverse edge of the plate. In ABAQUS analysis, linear eigenvalue was first conducted to find the critical buckling loads and associated modes. The mode shapes from the initial buckling analysis are stored in a displacement results file and are then introduced into a nonlinear Riks analysis (Riks, 1972) as initial geometric imperfections. To conduct a postbuckling analysis within ABAQUS, a small perturbation imperfection was imposed on

the model to find the postbuckling equilibrium path for the model. This perturbation imperfection should be kept as small as possible to ensures compatibility with the Simulated VICON perfect plate model, taking a magnitude of 0.1% of the plate thickness in the following analyses. The Riks arclength technique utilizes the Newton–Raphson method to track the equilibrium path and the user can choose appropriate increments manually and automatically for each step to ensure convergence in the software. The keyword *STEP, NLGEOM was used during the Riks analysis to account for geometric nonlinearities within the model (Smith et al. 2013).

All plates and stiffened panels examined were subjected to constant axial compression in the x-direction and therefore it is important to calculate the non-dimensional average strain ε_x which is based on the end shortening u_{end} in the x-direction. For a finite plate buckled into a single half-wavelength λ which is equal to the length of the plate l, the average strain ε_x is the ratio between the end shortening u_{end}, and the length of the plate l, that is:

$$\varepsilon_{x,average} = \frac{u_{end}}{l} \tag{4.17}$$

The emphasis in this study is in predicting the general postbuckling response in the form of the load-strain curves and in comparing such predictions with alternative analytical predictions. The transverse displacement w_{max} is not considered here since the procedures described above are based on the load-strain and stiffness relationships.

It is well known that the postbuckling response of a plate is highly reliant on both in-plane and out-of-plane boundary conditions. In order to compare the results given by VIPASA, Simulated VICON and ABAQUS, therefore, the boundary conditions in these models had to be equivalent. In each case all four boundaries of the plate were simply supported, with the lateral edges of the plate being allowed to have trigonometrically

varying in-plane displacements, that is, no straightness constraints were imposed on the edges. It was crucial to understand the influence of the in-plane boundary conditions at the two loaded ends of the plate when constructing the ABAQUS models because the VIPASA and Simulated VICON analysis were developed for infinitely long plates and do not contain information regarding the loaded ends of a long plate. The ABAQUS model simulates this long plate effect by applying Multi-point constraints (MPC) coupled by means of the keyword *EQUATION on the loaded edges so that each node in the loaded edges has equal longitudinal in-plane displacements. It is observed from Figure 4.5 that a close match in terms of deformation shape has been achieved by following the above setup of boundary conditions.

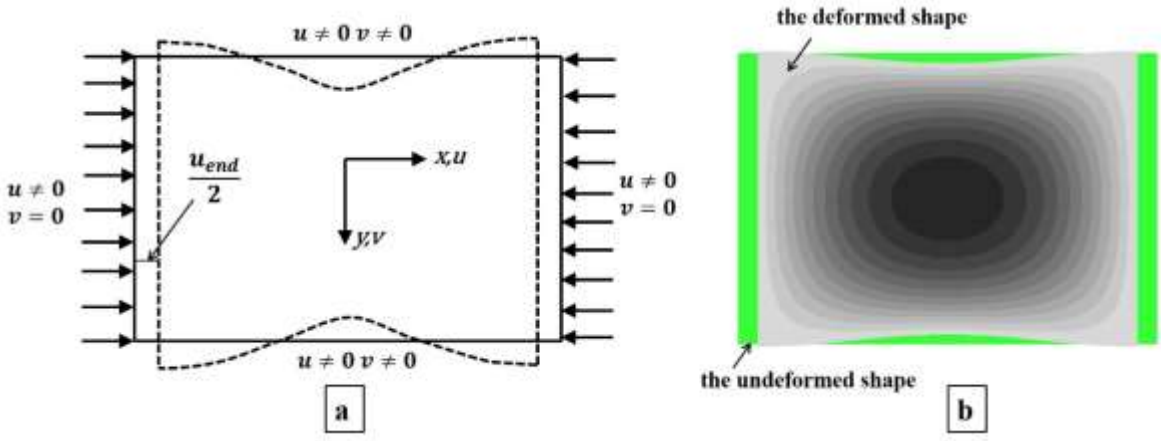

Figure 4.5 Comparison of deformed shape: (a) VIPASA, Simulated VICON analysis and (b) ABAQUS analysis

4.6.1 Example-1: Postbuckling of an isotropic rectangular plate

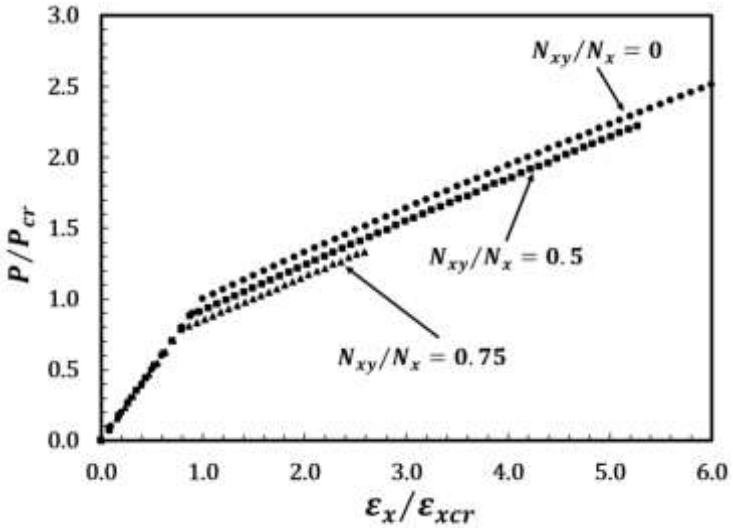

Figure 4.6 Normalised loads (P/P_{cr}) versus strain ($\varepsilon_x/\varepsilon_{xcr}$) for rectangular isotropic plates with different sets of combined loads.

Normalised load versus end shortening results are presented in Figure 4.6 to show how the postbuckling response changes with N_{xy}/N_x ratio varying from 0 to 0.75 for a single isotropic plate under combined shear and compression. The curves in Figure 4.6 are generated using the VIPASA postbuckling analysis and show the normalised axial load P/P_{cr} as a function of the normalised strain $\varepsilon_x/\varepsilon_{xcr}$. The axial load P and strain the ε_x are normalised with respect to P_{cr} and ε_{xcr}, respectively, that is, the critical strain and critical buckling load for the same plate under compression only. It can be observed from Figure 4.6 that the postbuckling behaviour of the plates under different loading combination predicted by VIPASA is very similar. In particular, the postbuckling stiffness which is represented by the slope after the bifurcation point is virtually unaffected by an increase of shear loading due to the same in-plane conditions being used for all of these analyses. The only significant difference is that the bifurcation position is lowered with an increase of the shear loading. It should be noted that the largest N_{xy}/N_x ratio is limited to 0.75 due

to the VIPASA convergence requirement with only 25 increments being able to be calculated for this ratio using current convergence procedures.

Non-normalised load end shortening curves are also presented in Figure 4.7 to illustrate the differences between the postbuckling responses at various combination of loading predicted using different approaches. The results presented in Figure 4.7a are based on modelling rectangular plates in pure compression using VIPASA analysis, Simulated VICON analysis and Koiter's method (1970). In Figure 4.7a, the results predicted by the VIPASA and Simulated VICON are identical. In this case, little difference between the two is expected as they give the same prediction of buckling load in the absence of shear loading. It can be seen that the VIPASA and Simulated VICON results compare very closely with the lower bound results of Koiter which are denoted by the dashed line.

The postbuckling results for a moderate combination of shear and compression ($N_{xy}/N_x = 0.5$) are presented in Figure 4.7b. The graphs are based on calculations made using VIPASA analysis, Simulated VICON analysis and ABAQUS. It can be seen from Figure 4.7b that the differences between VIPASA and the proposed Simulated VICON are very noticeable, with VIPASA predicting a lower burfication point as well as lower postbuckling stiffness.

Errors in the conservative VIPASA postbuckling predictions are typically of the order of 5% but range up to around 10% compared with the Simulated VICON analysis. Figure 4.7b also shows that ABAQUS finite element results compare closely with the Simulated VICON results with identical curves up to a strain level of around 0.0001, followed by small divergence thereafter. Figure 4.7c shows the postbuckling results for the case where the shear and compression ratio increases to 0.75. It is clear that significant differences exist between the results of the VIPASA and Simulated VICON analyses. The postbuckling load versus strain curve given by the Simulated VICON analysis is 20%

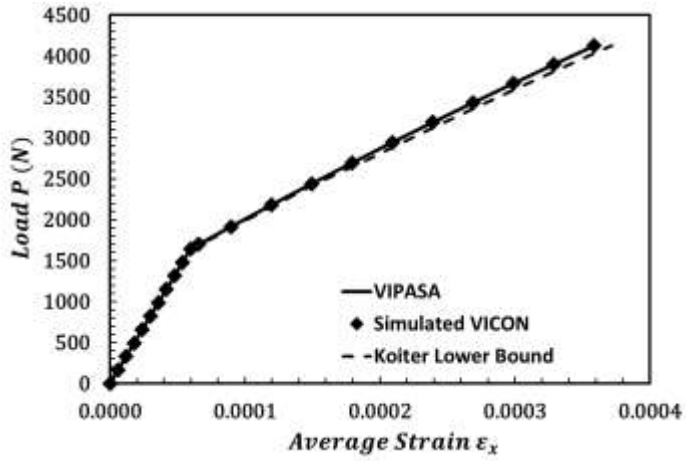

a

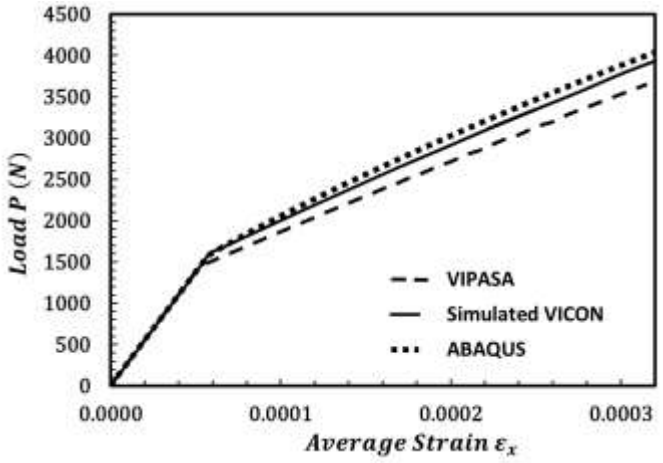

b

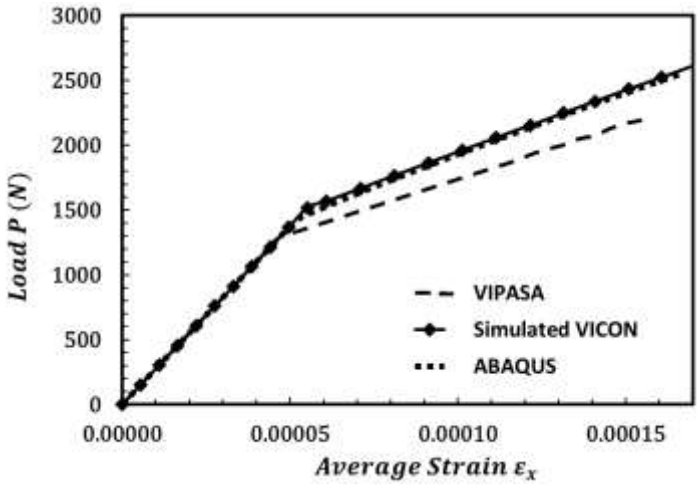

c

Figure 4.7 Comparison of non-normalised load versus average strain curves for isotropic rectangular plate with different sets of combined loads for VIPASA, Simulated VICON, ABAQUS: (a) $N_{xy}/N_x = 0$; (b) $N_{xy}/N_x = 0.5$ and (c) $N_{xy}/N_x = 0.75$

higher than that from the VIPASA analysis, reflecting the conservative nature of the VIPASA analysis under shearing action due to the unsatisfied boundary conditions. However, excellent agreement is observed between the Simulated VICON analysis and the finite element analysis and hence the validity of the procedures developed in this study is confirmed.

4.6.2 Example-2: Postbuckling of an anisotropic rectangular plate

Example 2 is derived from Example 1 by changing the material from isotropic to anisotropic to further validate the proposed method. The laminated graphite/epoxy plate under consideration here has the same dimensions as Example 1 but is formed from various layers of plies having the material properties listed in Table 4.2 and referred to as Graphite-epoxy 1. The Simulated VICON approach is used to analyse two types of composite laminate plate under combined loading, a symmetric layup $[+45/-45/+45/-45/90/0/+45\ /-45/0/90/0/90]_S$ and an unsymmetric layup $[+45/-45/+45/-45/90/0/+45/-45/0/90/0/90]_A$. It is well known that symmetric configurations exhibit membrane and flexural coupling, while unsymmetric layups show the coupling of in-plane and out-of-plane behaviours. It is important to test the proposed method by using an unsymmetric layup because they exhibit the most general type of anisotropy for laminated composites and little study has been found in the literature for such configurations under combined loading. It is noted that a number of unsymmetric layups were tested in VIPASA postbuckling analysis and some of them failed to converge. Discarding unconverged layups, the above chosen unsymmetric layups have a reasonable amount of anisotropy while maintaining the normal convergence in VIPASA postbuckling analysis. These layups may be used less often in practice but are nonetheless important in demonstrating the validity of the proposed method.

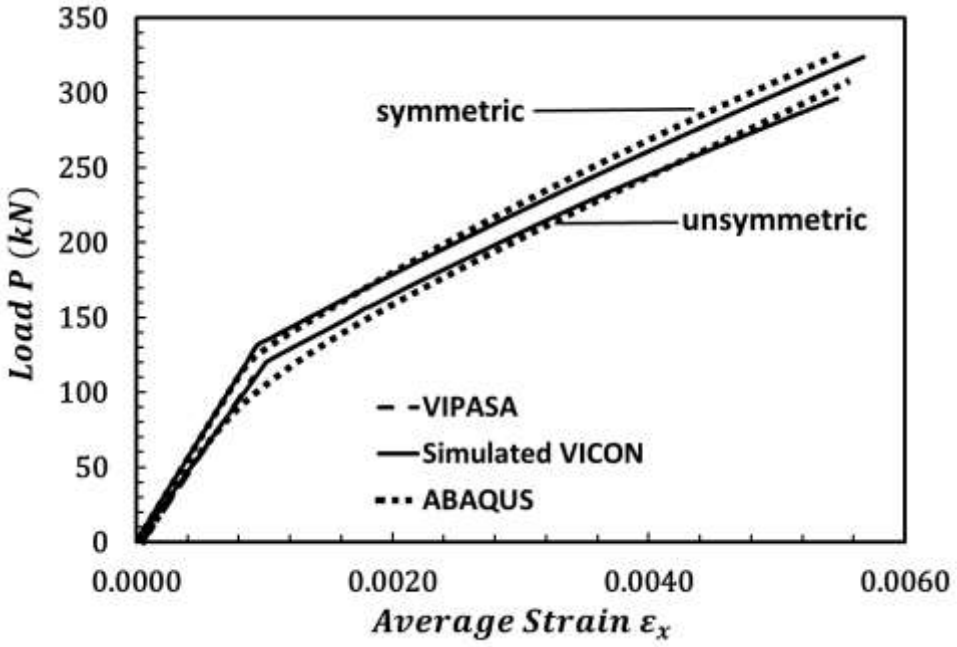

Figure 4.8 Non-normalised load versus average strain curves for symmetric and unsymmetric composite laminate plates under pure axial compression.

Figure 4.8 shows the nonlinear response of both symmetric and unsymmetric composite plates to progressive axial compression only. In the context of the symmetric layup, the comparison between the Simulated VICON, VIPASA and ABAQUS results shows that the drop in stiffness immediately after buckling is correctly predicted and good agreement between these analyses is evident. Regarding the postbuckling curve for the unsymmetric laminate configuration in Figure 4.8, the initial buckling load predicted by VIPASA is 20% lower than that for the symmetric layup. However, bifurcational buckling does not occur in the FEA during the progressive loading process. This observation is consistent with the study made by Lagace et al. (1986); Qatu and Leissa (1993) and is due to the plate's susceptibility to bending under a small amount of load due to the presence of in-plane and out-of-plane coupling (B_{16} and B_{26} coefficients). It can also be noted from this study that, although the VIPASA analysis matches the Simulated VICON analysis very closely, the discrepancy between the Simulated VICON and the ABAQUS curves is round 5% and becomes more pronounced at a higher level of material anisotropy.

A graphical presentation of results for symmetric and unsymetric laminate plate postbuckling response under different combination of loading is given in Figure 4.9, wherein P_{cr} and ε_{xcr} are the critical buckling load and strain for the corresponding laminate configuration. Figures 4.9a and 4.9b illustrate the postbuckling response of composite plates with symmetric layups when the shear to compression ratio (N_{xy}/N_x) is equal to 0.5 and 0.75, respectively. Comparison of the postbuckling curves shows good agreement between the Simulated VICON results and the FEA results. On the other hand, VIPASA predicts a lower postbuckling stiffness than the other two methods showing that unsatisfactory boundary conditions in postbuckling analysis lead to conservative results. Figure 4.9c and 4.9d show the results for the composite plate with an unsymetric layup under the same shear compression ratio as above. By plotting the normalised axial load P/P_{cr}as a function of the normalised strain $\varepsilon_x/\varepsilon_{xcr}$, it can be observed that the bifurcation buckling reappears under combined shear and compression.

This somewhat surprising result which reveals that an unsymmetrical laminate which does not exhibit bifurcation buckling under pure compression may exhibit bifurcation buckling behaviour under combined loading may be understood by examining the postbuckling mode shape. It is found that the unsymmetric laminate under pure compression shows a more skewed mode shape than that under combined loading, which implies that the shear load may reduce the effect of the skewing due to the material anisotropy. Comparing the results given by different analysis schemes in Figure 4.9c, good agreement betweenthe Simulated VICON analysis and the FEM analysis is observed for lower shear and compression ratios. However, the discrepancy between the two analyses starts to grow at higher shear and compression ratios (Figure 4.9d). This implies a basic transformation in deformed shape at some stage in the post-buckling regime. This is useful to know but, of course, it is not possible to investigate such a transformation

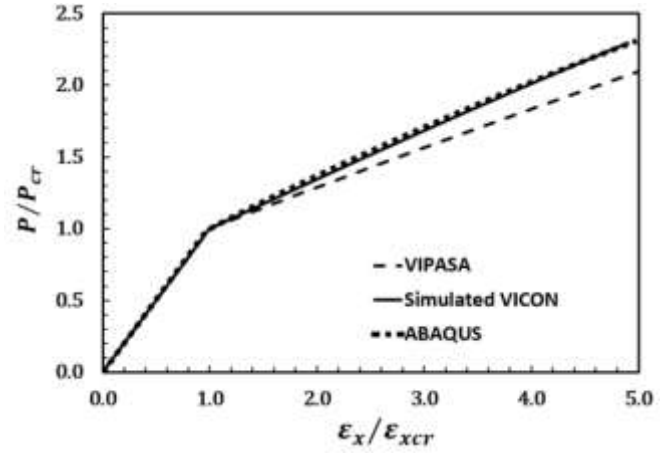

a

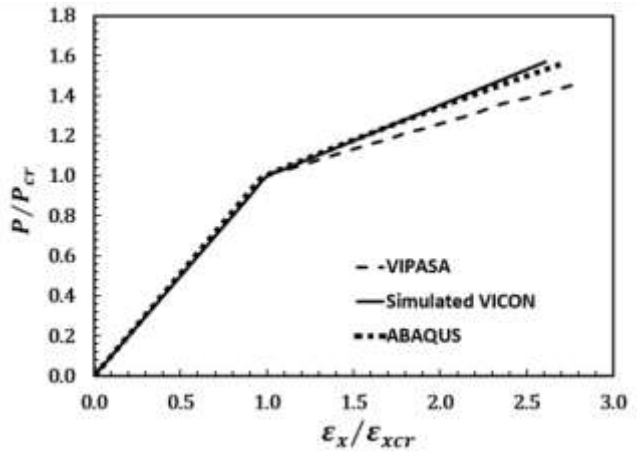

b

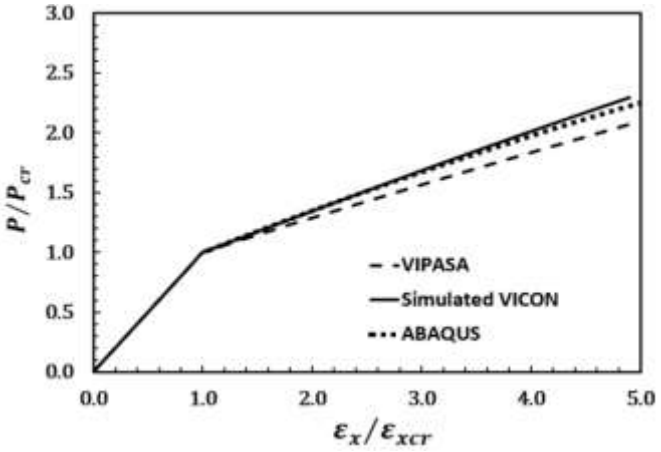

c

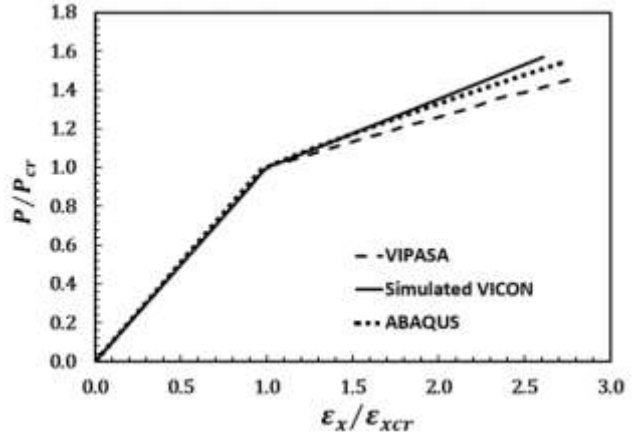

d

Figure 4.9 Normalised loads P/P_{cr} as a function of the normalised strain $\varepsilon_x/\varepsilon_{xcr}$ for composite laminates with different sets of combinations of loads: (a) symmetric layup with $N_{xy}/N_x = 0.5$; (b) symmetric layup with $N_{xy}/N_x = 0.75$; (c) unsymmetric layup with $N_{xy}/N_x = 0.5$ and (d) unsymmetric layup with $N_{xy}/N_x = 0.75$.

further in a continuous fashion using the present approach since the basis of the approach, in obtaining any one curve, is that the longitudinal half-wavelength, once selected, does not change.

4.6.3 Example-3: Postbuckling of a square stiffened panel

Two stiffened panels, one metallic panel and another made from graphite-epoxy composite material, were analysed with VIPASA, Simulated VICON and the finite element package ABAQUS. Results of these analyses are presented in this section. A schematic drawing showing the loading and overall dimensions of these panels is shown in Figure 4.4b. The panel is 600mm square and has four equally spaced stiffeners, which were carefully chosen to achieve a skin mode in the buckled state. The loads applied were combinations of longitudinal compression (N_x) and shear (N_{xy}). The out-of-plane boundary conditions for postbuckling represented simple supports on all four skin edges and the stiffeners. The in-plane boundary conditions consisted of a uniform strain in the loading direction with free transverse expansion along the unloaded edges, so that N_y along the longitudinal edge is zero. The values of Young's moduli, shear modulus, and Poisson's ratio for the composite material used in the calculations for this example are given in Table 4.2 and are referred to as graphite-epoxy 2. A symmetric layup $[+45/-45/+45/-45/90/0/+45/-45/0/90/0/90]_S$ was analysed in this example.

Figure 4.10 shows the typical bifurcation postbuckling response of the stiffened panel, plotting the normalized axial loads P/P_{cr} versus normalized strain $\varepsilon_x/\varepsilon_{xcr}$ for both isotropic and anisotropic stiffened panels under different shear compression ratios as for previous examples. As can be seen in this figure, the responses are typical of a post-buckled plate, and one can see the postbuckling stiffness of the stiffened panel is higher

than that of a single plate, which implies that the stiffened panel is more capable of continuing to carrying load after initial buckling than a single plate.

In accordance with the results from former examples, the VIPASA and FE analyses show relatively large differences in their postbuckling equilibrium paths due to boundary condition problems for both for the isotropic case (Figure 4.10a and 4.10b) and the anisotropic case (Figures 4.10c and 4.10d), respectively. Contrary to this, very small differences regarding the postbuckling curve between the Simulated VICON analysis and the FEA analyses can be observed. Note in Figure 4.10 that the discrepancies between the solutions near the buckling loads are due to the imperfection introduced into the FEM model.

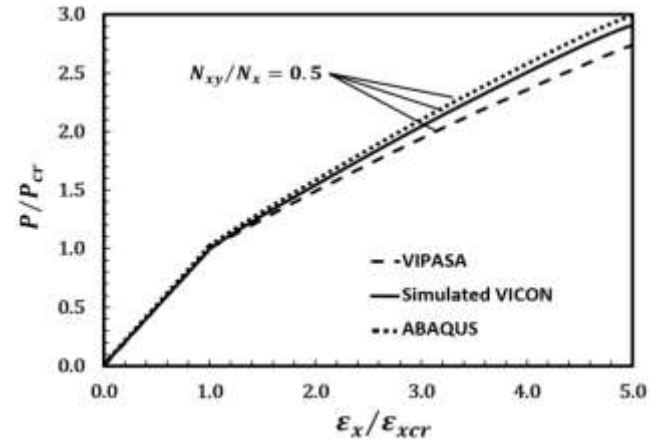

a

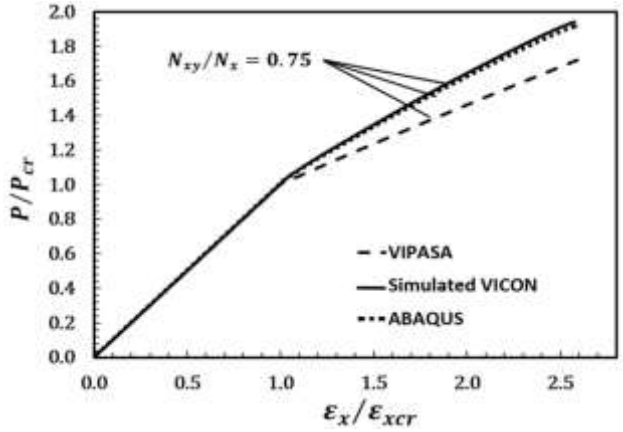

b

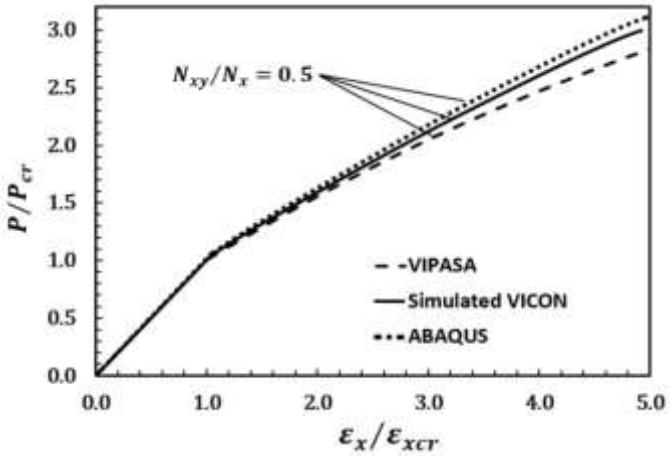

c

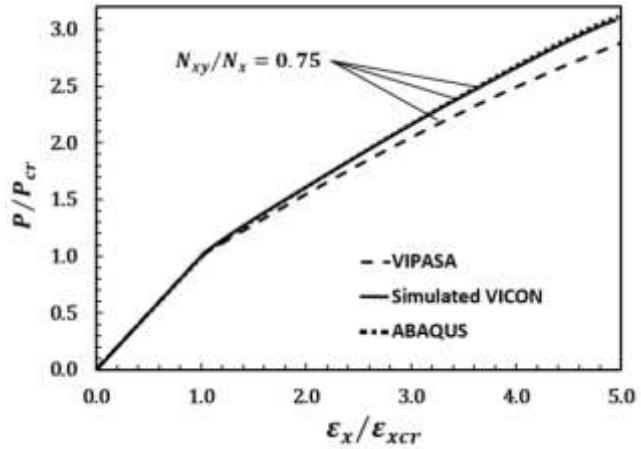

d

Figure 4.10 Normalised loads P/P_{cr} as a function of the normalised strain $\varepsilon_x/\varepsilon_{xcr}$ for composite laminates with different combined actions of loads: (a) isotropic stiffened panel with $N_{xy}/N_x = 0.5$; (b) isotropic stiffened panel with $N_{xy}/N_x = 0.75$; (c) anisotropic stiffened panel with $N_{xy}/N_x = 0.5$ and (d) anisotropic stiffened panel with $N_{xy}/N_x = 0.75$.

4.7 Conclusions

The following conclusions may be drawn based on the results of this study.

- The VIPASA postbuckling analysis according to the current analysis scheme for the conditions of combined loading is found to be relatively conservative compared with other numerical results. This is due to the assumptions upon which the longitudinal shape functions are based. This conservatism extends to both initial buckling and postbuckling calculations under combined loading.

- The scope of the VIPASA type of buckling analysis has been extended to VICON analysis by the use of Lagrangian multipliers to incorporate a set of constraints to represent regularly repeating interior supports, so that the loaded boundary conditions can be closely matched. VICON analysis involves the coupling of different wavelengths which would make it computationally expensive to expand into full postbuckling analysis since it would requires the postbuckling analysis to be performed on multiple wavelengths.

- A new approach taking advantage of VICON features while maintaining VIPASA postbuckling capacity has been presented in this chapter to simulate VICON performing post-buckling analysis. This approach needs the output data from a VIPASA analysis to be carefully manipulated to satisfy the input prerequisites of a VICON analysis. The axial stiffness differences between VIPASA and VICON corresponding to each predetermined increment of longitudinal strain in postbuckling is calculated and compared. Based on these differences an equilibrium path for postbuckling using VICON analysis can be achieved.

- Proof of concept work has been conducted for the prediction of the postbuckling response of isotropic and anisotropic single plates and stiffened panels under combined loading. Comparisons with standard FEA results has validated the proposed Simulated VICON analysis and the results given by this new analysis in most of the cases are in good agreement with those results given by FEA. Because the Simulated VICON analysis is computationally inexpensive, it can be easily integrated into the VIPASA postbuckling analysis as a subroutine to allow one to use it for the preliminary design of laminated plates under combined loading in the postbuckling regime.

- In the current study, the Simulated VICON analysis is developed within the context of calculation of the postbuckling stiffness difference between the VIPASA and VICON analyses, which is considered to be reasonable for the sort of applications considered in this chapter. However, the Simulated VICON analysis still relies on the initial postbuckling analysis of VIPASA which has undergone no significant improvement to change its conservative nature, such as the stress invariant issues. Hence, further research needs to be carried out to improve the VIPASA postbuckling approach itself. Such a development in improving the VIPASA postbuckling analysis will be the subject of the following chapters wherein the in-plane displacement assumptions will be redescribed and a systematic recalculation of strain and hence stress followed by solving of the governing equations will be demonstrated.

Chapter 5

Improved VIPASA analysis

This chapter proposes an improved approach to the existing VIPASA postbuckling analysis scheme. In this new approach, although the VIPASA out-of-plane displacements are used as before, the in-plane displacements, strains and stress resultants are now allowed to vary with half-wavelengths λ and $\lambda/2$, and no longer have to have the same sinusoidal variation as the out-of-plane displacements. The in-plane governing equilibrium equations are derived and solved analytically for isotropic or anisotropic plates, allowing in-plane membrane and out-of-plane bending to be coupled. Thus, more accurate distributions of longitudinal and transverse stress resultants are expected to be obtained. The chapter is organised as follows: Section 5.1 discusses Stein's analytical postbuckling model which gives the general background for the research conducted in this chapter. Section 5.2 describes the details of the proposed method including the assumptions of the displacement functions, the formulation of the strain-stress relationships, the application of the numerical method and the derivation of the equilibrium equations. Section 5.3 explains the implementation of the proposed method in the VIPASA postbuckling analysis, where the energy method is used to convert the stress resultants from node level to strip level. Section 5.4 concludes this chapter.

5.1 Stein's postbuckling model

From a mathematical point of view, the solution of a partial differential equation (PDE) is difficult to obtain because there exist numerous functions that can satisfy the PDE and the general solution only describes the dependent variable in general terms and does not give its specific form. For these reasons, it is customary to solve a PDE by assuming some specific function which satisfies all or part of the PDE and then to transform this to other forms of differential equations, such as homogeneous differential equations. Stein (1959a; 1985) proposed two methods to convert the postbuckling governing equations which are essentially PDEs to solvable differential equations.

5.1.1 Power series method

In Stein's early work (Stein 1959a), both in-plane (u and v) and out-of-plane (w) displacements were expanded into a power series in terms of a perturbation parameter ϵ^n ,and thus the displacement function could be written as

$$u = \sum_{n=0,2}^{\infty} u^{(n)} \epsilon^n \tag{5.1}$$

$$v = \sum_{n=0,2}^{\infty} v^{(n)} \epsilon^n \tag{5.2}$$

$$w = \sum_{n=1,3}^{\infty} w^{(n)} \epsilon^n \tag{5.3}$$

where $u^{(n)}$, $v^{(n)}$, $w^{(n)}$ are functions only with respect to the normal coordinates x, y and z, and the parameter ϵ^n can be regarded as having either a plus or minus sign. The power series of u and v were expected to start from zero power and have only even powers. In contrast, the power series of w was expected to begin with a non-zero power and have

only odd powers. The reasoning behind these assumptions was based on the deformed shape of the post-buckled plate. A plate subjected to compression only can buckle in either a positive or a negative direction with the deformed shape w then depending on a plus or minus sign. Thus, the series for *w* can contain only odd powers of parameter ϵ satisfying the requirement that the deformed shape only changes with the sign. The in-plane displacements u and v on the other hand not are affected by the direction of the buckling mode and therefore, even powers of ϵ were used.

These assumptions regarding the in-plane and out-of-plane displacement lead to the power series expressions of the stress resultants N_x, N_y, N_{xy}, and enable the von Karman large deflection equations to be transformed into a series of homogeneous differential equations and solved analytically. The details of this transformation process can be found in Appendix C. This analysis achieves accurate results and correlates well with experiments when up to two terms in the displacement function are included. However, the disadvantages of this type of analytical model are that it usually involves lengthy computations and becomes incalculable for anisotropic plates, and because no explicit relationships among the variables are obtained, the analysis results are difficult to generalise.

5.1.2 Trigonometric function method

A further semi-analytical method was proposed by Stein (1983; 1985) for the postbuckling of long isotropic or orthotropic plates under compression, shear and combined loading. In contrast to his previous work, the trigonometric functions employed to represent the displacement in the presence of shear or a combination of compression and shear were as follows:

$$\mathrm{u} = -u_{cn}\left(\frac{x}{a} - \frac{1}{2}\right) + u_0(y) + u_s(y)\sin\frac{2\pi x}{\lambda} + u_c(y)\cos\frac{2\pi x}{\lambda} \qquad (5.4)$$

$$\mathrm{v} = v_0(y) + v_s(y)\sin\frac{2\pi x}{\lambda} + v_c(y)\cos\frac{2\pi x}{\lambda} \tag{5.5}$$

$$\mathrm{w} = w_s(y)\sin\frac{\pi x}{\lambda} + w_c(y)\cos\frac{\pi x}{\lambda} \tag{5.6}$$

where u_{cn} is the applied longitudinal compressive displacement and a is the length of the plate. The deflection w varies sinusoidally with half-wavelength λ at buckling and beyond. The in-plane displacements u and v vary sinusoidally with half-wavelength λ/2.

The use of sinusoidal functions in the longitudinal direction allows the out-of-plane governing equation to be converted into an ordinary nonlinear differential equation. Compared with other methods, Stein introduced different sinusoidal functions in the in-plane equations which are convenient to represent the in-plane displacements so that a wide range of dimensions and material properties can be analysed by using this method. Combining proper boundary conditions, such as free or fixed edges for in-plane and simply supported or clamped for out-of-plane, with solving techniques from Lentini and Pereyra (1977) which are based on a Newton method, a system of first-order ordinary differential equations was solved for combined loading postbuckling problems.

The use of trigonometric functions and dimensionless parameters gives a good representation of the displacement field for postbuckling analysis while reducing the computational cost, which enables this method to be used in more complicated combined load cases. However, only postbuckling analysis of isotropic and specially designed orthotropic plates are considered in Stein's work, and the theory cannot be used for analysing postbuckling of a general anisotropic plate.

5.1.3 Combining Stein's method with VIPASA postbuckling analysis

VIPASA analysis as outlined in Chapter 3 is highly efficient for investigating plate postbuckling reserves of strength owing to its use of the exact strip method (W. H. Wittrick and Williams 1974) and Newton iterations (Anderson and Kennedy 2008).

However, in order to achieve this efficiency, some conservative assumptions must be made. For example, the present VIPASA analysis assumes that the stresses in each strip are longitudinally invariant. Such an assumption has been described and proved to be valid for initial buckling analysis (Wittrick and Williams (1974); (Williams and Anderson (1983); Williams and Kennedy (1991)), but it is well known from classical works (von Karman 1932), that a longitudinal variation of stresses would occur as a results of the out-of-plane flexure. Therefore, the invariant stress assumption in VIPASA postbuckling analysis may lead to significant inaccuracy because convergence must be achieved on consistent mode shapes and stress resultants in each predefined increment of the postbuckling.

The calculation of stress resultants in the current VIPASA is based on the use of trigonometric in-plane functions in which the longitudinal and transverse displacements (u and v) are assumed to vary sinusoidally with the same half-wavelength λ as the out-of-plane deflections. In contrast, Stein's work postulates that the in-plane trigonometric functions vary sinusoidally with half-wavelength $\lambda/2$ only. This difference can be regarded as an important conceptual supplement to the assumptions used in the VIPASA postbuckling analysis, because few studies in the field of the exact strip method have been conducted which take into account the coupling of in-plane displacements varying with half-wavelengths λ and $\lambda/2$. Additionally, Stein's approach to transforming partial differential equations to a system of linear equations is worth applying in VIPASA analysis to avoid convergence problems. Furthermore, Stein's method can be expanded to the analysis of general anisotropic plates thanks to the existence of the B matrix in an extension to the VIPASA analysis (Anderson and Kennedy 1993). Hence, detailed procedures are proposed in the next section to improve the accuracy of the current VIPASA analysis.

5.2 The Improved VIPASA analysis

5.2.1 Overview of Improved VIPASA analysis

Before discussion of the calculation details, the framework of the analysis procedures for the Improved VIPASA analysis can be examined as illustrated in Figure 5.1. The solid outline boxes represent the imported or known quantities from either VIPASA analysis or assumptions, while the dashed outline boxes represent the unknown quantities which need to be determined. The analysis starts by combining the out-of-plane displacements w from VIPASA with unknown in-plane displacements u and v to express the Von Karman large deflection formula in algebraic form, where the derivative terms appearing in the equations are calculated by utilising first or higher order finite difference expressions (step 1-step 6). Then, the in-plane equilibrium equations are written out in association with appropriate in-plane boundary conditions, so that the unknown in-plane displacements u and v can be solved (step 7- step 10). Finally, the stress resultants and their derivatives with respect to each component of w can be calculated (step 11). Once the stress resultants at node level are obtained, the energy method is used to average out the stress resultants in each strip to pave the way for mode shape calculation in the next iteration of the VIPASA analysis (step 12-step 13). The detailed formulation of each stage of the procedure will be given in the following sections.

5.2.2 Displacement field of the Improved VIPASA analysis

In the Improved VIPASA analysis, the out-of-plane deflections $\boldsymbol{w_i}$ and rotations $\boldsymbol{\psi_i}$ about the x axis at each node i are assumed to vary sinusoidally in the longitudinal direction with half-wavelength λ, taking the form:

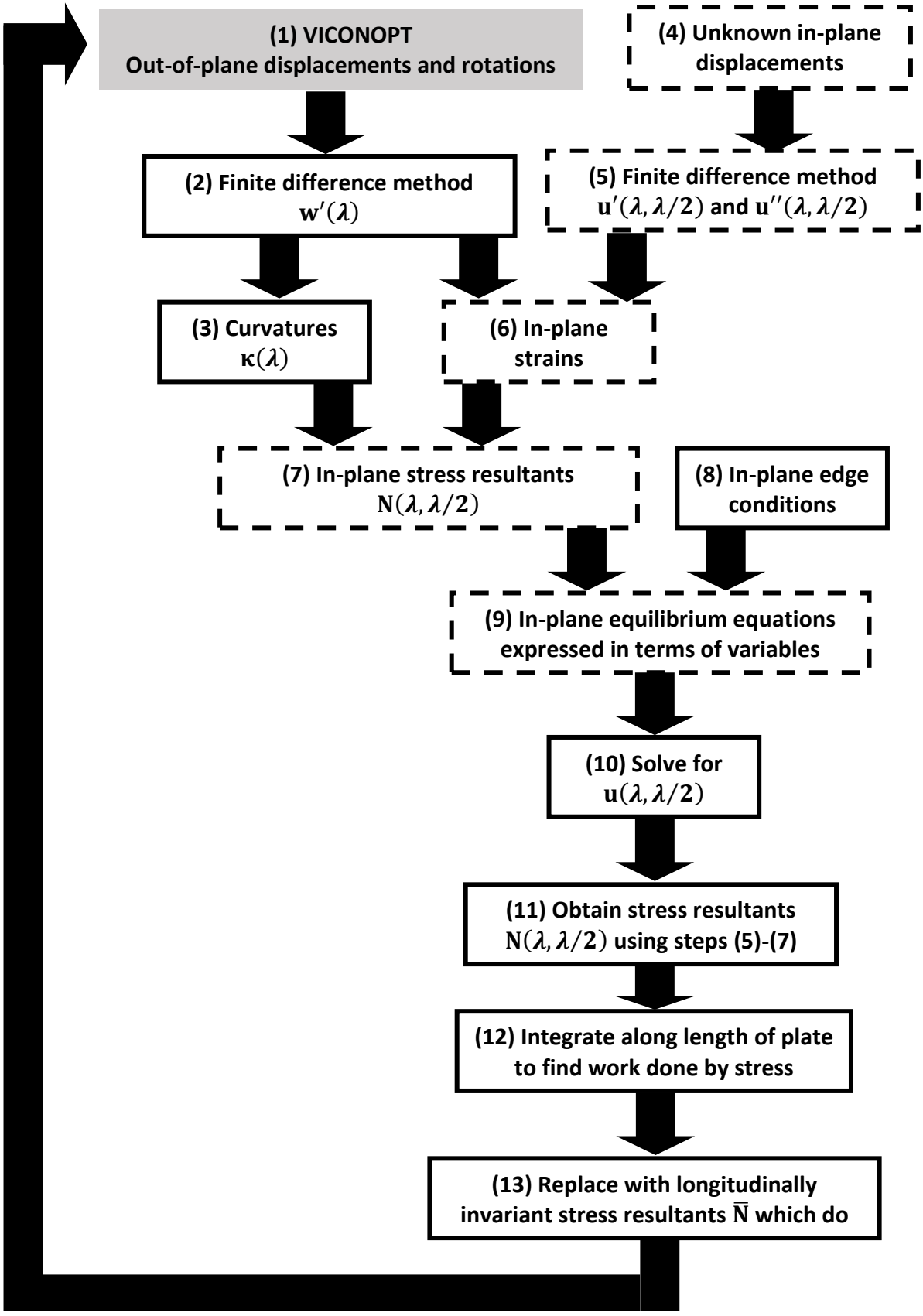

Figure 5.1 Flow chart of calculations in the improved VIPASA postbuckling analysis.

$$w_i = w_{ic}\cos\frac{\pi x}{\lambda} + w_{is}\sin\frac{\pi x}{\lambda} \tag{5.7}$$

$$\psi_i = \psi_{ic}\cos\frac{\pi x}{\lambda} + \psi_{is}\sin\frac{\pi x}{\lambda} \tag{5.8}$$

The presence of both sine and cosine terms allows for the skewing of the nodal lines which occurs for shear-loaded and anisotropic plates. In the absence of shear and anisotropy, w_{ic} and ψ_{ic} are zero. Note that the out-of-plane displacements are imported directly from the current version of the VIPASA analysis.

The in-plane displacements at each node i over the strip middle surface are represented as a summation of linear and sinusoidal terms. The sinusoidal terms are the products of in-plane displacement quantities and interpolation shape functions. The interpolation function G_u couples with five trigonometric terms to allow longitudinal displacement (u) and transverse displacement (v) to vary as the sums of sinusoidally varying responses with two half-wavelengths λ and λ/2.

The matrix form of the in-plane displacement can be written as

$$u_i = [d_L] + [d_i][G_u] \tag{5.9}$$

Where,

$$[d_L]_{2\times1} = \begin{bmatrix} -\bar{\varepsilon}_x\left(x - \frac{a}{2}\right) & 0 \end{bmatrix}^T \tag{5.10}$$

$$[d_i]_{2\times5} = \begin{bmatrix} u_{i0} & u_{ic} & u_{is} & u_{iC} & u_{iS} \\ v_{i0} & v_{ic} & v_{is} & v_{iC} & v_{iS} \end{bmatrix} \tag{5.11}$$

$$[G_u]_{5\times1} = \begin{bmatrix} 1 & \cos\frac{\pi x}{\lambda} & \sin\frac{\pi x}{\lambda} & cos\frac{2\pi x}{\lambda} & \cos\frac{2\pi x}{\lambda} \end{bmatrix}^T \tag{5.12}$$

The sinusoidal part of the displacement field in Equation (5.9) is versatile with regard to the specification of in-plane boundary conditions on the longitudinal edges which can be

applied directly and explicitly by setting to zero any of the values of the fundamental in-plane quantities ($u_{i0}, u_{ic}, u_{is}, u_{iC}, u_{iS}, v_{i0}, v_{ic}, v_{is}, v_{iC}, v_{iS}$) at a boundary.

The linear part of the displacement field of Equation (5.9) is introduced to represent a progressive uniform end shortening strain $\bar{\varepsilon}_x$ in the x-direction as well as the no lateral expansion assumption in the y-direction.

5.2.3 Formulation of the strain-stress relationship

The in-plane non-linear strains and curvatures neglecting the transverse effect at node i can be expressed by von Karman large deflection equations in the matrix form as

$$\begin{bmatrix} \varepsilon_{xi} \\ \varepsilon_{yi} \\ \gamma_{xyi} \\ \kappa_{xi} \\ \kappa_{yi} \\ \kappa_{xyi} \end{bmatrix} = \begin{bmatrix} \dfrac{\partial u_i}{\partial x} + \dfrac{1}{2}\left(\dfrac{\partial w_i}{\partial x}\right)^2 \\ \dfrac{\partial v_i}{\partial y} + \dfrac{1}{2}\left(\dfrac{\partial w_i}{\partial y}\right)^2 \\ \dfrac{\partial u_i}{\partial y} + \dfrac{\partial v_i}{\partial x} + \dfrac{\partial w_i}{\partial x}\dfrac{\partial w_i}{\partial y} \\ -\dfrac{\partial^2 w_i}{\partial x^2} \\ -\dfrac{\partial^2 w_i}{\partial y^2} \\ -2\dfrac{\partial^2 w_i}{\partial x \partial y} \end{bmatrix} \tag{5.13}$$

On substitution from Equations (5.9-5.12) into Equation (5.13), the neutral surface strains and curvatures can be expressed in terms of out-of-plane displacement w_i and in-plane displacement u_i via the following matrix form:

$$\begin{bmatrix} \varepsilon_i \\ \kappa_i \end{bmatrix} = \begin{bmatrix} \varepsilon_0(w_i, \psi_i) \\ \kappa_0(w_i, \psi_i) \end{bmatrix} + \frac{1}{b}\begin{bmatrix} \varepsilon_1 \\ 0 \end{bmatrix} u_i + \begin{bmatrix} \varepsilon_2 \\ 0 \end{bmatrix} u_i' \tag{5.14}$$

The terms $[\varepsilon_0(w_i, \psi_i)]$ and $[\kappa_0(w_i, \psi_i)]$ are functions of out-of-plane displacement w_i and rotation ψ_i. The calculations are shown in more detail in Appendix D, Equations (D1-D13).

After obtaining the above expressions for strain and curvature, the stress resultants N_{xi}, N_{yi}, N_{xyi} and their derivatives are needed for the equilibrium equations. For a general anisotropic plate, the in-plane stress-strain relationships at node i can be written as:

$$\begin{bmatrix} N_{xi} \\ N_{yi} \\ N_{xyi} \end{bmatrix} = \begin{bmatrix} A_{i_{11}} & A_{i_{12}} & A_{i_{16}} \\ A_{i_{12}} & A_{i_{22}} & A_{i_{26}} \\ A_{i_{16}} & A_{i_{26}} & A_{i_{66}} \end{bmatrix} \begin{bmatrix} \varepsilon_{xi} \\ \varepsilon_{yi} \\ \gamma_{xyi} \end{bmatrix} + \begin{bmatrix} B_{i_{11}} & B_{i_{12}} & B_{i_{16}} \\ B_{i_{12}} & B_{i_{22}} & B_{i_{26}} \\ B_{i_{16}} & B_{i_{26}} & B_{i_{66}} \end{bmatrix} \begin{bmatrix} \kappa_{xi} \\ \kappa_{yi} \\ \kappa_{xyi} \end{bmatrix} \tag{5.15}$$

Substitution from Equation (5.14) into Equation (5.15) gives:

$$\begin{bmatrix} \mathbf{N}_i \\ \mathbf{N}_i' \end{bmatrix} = \overline{\mathrm{A}}_i \begin{bmatrix} \boldsymbol{\varepsilon}_0(\mathrm{w}_i, \psi_i) \\ \boldsymbol{\varepsilon}_0'(\mathrm{w}_i, \psi_i) \end{bmatrix} + \overline{\mathrm{B}}_i \begin{bmatrix} \boldsymbol{\kappa}_0(\mathrm{w}_i, \psi_i) \\ \boldsymbol{\kappa}_0'(\mathrm{w}_i, \psi_i) \end{bmatrix} + \frac{1}{b} \overline{\mathrm{A}}_i \boldsymbol{\varepsilon}_1 \begin{bmatrix} \mathbf{u}_i \\ \mathbf{u}_i' \end{bmatrix} + \overline{\mathrm{A}}_i \boldsymbol{\varepsilon}_2 \begin{bmatrix} \mathbf{u}_i' \\ \mathbf{u}_i'' \end{bmatrix} \tag{5.16}$$

where

$$\mathbf{N}_i = \left[N_{xi0}\ N_{xic}\ N_{xis}\ N_{xiC}\ N_{xiS}\ N_{yi0}\ N_{yic}\ N_{yis}\ N_{yiC}\ N_{yiS}\ N_{xyi0}\ N_{xyic}\ N_{xyis}\ N_{xyiC}\ N_{xyiS} \right]^T \tag{5.17}$$

$$\mathbf{N}_i' = \left[N_{xi0}'\ N_{xic}'\ N_{xis}'\ N_{xiC}'\ N_{xiS}'\ N_{yi0}'\ N_{yic}'\ N_{yis}'\ N_{yiC}'\ N_{yiS}'\ N_{xyi0}'\ N_{xyic}'\ N_{xyis}'\ N_{xyiC}'\ N_{xyiS}' \right]^T \tag{5.18}$$

$$\mathbf{u}_i' = [\mathrm{u}_{i0}' \quad \mathrm{u}_{ic}' \quad \mathrm{u}_{is}' \quad \mathrm{u}_{iC}' \quad \mathrm{u}_{iS}' \quad \mathrm{v}_{i0}' \quad \mathrm{v}_{ic}' \quad \mathrm{v}_{is}' \quad \mathrm{v}_{iC}' \quad \mathrm{v}_{iS}'] \tag{5.19}$$

$$\mathbf{u}_i'' = [\mathrm{u}_{i0}'' \quad \mathrm{u}_{ic}'' \quad \mathrm{u}_{is}'' \quad \mathrm{u}_{iC}'' \quad \mathrm{u}_{iS}'' \quad \mathrm{v}_{i0}'' \quad \mathrm{v}_{ic}'' \quad \mathrm{v}_{is}'' \quad \mathrm{v}_{iC}'' \quad \mathrm{v}_{iS}''] \tag{5.20}$$

Details of the $\overline{\mathrm{A}}_i$ and $\overline{\mathrm{B}}_i$ matrices and the derivatives of $\boldsymbol{\varepsilon}_0(\mathrm{w}_i, \psi_i)$, $\boldsymbol{\kappa}_0(\mathrm{w}_i, \psi_i)$ are given in Appendix D, Equations (D14-D17).

5.2.4 Finite difference approximation in the improved VIPASA analysis

Since the calculation of strain and stress discussed in the previous section involves the use of first-order and second-order derivatives of in-plane and out-of-plane displacements u, v and w and rotation ψ, the finite difference method is applied to convert these quantities into finite difference expressions. The basis of the finite-

difference technique is that the derivative of an unknown function at a point is approximated by an expression consisting of the value of the function at that point and at several neighbouring points. Though the finite difference approach had been proved to be reliable in reducing the complexity of solving differential equations (Chapra and Canale 1998) and used extensively in solving buckling and postbuckling problems (Salvadori 1951; Bushnell et al. 1971; Samir and Al-Rawi 2006), few researchers have applied it by and combining it with the exact strip method.

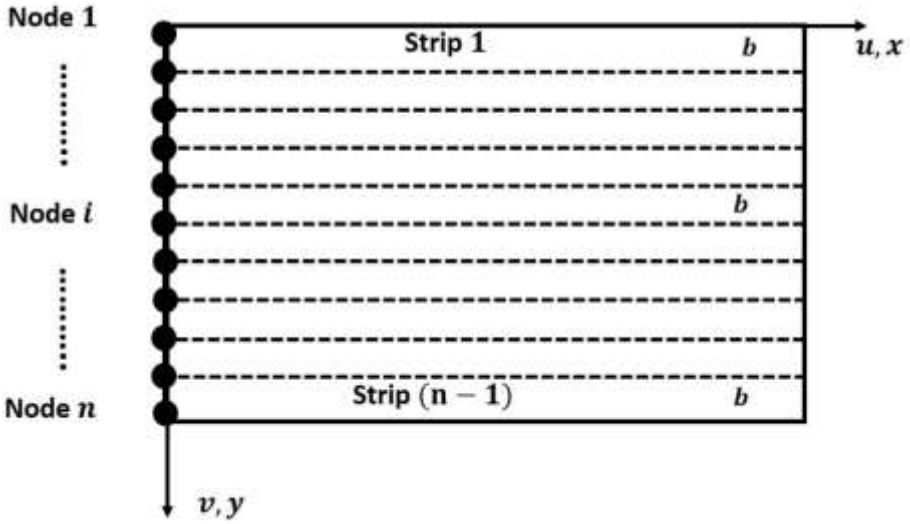

Figure 5.2 Plate of n nodes, divided into $n-1$ strips of equal width b in the VIPASA axis system.

In the exact strip method, the whole plate is divided into a number of strips in the longitudinal direction. The nodes are then evenly distributed in the transverse direction with spacing b (shown in Figure 5.2). The finite difference expressions then need to be derived and modified along the transverse direction, so that the derivatives of in-plane displacement function $\boldsymbol{u_i}$ can be expressed by the difference ratio at node i and several evenly spaced points to the right and left of node i. Since no neighbouring points can be addressed for the first and the last nodes, three scenarios are considered when it cames to deriving the finite difference expressions there. Note that the plots of the in-plane

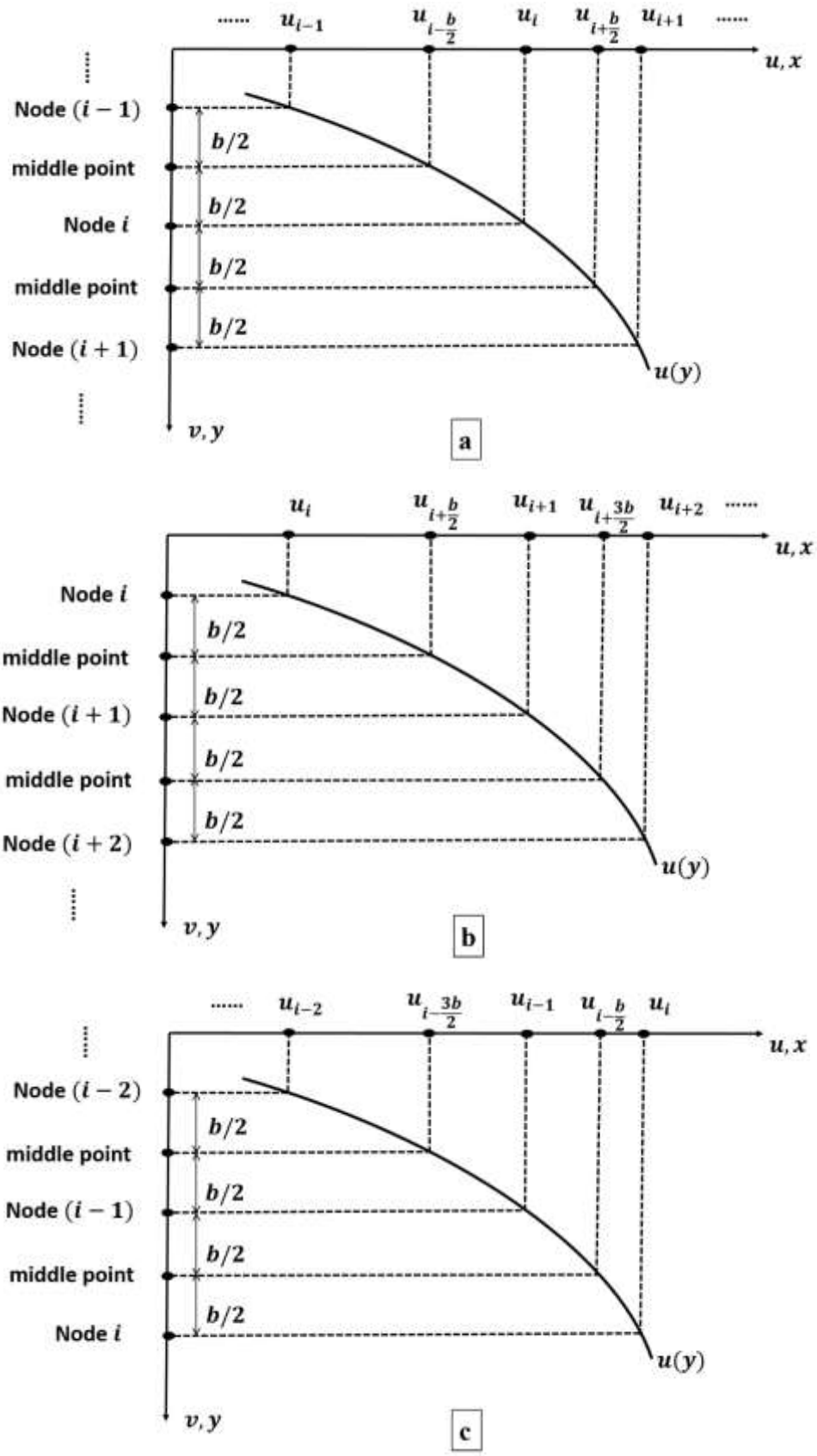

Figure 5.3 Graphic representation of finite difference method for calculating the derivatives at (a) an interior node; (b) an initial node and (c)a final node

displacement function $\boldsymbol{u_i}$ in Figure 5.3 are only for illustration purposes and do not represent the actual shape function which couples with different half-wavelengths λ. The details of the finite difference expressions are shown in the following calculations.

Case i. the node is an interior node (Figure 5.3a)

The first derivative of displacement function $\boldsymbol{u}$ at the node i can be expressed by the central difference expression as:

$$u_i' = \frac{u_{i+1} - u_{i-1}}{2b} \tag{5.21}$$

The second derivative can be obtained by taking the difference of the first difference. At the point $x = i$, this can be expressed as:

$$u_i'' = \frac{\left(u'_{i+\frac{b}{2}} - u'_{i-\frac{b}{2}}\right)}{b}$$

$$= \frac{\frac{u_{i+1} - u_i}{b} - \frac{u_i - u_{i-1}}{b}}{b} \tag{5.22}$$

$$= \frac{u_{i+b} - 2u_i + u_{i-b}}{b^2}$$

Case ii. the node is an initial node (Figure 5.3b)

The first derivative of the displacement function $\boldsymbol{u_i}$ at node i can be expressed by the backward difference expression as:

$$u_i' = u'_{i+\frac{b}{2}} - \frac{1}{2}\left(u'_{i+\frac{3b}{2}} - u'_{i+\frac{b}{2}}\right)$$

$$= \frac{u_{i+1} - u_i}{b} - \frac{1}{2}\left(\frac{u_{i+2} - u_{i+1}}{b} - \frac{u_{i+1} - u_i}{b}\right) \tag{5.23}$$

$$= \frac{-3u_i + 4u_{i+1} - u_{i+2}}{2b}$$

Similarly, at node i, the second derivative of displacement function $\boldsymbol{u_i}$ can be determined by:

$$\begin{aligned} u_i'' &= u_{i+1}'' - (u_{i+2}'' - u_{i+1}'') \\ &= 2u_{i+1}'' - u_{i+2}'' \\ &= \frac{2u_i - 5u_{i+1} + 4u_{i+2} - u_{i+3}}{b^2} \end{aligned} \tag{5.24}$$

Case iii. the node is a final node (Figure 5.3c)

The first derivative of the displacement function $\boldsymbol{u}$ at node i can be expressed by the forward difference expression:

$$\begin{aligned} u_i' &= u'_{i-\frac{b}{2}} + \frac{1}{2}\left(u'_{i-\frac{b}{2}} - u'_{i-\frac{3b}{2}}\right) \\ &= \frac{u_i - u_{i-1}}{b} + \frac{1}{2}\left(\frac{u_i - u_{i-1}}{b} - \frac{u_{i-1} - u_{i-2}}{b}\right) \\ &= \frac{3u_i - 4u_{i-1} + u_{i-2}}{2b} \end{aligned} \tag{5.25}$$

Again, the second derivative of the displacement function $\boldsymbol{u}$ can be approximated by the expression:

$$\begin{aligned} u_i'' &= u_{i-1}'' - (u_{i-2}'' - u_{i-1}'') \\ &= 2u_{i-1}'' - u_{i-2}'' \\ &= \frac{-u_{i-3} + 4u_{i-2} - 5u_{i-1} + 2u_i}{b^2} \end{aligned} \tag{5.26}$$

It can be observed from the above equations that the convergence of the solution to the derivatives at a point is closely related to the spacing between that point and several neighbouring points. Therefore, closer spacing between the nodes point can lead to better

approximation of the derivatives, and hence a more accurate solution to the differential equations.

The finite difference method provides a fast, yet reliable approach to calculating the derivatives of a function. It allows a continuous system to be replaced by a finite number of discrete variables so that the differential equation is replaced by a finite number of simultaneous algebraic equations in these variables, and these algebraic equations are usually easier to solve. Also, once these transformation processes are completed, faster solution times are achievable if a system of simultaneous algebraic equations is implemented into a computer program and solved by a special algorithm. The convergence study shows that consistent results can be achieved with the minimum number of ten strips. Thus it was determined that a ten-strip model would be used to generate accurate results with relatively low computational cost for the rest of the examples in Chapter 5 and Chapter 6.

The main disadvantage of the method is that it gives numerical values of the unknown functions at discrete points instead of an analytical expression that is valid for the entire system. This shortcoming has some effect on solving the equilibrium problems as the finite difference method sometimes requires the finding of fictitious points outside the domain of a structure, which results in discontinuous expressions for the deflection functions.

5.2.5 Equilibrium equations

$$\frac{\partial N_{yi}}{\partial y} + \frac{\partial N_{xyi}}{\partial x} = 0 \tag{5.27}$$

$$\frac{\partial N_{xyi}}{\partial y} + \frac{\partial N_{xi}}{\partial x} = 0 \tag{5.28}$$

Having obtained the derivatives of the in-plane displacement function $\boldsymbol{u}$, the in-plane equilibrium equations 5.27 and 5.28 can be expressed in component form since the displacement function $\boldsymbol{u_i}$ has ten components for each strip. The details of the equilibrium equations are shown in Appendix D, Equation D18.

To solve for the in-plane displacements u and v, these expressions for equilibrium at strip level are rearranged to obtain the equilibrium equations of individual nodes. The overall equations for the whole plate can then be assembled by using the conventional routines of matrix structural analysis. The corresponding equilibrium problem can finally be written in matrix form as

$$\mathbf{Hu} = \mathbf{G}(\mathbf{w}) \tag{5.29}$$

where $\mathbf{u}$ includes the unknown in-plane displacements $\mathbf{u}_i$ for all the nodes of the structure, $\mathbf{H}$ is a square matrix with constant coefficients and $\mathbf{G}(\mathbf{w})$ is a non-linear function of the out-of-plane displacements $\mathbf{w}$ which are known from the VIPASA analysis. Equation (5.29) is solved to give the in-plane displacements as

$$\mathbf{u} = \mathbf{H}^{-1}\mathbf{G}(\mathbf{w}) \tag{5.30}$$

Having obtained the in-plane displacement $\mathbf{u}_i$ for all the nodes, the stress resultants $\mathbf{N}_i$ can be calculated by substituting $\mathbf{u}_i$ into Equations (5.13-5.15).

5.3 Implementation of Improved VIPASA analysis

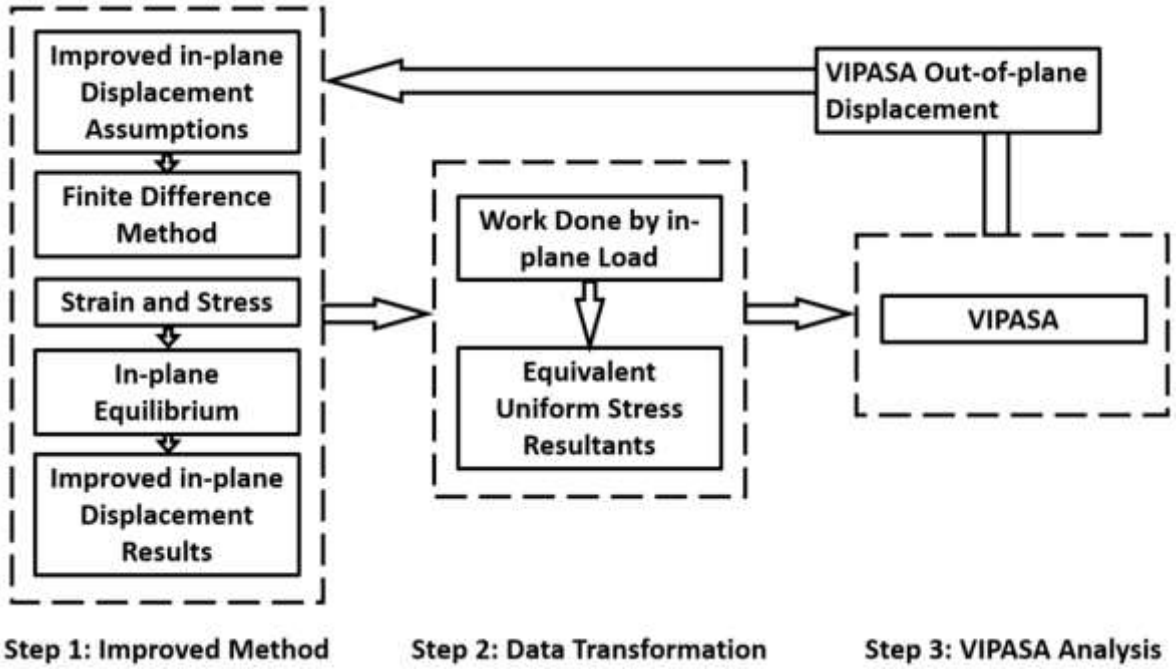

Figure 5.4 Implementation scheme of the Improved VIPASA analysis.

The Improved VIPASA analysis is designed to address the inaccurate assumptions in previous analyses and is capable of being implemented as a subroutine in the current VIPASA software, which will enable the proposed method to work with the existing iteration scheme to automate the postbuckling process and achieve better accuracy. The implementation of the Improved VIPASA analysis can be illustrated in Figure 5.4. The procedures described in Section 5.2 can be regarded as the first step of the implementation, which yields the stress resultants at each node. However, the stress resultants calculated at the node level cannot be used directly in the next iteration of VIPASA, because they include sinusoidal terms varying in the longitudinal direction while VIPASA iteration is based on uniform stress resultants at strip level. Hence, the sinusoidally varying stress resultants are transformed to longitudinally equivalent

uniform stress resultants based on energy considerations at step 2 in Figure 5.4, so as to pave the way for iteration of the existing VIPASA strategy.

The work done by the applied loading in strip i is given by

$$V = V_{xi} + V_{yi} + V_{xyi} \tag{5.31}$$

where

$$V_{xi} = \frac{ab_i}{\lambda}\int_0^{\lambda} N_{xi}\varepsilon_{xi}dx \tag{5.32}$$

$$V_{yi} = \frac{ab_i}{\lambda}\int_0^{\lambda} N_{yi}\varepsilon_{yi}dx \tag{5.33}$$

$$V_{xyi} = \frac{ab_i}{\lambda}\int_0^{\lambda} N_{xyi}\gamma_{xyi}dx \tag{5.34}$$

Writing the stress resultants as:

$$\begin{bmatrix} N_{xi} \\ N_{yi} \\ N_{xyi} \end{bmatrix} = \begin{bmatrix} N_{xi0} & N_{xic} & N_{xis} & N_{xiC} & N_{xiS} \\ N_{yi0} & N_{yic} & N_{yis} & N_{yiC} & N_{yiS} \\ N_{xyi0} & N_{xyic} & N_{xyis} & N_{xyiC} & N_{xyiS} \end{bmatrix} [G_u] \tag{5.35}$$

and substituting Equations (5.14), (5.16) and (5.35) into Equations (5.32)-(5.34), the components of V are written as:

$$V_{xi} = \frac{ab_i}{\lambda}(N_{xi0}\eta_{xi0} + N_{xic}\eta_{xic} + N_{xis}\eta_{xis} + N_{xiC}\eta_{xiC} + N_{xiS}\eta_{xiS}) \tag{5.36}$$

$$V_{yi} = \frac{ab_i}{\lambda}\left(N_{yi0}\eta_{yi0} + N_{yic}\eta_{yic} + N_{yis}\eta_{yis} + N_{yiC}\eta_{yiC} + N_{yiS}\eta_{yiS}\right) \tag{5.37}$$

$$V_{xyi} = \frac{ab_i}{\lambda}\left(N_{xyi0}\eta_{xyi0} + N_{xyic}\eta_{xyic} + N_{xyis}\eta_{xyis} + N_{xyiC}\eta_{xyiC} + N_{xyiS}\eta_{xyiS}\right) \tag{5.38}$$

where the parameters η_{xij}, η_{yij} and η_{xyij}, listed in Appendix E, are expressed in terms of the displacement coefficients $\bar{\varepsilon}_x$, $\mathbf{u}_i$ and $\mathbf{w}_i$.

Comparing with the corresponding expressions for uniform loading yields the following expressions for equivalent longitudinally invariant stress resultants, which are then used by VIPASA to calculate the strip stiffness matrices.

$$\bar{N}_{xi} = N_{xi0} + \frac{1}{\eta_{xi0}}(N_{xic}\eta_{xic} + N_{xis}\eta_{xis} + N_{xiC}\eta_{xiC} + N_{xiS}\eta_{xiS}) \tag{5.39}$$

$$\bar{N}_{yi} = N_{yi0} + \frac{1}{\eta_{yi0}}\left(N_{yic}\eta_{yic} + N_{yis}\eta_{yis} + N_{yiC}\eta_{yiC} + N_{yiS}\eta_{yiS}\right) \tag{5.40}$$

$$\bar{N}_{xyi} = N_{xyi0} + \frac{1}{\eta_{xyi0}}\left(N_{xyic}\eta_{xyic} + N_{xyis}\eta_{xyis} + N_{xyiC}\eta_{xyiC} + N_{xyiS}\eta_{xyiS}\right) \tag{5.41}$$

5.4 Conclusion

This chapter has presented a detailed description of an improved VIPASA postbuckling analysis based on the combination of Stein's method and the current exact strip method. The former VIPASA analysis uses a single half-wavelength trigonometric function to represent both the in-plane and out-of-plane displacement functions which results in a convenient single-term type of analysis over the postbuckling range, but where accurate in-plane mode shape and stress resultants are needed such an assumption is not adequate. The Improved VIPASA analysis takes into account the coupling between half-wavelengths λ and $\lambda/2$ of the in-plane displacement in the postbuckling range in order to achieve more accurate in-plane displacement results, so that a more accurate stress distribution can be obtained.

The suggested implementation scheme has been proposed to enable the Improved analysis to be incorporated into the current VIPASA software. However, it should be pointed out that the implementation (step 2, step 3 in Figure 5.4) should only be conducted once the improved analysis has been fully validated. Hence, the validation processes and results will be presented in the following chapters.

Chapter 6

Validation of the Improved VIPASA analysis

The Improved VIPASA analysis for the study of isotropic and anisotropic plate postbuckling behaviours was presented in Chapter 5. Improvements on the previous version of VIPASA postbuckling analysis are made through using enhanced trigonometric functions to predict longitudinal and transverse in-plane displacements more accurately. This chapter continues to discuss the validation process for the Improved VIPASA analysis and compares the results given by the proposed method with analytical results and FEA benchmark results. The main outputs of the Improved VIPASA analysis, namely, in-plane displacements (u and v), strains (ε_x and ε_y) and stress resultants (N_x and N_y), are all displayed and checked in this chapter. These results offer valuable insight into the mechanism of the Improved VIPASA analysis, exploring its advantages as well as its weaknesses. The chapter is organised as follows: Section 6.1 describes the VIPASA model and different composite layups used for the validation work. Section 6.2 discusses the relationship between material anisotropy and in-plane displacement results. Section 6.3 proposes an analytical model to interpolate the strain results from the proposed method. Section 6.4 gives the details of the finite element model used to verify the proposed method. Section 6.5 compares the postbuckling results given by the Improved VIPASA analysis with the FEA results. Section 6.6 concludes the chapter.

6.1 Introduction

6.1.1 VIPASA model

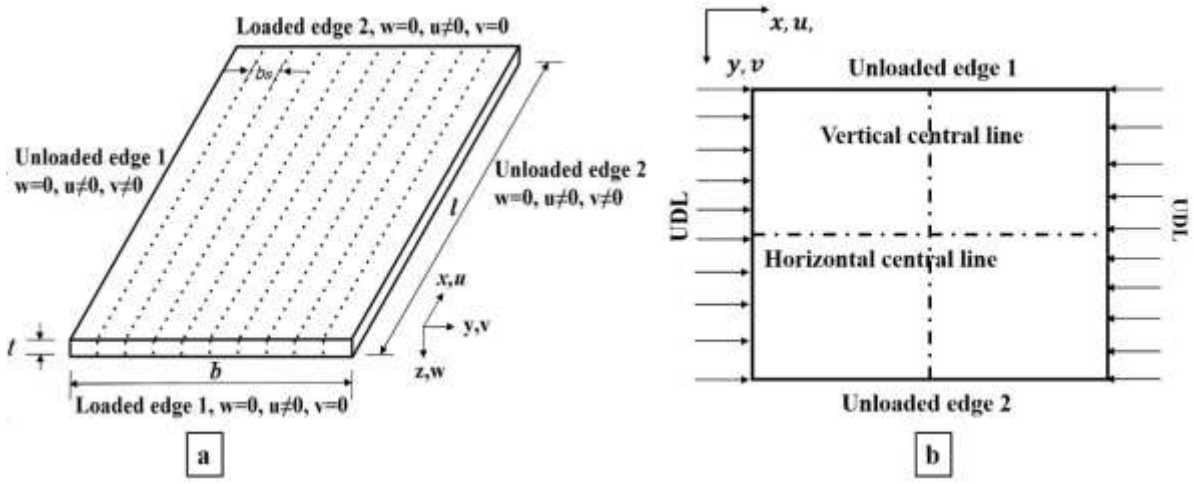

Figure 6.1 The VIPASA model: (a) in-plane and out-of-plane boundary conditions and (b) compressive loading.

A square plate of length $l = 300$ mm, width $b = 300$ mm and thickness $h = 1$mm is modelled in VIPASA, with-pure axial compression applied. The boundary conditions and strip layout are shown in Figure 6.1.

The model is utilised to provide the out-of-plane mode shape used to initiate the proposed Improved analysis scheme. Convergence studies found that a model with 10 strips and 11 nodes is sufficient to obtain good results whilst maintaining the computational advantages of exact strip analysis. Since for this strip layout, the width to thickness ratio of each strip is large, that is $b/h = 30$, thin plate assumptions are satisfied minimising transverse shear effects. The current version of VIPASA has four unknown coefficients at each node associated with the displacements (u, v and w) and rotation (ψ). The Improved VIPASA analysis discussed in Chapter 5, by contrast, possesss ten unknown at each node yielding a total of 110 coefficients representing the in-plane displacement field in the postbuckling range. The numerical results from the VIPASA

analysis and the Improved VIPASA analysis discussed in the following sections are all based on this model.

6.1.2 Material properties

The square plate mentioned above is first modelled using an isotropic material with Young's modulus $E = 110$ kNmm^{-2} and Poisson's ratio $\upsilon = 0.3$. To demonstrate that the proposed method is capable of analysing the postbuckling behaviour of more general anisotropic plates, the same square plate is then modelled using a composite material $E_{11} = 131$kNmm^{-2}, $E_{12} = 6.41$kNmm^{-2}, $E_{22} = 13$kNmm^{-2}, $G_{12} = G_{13} = G_{23} = 6.41$kNmm^{-2}, $\nu = 0.38$. The laminate lay-ups considered consist of 16 plies with a ply thickness of 0.125mm. Three types of composite laminate are considered, with their configurations as follows:

a. $[0/0/+45/0/-45/0/90/90/90/90/0/-45/0/+45/0/0]_T$,

b. $[0/-45/+45/0/-45/0/90/90/90/90/0/-45/0/+45/-45/0]_T$

c. $[0/-45/+45/0/-45/0/90/90/90/90/0/-45/-45/0/0/+45]_T$,

Configuration (a) is, of course, a symmetric and balanced layup where two elements in the **A** matrix, A_{16} and A_{26}, as well as the **B** matrix are zero. Configuration (b) is symmetric and unbalanced and possesses in-plane membrane coupling between its normal and shear actions which are not present in configuration (a). Configuration (c) has an unsymmetric, unbalanced stacking sequence and therefore all elements in the extensional (**A**), coupling (**B**) and bending (**D**) stiffness matrix are non-zero. This general anisotropic layup allows coupling to exist between in-plane (extension or membrane) and out-of-plane (bending or flexure) actions as well as in-plane shear and extension actions (York 2009). The coupling behaviours in different composite layout are shown in Figure 6.2.

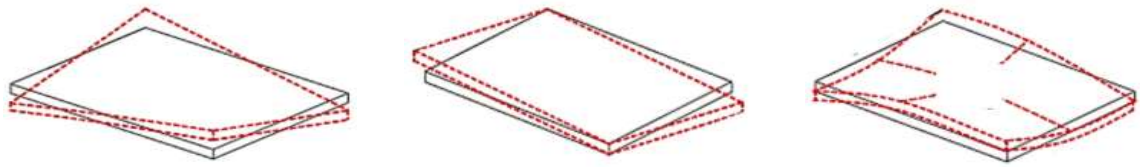

a b c

Figure 6.2 Illustration of the coupling behaviours in different composite layouts where red dashed lines stand for the possible distortion shape after composite curing: (a) symmetric and balanced: bending and twisting coupling, (b) symmetric and unbalanced: in-plane shear and extension coupling and (c) unsymmetric and unbalanced: in-plane and out-of-plane coupling.

6.2 Interpretation of in-plane displacement results

Detailed numerical results from the Improved VIPASA analysis showing the in-plane displacement (u and v) at an initial postbuckling load level, where the longitudinal strain in the Improved VIPASA analysis exceeded the critical buckling strain by 0.2% and the load factor is $P/P_{cr} = 1.0086$ ($P/P_{cr} = 1.0086$), are given in Tables 6.1, 6.2 and 6.3 for the isotropic case, the symmetric and balanced composite case and the unsymmetric and unbalanced composite case, respectively. These values are obtained directly from the Improved VIPASA analysis step 1 (described in Figure 5.4) and are compared here to show the relationship between the in-plane trigonometric functions and material anisotropy so that the fundamental assumptions of the in-plane shape functions can be proved to be valid.

Since the in-plane displacements are assumed to be a combination of sinusoidal functions with half-wavelengths λ and $\lambda/2$ (Equations 5.9 to 5.12), the results have five components in total. In these tables, the in-plane displacement results associated with the cosine function with half-wavelengths λ and $\lambda/2$ are tabulated in the 'c' and 'C' columns, while results corresponding to the sine function with half-wavelengths λ and $\lambda/2$ are listed in the 's' and 'S' columns, respectively. The '0' column represents the linear component of the in-plane displacement field. The purpose of these tables is not to

demonstrate the increase in the amplitude of the postbuckling in-plane displacements with changing applied load but rather to show how the sinusoidal functions and the material anisotropy are related in the Improved VIPASA analysis.

Table 6.1 tabulates the in-plane displacement results for the isotropic square plate. Apart from the linear term in the transverse displacement v, only the cosine or sine terms with half-wavelength $\lambda/2$ appear in the results showing that the postbuckling in-plane displacement field is only related to a single term trigonometric function for the isotropic case. On comparing the results of Table 6.2 with Table 6.1, it can be seen that the in-plane displacements (u and v) involve more trigonometric terms, with an additional sine or cosine term with half-wavelength $\lambda/2$ appearing in the table, as the material changes from metal to a symmetric balanced composite. This confirms the findings of Stein who suggested that sinusoidal functions with half-wavelength $\lambda/2$ are sufficient to capture the in-plane displacement field of these plates during the postbuckling stage. The results of Table 6.3 can be compared to those of Table 6.1 and Table 6.2, respectively. The most direct observation is that for this general anisotropic case all the trigonometric terms appear. These results reflect the current improvements made to Stein's work as the presence of both cosine and sine terms with half-wavelength λ in the in-plane displacement field allows the most general anisotropic material response to be taken into account.

Since the tabulated numerical data considered in this section reflects only the direct analysis results of the Improved VIPASA analysis, it is insufficiently robust to compare in-plane displacements without mentioning other quantities obtained by using the proposed analysis. Hence, in the next section, an analytical approach is employed to further validate the middle surface strain predicted by the Improved VIPASA analysis.

Table 6.1 Tabulation of actual nodal in-plane displacements $u(\mathrm{m})$ and $v(\mathrm{m})$ obtained from the Improved VIPASA analysis for an isotropic square plate with simply supported out-of-plane boundary conditions.

	Components / Node	0	c	s	C	S
u	**1**	0	0	0	0	0
	2	0	0	0	0	-7.42845E-10
	3	0	0	0	0	-2.29907E-09
	4	0	0	0	0	-4.24524E-09
	5	0	0	0	0	-5.84617E-09
	6	0	0	0	0	-6.46281E-09
	7	0	0	0	0	-5.84617E-09
	8	0	0	0	0	-4.24524E-09
	9	0	0	0	0	-2.29907E-09
	10	0	0	0	0	-7.42845E-10
	11	0	0	0	0	0
v	**1**	-1.79927E-06	0	0	-4.64683E-09	0
	2	-1.44084E-06	0	0	-9.60501E-10	0
	3	-1.08186E-06	0	0	1.48456E-09	0
	4	-7.22009E-07	0	0	2.29732E-09	0
	5	-3.61276E-07	0	0	1.60004E-09	0
	6	7.76220E-15	0	0	-2.04163E-23	0
	7	3.61276E-07	0	0	-1.60004E-09	0
	8	7.22009E-07	0	0	-2.29732E-09	0
	9	1.08186E-06	0	0	-1.48456E-09	0
	10	1.44084E-06	0	0	9.60501E-10	0
	11	1.79927E-06	0	0	4.64683E-09	0

Table 6.2 Tabulation of actual nodal in-plane displacements $u(\mathrm{m})$ and $v(\mathrm{m})$ obtained from the Improved VIPASA analysis for a symmetric and balanced composite square plate with simply supported out-of-plane boundary conditions.

	Components / Node	0	c	s	C	S
u	**1**	0	0	0	0	0
	2	3.53493E-09	0	0	-4.27515E-09	6.38517E-10
	3	4.53753E-09	0	0	-8.72891E-09	-1.21572E-09
	4	5.31461E-09	0	0	-1.43595E-08	-5.68422E-09
	5	7.43108E-09	0	0	-1.74322E-08	-1.12925E-08
	6	1.1051E-08	0	0	-1.69716E-08	-1.56109E-08
	7	1.48916E-08	0	0	-1.33572E-08	-1.6547E-08
	8	1.68666E-08	0	0	-8.21468E-09	-1.35603E-08
	9	1.51396E-08	0	0	-3.55726E-09	-8.08329E-09
	10	9.11888E-09	0	0	-7.60015E-10	-2.80724E-09
	11	0	0	0	0	0
v	**1**	-5.38386E-06	0	0	-2.91563E-09	1.33699E-08
	2	-4.31193E-06	0	0	-2.24867E-09	7.59206E-10
	3	-3.2382E-06	0	0	1.41089E-09	-6.89562E-09
	4	-2.16145E-06	0	0	4.76241E-09	-7.91894E-09
	5	-1.08167E-06	0	0	5.12347E-09	-3.88157E-09
	6	0	0	0	1.79862E-09	1.85278E-09
	7	1.08167E-06	0	0	-3.49798E-09	5.62657E-09
	8	2.16145E-06	0	0	-7.41655E-09	5.36714E-09
	9	3.2382E-06	0	0	-6.60021E-09	1.57347E-09
	10	4.31193E-06	0	0	6.00066E-10	-2.99615E-09
	11	5.38386E-06	0	0	1.30724E-08	-4.72004E-09

Table 6.3 Tabulation of actual nodal in-plane displacements u(m) and v(m) obtained from the Improved VIPASA analysis for a square general anisotropic plate with simply supported out-of-plane boundary conditions.

	Components / Node	0	c	s	C	S
u	1	0	0	0	0	0
	2	-1.04696E-08	4.37350E-09	-5.06391E-09	1.45504E-09	-1.91917E-09
	3	-1.67161E-08	6.80338E-09	-5.41639E-09	5.75414E-09	-4.67916E-09
	4	-1.77680E-08	7.28463E-09	-3.13963E-09	1.07899E-08	-5.48809E-09
	5	-1.49594E-08	5.94348E-09	2.36185E-10	1.54673E-08	-2.87832E-09
	6	-1.06802E-08	3.14243E-09	3.54349E-09	1.70268E-08	2.05212E-09
	7	-6.91629E-09	-4.76003E-10	5.92910E-09	1.44937E-08	6.41599E-09
	8	-4.41302E-09	-3.98793E-09	6.85708E-09	9.21080E-09	7.65607E-09
	9	-2.79927E-09	-6.19084E-09	6.10711E-09	3.86086E-09	5.43461E-09
	10	-1.40277E-09	-5.55042E-09	3.73679E-09	6.46122E-10	1.89948E-09
	11	0	0	0	0	0
v	1	-3.10009E-06	-1.41516E-08	-4.80058E-09	-3.98297E-09	-5.10878E-09
	2	-2.48295E-06	-1.79600E-08	-6.00420E-09	3.92884E-09	-1.71995E-09
	3	-1.86480E-06	-2.02738E-08	-8.76037E-09	6.09473E-09	4.361230E-09
	4	-1.24484E-06	-2.09283E-08	-1.24374E-08	3.03645E-09	7.704880E-09
	5	-6.23003E-07	-1.98898E-08	-1.62883E-08	-1.31719E-09	5.596600E-09
	6	0	-1.73601E-08	-1.95757E-08	-2.79216E-09	-3.23259E-10
	7	6.22885E-07	-1.37939E-08	-2.16943E-08	1.124130E-11	-5.70101E-09
	8	1.24460E-06	-9.84642E-09	-2.22650E-08	4.741490E-09	-6.68024E-09
	9	1.86445E-06	-6.27401E-09	-2.11756E-08	6.987960E-09	-2.79105E-09
	10	2.48248E-06	-3.81420E-09	-1.85489E-08	3.533190E-09	2.462290E-09
	11	3.09950E-06	-3.07447E-09	-1.46240E-08	-4.92706E-09	3.828010E-09

6.3 Analytical validation of strain

6.3.1 Formulation of middle surface strain

In-plane (membrane) strains will be developed in the middle surface of the plate when it starts to bend. As long as the transverse deflections of the plate are small compared to the plate thickness, these membrane strains may be safely neglected (small deflection theory). However, as the transverse deflections increase during the postbuckling stage, they become of the order of magnitude of the plate thickness. Hence, the membrane strain is no longer negligible and can be used as an important quantity in measuring the plate postbuckling behaviour. An analytical derivation of the postbuckling strains ε_x and ε_y of an isotropic plate under pure axial compression is presented in this section to verify the results obtained from the Improved VIPASA analysis.

The formulation begins with defining the plate's post-buckled in-plane and out-of-plane mode shapes. These in-plane and out-of-plane expressions are slightly different to Equations 5.9-5.12 in the sense that they are expressed along both longitudinal and transverse directions, which, given the coordinates, are the x and y axes. The plate is assumed to have taken an overall buckling mode with half-wavelength λ equal to l in the x-direction and b in the y-direction. Therefore, the out-of-plane deformed shape can be expressed as

$$w = w_{max} \sin\frac{\pi y}{b} \sin\frac{\pi x}{l} \tag{6.1}$$

where w_{max} is the maximum out-of-plane displacement. The in-plane displacements obtained from the Improved VIPASA analysis will have cosine or sine terms with a half-wavelength λ equal to $l/2$ in the x direction, so that they can be expressed as

$$u = u_{max} \sin\frac{\pi y}{b} \sin\frac{2\pi x}{l} \tag{6.2}$$

$$v = v_{max} \cos\frac{\pi y}{b} \cos\frac{2\pi x}{l} \tag{6.3}$$

where u_{max} and v_{max} are the maximum longitudinal displacement and transverse displacement.

According to large deflection theory, the middle surface strains can be written as:

$$\varepsilon_x = \frac{\partial u}{\partial x} + \frac{1}{2}\left(\frac{\partial w}{\partial x}\right)^2 \tag{6.4}$$

$$\varepsilon_y = \frac{\partial v}{\partial y} + \frac{1}{2}\left(\frac{\partial w}{\partial y}\right)^2 \tag{6.5}$$

By substituting Equations 6.1-6.3 into Equations 6.4-6.5, the following expressions are obtained:

$$\varepsilon_x = \frac{2\pi}{l} u_{max} \cos\frac{2\pi x}{l} \left(\sin\frac{\pi y}{b}\right) + \frac{\pi^2}{2l^2} {w_{max}}^2 \cos^2\frac{\pi x}{l} \left(\sin^2\frac{\pi y}{b}\right) \tag{6.6}$$

$$\varepsilon_y = -\frac{\pi}{b} v_{max} \cos\frac{2\pi x}{l} \left(\sin\frac{\pi y}{b}\right) + \frac{\pi^2}{2b^2} {w_{max}}^2 \sin^2\frac{\pi x}{l} \left(\cos^2\frac{\pi y}{b}\right) \tag{6.7}$$

Then, based on Equation 6.6 and Equation 6.7, the middle surface strain can be rearranged and elaborated as:

$$\varepsilon_x = \frac{\pi^2}{8l^2} {w_{max}}^2 - \frac{\pi^2}{8l^2} {w_{max}}^2 \cos\frac{2\pi y}{b} + \left[\frac{2\pi}{l} u_{max} \left(\sin\frac{\pi y}{b}\right) + \frac{\pi^2}{4l^2} {w_{max}}^2 \left(\sin^2\frac{\pi y}{b}\right)\right] \cos\frac{2\pi x}{l} \tag{6.8}$$

$$\varepsilon_y = \frac{\pi^2}{8b^2} {w_{max}}^2 + \frac{\pi^2}{8b^2} {w_{max}}^2 \cos\frac{2\pi y}{b} - \left[\frac{\pi}{b} v_{max} \left(\sin\frac{\pi y}{b}\right) + \frac{\pi^2}{4b^2} {w_{max}}^2 \left(\cos^2\frac{\pi y}{b}\right)\right] \cos\frac{2\pi x}{l} \tag{6.9}$$

The details of the derivation process can be seen in Appendix F. Note that the middle surface strain expressions consist of a summation of three parts, where the first part is a

constant term, and the second part and third part represent positive or negative cosine function variations along the y and the x axes, indicating that the buckled plates possess a double curvature in both x and y directions.

The analytical expressions derived in Equations 6.1–6.9 are extremely helpful in checking the variational pattern of the middle surface strain across the plate as they separate the variation trends in different directions. Hence, contour plots of the middle surface strain obtained from the Improved VIPASA analysis will be compared with these analytical solutions in the following sections.

6.3.2 Interpolation of strain results from the Improved VIPASA analysis

Contour plots of middle surface strain (ε_x and ε_y) for square metal plates at an early postbuckling stage, i.e. when the longitudinal strain in the Improved VIPASA analysis exceeded the critical buckling strain by 0.2% and the load factor is $P/P_{cr} = 1.0086$, obtained from the Improved VIPASA analysis are shown in Figures 6.3 and 6.4. A comprehensive approach to interrogating these plots can be achieved by comparing the variation trends extracted from the contours with those predicted using the analytical expressions given in Equations 6.8 and 6.9. Therefore, four paths, including lines along the plate's boundaries and across its centre, are chosen and marked on the contour plots, and a series of strain ε_x and ε_y values along these paths are extracted. Figures 6.5 and 6.6 provide the traces of these extracted values for different paths in the strain contour plots giving information on how these strains vary. At the same time, Tables 6.4 and 6.5 compare simplified analytical expressions of strain ε_x and ε_y with different variations shown in Figures 6.5 and 6.6. In terms of ε_x, the values taken along path 1 and path 2 descibe a positive sine function shape as shown in Figure 6.5, which corresponds to the

analytical expressions of the half-wave sine representation for these two paths in Table 6.4.

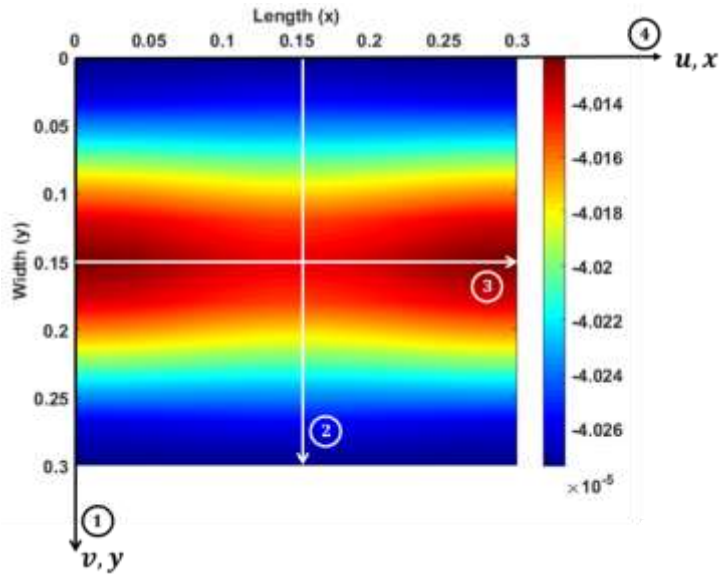

Figure 6.3 Contour plot of strain ε_x and the paths to extract the corresponding values.

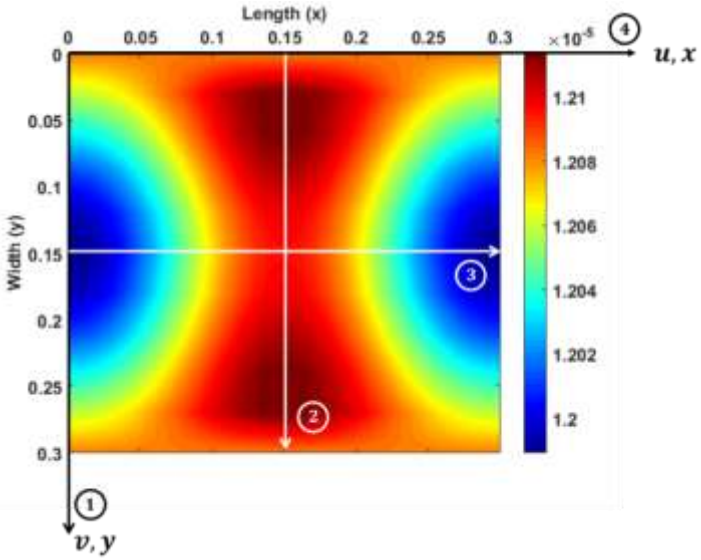

Figure 6.4 Contour plot of strain ε_y and the paths to extract the corresponding values.

Similarly, agreements are obtained between the numerical trends and the analytical expressions along path 3 and path 4. Note that in Table 6.4 the analytical expression for the longitudinal edge (path 4) is zero, indicating the absence of a sinusoidal variation in the strain. As a result, a straight line is observed in Figure 6.5 and the value is equal to the

end-shortening strain at that particular load level. A similar comparison study is done on strain ε_y shown in Figure 6.6 and Table 6.5. As is to be expected, the traces of the results extracted from the contour are in good agreement with the prediction obtained from the analytical expressions.

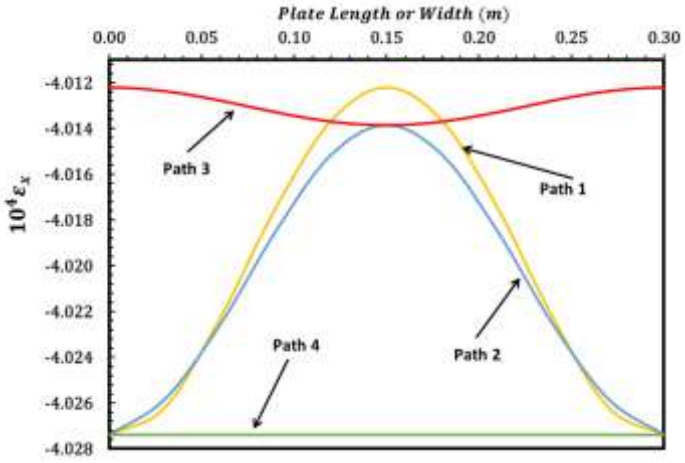

Figure 6.5 Trace of strain ε_x pattern along different paths of the contour plots

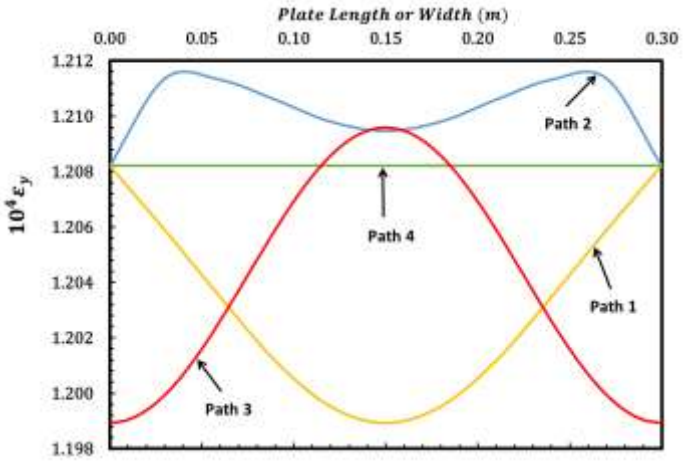

Figure 6.6 Trace of strain ε_y pattern along different paths of the contour plots.

Thus, the shape the contour plot should take can be predicted by the corresponding analytical expressions. This is particularly useful when programming and debugging the Improved VIPASA analysis. Further validation of the improved technique can be obtained by comparing the values of the stress resultants, which are of great interest to aerospace designers, with benchmark results from the FEA software ABAQUS.

Table 6.4 Analytical interpolation of the strain contour plot ε_x along different paths

Location	Path Descriptions	Simplified Strain Expression from Equation 6.8	Variational Trend
Path 1	$x = 0, x/l = 0,$ and $\cos\frac{2\pi y}{b} = 1$	$\varepsilon_x = \left(\frac{\pi^2}{4l^2}{w_{max}}^2 \sin\frac{\pi y}{b} + \frac{2\pi}{l}u_{max}\right)\sin\frac{\pi y}{b}$	Positive sine function variation
Path 2	$x = 0.15\,, x/l = 1/2,$ and $\cos\frac{2\pi y}{b} = -1$	$\varepsilon_x = -\frac{2\pi}{l}u_{max}\sin\frac{\pi y}{b}$	Positive sine function variation
Path 3	$y = 0.15, y/b = 1/2,$ and $\cos\frac{2\pi y}{b} = -1, \sin\frac{\pi y}{b} = 1$	$\varepsilon_x = \frac{\pi^2}{4l^2}{w_{max}}^2 + \left(\frac{\pi^2}{4l^2}{w_{max}}^2 + \frac{2\pi}{l}u_{max}\right)\cos\frac{2\pi x}{l}$	Positive cosine function variation
Path 4	$y = 0, y/b = 0,$ and $\cos\frac{2\pi y}{b} = 1, \sin\frac{\pi y}{b} = 0$	$\varepsilon_x = constant$	No variational part appears

Table 6.5 Analytical interpolation of the strain contour plot ε_y along different paths

Location	Path Descriptions	Simplified Strain Expression from Equation 6.9	Variational Trend
Path 1	$x = 0, x/l = 0,$ and $\cos\frac{2\pi y}{b} = 1$	$\varepsilon_y = -\frac{\pi}{b}v_{max}\sin\frac{\pi y}{b}$	Negative sine function variation
Path 2	$x = 0.15\,, x/l = 1/2,$ and $\cos\frac{2\pi y}{b} = -1$	$\varepsilon_y = \frac{\pi^2}{2b^2}{w_{max}}^2 - \left(\frac{\pi}{b}v_{max} + \frac{\pi^2}{2b^2}{w_{max}}^2\sin\frac{\pi y}{b}\right)\sin\frac{\pi y}{b}$	Negative sine function variation
Path 3	$y = 0.15, y/b = 1/2,$ and $\cos\frac{2\pi y}{b} = -1, \sin\frac{\pi y}{b} = 1$	$\varepsilon_y = -\frac{\pi}{b}v_{max}\cos\frac{2\pi x}{l}$	Negative cosine function variation
Path 4	$y = 0, y/b = 0,$ and $\cos\frac{2\pi y}{b} = 1, \sin\frac{\pi y}{b} = 0$	$\varepsilon_y = constant$	No variational part appears

6.4 Finite element modelling

6.4.1 General description of the finite element model

The commercial finite element (FE) software Abaqus has been shown in Chapter 4 to be capable of predicting initial buckling modes and subsequently tracing the nonlinear post-buckling equilibrium paths of plates. It has also been used in other researchers' work (Wu et al. 2012; Raju et al. 2012; Loughlan and Hussain 2014) to predict the strain and stress fields at different buckling and postbuckling stages. It is therefore used in this section to validate a series of stress resultant contour plots for an axially compressed plate with the same section and material properties as the Improved VIPASA model, discussed in Section 6.1.

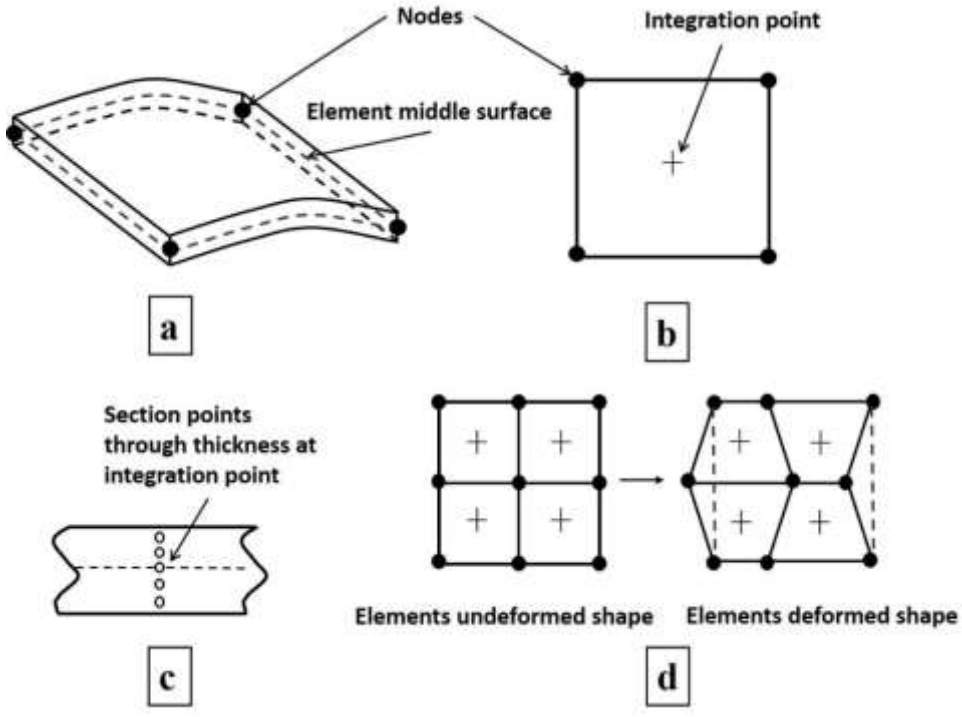

Figure 6.7 Element S4R chosen to model the current problem, (a) shows a three-dimensional sketch of the element, (b) is the plan view of the element showing node and integration point positions, (c) is the elevation view through the thickness of the element and (d) is the hourglass mode on a small system of four-noded quadrilateral elements with one integration point. (Adapted from Smith (2009)and Cook (1994))

The plate was modelled using four-node reduced-integration S4R shell elements where each node has three translational and three rotational degrees of freedom to account for the double curvature effect of the thin shell. Five section points through the thickness are used as the integration points, so that the stress resultants at the middle surface of the element can be extracted by using the ABAQUS keyword *ELEMENT OUTPUT. The features of this element are shown in Figure 6.7a-c. In comparison with full integration techniques, the advantage of using a reduced number of integration points is that the computational cost can be minimised without compromising accuracy (Smith et al. 2013). However, the implications of using reduced integration in first-order, linear elements is that it may lead to local element instabilities occuring in the model, known as hourglassing (Belytschko et al. 2013). This is where the elements display deformations but at the corresponding integration points exhibit zero strain (Figure 6.7d). Though single point integration is used, the hourglass mode was not observed in these models and a mesh sensitivity study was conducted to obtain a suitable mesh size to avoid additional computational cost.

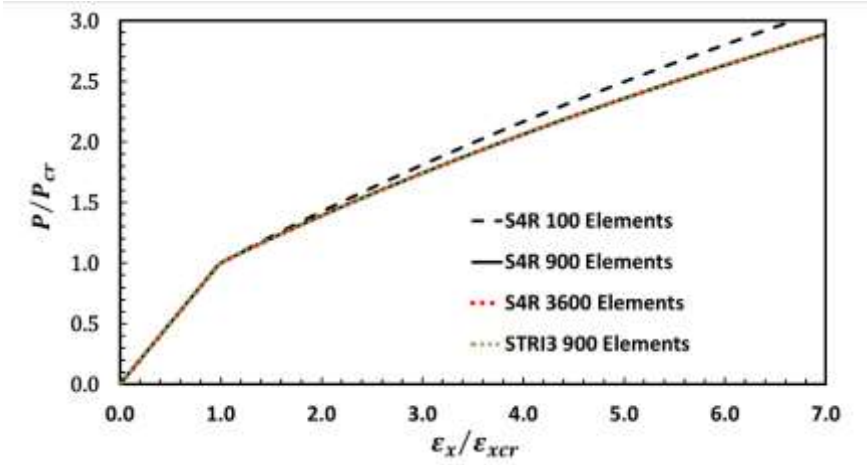

Figure 6.8 ABAQUS convergence comparison.

Since no particular geometrical complexity exists in the current plate model, it was found from Figure 6.8 that a 900-element model (with uniform square elements applied across the entire plate) achieves the same convergence as a 3600-element model, indicating that a mesh size where the length of each element was approximately 10 mm provided a sufficiently high degree of accuracy versus computational costs. Note that the 900-element S4R model was also checked against a model using STR13 triangular elements, and no dramatic difference regarding to the postbuckling results had been observed.

6.4.2 In-plane boundary conditions in the FE model

In order to compare the stress resultants calculated by the Improved VIPASA postbuckling analysis with FE results, two types of free in-plane boundary conditions were simulated in the FE model. In the first instance the two free unloaded edges had linear constraints imposed on their longitudinal in-plane displacement u, in order to represent the VIPASA in-plane boundary conditions. Analyses based on this boundary conditions are denoted Type-A in the following discussions. These linear constraints were applied through the use of the ABAQUS *EQUATION constraints on the two unloaded edges. In the second FE model, the two free unloaded edges had no constraints imposed on their in-plane displacement, in order to simulate the Improved VIPASA analysis in-plane boundary conditions. This is referred to as a Type-B analysis. The difference between Type A and Type B analyses is illustrated in Figure 6.9 where the longitudinal displacements at each node along the unloaded edge are plotted. Due to the linear constraints imposed, the longitudinal displacements obtained with the Type-A analysis are fitted with a straight line, indicating only the linear term in Equation 5.9 appears. In contrast, the numerical results obtained from the Type-B analysis are fitted with a curve, showing the nonlinear terms in Equation 5.9 are also included. For the

loaded edges in both Type A and Type B analyses, all nodes were tied together using the ABAQUS *TIE constraint to ensure that they had uniform longitudinal displacements u while transverse displacements v were free to vary. Having established reliable FE models, the numerical FE results are used to validate the improved method in next section.

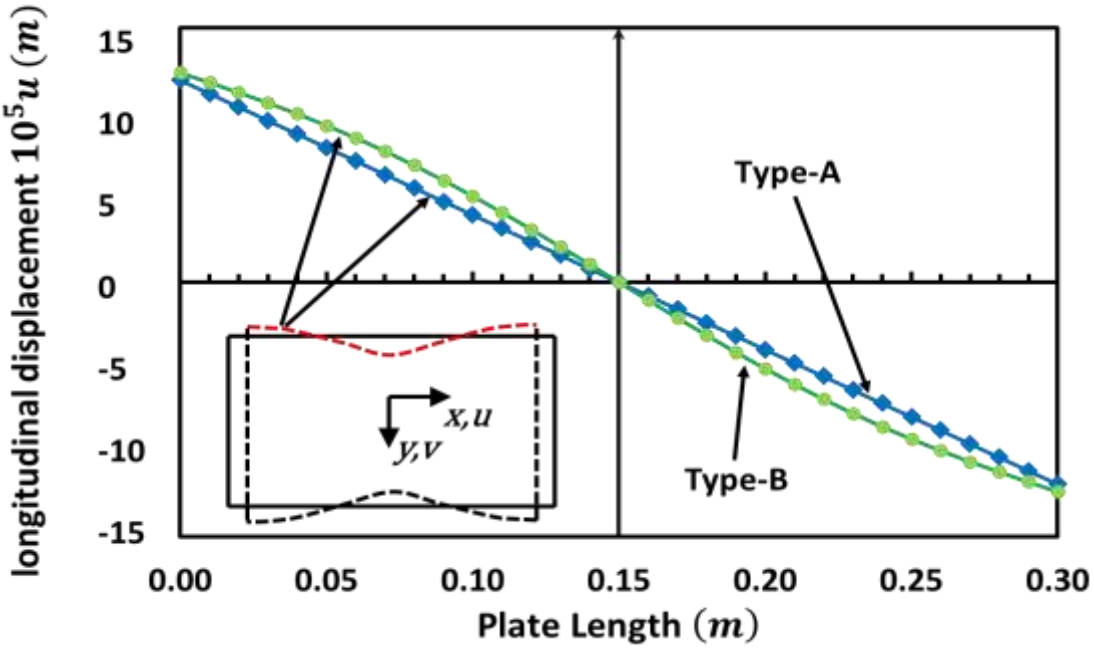

Figure 6.9 Comparison of Type A and Type B analysis for in-plane longitudinal displacements along the unloaded edge.

6.5 Validation of stress resultant contour plots

6.5.1 Isotropic plate stress resultant contour

This section presents the postbuckling stress contour plots of an isotropic plate, with the dimensions and material properties defined in section 6.1. Results are presented for a perfect flat plate under 50kN/m axial compression with the two types of in-plane boundary conditions described above (Type-A and Type-B) applied and all four edges simply supported out-of-plane.

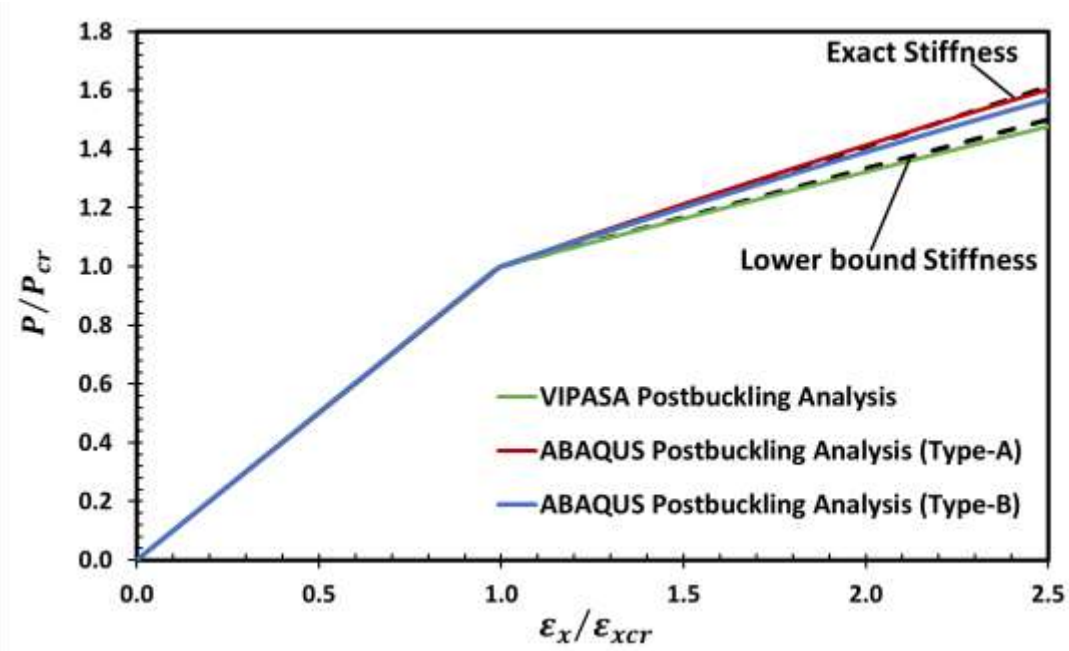

a

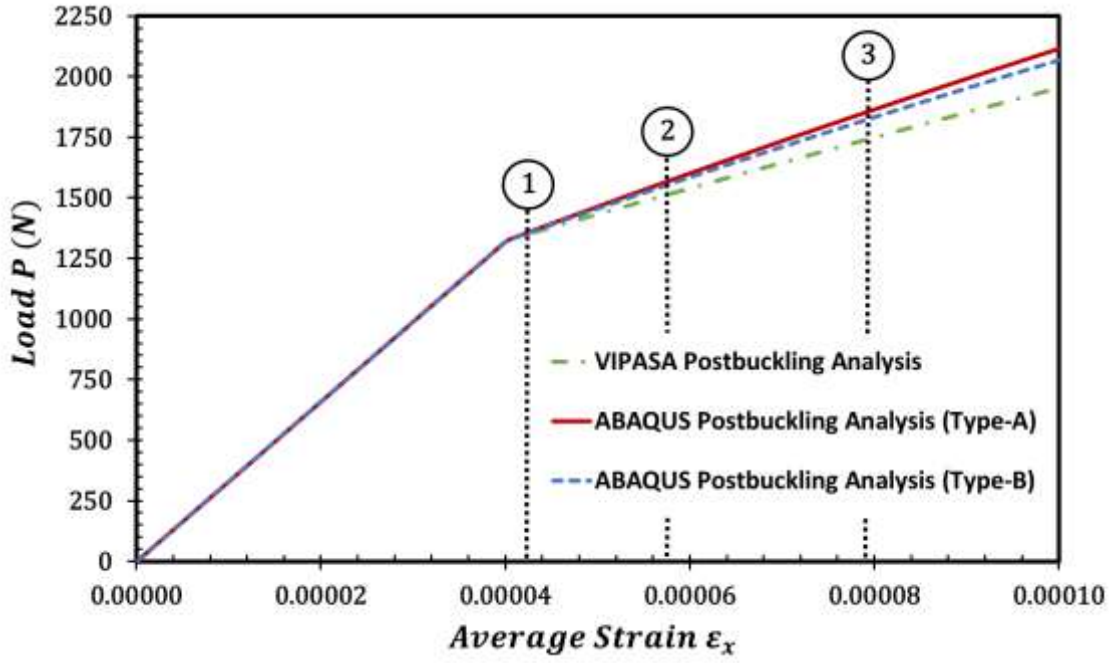

b

Figure 6.10 Postbuckling behaviours of a square, isotropic plate in compression: (a) normalised load-strain curves and (b) actual load-strain curves.

Normalised load versus end shortening strain results are presented in Figure 6.10a. The end shortening strain ε_x resulting from the applied load P is normalised with respect to the critical buckling strain ε_{xcr} and the load P is normalised with respect to the critical

buckling load P_{cr}. The slope of the load-strain curve is a measure of the overall plate stiffness. As shown in Figure 6.10a, the curve is a straight line of slope equal to one prior to buckling while it has a reduced slope after buckling. The postbuckling to prebuckling stiffness ratio K^*/K predicted by the VIPASA analysis is calculated to be 0.333, comparing well with Koiter's lower bound solution. The same ratio for ABAQUS is 0.408 which largely coincides with Koiter's exact stiffness solutions and other published results. Since the only difference between Type-A and Type-B analyses is the mathematical interpolation of free in-plane boundary conditions, it is seen they show only a small discrepancy in their load-strain curves, however, it is believed that the difference will be more noticeable when it comes to comparing the stress resultants contour plots.

Non-normalised load end shortening curves are presented in Figure 6.10b. Three strain-controlled locations shown in Figure 6.10b are chosen to investigate the stress field under the postbuckling regime. Contour plots of stress resultant (N_x) for square metal plates at corresponding locations which illustrate the comparison between VIPASA, Improved VIPASA analysis and ABAQUS Type-A analyses during postbuckling are shown in Figures 6.11, 6.12 and 6.13. The contour plots from VIPASA in Figures 6.11a, 6.12a and 6.13a are noted to be invariant in the longitudinal direction due to the fact that sinusoidal terms are absent in the in-plane displacements assumption. Thus, the initial stress resultants for each strip are given by $N_L = P/B$. The Improved method is shown to overcome this inaccuracy by allowing stress resultant (N_x) to vary sinusoidally along the length as shown in Figures 6.11b, 6.12b and 6.13b. The distribution patterns for the stress resultant (N_x) shown in these figures are referred to as being symmetric in nature for the reason that the maximum amplitude of stress occurs at the two longitudinal edges while minimum stress appears at the central region of the plate. With reference to Figures 6.11c, 6.12c and 6.13c in which contours from the ABAQUS Type-A analyses are displayed, it is

seen that slight differences occur between the Improved method and ABAQUS predictions of the amplitude of stress resultants at the centre of the plate but that the differences become negligible at the longitudinal edges.

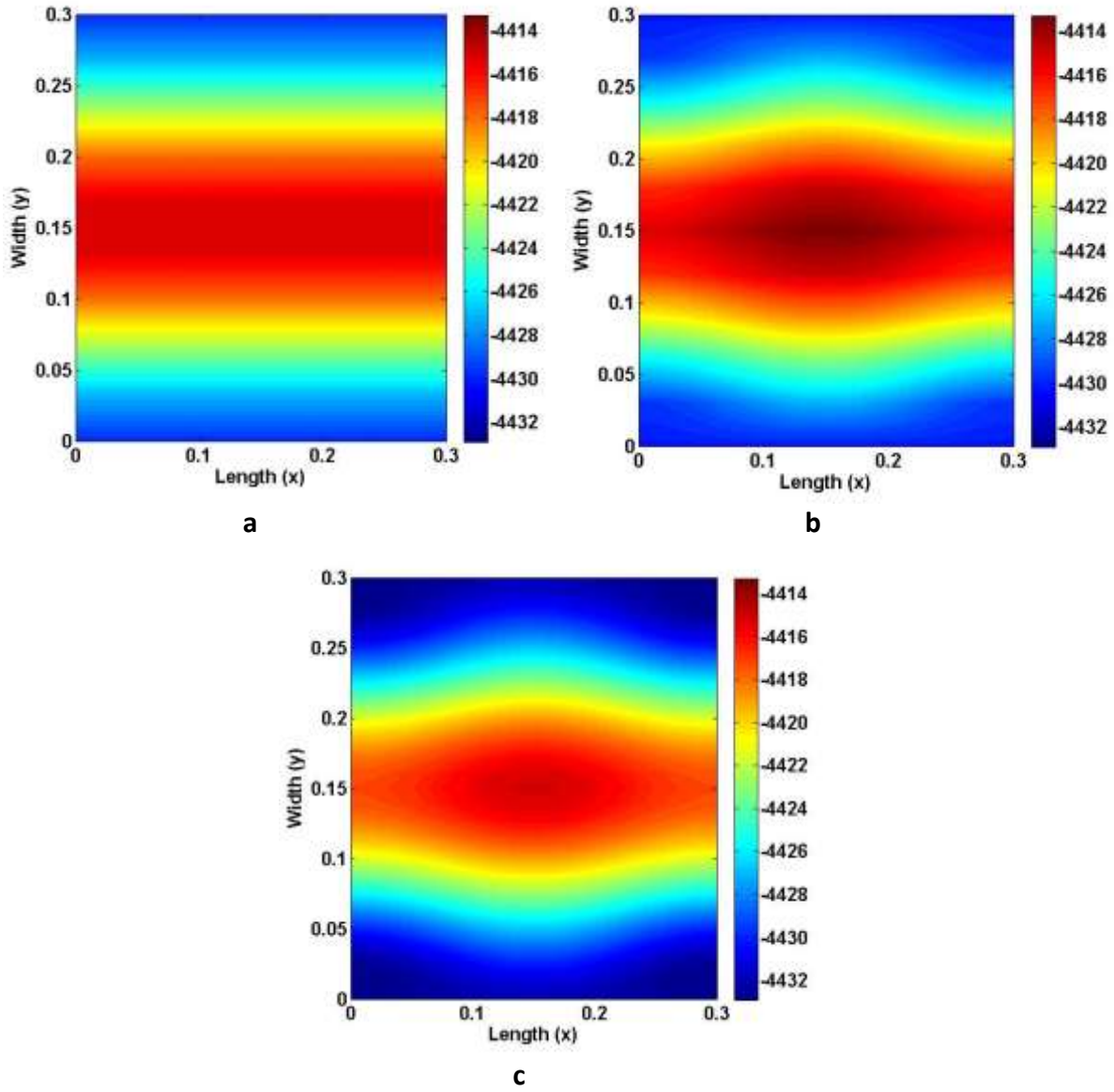

Figure 6.11 Contour plots of stress resultants $N_x(N/m)$ at postbuckling Location 1 from different software: (a)VIPASA, (b) Improved VIPASA analysis and (c) ABAQUS Type-A analysis.

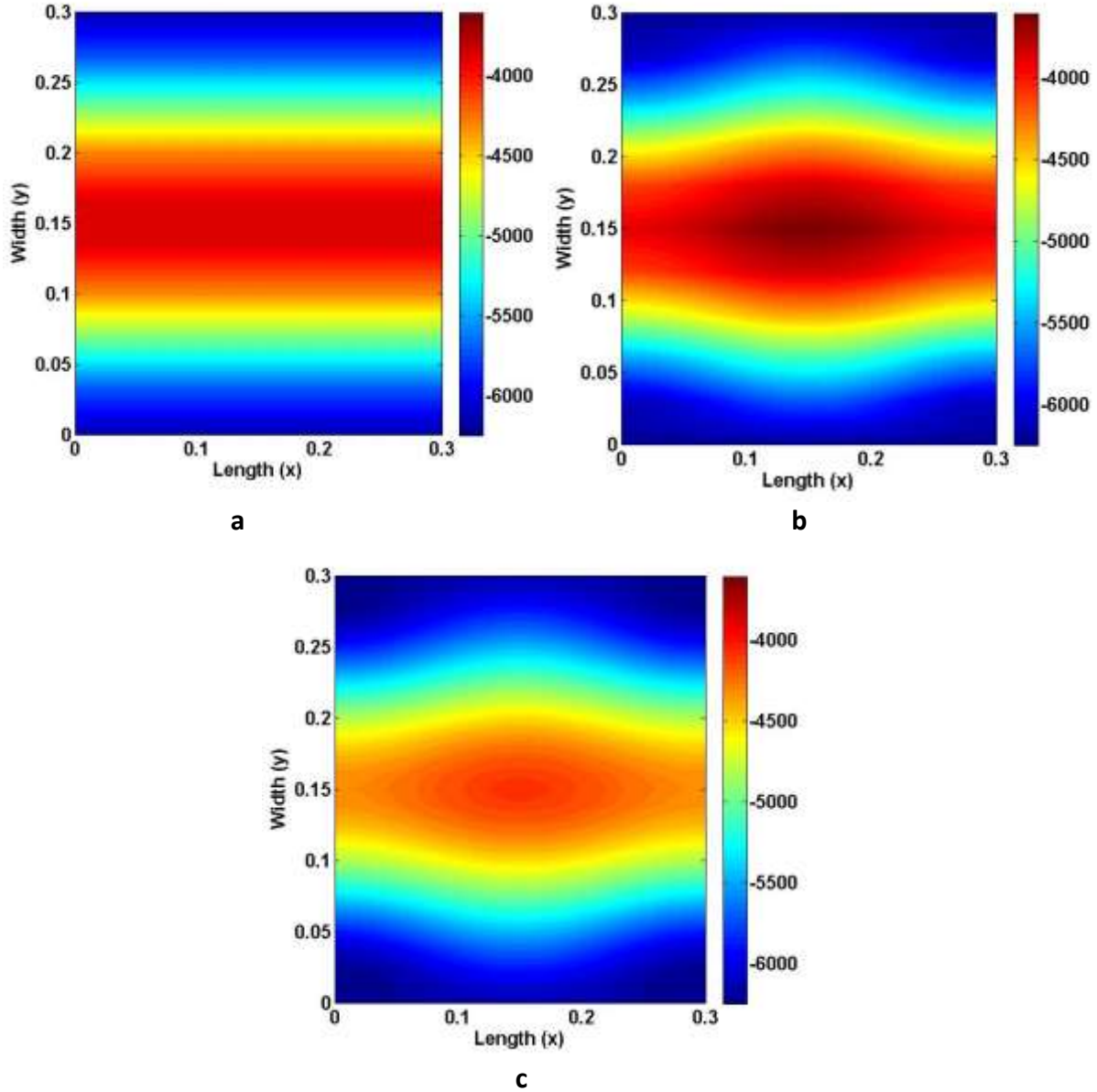

Figure 6.12 Contour plots of stress resultants $N_x(N/m)$ at postbuckling Location 2 from different software: (a)VIPASA, (b) Improved VIPASA analysis and (c) ABAQUS Type-A analysis.

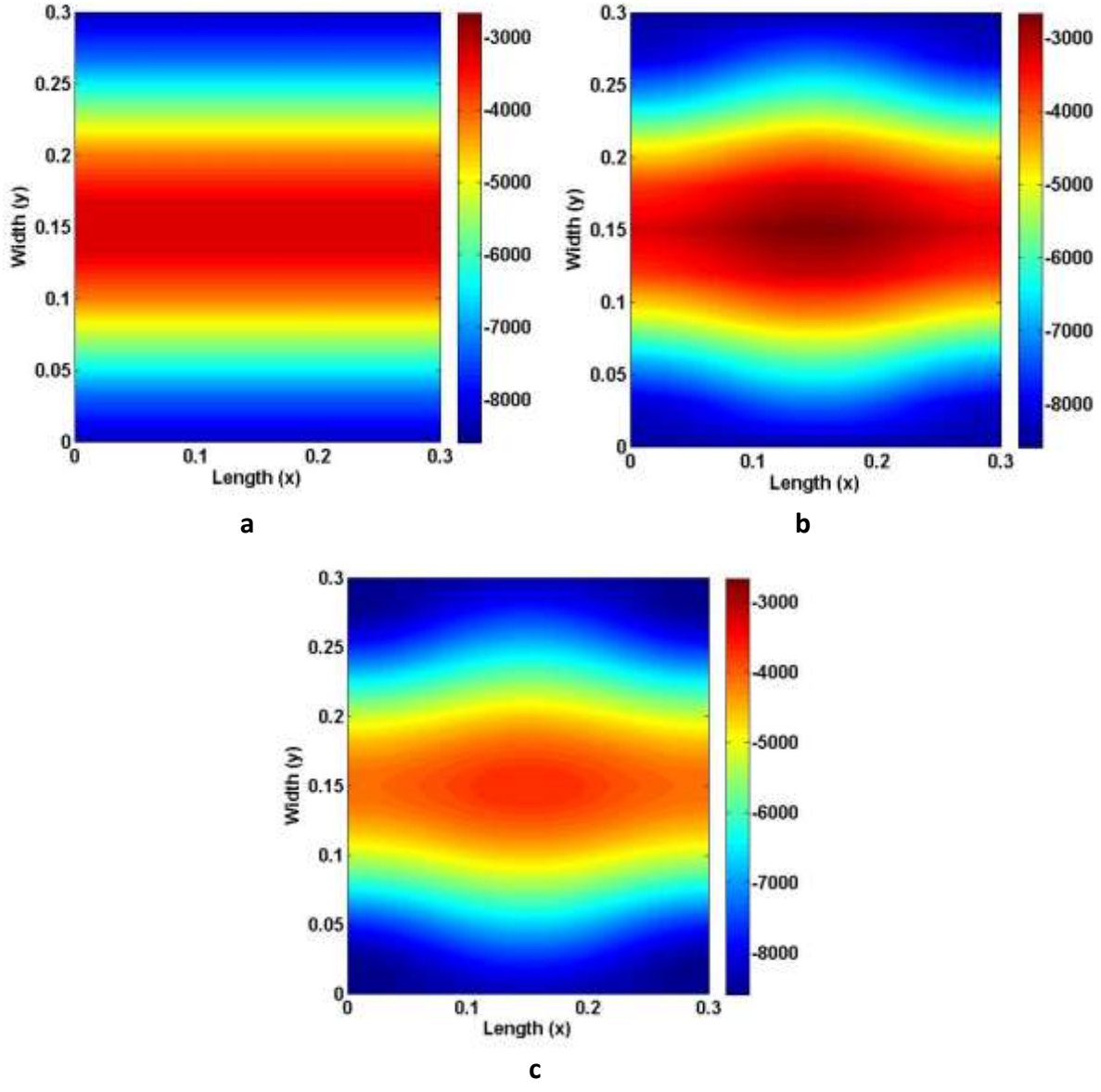

Figure 6.13 Contour plots of stress resultants $N_x(N/m)$ at postbuckling Location 3 from different software: (a)VIPASA, (b) Improved VIPASA analysis and (c) ABAQUS Type-A analysis.

The stress resultant contour plots at the three postbuckling locations for the Improved VIPASA analysis are also compared with the corresponding ABAQUS Type-B analyses in Figures 6.14-6.16. In contrast with the contours shown in Figures 6.11-6.13, as expected, the stress resultants from Type-B analysis begin to vary along the plate longitudinal edges due to the introduction of nonlinear terms in in-plane displacement assumptions. It appears that the stress tends to be concentrated near the middle of the plate edge but with lower levels of compression at the two ends of this edge, which is closer to the free edge in-plane conditions defined by Bulson (1969).

Contour plots for the transverse stress resultant (N_y) from the Improved VIPASA analyses and the ABAQUS Type-A analyses are also presented in Figures 6.17, 6.18 and 6.19. The presence of a varying amount of transverse stress resultant (N_y) is mainly due to the tangential restraint (i.e.,$v = 0$) on the loaded edges as shown in Figure 6.1. N_y, however, does not build up near to the unloaded edges as the axial load is applied because they are free to move in-plane (i.e.,$u \neq 0, v \neq 0$). To avoid repetition, the contour plots of transverse stress resultant N_y from ABAQUS Type-B analyses are not reported here since they are very similar to the results from the ABAQUS Type-A analyses.

Although all the above-mentioned plots show good agreement between the Improved VIPASA analyses and the FE analyses at different postbuckling stages, a preliminary error evaluation study is needed to explore the limitations of the Improved VIPASA analysis.

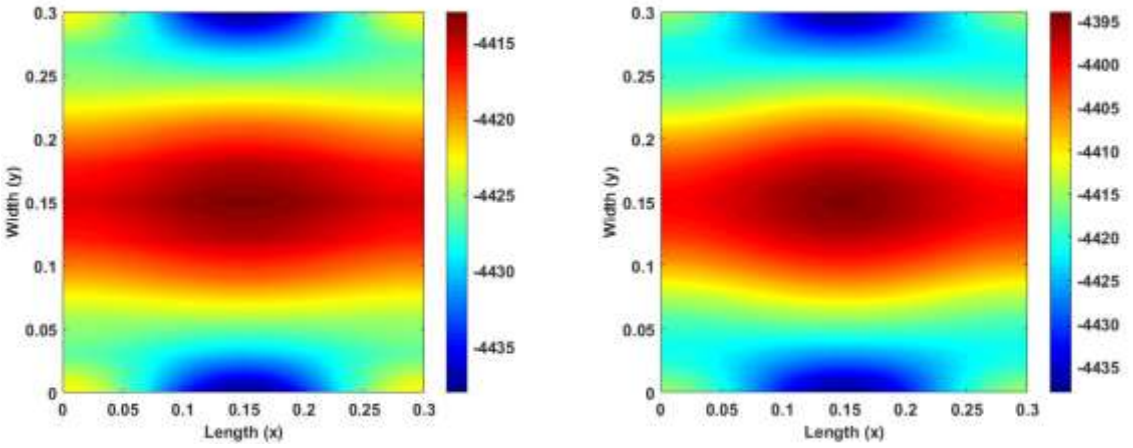

a **b**

Figure 6.14 Contour plots of stress resultants N_x (N/m) at postbuckling location 1 from: (a) Improved VIPASA analysis and (b) ABAQUS Type-B analysis.

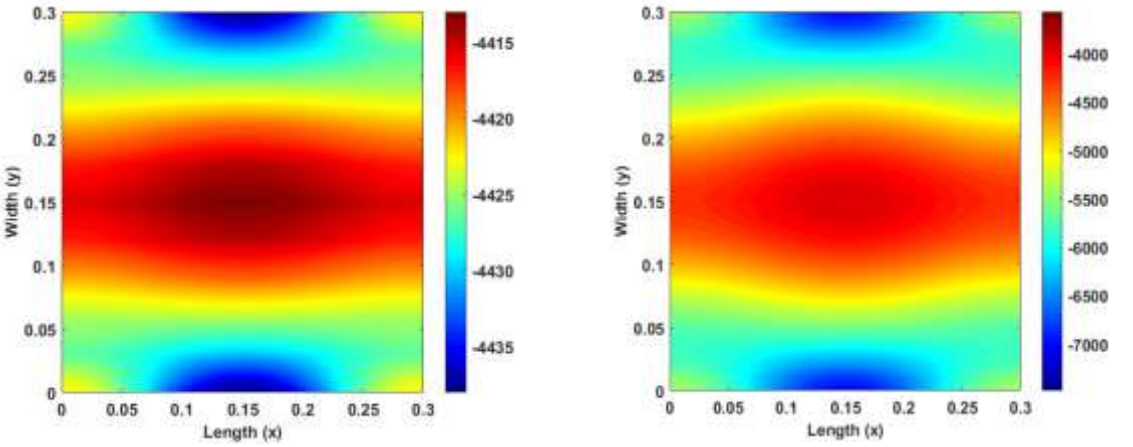

a **b**

Figure 6.15 Contour plots of stress resultants N_x (N/m) at postbuckling location 2 from: (a) Improved VIPASA analysis and (b) ABAQUS Type-B analysis.

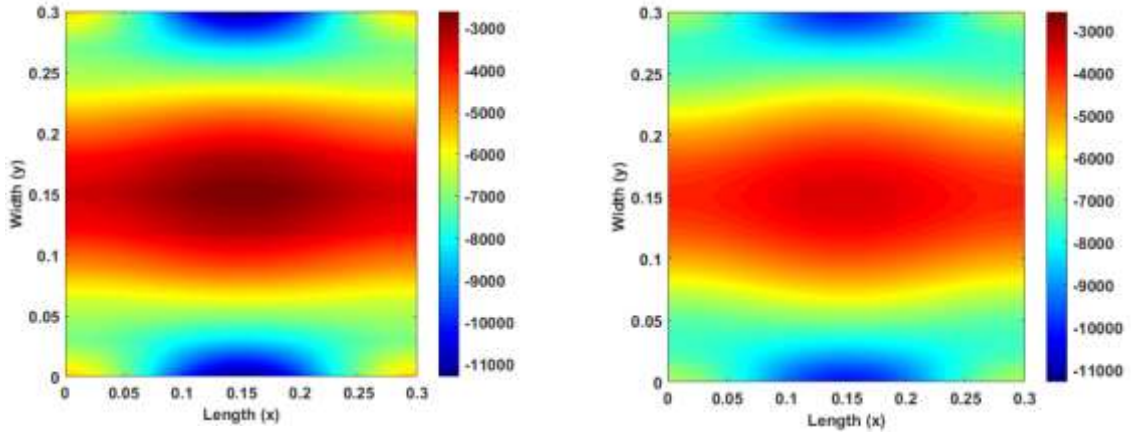

a **b**

Figure 6.16 Contour plots of stress resultants N_x (N/m) at postbuckling location 3 from: (a) Improved VIPASA analysis and (b) ABAQUS Type-B analysis.

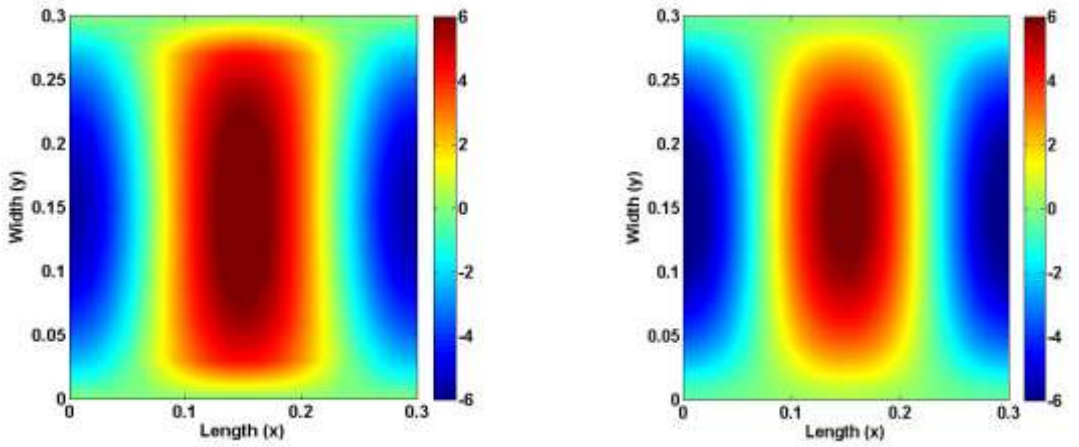

a b

Figure 6.17 Contour plots of stress resultants N_y (N/m) at postbuckling location 1 from: (a) Improved VIPASA analysis and (b) ABAQUS Type-A analysis.

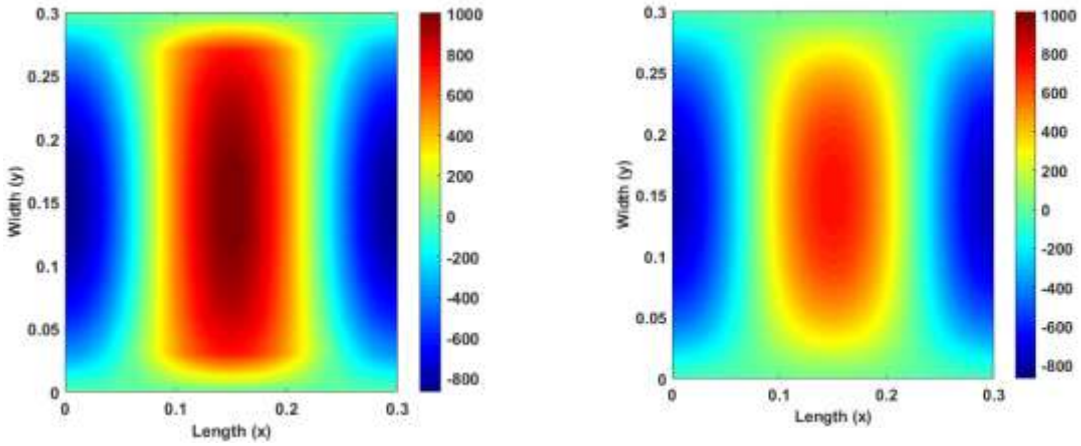

a b

Figure 6.18 Contour plots of stress resultants N_y (N/m) at postbuckling location 2 from: (a) Improved VIPASA analysis and (b) ABAQUS Type-A analysis.

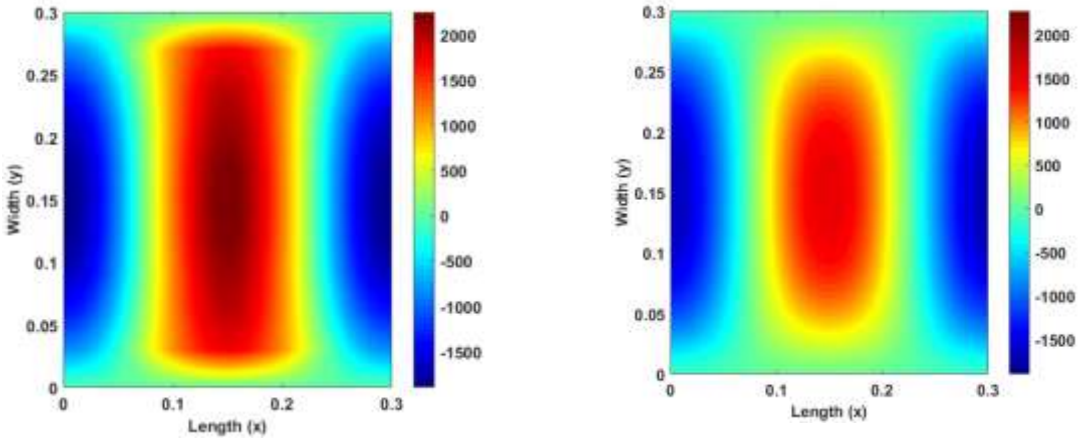

a b

Figure 6.19 Contour plots of stress resultants N_y (N/m) at postbuckling location 3 from: (a) Improved VIPASA analysis and (b) ABAQUS Type-A analysis.

6.5.2 Error evaluation

Stress distribution plots and stress resultant data along the central line of the plate are extracted and used to carry out a preliminary error evaluation study at the above mentioned three postbuckling locations. Axial stress resultants N_x are traced along the vertical central line (shown in Figure 6.1b) while transverse stress resultants N_y are traced along the horizontal central line (shown in Figure 6.1b) to demonstrate the maximum variational trend across the plate. The traces of the value of N_x for the Improved VIPASA are compared to results for the ABAQUS Type-A and Type-B analyses in Figures 6.20-6.21 and Tables 6.7-6.8. As indicated in these tables and figures, the difference between the Improved method and ABAQUS appears to increase with the postbuckling location. At the very initial stages of postbuckling (postbuckling Location 1), the differences between the two analyses are very small ranging from 0.03% to 0.1% across the width. As the applied load increases (postbuckling location 3), there is more than a 20% discrepancy between stress resultants from the Improved VIPASA analysis and the ABAQUS analysis at the centre of the plate.

The stress distribution plot of the transverse stress resultant N_y and its corresponding values at different postbuckling locations are displayed in Figure 6.23 and Table 6.8. Examination of the correlation between the two shows that the results from the Improved VIPASA analysis and ABAQUS may predict stress resultants which differ by up to 40% at the centre of the plate.

These differences are due to the increasing difference in the predicted maximum out-of-plane displacement between the current VIPASA and ABAQUS results as shown in Figure 6.22. Since the Improved VIPASA analysis depends on the current VIPASA mode shape, the differences in the amplitudes of the maximum deflections will be inherited in the subsequent strain and stress calculation. It has also been noticed that ABAQUS predicts a

higher load under the same strain compared with VIPASA analysis, which means ABAQUS can display a more nonuniform stress distribution at the further postbuckling location (postbuckling location 3) shown in Figures 6.20c, 6.21c and 6.22c, so that leads to a more significant discrepancy compared with VIPASA analysis. Furthermore, the relative differences calculated in Tables 6.6, 6.7 and 6.8 show the relative error between the Improved analysis and ABAQUS in each strip. But if the average stress resultants across the plate are compared, the relative difference is much smaller, i.e. less than 10% at postbuckling location 3. Nevertheless, it should be noticed that ABAQUS results also depend on the imperfection which is assumed at the start of each postbuckling analysis, and it hard to tell which one is more accurate than the other. Having acknowledged this, comparing with other methods including experimental works in future would be more helpful to give a more comprehensive indication of the practicality of the Improved analysis.

Since convergence on transverse stress resultants N_y is not required in the current VIPASA postbuckling analysis, the single term cosine displacement assumption in the analysis may not be adequate to capture the correct mode shape in the transverse direction during the postbuckling stage. These less accurate transverse mode shapes and amplitudes affect the predictions of stress and strain distributions and values. Note that these results are based on one iteration of the postbuckling calculation process as explained in Figure 5.4. It is anticipated that more accurate results for transverse stress resultants will be obtained after full implementation of the Improved method when more iterations can be conducted.

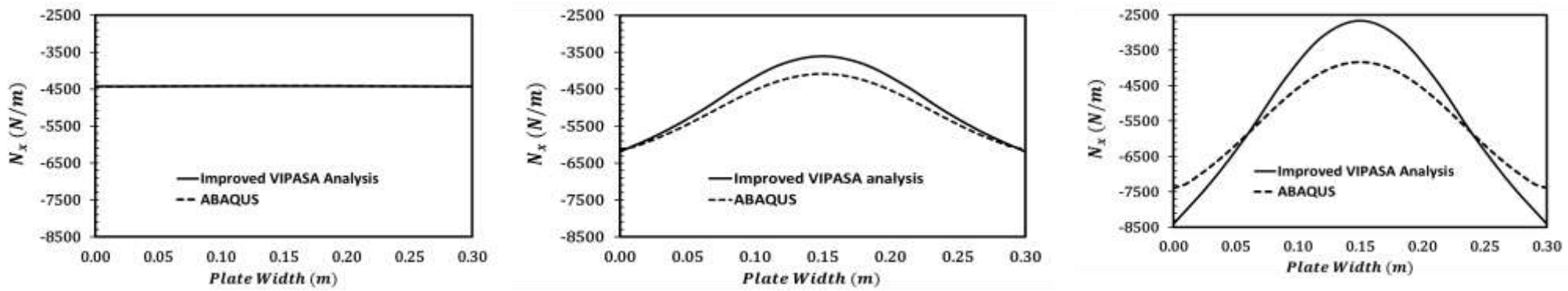

Figure 6.20 Comparison of axial stress resultant N_x across the vertical centre line of plate for different locations during postbuckling analysis by the Improved VIPASA analysis and ABAQUS, with Type-A longitudinal edge in-plane condition: (a) Location 1, (b) Location 2 and (c) Location 3.

Table 6.6 Summary of stress resultant N_x values and relative difference for Type-A longitudinal edge at three postbuckling locations.

Location 1				Location 2				Location 3			
Width (m)	Improved Analysis	ABAQUS	Relative Difference (%)	Width (m)	Improved Analysis	ABAQUS	Relative Difference (%)	Width (m)	Improved Analysis	ABAQUS	Relative Difference (%)
0	-4430.150	-4435.730	0.126	0	-6197.610	-6119.470	-1.277	0	-8406.943	-7392.420	-13.724
0.03	-4427.133	-4432.530	0.122	0.03	-5703.622	-5786.320	1.429	0.03	-7235.813	-6782.890	-6.677
0.06	-4423.201	-4427.340	0.093	0.06	-5090.788	-5261.680	3.248	0.06	-5852.231	-5850.830	-0.024
0.09	-4418.526	-4421.420	0.065	0.09	-4379.569	-4688.460	6.588	0.09	-4291.910	-4861.120	11.709
0.12	-4414.753	-4416.690	0.044	0.12	-3819.566	-4244.860	10.019	0.12	-3101.910	-4112.460	24.573
0.15	-4413.311	-4414.880	0.036	0.15	-3608.647	-4078.680	11.524	0.15	-2663.056	-3835.670	30.571
0.18	-4414.753	-4416.690	0.044	0.18	-3819.566	-4244.860	10.019	0.18	-3101.910	-4112.460	24.573
0.21	-4418.526	-4421.420	0.065	0.21	-4379.569	-4688.460	6.588	0.21	-4291.910	-4861.120	11.709
0.24	-4423.201	-4427.340	0.093	0.24	-5090.788	-5261.680	3.248	0.24	-5852.231	-5850.840	-0.024
0.27	-4427.133	-4432.530	0.122	0.27	-5703.622	-5786.320	1.429	0.27	-7235.813	-6782.900	-6.677
0.3	-4430.150	-4435.690	0.125	0.3	-6197.610	-6119.520	-1.276	0.3	-8406.943	-7392.350	-13.725

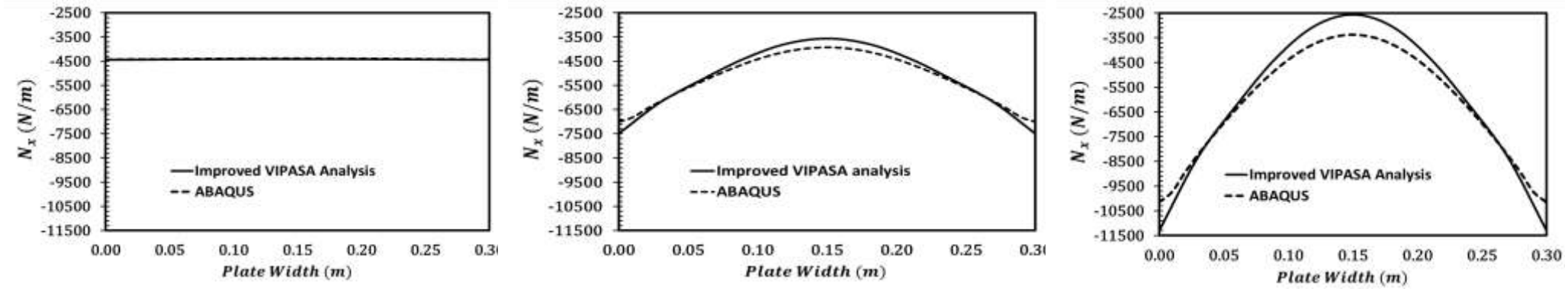

Figure 6.21 Comparison of axial stress resultant N_x across the vertical centre line of plate for different locations during postbuckling analysis by the Improved VIPASA analysis and ABAQUS, with Type-B longitudinal edge in-plane condition: (a) Location 1, (b) Location 2 and (c) Location 3.

Table 6.7 Summary of stress resultant N_x values and relative difference for Type-B longitudinal edge at three postbuckling locations.

Location 1				Location 2				Location 3			
Width (m)	Improved Analysis	ABAQUS	Relative Difference (%)	Width (m)	Improved Analysis	ABAQUS	Relative Difference (%)	Width (m)	Improved Analysis	ABAQUS	Relative Difference (%)
0	-4438.476	-4437.636	-0.019	0	-7487.053	-7011.662	-6.780	0	-11298.63	-10152.36	-11.291
0.03	-4430.252	-4426.104	-0.094	0.03	-6190.796	-6164.927	-0.420	0.03	-8328.34	-8235.46	-1.128
0.06	-4424.227	-4414.731	-0.215	0.06	-5253.955	-5333.113	1.484	0.06	-6218.15	-6358.64	2.210
0.09	-4418.662	-4404.623	-0.319	0.09	-4404.457	-4618.427	4.633	0.09	-4347.72	-4802.43	9.468
0.12	-4414.546	-4397.199	-0.395	0.12	-3790.860	-4112.662	7.825	0.12	-3037.53	-3744.97	18.890
0.15	-4413.016	-4394.439	-0.423	0.15	-3566.274	-3928.902	9.230	0.15	-2568.03	-3370.43	23.807
0.18	-4414.546	-4397.199	-0.395	0.18	-3790.860	-4112.662	7.825	0.18	-3037.53	-3744.97	18.890
0.21	-4418.662	-4404.623	-0.319	0.21	-4404.457	-4618.427	4.633	0.21	-4347.72	-4802.43	9.468
0.24	-4424.227	-4414.731	-0.215	0.24	-5253.955	-5333.113	1.484	0.24	-6218.15	-6358.65	2.210
0.27	-4430.252	-4426.104	-0.094	0.27	-6190.796	-6164.927	-0.420	0.27	-8328.34	-8235.46	-1.128
0.3	-4438.476	-4437.636	-0.019	0.3	-7487.053	-7011.663	-6.780	0.3	-11298.63	-10152.36	-11.291

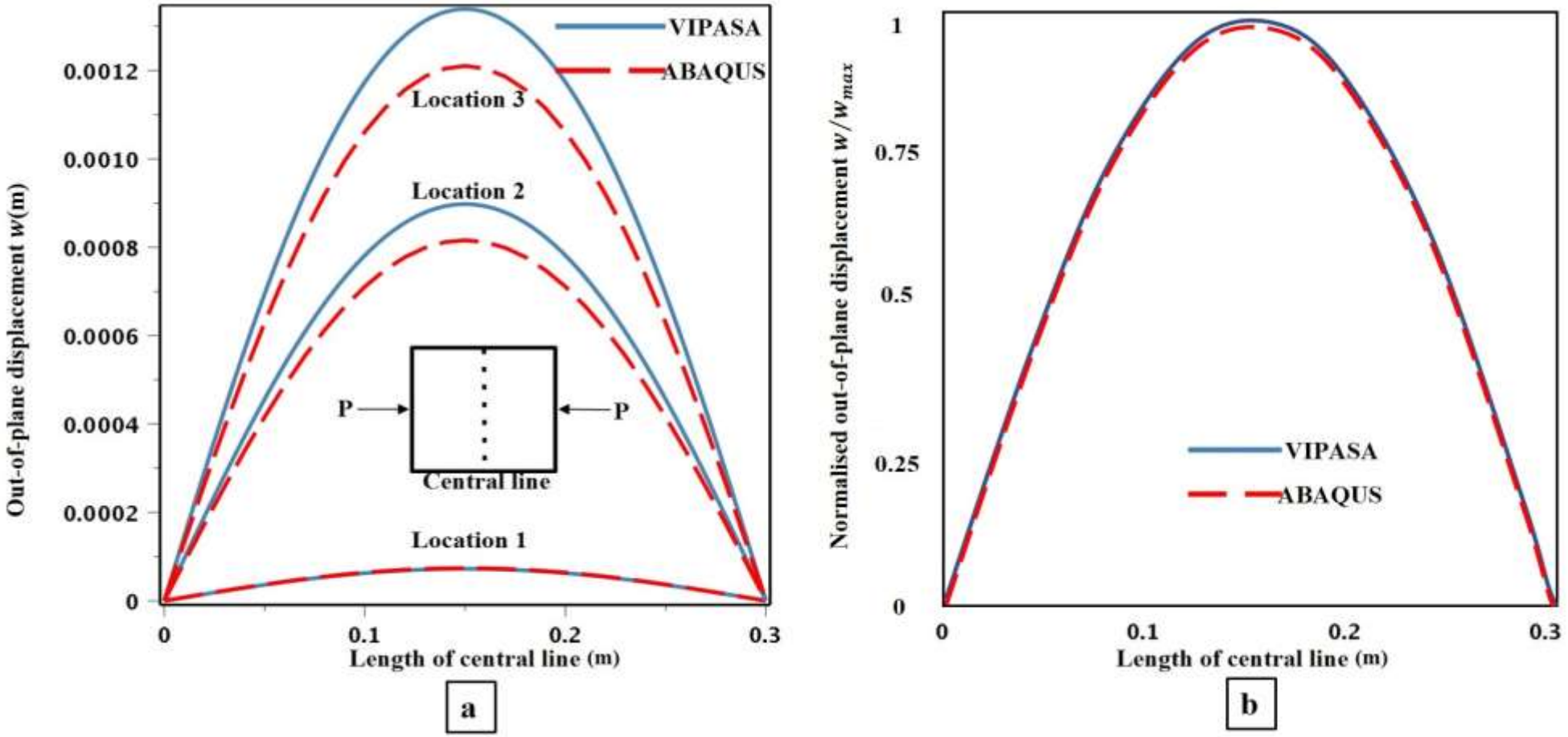

Figure 6.22 Comparison of out-of-plane displacement with VIPASA and ABAQUS analysis: (a) actual out-of-displacements at three different postbuckling locations and (b) normalised curves show VIPASA and ABAQUS have the same mode shape.

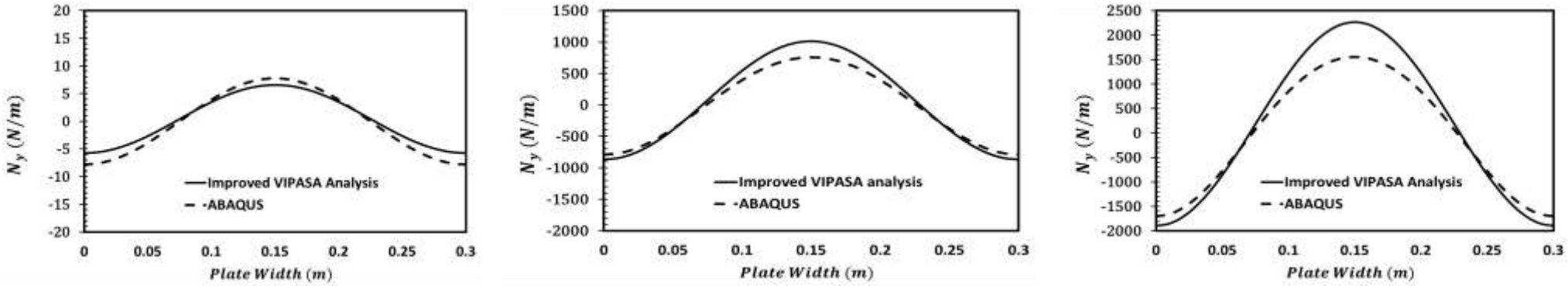

Figure 6.23 Comparison of axial stress resultant N_y across the vertical centre line of plate for different locations during postbuckling analysis by the Improved VIPASA analysis and ABAQUS Type-A, with free in-plane edge condition: (a) Location 1, (b) Location 2 and (c) Location 3.

Table 6.8 Summary of stress resultant N_y values and relative difference for Type-A longitudinal edge at three postbuckling locations.

Location 1				Location 2				Location 3			
Width (m)	Improved Analysis	ABAQUS	Relative Difference (%)	Width (m)	Improved Analysis	ABAQUS	Relative Difference (%)	Width (m)	Improved Analysis	ABAQUS	Relative Difference (%)
0	-5.732	-7.791	26.421	0	-869.077	-789.359	-10.099	0	-1898.02	-1704.80	-11.334
0.03	-4.558	-6.301	27.672	0.03	-689.228	-630.306	-9.348	0.03	-1500.36	-1341.51	-11.841
0.06	-1.482	-2.405	38.363	0.06	-218.378	-225.533	3.172	0.06	-459.27	-443.48	3.560
0.09	2.319	2.409	-3.700	0.09	363.624	251.9977	44.297	0.09	827.58	563.02	46.989
0.12	5.395	6.300	-14.365	0.12	834.474	620.2121	34.547	0.12	1868.67	1295.90	44.199
0.15	6.570	7.785	-15.617	0.15	1014.323	756.6398	34.056	0.15	2266.34	1557.05	45.553
0.18	5.395	6.300	-14.362	0.18	834.474	620.2119	34.547	0.18	1868.67	1295.90	44.199
0.21	2.319	2.408	-3.700	0.21	363.624	251.9977	44.297	0.21	827.58	563.02	46.989
0.24	-1.482	-2.405	38.362	0.24	-218.379	-225.533	3.172	0.24	-459.27	-443.48	3.560
0.27	-4.558	-6.301	27.669	0.27	-689.228	-630.306	-9.348	0.27	-1500.36	-1341.51	-11.841
0.3	-5.732	-7.790	26.418	0.3	-869.077	-789.358	-10.099	0.3	-1898.02	-1704.80	-11.334

6.5.3 Anisotropic plate postbuckling results

To demonstrate the Improved method is capable of analysing the postbuckling behaviours of more general anisotropic plates, three composite laminate plates of the same length $l = 300\ mm$, width $b = 300\ mm$, and thickness $h = 2\ mm$ are investigated. All three plates are made from the same composite material described in section 6.1.2. The laminate lay-ups considered consist of 16 plies and have a ply thickness of 0.125mm. The three different laminate configurations are summarised in Section 6.1.2.

Both VIPASA and ABAQUS normalised load end shortening results are presented in Figure 6.24a for the postbuckling of a square plate loaded in longitudinal compression. Results correspond to the three different laminate cases, with the Type-A in-plane and simply supported out-of-plane boundary conditions applied as discussed in Section 6.4.2. The symmetric and balanced laminate (a) has the lowest postbuckling stiffness when compared with the two unbalanced laminates cases, (b) and (c). The results obtained from laminate (b) are almost identical to those obtained from laminates (c) because these two laminates have similar degrees of in-plane extension-shear coupling, i.e. the values of A_{16} and A_{26} are similar in these two cases. They have, however, quite different levels of bend-twist coupling which is determined by the coupling ($\boldsymbol{B}$) stiffness matrix. Non-normalised load-end-shortening curves are also presented in Figure 6.24b to show the location where the stress fields are extracted and investigated. Location 1 represents the point at which longitudinal strain ε_x is equal to 0.0002 for each case.

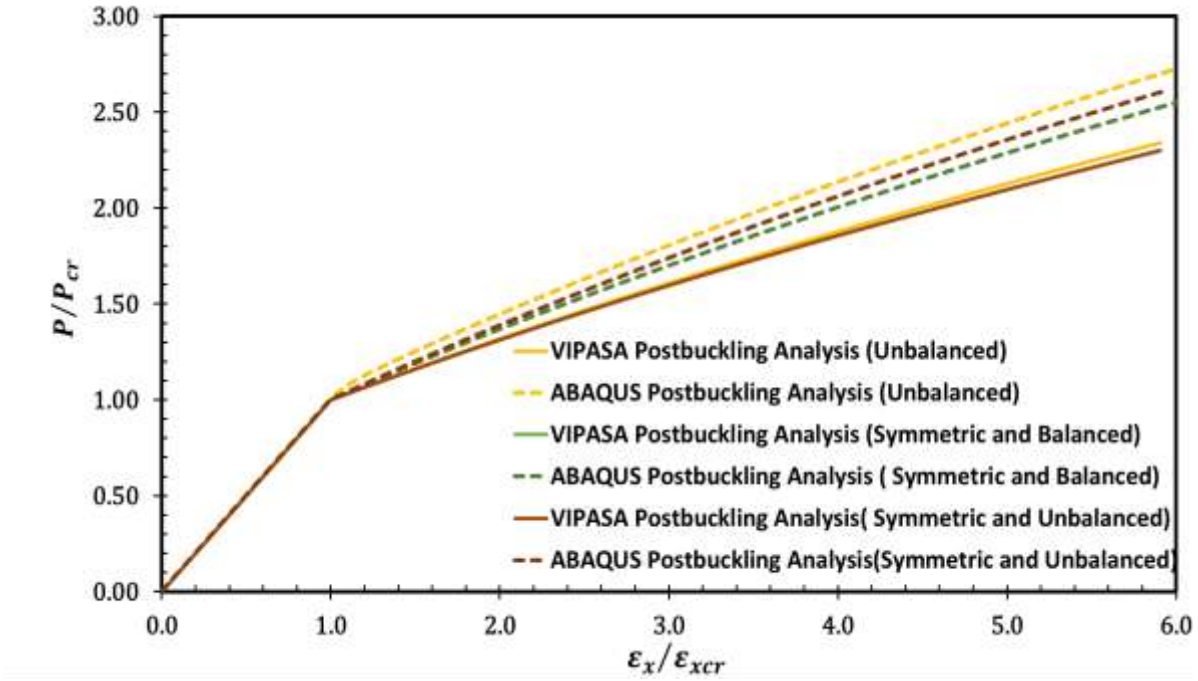

a

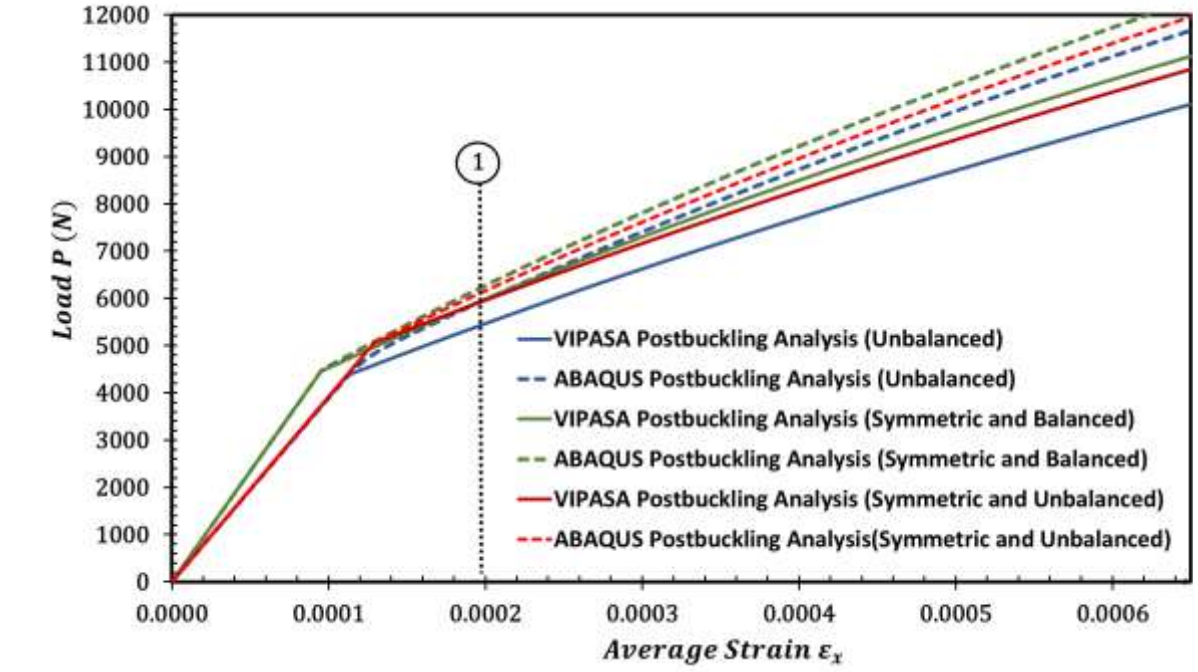

b

Figure 6.24 Postbuckling behaviours of a square, anisotropic plate in compression: (a) normalised load-strain curves and (b) actual load-strain curves.

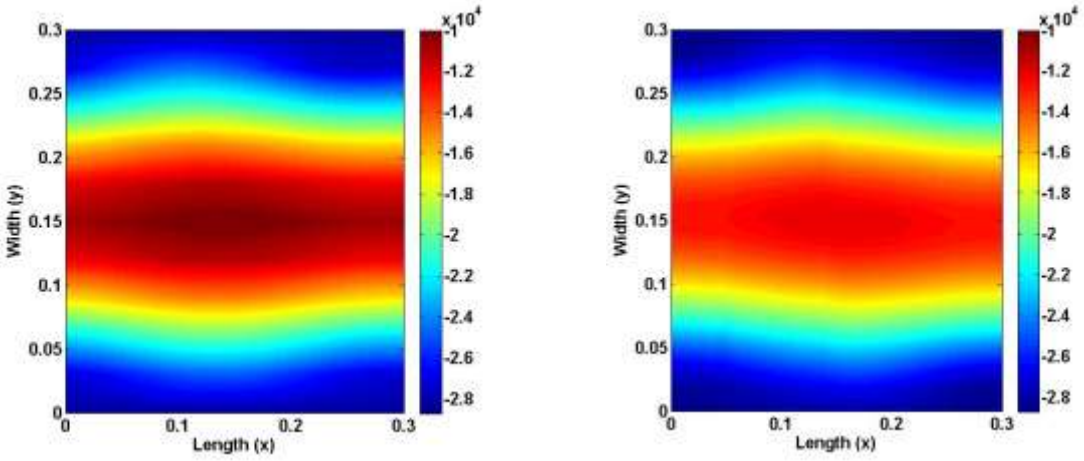

a b

Figure 6.25 Contour plots of stress resultants N_x (N/m) for postbuckling of symmetric and balanced laminate: (a) Improved method and (b) ABAQUS Type-A analysis.

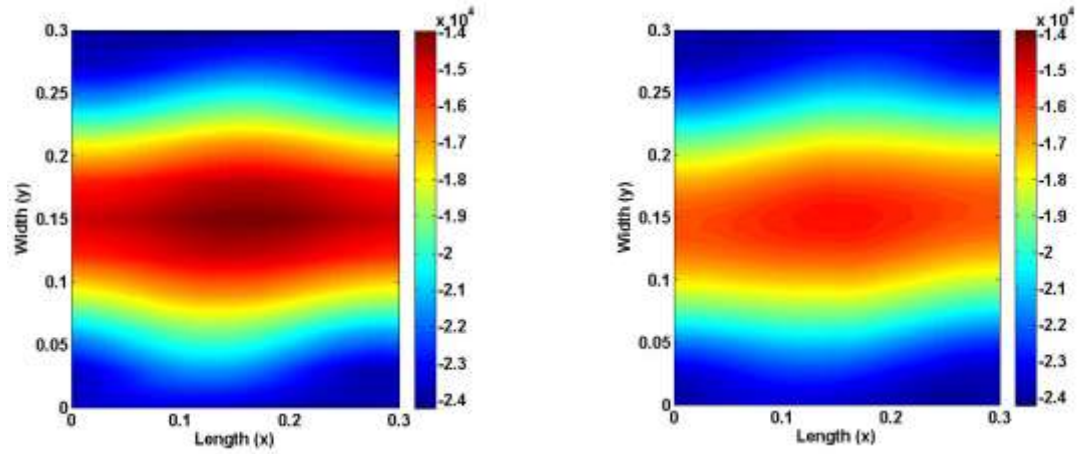

a b

Figure 6.26 Contour plots of stress resultants N_x (N/m) for postbuckling of symmetric and unbalanced laminate: (a) Improved method and (b) ABAQUS Type-A analysis.

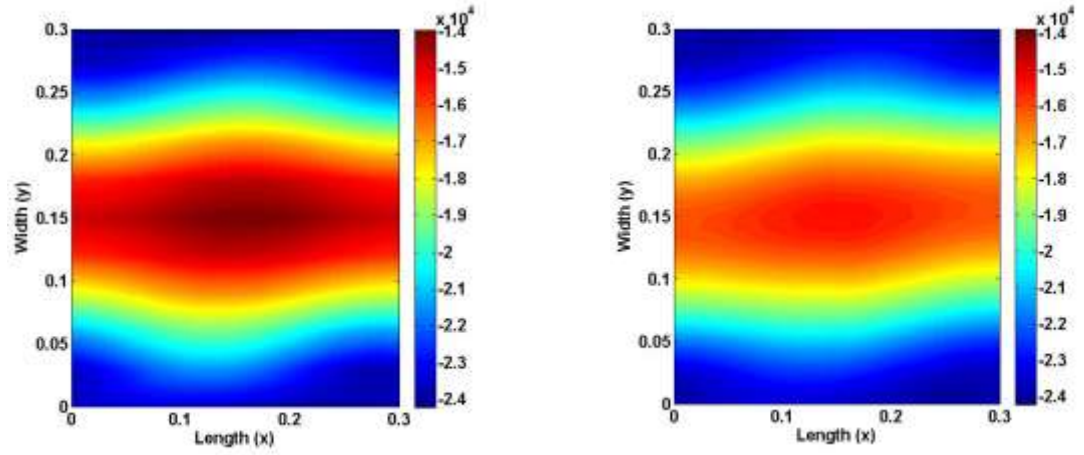

a b

Figure 6.27 Contour plots of stress resultants N_x (N/m) for postbuckling of unsymmetric and unbalanced laminate: (a) Improved method and (b) ABAQUS Type-A analysis.

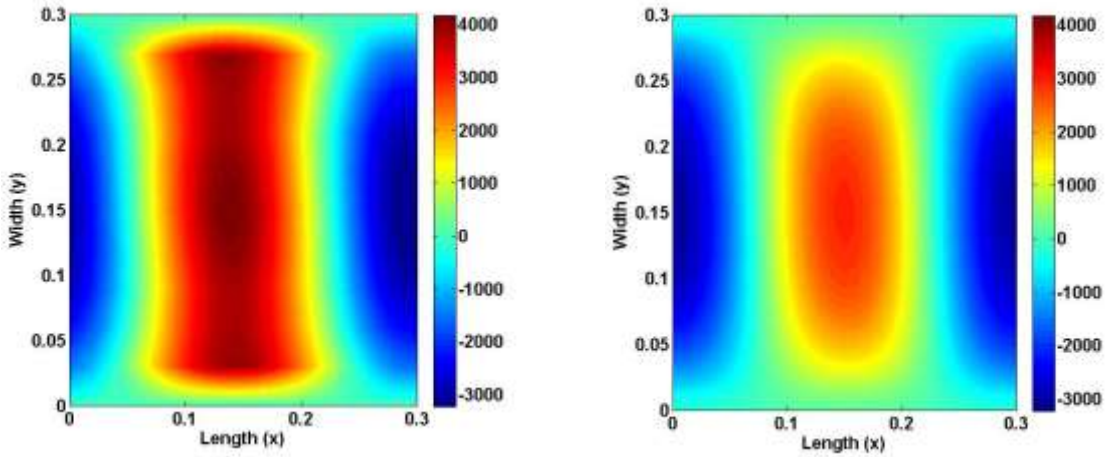

a **b**

Figure 6.28 Contour plots of stress resultants N_y (N/m) for postbuckling of symmetric and balanced laminate: (a) Improved method and (b) ABAQUS Type-A analysis.

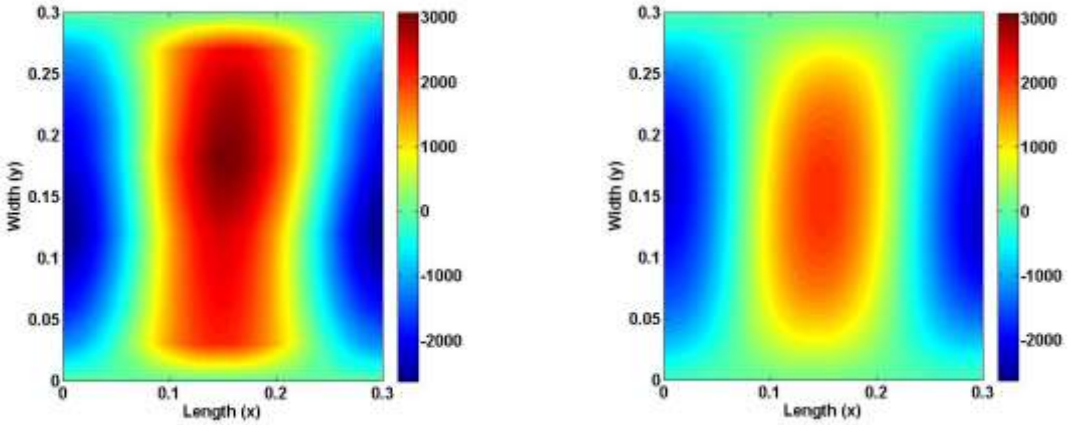

a **b**

Figure 6.29 Contour plots of stress resultants N_y (N/m) for postbuckling of symmetric and unbalanced laminate: (a) Improved method and (b) ABAQUS Type-A analysis.

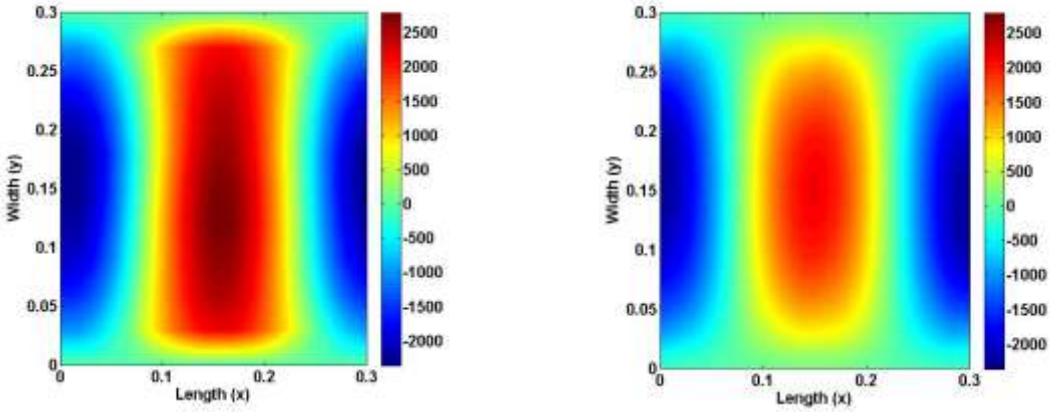

a **b**

Figure 6.30 Contour plots of stress resultants N_y (N/m) for postbuckling of unsymmetric and unbalanced laminate: (a) Improved method and (b) ABAQUS Type-A analysis.

Contour plots of stress resultant N_x for the three laminate configurations mentioned above at this location are shown in Figures 6.25-6.27, which illustrate the comparison between the Improved method and ABAQUS postbuckling analysis. The N_x contour is skewed due to anisotropy in Figure 6.25a although this skewing is slight for the case of the symmetric, balanced laminate plate. The increased distortion of the stress resultant pattern due to the increasing level of anisotropy is clearly evident in Figure 6.26a which shows the contour for the symmetric, unbalanced laminate plate. The N_x contour is again seen to be skewed for the unsymmetric, unbalanced laminate shown in Figure 6.27a. With reference to Figures 6.25b, 6.26b and 6.27b where the ABAQUS contours are displayed, a good agreement has been achieved between the Improved method results and the ABAQUS results.

Contour plots for transverse stress resultant N_y from the Improved method and ABAQUS are also presented in Figures 6.28, 6.29 and 6.30 showing that the results achieved from these two programs largely agree with each other.

6.6 Conclusion

This chapter has presented a detailed validation of the Improved VIPASA analysis proposed in Chapter 5. It focuses on using different approaches to demonstrate the feasibility and limitations of the analysis. Some useful conclusions can be summarised as follows:

Specialised trigonometric series functions with five sinusoidal terms have been introduced to enrich the degrees of freedom along nodal lines to accurately capture the in-plane displacements along a plate. It has been found that the number of sinusoidal terms which appear in the results is closely related to the material anisotropy. Compared

with Stein's work (1983), the current study is capable of solving both isotropic and general anisotropic plate postbuckling problems.

An analytical model has been derived, which can be used to interpolate the strain results given by the Improved VIPASA analysis. The strain distributions along four paths have been checked with analytical solutions, showing that the strains calculated using the proposed method are reasonable.

The details of numerical FE models constructed using the commercial software ABAQUS have been discussed and two type of in-plane free boundary conditions have been analysed to show the improvement made by the proposed method. The postbuckling stress resultant contours for isotropic and anisotropic plates predicted by the Improved VIPASA analysis match well with the FE results, particularly in the longitudinal direction during the initial postbuckling stages.

It has been observed that the VIPASA analysis does not capture the correct amplitude of the out-of-plane displacement profile along the transverse direction during the postbuckling, causing the results from the Improved VIPASA analysis and FE models to diverge in predicting the transverse stress distribution contours.

In this chapter, the improved analysis has been applied to single plates only. For further study, it would be desirable to extend the proposed method to analyse multiple joined plates and stiffened panels, so that the flexibility of the Improved VIPASA analysis can be further explored.

Chapter 7

Further development of the Improved VIPASA analysis

In Chapter 5, an improved analysis scheme was proposed to address the inaccurate stress distributions in VIPASA postbuckling analyses. Subsequent to the presentation of the proposed method, a series of validation analyses focusing on a single plate were conducted in Chapter 6 to show the method's applicability for predicting more accurate stress distribution fields. This chapter explores the possible extension of the method and adjusts it to make it flexible enough to analyse more realistic structural components such as stiffened panels. The chapter is organised as follows: Section 7.1 explains the necessity of further expanding the Improved VIPASA analysis. Section 7.2 introduces a two-plate model as the first step towards further development. Section 7.3 gives the results for this two-plate model and compares them with a single plate benchmark. Section 7.4 introduces a stiffened panel model. Section 7.5 presents the stiffened panel results which are compared with finite element results. Section 7.6 focuses on some of the issues identified from the analysis of the stiffened panel and suggests possible solutions to these problems. Section 7.7 concludes this chapter.

7.1 Introduction

As mentioned in previous chapters, the VICONOPT software has long been known as an efficient numerical tool for the preliminary stages of aerospace structural designs prior to the use of FEM for more detailed analysis and design. The versatility and efficiency of VICONOPT has been illustrated by many published results analysing real-life structural scenarios, such as folded-plate structures (Wittrick and Horsington 1984), corrugated panels (Stroud et al. 1984), blade stiffened panels (Anderson and Kennedy 2008), and a corrugated, ring-stiffened, laminated cylinder fuselage (Williams et al. 1990).

Although the Improved VIPASA analysis was proposed in Chapter 5 and validated in Chapter 6, the applications in these studies were limited to simple geometries, e.g. single isotropic and anisotropic plates. A significant gap exists between these analyses and those which would be required to apply this innovative method to more practical structural configurations. Hence, the most straightforward step to fill this gap is to conduct a preliminary numerical investigation to explore the potential of using the Improved VIPASA analysis to analyse the postbuckling behaviour of a stiffened panel.

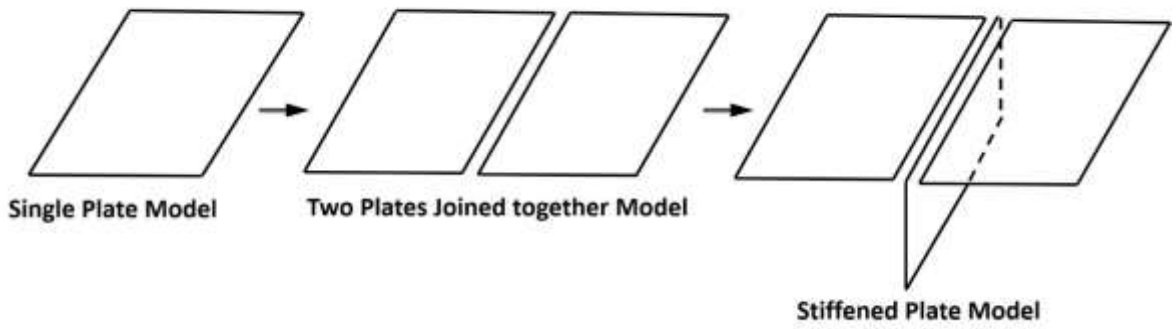

Figure 7.1 The progression from single plate model to stiffened plate model used in this study.

Stiffened panels have a high stiffness to weight ratio and are used extensively in aeronautical structures to reduce mass while maintaining a high degree of stiffness (Megson 2012). A typical configuration of a stiffened panel consists of a plate braced by

longitudinal stiffeners, which divide a wide plate into a number of narrower but more stable plates in order to increase the panels overall flexural rigidity and in-plane stiffness (Falzon et al. 2000). Since the stiffeners can be regarded as panel breakers, it is useful first to verify the Improved VIPASA analysis on a model where two plates are joined together without the interaction of the stiffener, and then to further extend it to a stiffened panel (shown in Figure 7.1).

7.2 Two plates joined together model

The joined plate model was developed by using two single square plates linked along their common boundary with a rigid connection so that they act as a single plate. Normal free in-plane and simply supported out-of-plane boundary conditions were applied to any unconnected boundaries.

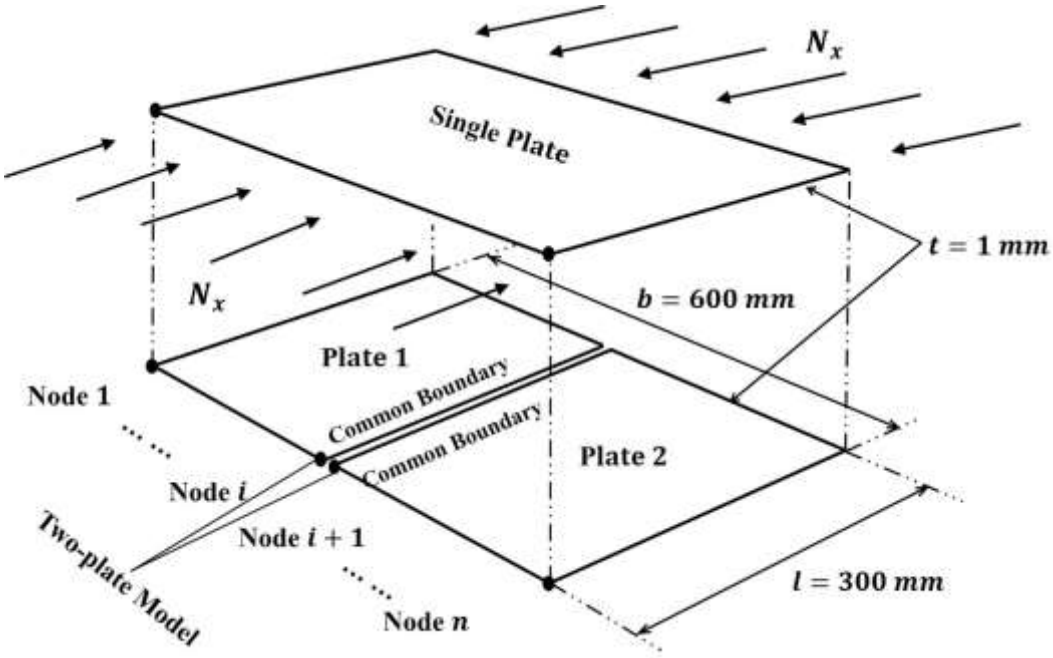

Figure 7.2 The comparison between the single and two-plate model.

A conventional single plate model was also constructed for comparison with the two plates joined together model. It is worth noting that both the two-plate model and the

single plate have the same dimensions with the aspect ratio (l/b) equal to 0.5, the only difference being that the two-plate model has a double-node connection at the middle of the plate while the single model treats the middle node as an interior node. The aim of these set-ups is to conduct a comparative study to demonstrate that the Improved VIPASA analysis is capable of analysing a geometry in which multiple plates are joined together, so as to pave the way for analysing more complex stiffened plate cases. Details of the layouts and dimensions used in Sections 7.2 and 7.3 are given in Figure 7.2.

As described in Equations 5.9-5.12 and 5.27-5.28, five longitudinal and five transverse degrees of freedom are required for each node to accurately capture in-plane behaviours in postbuckling, resulting in ten equilibrium equations per node being required to solve the unknowns. Note that the out-of-displacement in the two-plate model comes from the VIPASA postbuckling analysis, which is the analytical solution of the governing equations based on the use of the exact stiffness method. Therefore, the out-of-displacement continuity is guaranteed for the two-plate model. At the two longitudinal edges of the single plate, twenty equations derived from relationships $\boldsymbol{u_i} = \mathbf{0}$ and $N_{yi} = 0$ are used to describe the free in-plane boundary conditions and these replace the corresponding twenty equilibrium equations at the initial node and the final node, respectively. Since the two-plate model involves a connection between the final node in plate 1 and an initial node in plate 2 at their common edge, alternative boundary conditions and equilibrium equations are needed at those connecting nodes to obtain a proper joined condition between the two plates (Aliabadi and Baiz 2008).

The first ten equations can be expressed by considering the continuity along the two plates. In order to preserve in-plane displacement continuity, the longitudinal and transverse displacements (u and v) at node i and the adjacent node ($i + 1$) are assumed

to be the same, indicating the two nodes are joined and move together. The detailed relationships between each sinusoidal component are listed below:

$$\begin{aligned} u_{(i)0} &= u_{(i+1)0} & v_{(i)0} &= v_{(i+1)0} \\ u_{(i)\mathrm{c}} &= u_{(i+1)\mathrm{c}} & v_{(i)\mathrm{c}} &= v_{(i+1)\mathrm{c}} \\ u_{(i)\mathrm{s}} &= u_{(i+1)\mathrm{s}} & v_{(i)\mathrm{s}} &= v_{(i+1)\mathrm{s}} \\ u_{(i)\mathrm{C}} &= u_{(i+1)\mathrm{C}} & v_{(i)\mathrm{C}} &= v_{(i+1)\mathrm{C}} \\ u_{(i)\mathrm{S}} &= u_{(i+1)\mathrm{S}} & v_{(i)\mathrm{S}} &= v_{(i+1)\mathrm{S}} \end{aligned} \tag{7.1}$$

Another ten equations can be achieved by considering the equilibrium state at the joined nodes. At the joined node, the total in-plane force is the sum of the force from node i and the adjacent node $i+1$; hence, the in-plane equilibrium equations (Equations 5.27 and 5.28) can be expanded by equating the sum of the edge forces in each plate to zero. The modified in-plane equilibrium equations at the common node are thus expressed as follows:

$$\left(\frac{\partial N_{y(i)}}{\partial y}+\frac{\partial N_{xy(i)}}{\partial x}\right)+\left(\frac{\partial N_{y(i+1)}}{\partial y}+\frac{\partial N_{xy(i+1)}}{\partial x}\right)=0 \tag{7.2}$$

$$\left(\frac{\partial N_{xy(i)}}{\partial y}+\frac{\partial N_{x(i)}}{\partial x}\right)+\left(\frac{\partial N_{xy(i+1)}}{\partial y}+\frac{\partial N_{x(i+1)}}{\partial x}\right)=0 \tag{7.3}$$

The relationships described in Equation 7.1 and the in-plane equilibrium equations mentioned in Equations 7.2-7.3 are implemented rigorously in the Improved VIPASA analysis code. A set of results for the two-plate model will be generated and compared with results for the single plate model in the next section.

7.3 Two-plate model postbuckling results

Postbuckling results for the single-plate model and the two-plate model are presented in this section. Both of these modelling techniques are used to represent a plate with an aspect ratio equal to 0.5 (length $l = 300$ mm and width $b = 600$ mm). All plates are assumed to be made of titanium with Young's modulus $E = 110\text{kNmm}^{-2}$ and Poisson's ratio $\nu = 0.3$. Results are presented for a model under axial compression both with the unloaded edges free to move in-plane, and all four edges are simply supported.

Normalised and non-normalised load versus end shortening results are shown in Figure 7.3. As is to be expected, the load-strain curve for the single-plate model and the two-plate model are nearly identical, indicating that there is no loss of axial stiffness when the whole plate is modelled by the two-plate technique. These findings confirm that a rigid connection has been established between the two plates, and hence the validity of the relationships used in Equation 7.1.

The postbuckling load-strain curves of the square plate ($l/b = 1$) example used in the previous chapter are also included for completeness in Figure 7.3. From these curves, it can be observed that the square plate buckles at a higher load but at a higher level of end shortening strain, in comparison with the short rectangular plate, which although buckling at a lower load, can sustain a higher postbuckling load and therefore has a greater reserve of strength.

It is also worth noting from Figure 7.3b that the differences in postbuckling stiffness ratios between VIPASA and ABAQUS analyses are less noticeable in the short rectangular plate than in the square plate. One possible explanation for this change is that VIPASA follows the lower bound solution which ignores the transverse constraint effect, but this effect becomes smaller in the short rectangular plate as it has a shorter longitudinal edges.

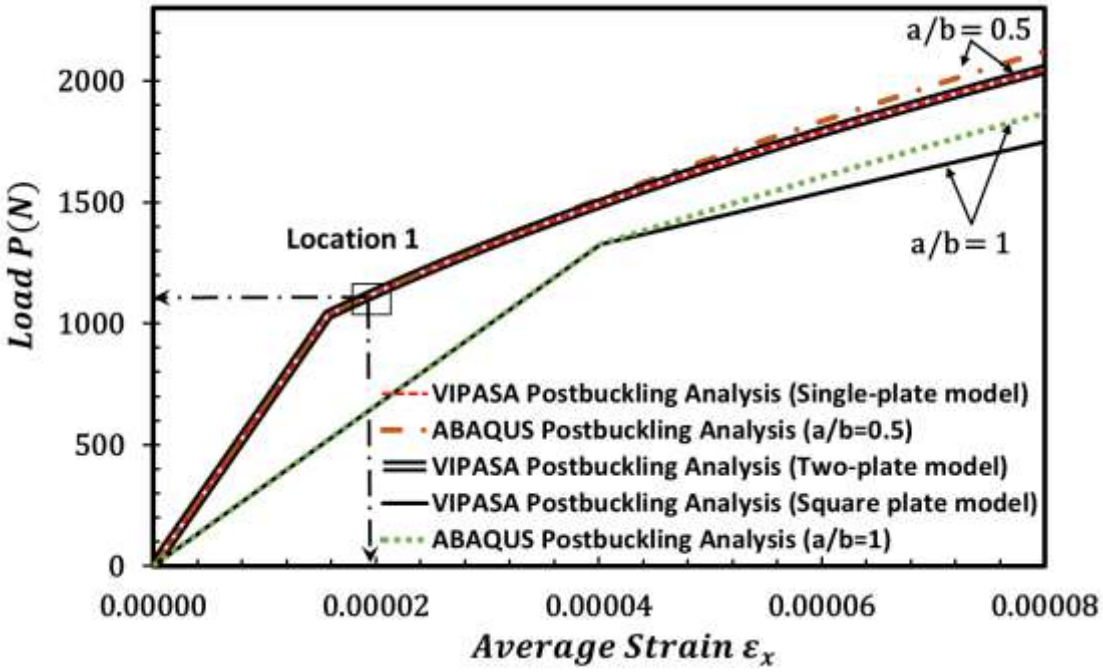

a

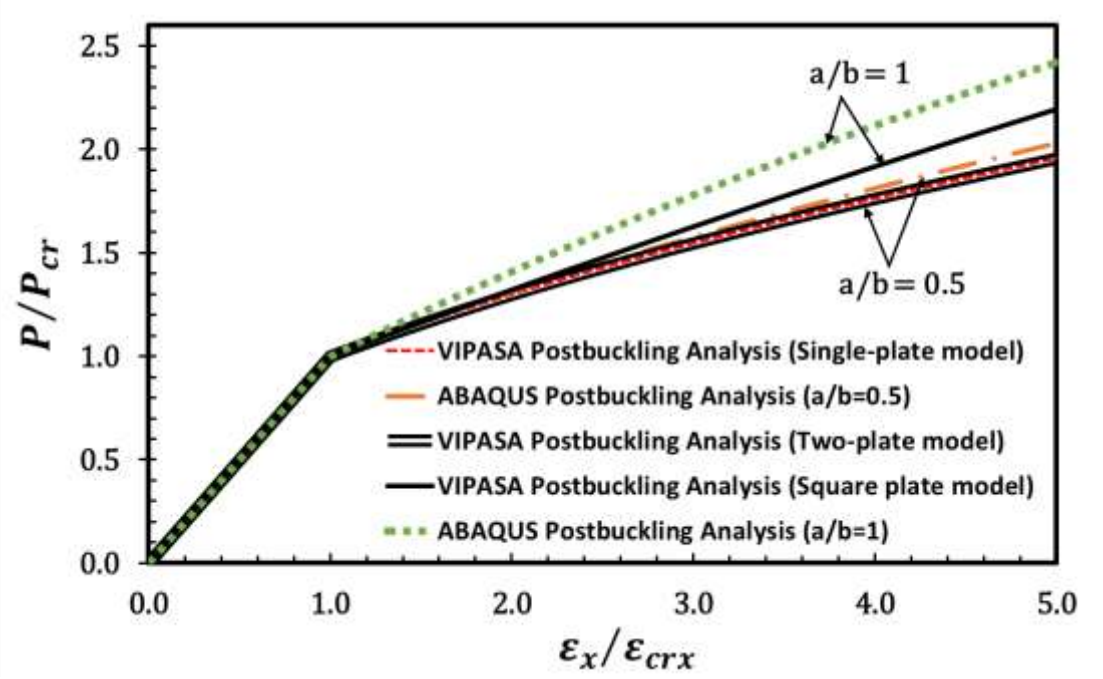

b

Figure 7.3 Postbuckling behaviours of plates with different aspect ratios in compression: (a) normalised load-strain curves and (b) actual load-strain curves.

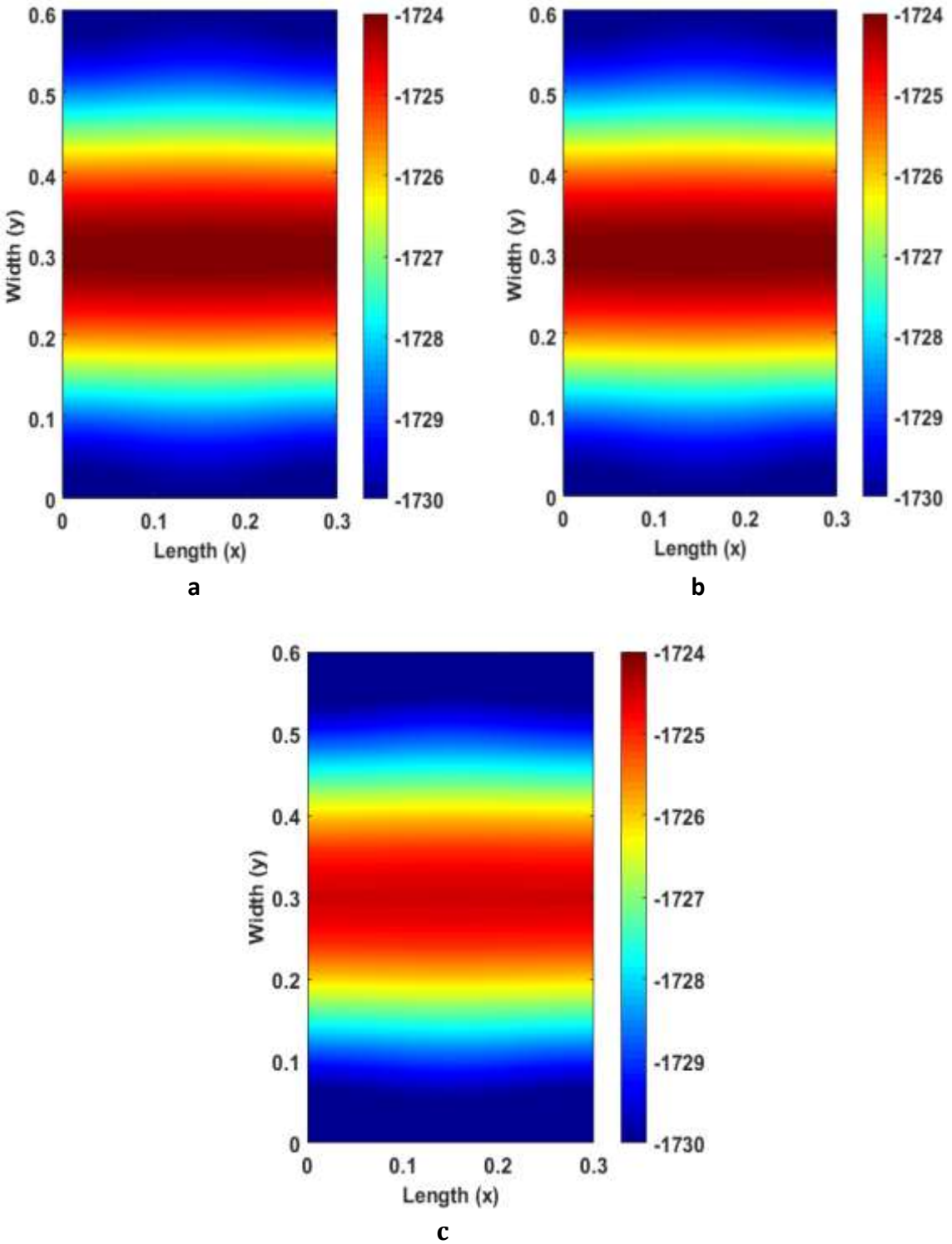

Figure 7.4 Contour plots of stress resultants N_x (N/m) at postbuckling Location 1 from different models: (a)Improved VIPASA analysis (single plate model), (b) Improved VIPASA analysis (two-plate model) and (c) ABAQUS Type A.

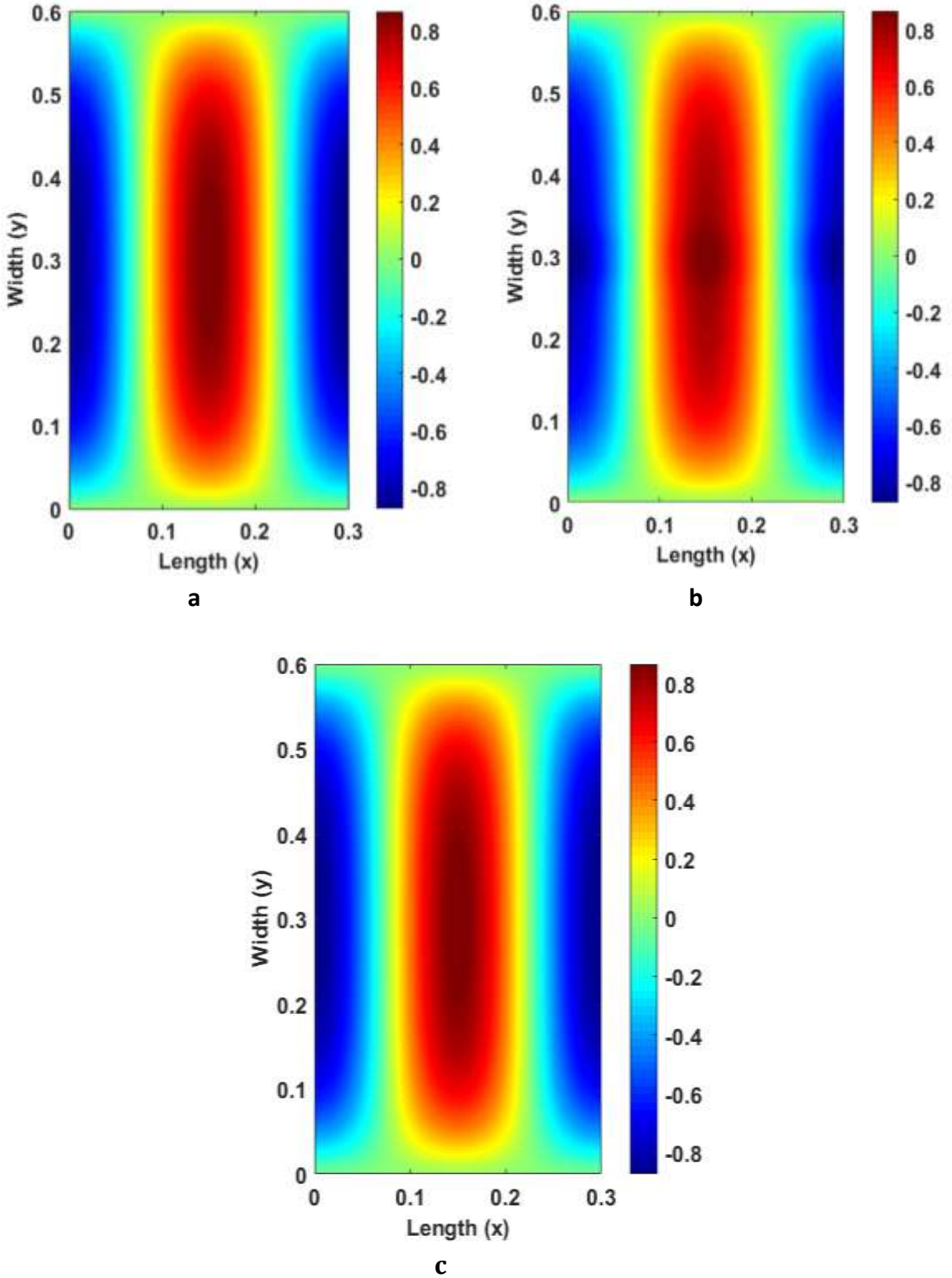

Figure 7.5 Contour plots of stress resultant N_y (N/m) at postbuckling Location 1 from different models: (a)Improved VIPASA analysis (single plate model), (b) Improved VIPASA analysis (two-plate model) and (c) ABAQUS Type A.

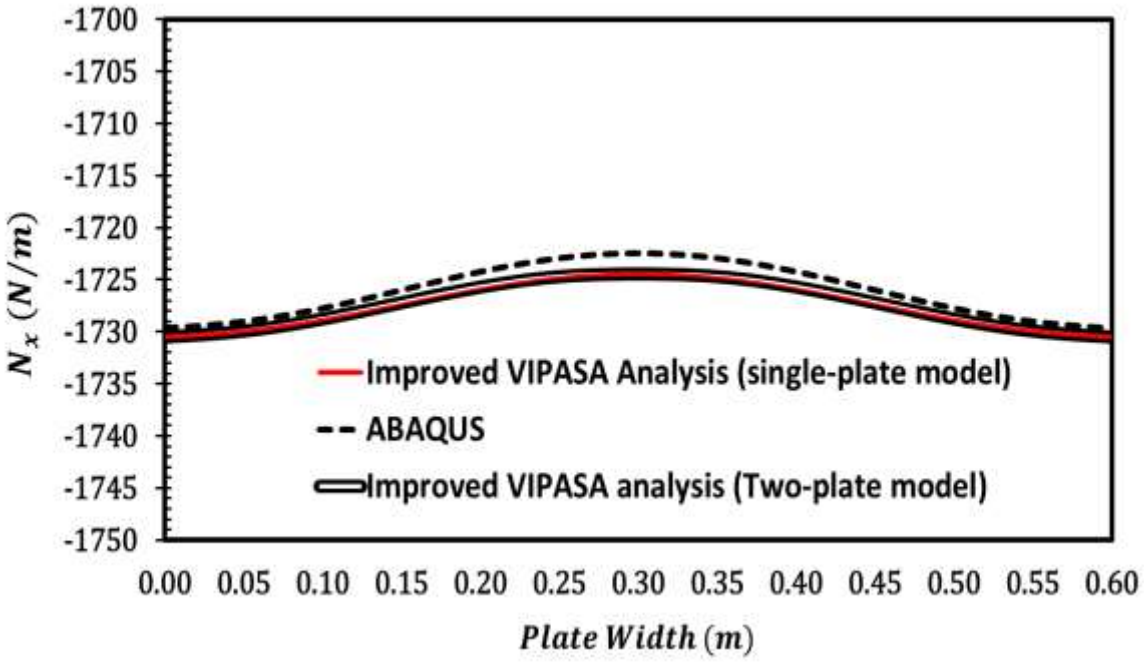

Figure 7.6 Comparison of axial stress resultant N_x along the vertical centre line of the plate for postbuckling Location 1 predicted by the Improved VIPASA analysis (single-plate model and two-plate model) and ABAQUS.

To further check the equilibrium and continuity of the two-plate model, one strain controlled postbuckling location ($\varepsilon_x = 1.93 \times 10^{-5}$ marked with 'Location 1' in Figure 7.3b) is identified to investigate the stress field during the postbuckling regime. Contour plots of stress resultants (N_x and N_y) at Location 1 for the plate with an aspect ratio equal to 0.5 are presented in Figures 7.4 and 7.5 to illustrate the comparison between the single plate model, the two-plate model used in the Improved VIPASA analysis and ABAQUS during postbuckling analysis. Compared with the square plate contour plots in the previous chapters, the distribution patterns of the transverse stress resultant (N_y) are very similar but the variation trends of axial stress resultants (N_x) are less dramatic in the longitudinal direction showing an almost constant pattern.

Using the single-plate model contours (Figures 7.4a and 7.5a) as benchmarks, it can be seen that little discontinuity appears in the two-plate model contour (Figures 7.4b and 7.5c). Furthermore, the axial stress resultant values extracted along the vertical central

line in the single-plate model and the two-plate model show excellent agreement in Figure 7.6. These findings suggest that the equilibrium equations expressed in Equation 7.2 and Equation 7.3 are applicable to the two-plate model and the integrity of the plate has been preserved. With reference to Figures 7.4c and 7.5c in which ABAQUS contours are displayed, it is seen that both the single-plate model and the two-plate model results correlate well with those obtained from ABAQUS.

The results presented in this section lead us to try, with some confidence, to start from the two-plate model and to further develop the Improved VIPASA analysis to apply to a more complicated geometry – the stiffened panel.

7.4 Stiffened panel modelling

Let us consider three flat plates joined together at position J where three nodes, node i in plate 1, node j in plate 2 and node k in plate 3 meet as shown in Figure 7.7. The global coordinate system is given by x, y and z, corresponding to u, v and w dsiplacements, and the local coordinate system for each plate is expressed as $x^{()}$, $y^{()}, z^{()}$ where superscript () refers to the plate number.

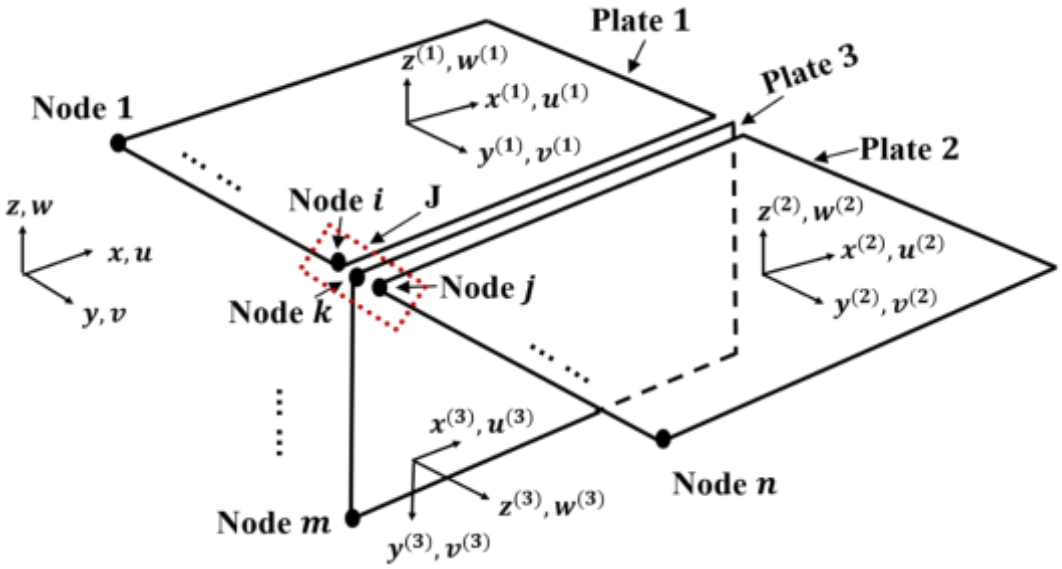

Figure 7.7 Assembly of the stiffened plate model and its global and local coordinate system.

Based on the coordinate systems shown in Figure 7.7, it can be observed that the three plates have the same longitudinal orientation (i.e. x-axis); therefore, the continuity equations along the junction line can be written in terms of longitudinal displacement (u) as follows:

$$\begin{aligned} u_{(i)0}^{(1)} &= u_{(j)0}^{(2)} = u_{(k)0}^{(3)} \\ u_{(i)c}^{(1)} &= u_{(j)c}^{(2)} = u_{(k)c}^{(3)} \\ u_{(i)s}^{(1)} &= u_{(j)s}^{(2)} = u_{(k)s}^{(3)} \\ u_{(i)C}^{(1)} &= u_{(j)C}^{(2)} = u_{(k)C}^{(3)} \\ u_{(i)S}^{(1)} &= u_{(j)S}^{(2)} = u_{(k)S}^{(3)} \end{aligned} \tag{7.4}$$

Along the junction boundary of the three plates, it is anticipated that the skin out-of-plane displacements ($w^{(1)}$ and $w^{(2)}$) should match the stiffener in-plane transverse displacement ($v^{(3)}$) and vice versa. Another set of continuity equations which will ensure the interaction between the skin and stiffener can be expressed as follows:

$$\begin{aligned} v_{(i)0}^{(1)} &= 0 & v_{(j)0}^{(2)} &= 0 & v_{(k)0}^{(3)} &= 0 \\ v_{(i)c}^{(1)} &= -w_{(k)c}^{(3)} & v_{(j)c}^{(2)} &= -w_{(k)c}^{(3)} & v_{(k)c}^{(3)} &= w_{(i)c}^{(1)} \\ v_{(i)s}^{(1)} &= -w_{(k)s}^{(3)} & v_{(j)s}^{(2)} &= -w_{(k)s}^{(3)} & v_{(k)s}^{(3)} &= w_{(i)s}^{(1)} \\ v_{(i)C}^{(1)} &= 0 & v_{(j)C}^{(2)} &= 0 & v_{(k)C}^{(3)} &= 0 \\ v_{(i)S}^{(1)} &= 0 & v_{(j)S}^{(2)} &= 0 & v_{(k)S}^{(3)} &= 0 \end{aligned} \tag{7.5}$$

These equations are used to maintain a smooth junction line when plates with different local coordinate systems are linked together. Since VIPASA out-of-plane displacements (Equation 5.7) only have two sinusoidal terms while in-plane displacements (Equation 5.9) have five sinusoidal terms, the corresponding absent components are assumed to be equal to zero, resulting in several '0' terms appearing in Equation 7.5.

The global equilibrium equations required at the junction can be written in a similar way to the two-plate model, except for the equilibrium in the x-direction, in which the total in-plane force along the x-direction is the sum of the force from three nodes (node i, node j and node k) instead of two. Hence, the equilibrium equations can be modified as

$$\sum_{n=i,j,k} \left(\frac{\partial N_{x(n)}}{\partial x} + \frac{\partial N_{xy(n)}}{\partial y} \right) = 0 \tag{7.6}$$

Combining Equations 7.4-7.6, 30 equations need to be implemented into the Improved VIPASA analysis to generate the postbuckling results for the stiffened plate model.

7.5 Stiffened panel postbuckling results

Postbuckling results for a stiffened panel are presented in this section. The stiffened panel consists of three square plates joined together along their common boundary using the techniques described in the previous section. Results are shown here for a panel under axial compression with the skin constrained in-plane and the stiffeners free in-plane. Detailed dimensions and boundary conditions for the representative section are summarised in Figure 7.8. It should be noted that the stiffened panel investigated in this section is relatively narrow and deep and not therefore representative of aerospace applications such as wing cover panels, but it is still very useful for validation purposes.

Non-normalised load end shortening curves are plotted in Figure 7.9**.** In contrast to the flat plate, the numerical results from the stiffened panel show that the load end shortening curves are no longer bifurcational due to the change in geometric configuration. Instead the curves have a smooth transition from the unbuckled to the buckled

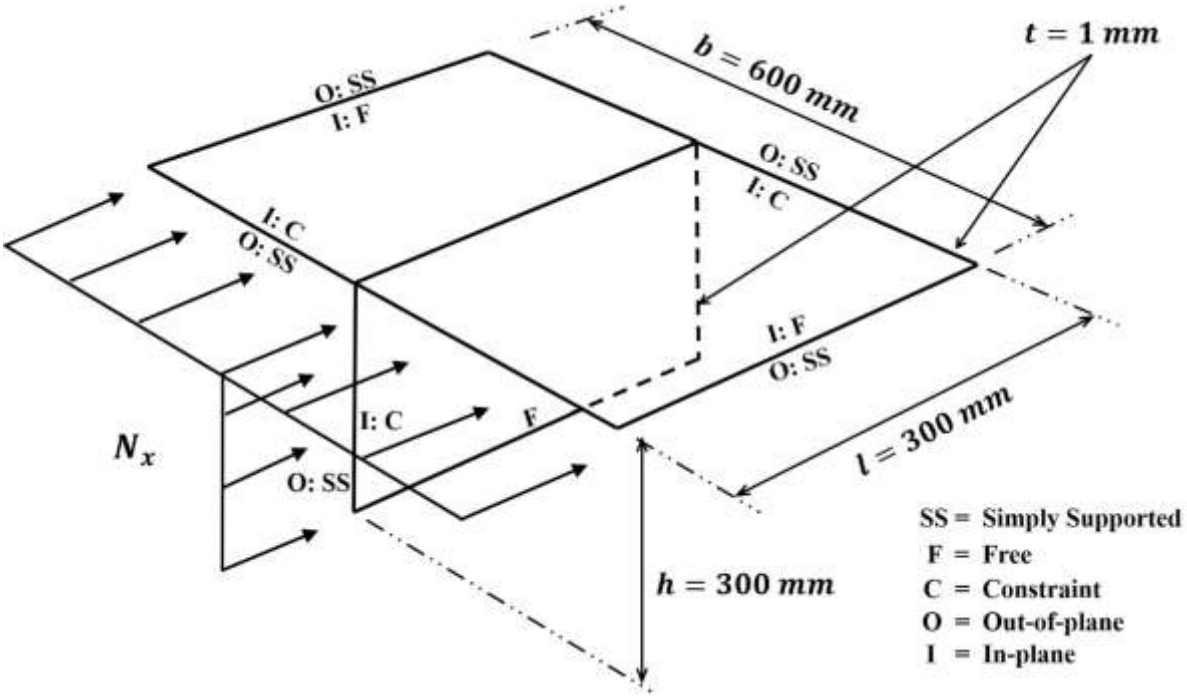

Figure 7.8 The dimension and boundary conditions of the proposed model.

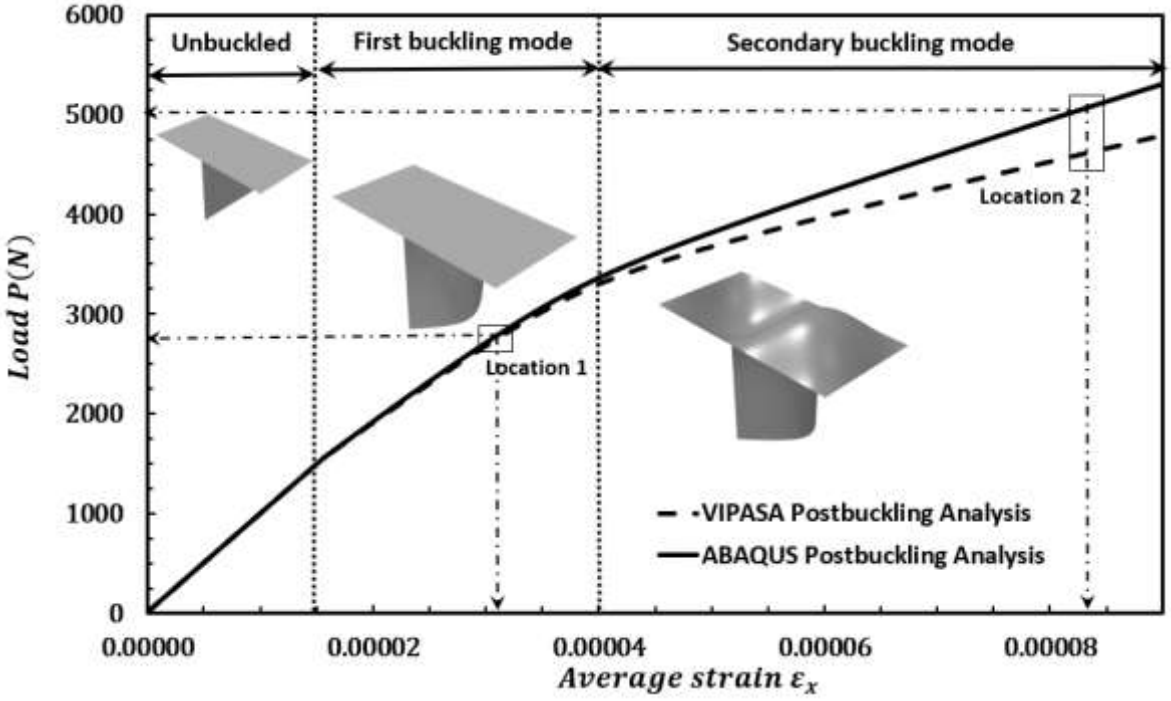

Figure 7.9 Load and end-shortening curves for postbuckling in compression of stiffened plate.

state indicating the differences between the unbuckled and initial postbuckled stiffness of the panel are quite trivial. Having examined the details of the buckling modes, it can be seen that the absence of a bifurcation point is closely related to the location of the buckling mode. It is observed that buckling first appears in the stiffener and then begins to appear in the skin with increasing compressive load. Since buckled stiffeners will have a less significant effect on overall plate stiffness, the bifurcation point is less obvious. Buckled skin, by contrast, reduces the overall stiffness and leads to a change in the slope of the curve in the later stages of the postbuckling process.

Two strain-defined locations, one at the first buckling mode which is a stiffener mode ($\varepsilon_x = 3.24 \times 10^{-5}$) and the other one at the secondary buckling mode which is a skin mode ($\varepsilon_x = 8.47 \times 10^{-5}$) are chosen to investigate the stress field under the postbuckling regime. Figures 7.10 and 7.11 illustrate the stress resultant (N_x) distribution of the skin and stiffener in the stiffened panel, respectively. The results obtained using the Improved VIPASA analysis match well with those from the finite element analysis clearly showing the robustness of the proposed method. Figures 7.10a and 7.10b show that the contour plot is invariant in the skin since the skin plate is unbuckled and subjected to constant compression at Location 1. Figures 7.10c and 7.10d show that the stresses redistribute away from the central region of each skin plate towards the transverse edges and the stiffeners at Location 2. Figures 7.11a and 7.11b show that the redistributed stress appears in the tip of the stiffener at Location 1 thereby confirming that buckling is initiated in the stiffener. Further into the postbuckling stage, since the stiffener is free edged, the stress redistribution increases so far that it not only reduces the compression but leads to tension developing at the two tips of the stiffener edge. On the other hand, it can be seen that the compression reaches a maximum in the middle of the stiffener edge as shown in Figures 7.11c and 7.11d.

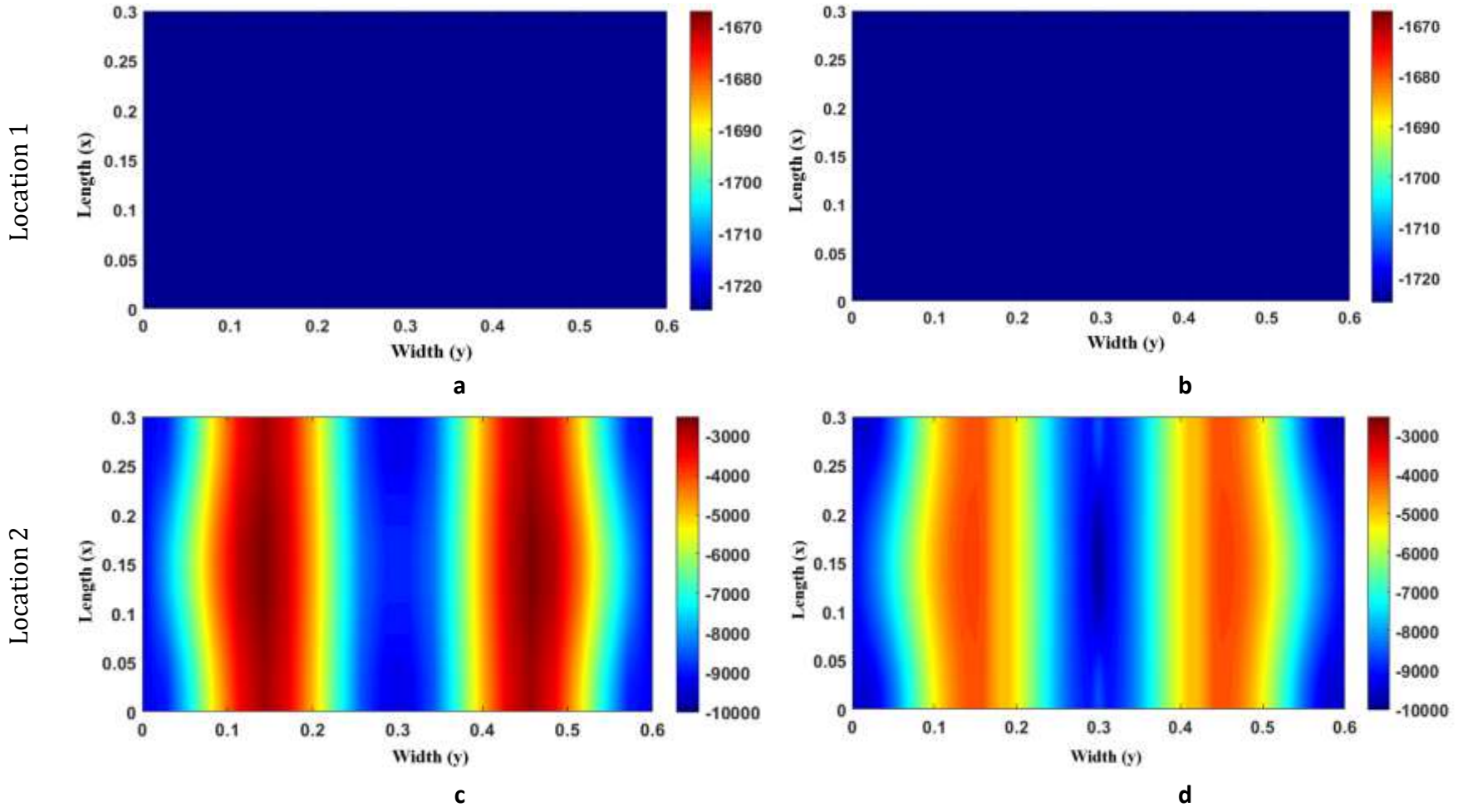

Figure 7.10 Contour plots of stress resultants N_x (N/m) in the skin at different postbuckling locations using different software: (a) Improved VIPASA analysis at location 1; (b)ABAQUS at Location 1; (c) Improved VIPASA analysis at Location 2; (d)ABAQUS at Location 2

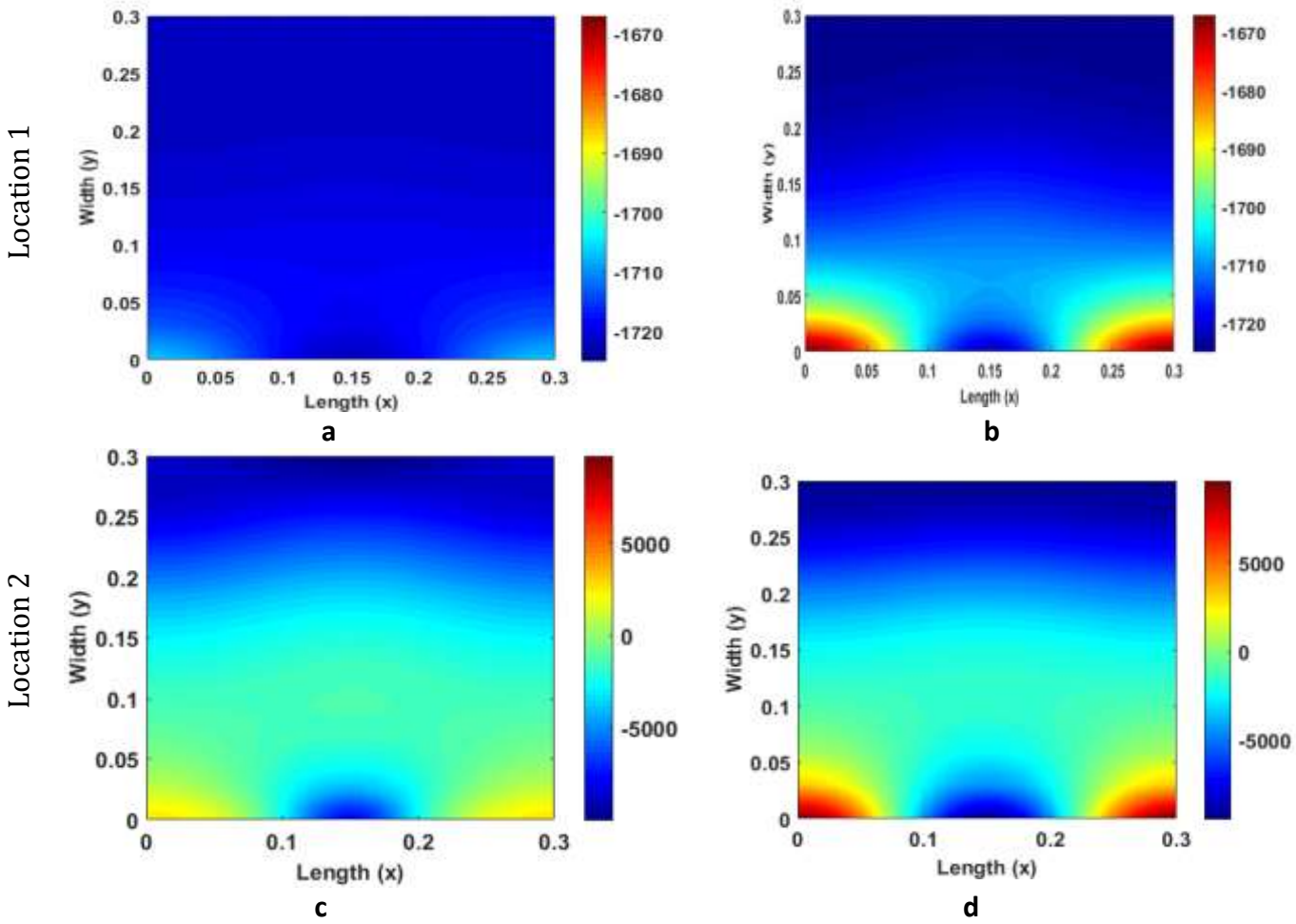

Figure 7.11 Contour plots of stress resultants N_x (N/m) in the stiffener at different postbuckling locations using different software analysis: (a) Improved VIPASA analysis at Location 1; (b)ABAQUS at Location 1; (c) Improved VIPASA analysis at Location 2; (d)ABAQUS at Location 2.

7.6 Transverse stress distribution

The contour plots of the transverse stress resultant N_y across the skin panel at postbuckling Location 2 are displayed in Figure 7.12. A discontinuity at the centre of the contour can be identified in Figure 7.12a, which indicates that the Improved VIPASA analysis has some difficulties with the coupling of the stress resultants N_y at the junction. A plausible explanation might be that the two-term out-of-plane function used in VIPASA analysis when coupled with the five-term in-plane displacement function used in the proposed method, may have induced some compatibility issues in adding different wavelength (λ and $\lambda/2$) together at the junction and influencing the stress continuity yielding a gap in the contour.

One feasible solution to bridge this discontinuity is to change the finite difference expressions used in calculating the derivative at the junction of nodes i and j. Instead of treating node i as a final node in plate 1 and node j as an initial node for plate 2, the changed model now assumes that they are now connected together as interior nodes in the skin panel. Hence, the adjustments of finite difference expressions can be summarised in Table 7.1

Table 7.1 The adjustments made to the finite difference expressions at node i and node j.

	Before	After
At node i	$u_i' = \frac{3u_i - 4u_{i-1} + u_{i-2}}{2b}$	$u_i' = u_j' = \frac{u_{j+1} - u_{i-1}}{2b}$
	$v_i' = \frac{3v_i - 4v_{i-1} + v_{i-2}}{2b}$	
At node j	$u_j' = \frac{-3u_j + 4u_{j+1} - u_{j+2}}{2b}$	
	$v_j' = \frac{-3v_j + 4v_{j+1} - v_{j+2}}{2b}$	$v_i' = v_j' = \frac{v_{j+1} - v_{i-1}}{2b}$

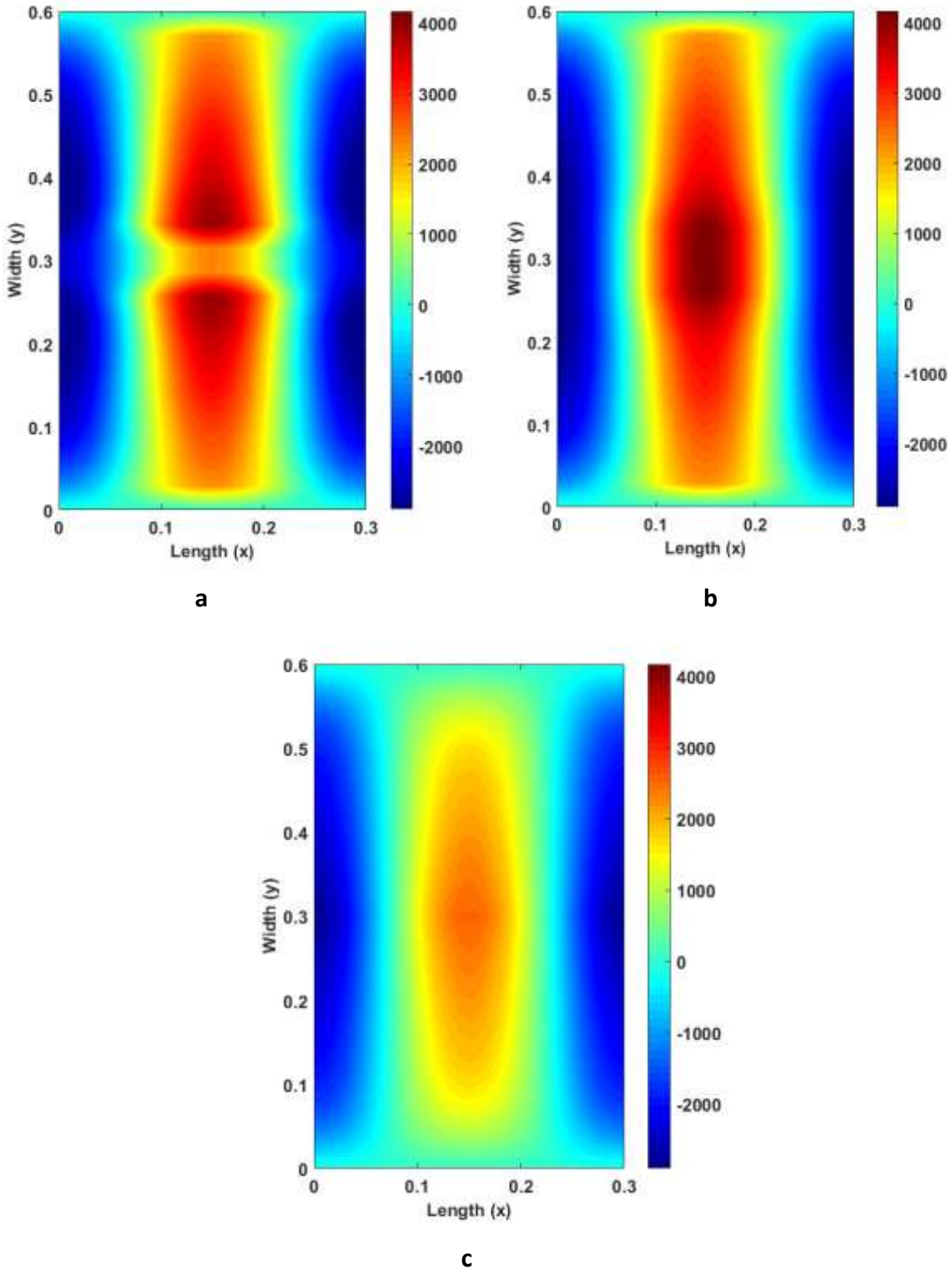

Figure 7.12 Contour plots of stress resultants $N_y(N/m)$ at postbuckling Location 2 from different software: (a) Improved VIPASA analysis results before changing the finite difference expressions, (b) Improved VIPASA analysis results after changing the finite difference expressions and (c) ABAQUS.

Although using a specific finite difference expression at particular nodes is not good in terms of developing a universally applicable method for the Improved VIPASA analysis, this approach does address the discontinuity problem. The effect of changing the finite difference expressions can be observed in Figure 7.12b, in which the transverse stress resultant N_y contour shows little discontinuity in the centre of the plate.

Comparing the results with ABAQUS (Figure 7.12c), a good correlation of the stress distribution pattern can be seen to have been achieved. However, by using this approach, it can also be seen that the Improved VIPASA analysis gives an approximately 40% higher prediction of the value of the stress resultants in the middle than ABAQUS. This relatively substantial difference between the Improved VIPASA results and ABAQUS results can be explained by the over-simplified assumptions made in the out-of-displacement expression in the VIPASA analysis.

7.7 Conclusion

This chapter began the process of expanding the Improved VIPASA analysis to predict the postbuckling behaviours of a stiffened panel. Two models with increasingly complicated geometry and equilibrium set-ups based on using Improved VIPASA analysis have been presented to account for more practical situations. Each model has been presented alongside appropriate results that have highlighted the important adjustments made to the Improved VIPASA analysis and their effect on the postbuckling response of the corresponding model.

The two-plate model was first constructed in the Improved VIPASA analysis by using two single square plates joined along their common boundary. The results of the two-plate model revealed no continuity issues in comparison to the single-plate results obtained by

using the Improved VIPASA analysis and ABAQUS. Good correlation with the stress contour plot demonstrates that the Improved VIPASA analysis can solve multi-plate problems satisfactorily, which provides some confidence in expanding it further to solve stiffened panel postbuckling problems.

The adjustments which would need to be made to the continuity and equilibrium equations to model a stiffened panel using the Improved VIPASA analysis were then examined. Although it was also seen that discontinuous patterns may appear in the transverse resultant contour plot at the junction area, a possible solution which changes the finite difference expressions for the junction nodes was shown to remove the discontinuity.

Preliminary numerical investigation of a stiffened panel with three square plates joined together revealed an acceptable level of agreement in comparison to finite element results. Based on the good correlation in the predicted stress contour plots and a good match on stress resultant value, the Improved VIPASA analysis can, therefore, be seen to give reasonable results which simulate the postbuckling behaviour of the considered structure. The proposed method shows excellent computational speed on the stiffened panel numerical examples. All the stiffened panel results presented in this chapter were obtained in approximately 0.5 minutes of computer time on a standard Core i7 2.40 GHz PC by using the proposed method compared with almost 3 minutes by using finite elements software ABAQUS. This computational cost advantage will be significant when the problem is scaled up, i.e. analysing a full aircraft wing. In future, the proposed method can also be compared with experimental test data, which will give a good indication against real-life situations.

Chapter 8

Conclusion

This thesis has presented a series of numerical approaches to enhance the postbuckling analysis function in the VICONOPT software. Based on the current postbuckling analysis features in VICONOPT, the developments made in this thesis focus on three areas. Firstly, an updating technique was proposed to resolve the problem of the VIPASA postbuckling analysis being overly conservative. Secondly, a comprehensive approach with enhanced in-plane shape functions was used to correct the inaccurate stress distribution predicted by the VIPASA postbuckling analysis. Finally, this new approach was expanded to analyse complex structures like stiffened panels. This chapter summarises some of the contributions made to improving the VICONOPT postbuckling capabilities and concludes the work presented in this thesis. The chapter is organised as follows: Section 8.1 lists the main contributions of this research. Section 8.2 provides the conclusions, while directions for future work are presented in Section 8.3.

8.1 Contribution

i. The Simulated VICON analysis developed in this thesis provides a useful updated technique for VIPASA postbuckling analysis of a prismatic plate under combined loading. This analysis is based on investigating the axial stiffness difference between the VIPASA and the VICON analyses to address the overly conservative issues associated with the VIPASA postbuckling analysis of plates under combined

loading or those with anisotropic lay-ups. The differences in the axial stiffnesses predicted by VIPASA and VICON analyses under combined loading during postbuckling analysis are calculated by simple, yet reliable geometric relationships, which are used to serve as the basis of the Simulated VICON analysis. The analysis can capture the characteristic plate postbuckling features, such as load-strain curves, and comparisons between the proposed method and ABAQUS show good agreement for the postbuckling equilibrium path.

ii. An Improved VIPASA postbuckling analysis based on the combination of Stein's method and the exact strip method has been developed for the analysis of the initial postbuckling behaviour of prismatic plate structures. Enhanced trigonometric functions are used to represent the longitudinal and transverse in-plane displacements accurately. This improved analysis enables correct stress distributions to be found at an early stage of the postbuckling analysis, so that stress invariant problems in VIPASA postbuckling analysis can be satisfactorily solved. Additional terms in the in-plane functions allow the Improved VIPASA analysis to model a general anisotropic plate that has fully populated **A, B** and **D** stiffness matrices. A comparison is made between the results obtained from the Improved VIPASA analysis and ABAQUS in relation to the stress distributions during postbuckling, and these are seen to correlate well.

iii. A preliminary approach for extending the Improved VIPASA analysis for application to more realistic structural components is developed. This work focuses on making the proposed method flexible enough to analyse multi-plate models including stiffened panels. By adjusting the continuity and equilibrium equations along the common boundaries of the joined plates, the Improved VIPASA analysis is found to be capable of analysing two joined plates and stiffened

panel postbuckling problems. Preliminary numerical investigations demonstrate that this extended numerical analysis procedure (model building and solution) is an appropriate approach to simulate the postbuckling behaviour of the considered structures.

8.2 General Conclusion

The main aim of this study was to improve the postbuckling analysis capabilities of the computer program VICONOPT. In this thesis, several numerical approaches building on the existing exact strip method have been developed to fulfil this goal. The main findings can be summarised from the following perspectives:

8.2.1 The exact strip method

The literature on the numerical solution of thin-wall structures postbuckling problems is vast. It can be seen that FEA is the most versatile approach for carrying out postbuckling analysis due to its robustness and ability to handle complex geometry, load cases and materials. It should be noted however that computational expensive processes, such as Newton-Raphson or Riks iterations, have to be adopted to solve the non-linear equations encountered in these problems to give the required accuracy, which makes the FEM less suitable for preliminary design purposes. The finite strip method (FSM), which can be used as an alternative to finite element approach, divides plates into longitudinal strip elements and interpolates the deformed shape using polynomial functions. With fewer nodal degrees of freedom and simpler shape functions, computational cost can thus be reduced. Subsequent to FSM, the exact-FSM developed as a specialised FSM approach uses the exact solution to the differential equations that describe the behaviour of a plate

element to formulate the corresponding stiffness matrices. The exact strip method coupled with the reliable Wittrick-Williams algorithm forms the foundation of the specialist design and optimisation software VICONOPT with VIPASA and VICON analysis package.

It has been demonstrated in the literature review that exact-FSM can be very accurate because it is based on the direct solution of the governing equations, rather than on the use of approximate energy or work principles associated with standard FSM approaches. The exact-FSM has been found to be much less computationally expensive than the FEM for the analysis of prismatic plate structures because the discretisation of the plate can be avoided. The exact-FSM has potential to provide reduced order computationally efficient approaches for predicting postbuckling behaviours and to be used to optimise the design of aircraft structures. Although modern supercomputers enable large-scale finite element simulations and optimisations to be conducted on complex structures by sophisticated FEM software, faster, reliable analysis and design software are still needed when carrying out parametric preliminary design processes where an excessive number of models and structural configurations are studied before more detailed analysis is performed on the most promising ones. Based on the existing exact-FSM and its applications, the following two new analysis schemes have been developed.

8.2.2 The Simulated VICON analysis

It was discovered at the beginning of this research that VIPASA and VICON buckling analyses show different results if the plate under consideration is subjected to combined loading. Comparing existing theoretical equations and numerical examples reveals that the simple sinusoidal mode shape function used in VIPASA analyses results in a

convenient analytical derivation of the plate stiffness matrix, but that the boundary conditions are not strictly satisfied when nodal lines are skewed due to shear and anisotropy. VICON analysis, however, due to its use of Lagrangian multipliers to incorporate a set of constraints to represent regularly repeating interior supports, allows boundary conditions in these cases to be closely matched. Therefore, VICON buckling analysis is more accurate than VIPASA analysis in cases of shear and material anisotropy. It has also been found that since VICON analysis involves the coupling of different wavelengths it would be computationally expensive to expand it into a full postbuckling analysis, and so an alternative approach is worth exploring. The differences between the gradients of the load-strain behaviours predicted by VIPASA and VICON initial buckling analysis, for a plate having combined loading, are found to be useful in developing a simulated VICON postbuckling analysis. A fast and reliable trigonometric calculation procedure is proposed which uses the VIPASA buckling and post-buckling axial stiffness to work out the corresponding VICON postbuckling stiffness and strain. Based on these calculations, the equilibrium path for plate postbuckling using VICON analysis can be achieved. This new approach takes advantage of the VICON analysis features whilst maintaining the VIPASA postbuckling capacity.

Proof of concept work has been conducted for the prediction of the postbuckling response of isotropic and anisotropic single plates and stiffened panels under combined loading. The postbuckling stiffness predicted by the Simulated VICON analysis is found to be about 25% higher than that given by the conservative VIPASA postbuckling analysis. Comparisons with standard finite element method results validate the proposed Simulated VICON analysis and the results given by this new analysis are in good agreement with the results given by the FEM in most of the cases examined.

8.2.3 The Improved VIPASA analysis

The VIPASA analysis assumes that both the in-plane and the out-of-plane displacements vary with half-wavelength λ; however, it has been found that the in-plane displacement assumptions are not accurate enough to account for the stress redistribution phenomenon which occurs across the plate in the postbuckling stage. Due to this, VIPASA analysis loses some accuracy by assuming the stresses in each strip are longitudinally invariant. The Improved VIPASA analysis is proposed which takes into account the coupling between half-wavelengths λ and $\lambda/2$ of the in-plane displacement to work out the stresses and to solve the in-plane equilibrium equations. The improved analysis is found to be very efficient in addressing the inaccurate stress distribution issues in the VIPASA postbuckling analysis.

Validation examples have shown that the Improved VIPASA analysis is capable of predicting correct stress patterns at the postbuckling stage. Comparison of results from the improved method and finite element analysis for the variation patterns of stress resultants N_x and N_y show a good agreement. The ability of the proposed method to accurately and efficiently analyse composite plates has been demonstrated on three examples of layups with increasing anisotropy. Additionally, the skewed mode associated with different composite layups has been shown to be accurately captured by the proposed method. It is anticipated that the Improved VIPASA analysis can be implemented into the VICONOPT software as a subroutine to enhance its postbuckling analysis function.

Further development of the Improved method reveals that some adjustments are needed to make it robust enough to analyse more realistic structural components with added geometric complexity. By changing the continuity and equilibrium equations in the Improved VIPASA analysis, results based on a two-plate joined model demonstrate the

same level of continuity as single plate results. By adjusting the finite difference arrangements, stiffened plate postbuckling problems can be solved. Good correlation with ABAQUS stress contours demonstrate the Improved VIPASA analysis can solve the multi-plate joined postbuckling problems and has the potential to be further expanded.

8.3 Future work

The following describes potential work that can be considered in the future:

- The calculation of postbuckling strain and stiffness in the Simulated VICON analysis still relies on postbuckling results from an initial VIPASA analysis which is known to be conservative. The VICON out-of-plane displacement is not considered and therefore the load-deflection curves cannot be generated by using the Simulated VICON analysis. However, the out-of-plane displacement and mode shape depend on the coupling of different wavelengths. It is worth extracting all of the mode shapes corresponding to different wave length and working out a methodology to allow them to be coupled together to find the most appropriate out-of-plane displacements so that the postbuckling analysis can be carried out based fully on the VICON type of analysis.
- It was found that the discrepancy between the Improved VIPASA analysis and ABAQUS in predicting the stress values starts to grow when it comes to later postbuckling stages, which is primarily due to the difference in the out-of-plane displacement values in the two analyses. It is believed that the VIPASA out-of-plane assumptions are over-simplified. Future work may explore a more comprehensive assumption of the out-of-plane displacement and solve the in-plane and out-of-plane governing equations together.

- The discontinuity issues identified in the stiffened panel example are partially solved by changing the finite difference expressions. This solution is too specific to be applied to other models. Therefore, more research is needed to find a more comprehensive solution. It is believed that the general cause of the discontinuity is related to the different half-wavelength terms used in Equations 5.7 and 5.9, causing some zero terms to appear in Equation 7.5. One possible direction is to develop a general junction strip which assumes both the in-plane and out-of-plane displacements vary with the same number half-wavelengths (i.e. λ and $\lambda/2$) along the longitudinal direction.

References

Abramovich, H. Weller, T. and Bisagni, C. 2008. Buckling behavior of composite laminated stiffened panels under combined shear-axial compression. *Journal of Aircraft* 45(2), pp. 402–413.

Airbus 2012. Airbus in Illescas delivers first A350 XWB Wing Lower Cover to Airbus in Broughton [Online] Available at: https://www.airbus.com/newsroom/press-releases/en/2011/09/airbus-in-illescas-delivers-first-a350-xwb-wing-lower-cover-to-airbus-in-broughton.html [Accessed: 18 September 2018].

Airbus 2016. The A350 XWB "MSN1" forward fuselage takes shape [Online] Available at: https://www.airbus.com/newsroom/news/en/2011/09/the-a350-xwb-msn1-forward-fuselage-takes-shape.html [Accessed: 18 September 2018].

Aliabadi, M.H. and Baiz, P.M. 2008. The boundary element method for buckling and postbuckling analysis of plates and shells. In: *Buckling and Postbuckling Structures: Experimental, Analytical and Numerical Studies*. World Scientific, pp. 375–412.

Almroth, B.O. Brogan, F.A Stanley, G.M. 1981. *Structural analysis of general shells.* Volume 2: User instructions for STAGSC-1.

Amazigo, J.C. and Hutchinson, J.W. 1967. Imperfection-sensitivity of eccentrically stiffened cylindrical shells. *AIAA Journal* 5(3), pp. 392–401.

Ambart͡sumi͡an, S.A. 1970. *Theory of anisotropic plates: strength, stability, vibration*. Technomic Publishing Company.

Anderson, M. and Kennedy, D. 1993. Transverse shear deformation in exact buckling and vibration of composite plate assemblies. *AIAA Journal*, 31(10), pp.1963-1965.

Anderson, M. and Kennedy, D. 2008. Postbuckling of composite stiffened panels using exact strip analysis with Newton iteration. *Proceeding of 49th AIAA/ASME/ASCE/AHS/ASC Structures, Structural Dynamics, and Materials Conference,* Schaumburg, USA, Paper AIAA-2008-2184

Anderson, M.S. Williams, F W and Wright, C J. 1983. Buckling and vibration of any prismatic assembly of shear and compression loaded anisotropic plates with an arbitrary supporting structure. *International Journal of Mechanical Sciences* 25(8), pp. 585–596.

Barsoum, R.S. and Gallagher, R.H. 1970. Finite element analysis of torsional and torsional–flexural stability problems. *International Journal for Numerical Methods in Engineering* 2(3), pp. 335–352.

Belytschko, T. Liu, W.K. Moran, B. and Elkhodary, K. 2013. *Nonlinear finite elements for continua and structures*. John wiley & sons.

Bisagni, C. 2008. Buckling and Postbuckling Tests on Stiffened Composite Panels and Shells. In: *Buckling and Postbuckling Structures: Experimental, Analytical and Numerical Studies*. World Scientific, pp. 39–64.

Bisagni, C. and Vescovini, R. 2009. Analytical formulation for local buckling and post-buckling analysis of stiffened laminated panels. *Thin-Walled Structures* 47(3), pp. 318–334.

Bryan, G.H. 1890. On the stability of a plane plate under thrusts in its own plane, with applications to the "Buckling" of the sides of a ship. *Proceedings of the London Mathematical Society* 1(1), pp. 54–67.

Budiansky, B. 1966. Dynamic buckling of elastic structures: criteria and estimates. *Dynamic stability of structures*, pp. 83–106.

Budiansky, B. 1974. Theory of buckling and post-buckling behavior of elastic structures. *Advances in Applied Mechanics* 14, pp. 1–65.

Budiansky, B. and Hutchinson, J.W. 1966. Dynamic buckling of imperfection-sensitive structures. In: *Applied Mechanics*. Springer, pp. 636–651.

Bulson, P.S. 1969. *The stability of flat plates*. Elsevier Publishing Company.

Bushnell, D. Almroth, B.O. Brogan, F. 1971. Finite-difference energy method for nonlinear shell analysis. *Computers and Structures* 1(3), pp. 361–387.

Butler, R. and Williams, F.W. 1992. Optimum design using VICONOPT, a buckling and strength constraint program for prismatic assemblies of anisotropic plates. *Computers and Structures* 43(4), pp. 699–708.

Byskov, E. 2013. Budiansky-Hutchinson Notation. In: *Elementary Continuum Mechanics for Everyone. Solid Mechanics and Its Applications*. Springer, Dordrecht.

Byskov, E. and Hutchinson, W. 1977. Mode interaction in axially stiffened cylindrical shells. *AIAA Journal* 15(7), pp. 941–948.

Chajes, A. 1974. *Principles of Structural Stability Theory*. Prentice Hall.

Chapra, S.C. and Canale, R.P. 1998. *Numerical methods for engineers*. Mcgraw-hill New York.

Cheung, Y.K. 1976. *Finite Strip Method in structural analysis*. Oxford: Oxford : Pergamon Press.

Chia, C.Y. and Prabhakara, M.K. 1974. Postbuckling behavior of unsymmetrically layered anisotropic rectangular plates. *Journal of Applied Mechanics* 41(1), pp. 155–162.

Chin, C-K. Al-Bermani, F.G.A. and Kitipornchai, S. 1993. Finite element method for buckling analysis of plate structures. *Journal of Structural Engineering* 119(4), pp. 1048–1068.

Coan, J.M. 1951. Large-deflection theory for plates with small initial curvature loaded in edge compression. *Journal of Applied Mechanics-Transactions of the ASME* 18(2), pp. 143–151.

Coburn, B.H. and Weaver, P.M., 2016. Buckling analysis, design and optimisation of variable-stiffness sandwich panels. *International Journal of Solids and Structures*, 96, pp.217-228.

Cochelin, B. Damil, N. Potier-Ferry, M. 1994. Asymptotic–numerical methods and Pade approximants for non-linear elastic structures. *International Journal for Numerical Methods in Engineering* 37(7), pp. 1187–1213.

Cook, R.D. 1994. *Finite element modeling for stress analysis*. Wiley.

Cook, R.D. 2007. *Concepts and applications of finite element analysis*. John Wiley & Sons.

Cox, H.L. 1933. Buckling of thin plates in compression. *R. & M* 1554(2).

Dawe, D.J. Lam, S.S.E. Azizian, Z.G. 1993. Finite strip post-local-buckling analysis of composite prismatic plate structures. *Computers and Structures* 48(6), pp. 1011–1023.

Dawe, D.J. 2002. Use of the finite strip method in predicting the behaviour of composite laminated structures. *Composite Structures* 57(1–4), pp. 11–36.

Dawe, D.J. and Wang, S. 1998. Postbuckling analysis of thin rectangular laminated plates by

spline FSM. *Thin Walled Structures* 30(1), pp. 159–180.

Diaconu, C.G. and Weaver, P.M. 2005. Approximate solution and optimum design of compression-loaded, postbuckled laminated composite plates. *AIAA Journal* 43(4), pp. 906–914.

Diaconu, C.G. and Weaver, P.M. 2006. Postbuckling of long unsymmetrically laminated composite plates under axial compression. *International Journal of Solids and Structures* 43(22), pp. 6978–6997.

Duberg, J.E. 1950. Column behavior in the plastic stress range. *Journal of the Aeronautical Sciences* 17(6), pp. 323–327.

Engesser, F. 1891. *Die knickfestigkeit gerader stäbe*. W. Ernst & Sohn.

Euler, L. 1759. Sur la force des colonnes. *Memoires de L'Academie des Sciences et Belles-Lettres* 13, pp. 252–282.

Falzon, B.G. Stevens, K.A and Davies, G.O. 2000. Postbuckling behaviour of a blade-stiffened composite panel loaded in uniaxial compression. *Composites Part A: Applied Science and Manufacturing* 31(5), pp. 459–468.

Falzon, B.G. and Cerini, M. 2006. An automated hybrid procedure for capturing mode-jumping in postbuckling composite stiffened structures. *Composite Structures* 73(2), pp. 186–195.

Falzon, B.G. and Cerini, M. 2007. A study of secondary instabilities in postbuckling composite aerostructures. *The Aeronautical Journal* 111(1125), pp. 715–729.

Feng, M. 1983. An energy theory for postbuckling of composite plates under combined loading. *Computers and Structures* 16(1–4), pp. 423–431.

Fischer, M. Kennedy, D. and Featherson, C. 2002. Multilevel optimization of a composite aircraft wing using Viconopt MLO. Proceeding of *9th AIAA/ISSMO Symposium on Multidisciplinary Analysis and Optimization*. Atlanta, GA,USA. p. 5511.

Fluent, A. 2009. Ansys Theory Guide 12.0. *Ansys Inc* 5(5).

Ghannadpour, S.A.M. Ovesy, H.R. and Zia-Dehkordi, E. 2015. Buckling and post-buckling behaviour of moderately thick plates using an exact finite strip. *Computers and Structures* 147, pp. 172–180.

Ghannadpour, S.A.M. and Ovesy, H.R. 2008. An exact finite strip for the calculation of relative post-buckling stiffness of I-section struts. *International Journal of Mechanical Sciences* 50(9), pp. 1354–1364.

Ghannadpour, S.A.M. and Ovesy, H.R. 2009. The application of an exact finite strip to the buckling of symmetrically laminated composite rectangular plates and prismatic plate structures. *Composite Structures* 89(1), pp. 151–158.

Gibson, R.F. 2011. *Principles of composite material mechanics*. CRC press.

Harris, G.Z. 1975. The buckling and post-buckling behaviour of composite plates under biaxial loading. *International Journal of Mechanical Sciences* 17(3), pp. 187–202.

Hunt, G.W. Da Silva, L.S. and Manzocchi, G.M.E 1988. Interactive buckling in sandwich structures. In: *Proceedings of the Royal Society of London A: Mathematical, Physical and Engineering Sciences*. The Royal Society, pp. 155–177.

Hunt, G.W. and Wadee, M.A. 1998. Localization and mode interaction in sandwich structures. In: *Proceedings of the Royal Society of London A: Mathematical, Physical and Engineering Sciences*. The Royal Society, pp. 1197–1216.

Hutchinson, J.W. and Koiter, W.T. 1970. Postbuckling theory. *Appl. Mech. Rev* 23(12), pp. 1353–1366.

International Air Transport Association (IATA) Fact Sheet, IATA Organisation, accessed 11 January 2019, < https://www.iata.org/policy/environment/Pages/climate-change.aspx >

Jaeger, L.G. 2013. *Elementary Theory of Elastic Plates: The Commonwealth and International Library: Structures and Solid Body Mechanics Division*. Elsevier.

enkinson, L.R. Simpkin, P. Rhodes, D. Jenkison, L.R. and Royce, R., 1999. Civil Jet Aircraft Design (Vol. 338). London: Arnold.

Kennedy, D. Ong, T.J. O'Leary, O.J. and Williams, F.W. 1999. Practical optimisation of aerospace panels. *Proceedings of the 1st ASMO UK/ISSMO Conference, Ilkley*.UK, MCB University Press Bradford, pp. 217–224.

Koiter, W.T. 1945. Over de stabiliteit van het elastisch evenwicht. Polytechnic Institute of Delft, Delft.

Koiter, W.T. and Pignataro, M. 1976. *An alternative approach to the interaction between*

local and overall buckling in stiffened panels. In Buckling of structures (pp. 133-148). Springer, Berlin, Heidelberg.

Kromm, A. and Marguerre, K. 1938. *Behavior of a plate strip under shear and compressive stresses beyond the buckling limit*. NASA Technical Report, NASA-TP-2215

Lagace, P.A. Jensen, D.W. Finch, D.C. 1986. Buckling of unsymmetric composite laminates. *Composite Structures* 5(2), pp. 101–123.

Lekhnitskii, S.G. 1968. *Anisotropic plates*. Foreign Technology Div Wright-Patterson AFB

Lentini, M. and Pereyra, V. 1977. An adaptive finite difference solver for nonlinear two-point boundary problems with mild boundary layers. *SIAM Journal on Numerical Analysis* 14(1), pp. 91–111.

Levy, S. 1942. Bending of rectangular plates with large deflections. *NACA Technical Note 846*, pp. 1–46.

Loughlan, J. and Hussain, N. 2014. The in-plane shear failure of transversely stiffened thin plates. *Thin-Walled Structures* 81, pp. 225–235.

Lynch, C. Murphy, A. Price, M. and Gibson, A. 2004. The computational post buckling analysis of fuselage stiffened panels loaded in compression. *Thin-Walled Structures* 42(10), pp. 1445–1464.

MacNeal, R.H. 1970. *The NASTRAN theoretical manual*. Scientific and Technical Information Office, National Aeronautics and Space Administration.

Marguerre, K. and Trefftz, E. 1937. Über die Tragfähigkeit eines längsbelasteten Plattenstreifens nach Überschreiten der Beullast. *ZAMM-Journal of Applied Mathematics and Mechanics/Zeitschrift für Angewandte Mathematik und Mechanik* 17(2), pp. 85–100.

Megson, T.H.G. 2012. *Aircraft structures for engineering students*. Elsevier.

O'Leary, O.J. 2000. Optimisation of prismatic plate structures with natural frequency constraints, PhD thesis, Cardiff University

O'Leary, O.J. Williams, F.W. and Kennedy, D. 2001. Optimum stiffened panel design with fundamental frequency constraint. *Thin-walled structures* 39(7), pp. 555–569.

Olesen, J.F. and Byskov, E. 1982. Accurate determination of asymptotic postbuckling stresses by the finite element method. *Computers and Structures* 15(2), pp. 157–163.

Ovesy, H.R. Loughlan, J. and Ghannadpour, S.A.M. 2005. Geometric non-linear analysis of thin flat plates under end shortening, using different versions of the finite strip method. *International Journal of Mechanical Sciences* 47(12), pp. 1923–1948.

Ovesy, H.R. Loughlan, J. Ghannadpour, S.A.M. and Morada, G.. 2006. Geometric non-linear analysis of box sections under end shortening, using three different versions of the finite-strip method. *Thin-walled Structures* 44(6), pp. 623–637.

Ovesy, H.R. Loughlan, J. and Ghannadpour, S.A.M. 2006. Geometric non-linear analysis of channel sections under end shortening, using different versions of the finite strip method. *Computers and Structures* 84(13–14), pp. 855–872.

Ovesy, H.R. and Ghannadpour, S.A.M. 2009. An exact finite strip for the calculation of relative post-buckling stiffness of isotropic plates. *Structural Engineering and Mechanics* 31(2), pp. 181–210.

Pevzner, P. Abramovich, H and Weller, T. 2008. Calculation of the collapse load of an axially compressed laminated composite stringer-stiffened curved panel–An engineering approach. *Composite Structures* 83(4), pp. 341–353.

Powell, S.M. Powell, S.M. Williams, F.W Askar, A.S. and Kennedy, D. 1998. Local postbuckling analysis for perfect and imperfect longitudinally compressed plates and panels. *Porceeding of AIAA/ASME/ASCE/AHS/ASC Structures, Structural Dynamics and Materials Conference*. pp. 595–603. Long Beach, CA, USA.

Prabhakara, M.K. and Chia, C.Y. 1973. Post-buckling behaviour of rectangular orthotropic plates. *Journal of Mechanical Engineering Science* 15(1), pp. 25–33.

Przemieniecki, J.S. 1968. *Theory of matrix structural analysis*. McGraw-Hill .

Qatu, M.S. and Leissa, A.W. 1993. Buckling or transverse deflections of unsymmetrically laminated plates subjected to in-plane loads. *AIAA Journal* 31(1), pp. 189–194.

Qu, S. 2011. Multilevel optimisation of aerospace and lightweight structures incorporating postbuckling effects. PhD thesis, Cardiff University.

Raju, G. Wu, Z. Kim, B.C. and Weaver, P. 2012. Prebuckling and buckling analysis of variable angle tow plates with general boundary conditions. *Composite Structures* 94(9), pp. 2961–2970.

Reddy, J.N. 2006. *Theory and analysis of elastic plates and shells*. CRC press.

Reissner, E. and Stavsky, Y. 1961. Bending and stretching of certain types of heterogeneous aeolotropic elastic plates. *Journal of Applied Mechanics* 28(3), pp. 402–408.

Riks, E. 1979. An incremental approach to the solution of snapping and buckling problems. *International Journal of Solids and Structures* 15(7), pp. 529–551.

Salvadori, M.G. 1951. Numerical computation of buckling loads by finite differences. *Transactions of the American Society of Civil Engineers* 116(1), pp. 590–624.

Samir, A.-S. and Al-Rawi, R.A.O. 2006. Finite difference scheme for large-deflection analysis of non-prismatic cantilever beams subjected to different types of continuous and discontinuous loadings. *Archive of Applied Mechanics* 75(8–9), pp. 459–473.

Sewell, M.J. 1965. The static perturbation technique in buckling problems. *Journal of the Mechanics and Physics of Solids* 13(4), pp. 247–265.

Sewell, M.J. 1969. A method of post-buckling analysis. *Journal of the Mechanics and Physics of Solids* 17(4), pp. 219–233.

Shen, H.S., Xiang, Y., Lin, F. and Hui, D., 2017. Buckling and postbuckling of functionally graded graphene-reinforced composite laminated plates in thermal environments. *Composites Part B: Engineering*, 119, pp.67-78.

Shanley, F.R. 1947. Inelastic column theory. *Journal of the Aeronautical Sciences* 14(5), pp. 261–268.

Shiau, L.-C. and Wu, T.-Y. 1995. Application of the finite element method to postbuckling analysis of laminated plates. *AIAA Journal* 33(12), pp. 2379–2385.

Shin, D.K. Griffin, O.H. and Gürdal, Z. 1993. Postbuckling response of laminated plates under uniaxial compression. *International Journal of Non-linear Mechanics* 28(1), pp. 95–115.

Singer, J. Arbocz, J. Weller, T. and Cheney, J.A. 2008. *Buckling Experiments: Experimental Methods in Buckling of Thin-Walled Structures. Shells, Built-up Structures, Composites and Additional Topics, Volume 2*. John Wiley & Sons.

Smith, I.M. Griffiths, D.V. Margetts, L. 2013. *Programming the finite element method*. John Wiley & Sons.

Smith, M. 2009. *ABAQUS/Standard User's Manual, Version 6.9*. Providence, RI: Simulia.

Steen, E. 1998. Application of the perturbation method to plate buckling problems. *Preprint series. Research Report in Mechanics* NBN: no-23419.

Stein, M. 1959a. Loads and deformations of buckled rectangular plates. *PhD Dissertation*, NASA (19980235521).

Stein, M. 1959b. The phenomenon of change in buckle pattern in elastic structures. *NASA Technical Report*, NASA (19980228195).

Stein, M. 1983. Postbuckling of orthotropic composite plates loaded in compression. *AIAA Journal* 21(12), pp. 1729–1735.

Stein, M. 1985. Postbuckling of long orthotropic plates in combined shear and compression. *AIAA Journal* 23(5), pp. 788–794.

Stroud, W.J. Greene, W.H. and Anderson, M.S. 1984. Buckling loads of stiffened panels subjected to combined longitudinal compression and shear: results obtained with PASCO, EAL, and STAGS computer programs. *NASA Technical Report*, NASA-TP-2215.

Supple, W.J. 1970. Changes of wave-form of plates in the post-buckling range. *International Journal of Solids and Structures* 6(9), pp. 1243–1258.

Thompson, J.M.T. 1963. Basic principles in the general theory of elastic stability. *Journal of the Mechanics and Physics of Solids* 11(1), pp. 13–20.

Thompson, J.M.T. 1969. A general theory for the equilibrium and stability of discrete conservative systems. *Zeitschrift für Angewandte Mathematik und Physik (ZAMP)* 20(6), pp. 797–846.

Thompson, J.M.T. and Hunt, G.W. 1973. *A general theory of elastic stability*. Wiley.

Thompson, J.M.T. and Hunt, G.W. 1984. *Elastic instability phenomena*. Wiley Chichester.

Timoshenko, S.P. 1936. *Theory of Elastic Stability, by S. Timoshenko...* McGraw-Hill Book Company, Incorporated.

Timoshenko, S.P. and Woinowsky-Krieger, S. 1959. *Theory of plates and shells*. McGraw-Hill.

Turvey, G.J. and Wittrick, W.H. 1973. The large deflection and post-buckling behaviour of

some laminated plates. *The Aeronautical Quarterly* 24(2), pp. 77–86.

Van der Neut, A. 1969. The interaction of local buckling and column failure of thin-walled compression members. In: *Applied Mechanics*. Springer, pp. 389–399.

Van der Plaats, G.N. 1973. CONMIN: a Fortran program for constrained function minimization: user's manual.

Vannucci, P. Cochelin, B. Damil,N. and Potier-Ferry, M. 1998. An asymptotic-numerical method to compute bifurcating branches. *International Journal for Numerical Methods in Engineering* 41(8), pp. 1365–1389.

Vescovini, R. and Bisagni, C. 2016. Fast analysis of non-symmetric panels using semi-analytical techniques. *Composites Part B: Engineering* 99, pp. 48–62.

Viswanathan, A.V. Tamekuni, M. and Baker, L. L. 1974. Elastic stability of laminated, flat and curved, long rectangular plates subjected to combined inplane loads. *NASA Technical Report, NASA-CR-2330*

Viswanathan, A. V and Tamekuni, M. 1973. Elastic buckling analysis for composite stiffened panels and other structures subjected to biaxial inplane loads. *NASA Technical Report, NASA-CR-2216*

Von Kármán, T. 1932. The strength of thin plates in compression. *Trans. ASME* 54(2), p. 53.

Von Kármán, T. 1910. *Festigkeitsprobleme im maschinenbau*. Teubner.

Wang, S. and Dawe, D.J. 1996. Finite strip large deflection and post-overall-buckling analysis of diaphragm-supported plate structures. *Computers and Structures* 61(1), pp. 155–170.

Watson, A. and Kennedy, D. 2004. Mode jumping in post-buckled stiffened panels. In: *Proceedings of 4th International Conference on Thin Walled Structures, Loughborough, UK.*

Whitney, J.M. and Leissa, A.W. 1969. Analysis of heterogeneous anisotropic plates. *Journal of Applied Mechanics* 36(2), pp. 261–266.

Williams, F.W. Anderson, M.S. Kennedy, D. Butler, R. Aston, G. and Hoh, S.M. 1990. User manual for VICONOPT: An exact analysis and optimum design program covering the buckling and vibration of prismatic assemblies of flat in-plane loaded, anisotropic plates, with approximations for discrete supports, and transverse stiffeners, Cardiff University

Williams, F.W. Kennedy, D. Anderson, M.S and Butler, R. 1991. VICONOPT: Program for exact vibration and buckling analysis or design of prismatic plate assemblies. *AIAA Journal* 29(11), pp. 1927–1928.

Williams, F.W. and Anderson, M.S. 1983. Incorporation of Lagrangian multipliers into an algorithm for finding exact natural frequencies or critical buckling loads. *International Journal of Mechanical Sciences* 25(8), pp. 579–584.

Williams, F.W. and Anderson, M.S. 1983. Incorporation of Lagrangian Multipliers into an algorithm for finding exact natural frequencies or critical buckling loads. *International Journal of Mechanical Sciences* 25(8), pp. 579–584.

Williams, F.W. and Anderson, M.S. 1985. Buckling and vibration analysis of shear-loaded prismatic plate assemblies with supporting structures, utilizing symmetric or repetitive cross-sections. *Aspects of the analysis of plate structures—a volume in honour of WH Wittrick*, pp. 51–77. Oxford University Press, USA.

Williams, F.W. and Wittrick, W.H. 1970. An automatic computational procedure for calculating natural frequencies of skeletal structures. *International Journal of Mechanical Sciences* 12(9), pp. 781–791.

Wittrick, W.H. 1968a. A unified approach to the initial buckling of stiffened panels in compression. *The Aeronautical Quarterly* 19(3), pp. 265–283.

Wittrick, W.H. 1968b. General sinusoidal stiffness matrices for buckling and vibration analyses of thin flat-walled structures. *International Journal of Mechanical Sciences* 10(12), pp. 949–966.

Wittrick, W.H. and Curzon, P.L. V 1968. Stability functions for the local buckling of thin flat-walled structures with the walls in combined shear and compression. *The Aeronautical Quarterly* 19(4), pp. 327–351.

Wittrick, W.H. and Horsington, R.W. 1984. Buckling and vibration of composite folded-plate structures of finite length in combined shear and compression. *Proceedings of the Royal Society of London A* 392(1802), pp. 107–144.

Wittrick, W.H. and Williams, F.W. 1974. Buckling and vibration of anisotropic or isotropic plate assemblies under combined loadings. *International Journal of Mechanical Sciences* 16(4), pp. 209–239.

Wittrick, W.H. and Williams, F.W. 1973. An algorithm for computing critical buckling loads of elastic structures. *Journal of Structural Mechanics* 1(4), pp. 497–518.

Wu, T.L., Shukla, K.K. and Huang, J.H., 2007. Post-buckling analysis of functionally graded rectangular plates. *Composite structures, 81*(1), pp.1-10.

Wu, Z. Raju, G and Weaver, P. 2012. Buckling of VAT plates using energy methods. In: *53rd AIAA/ASME/ASCE/AHS/ASC Structures, Structural Dynamics and Materials Conference* Honolulu, Hawaii

Wu, Z. Raju, G and Weaver, P. 2013. Postbuckling analysis of variable angle tow composite plates. *International Journal of Solids and Structures* 50(10), pp. 1770–1780.

Yamaki, N. 1960. Postbuckling behavior of rectangular plates with small initial curvature loaded in edge compression—(continued). *Journal of Applied Mechanics* 27(2), pp. 335–342.

York, C.B. 2009. Characterization of nonsymmetric forms of fully orthotropic laminates. *Journal of Aircraft* 46(4), pp. 1114–1125.

Yusuff, S. 1952. *Large deflection theory for orthotropic rectangular plates subjected to edge compression*.

Zienkiewicz, O.C. 2005. *The finite element method for solid and structural mechanics*. Elsevier.

Appendix

Appendix A

Derivation of the plate bending and buckling governing equations.

According to Figure 2.3, the bending strains at a distance z below the neutral plane are

$$\varepsilon_x = \frac{z}{\rho_x} \tag{A1}$$

$$\varepsilon_y = \frac{z}{\rho_y} \tag{A2}$$

By Hooke's law

$$\varepsilon_x = \frac{1}{E}(\sigma_x - \nu\sigma_y) \tag{A3}$$

$$\varepsilon_y = \frac{1}{E}(\sigma_y - \nu\sigma_x) \tag{A4}$$

Substituting for ε_x and ε_y from Equations (A1) and (A2) into Equations (A3) and (A4), and rearranging gives

$$\sigma_x = \frac{Ez}{1-\nu^2}\left(\frac{1}{\rho_x} + \frac{\nu}{\rho_y}\right) \tag{A5}$$

$$\sigma_y = \frac{Ez}{1-\nu^2}\left(\frac{1}{\rho_y} + \frac{\nu}{\rho_x}\right) \tag{A6}$$

The internal direct stress distribution on each vertical surface of the element must be in equilibrium with the applied bending moment. Thus

$$M_x \delta_y = \int_{-\frac{t}{2}}^{\frac{t}{2}} \sigma_x z \delta_y dz \tag{A7}$$

$$M_y \delta_x = \int_{-\frac{t}{2}}^{\frac{t}{2}} \sigma_y z \delta_x dz \tag{A8}$$

Substituting for σ_x and σ_y from Equations (A5) and (A6) into Equations (A7) and (A8), and integrating gives

$$M_x = D\left(\frac{1}{\rho_x} + \frac{\nu}{\rho_y}\right) \tag{A9}$$

$$M_y = D\left(\frac{1}{\rho_y} + \frac{\nu}{\rho_x}\right) \tag{A10}$$

where

$$D = \frac{Et^3}{12(1-\nu^2)} \tag{A11}$$

The curvature of the plate can be expressed in terms of the out-of-plane displacement w. Hence,

$$\frac{1}{\rho_x} = -\frac{\partial^2 w}{\partial x^2} \tag{A12}$$

$$\frac{1}{\rho_y} = -\frac{\partial^2 w}{\partial y^2} \tag{A13}$$

Equations (A9) and (A10) then become

$$M_x = -D\left(\frac{\partial^2 w}{\partial x^2} + \nu \frac{\partial^2 w}{\partial y^2}\right) \tag{A14}$$

$$M_y = -D\left(\frac{\partial^2 w}{\partial y^2} + \nu \frac{\partial^2 w}{\partial x^2}\right) \tag{A15}$$

More generally, if the bending and twisting effect is taken into consideration, the twisting moment can be expressed in a similar manner as

$$M_{xy} = D(1-v)\frac{\partial^2 w}{\partial x \partial y} \tag{A16}$$

The in-plane equilibrium equations can be obtained by considering a small element $\delta x \delta y$ of the middle plane of a thin deflected plate which is subjected to the in-plane forces indicated in Figure A.1. Direct and shear forces per unit length produced by the in-plane loads are giving the notation N_x, N_y and N_{xy}.

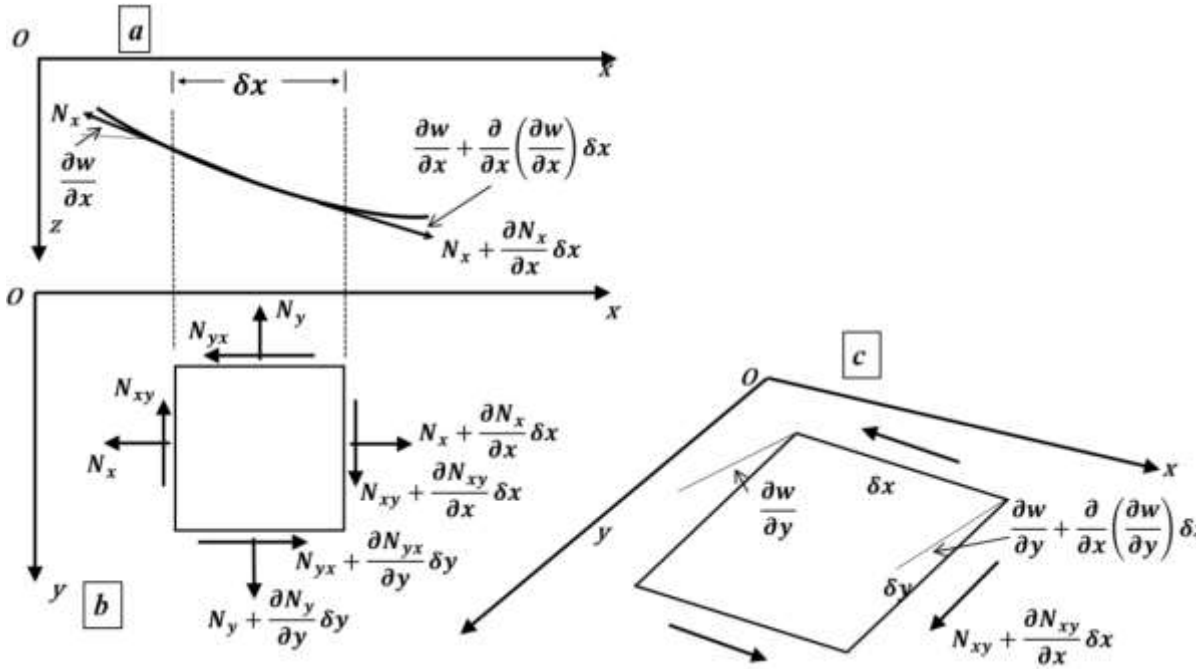

Figure 0.1 The elevation and plan of a small element δxδy of the middle plane of a thin deflected plate: (a) (b) in-plane force (N_x, N_y, N_{xy}) on the plate element and (c) component of shear load N_{xy} in the z direction. (Adapted from (Megson 2012; Chajes 1974))

The in-plane equilibrium in the x direction can be expressed as

$$\left(N_x + \frac{\partial N_x}{\partial x}\delta x\right)\delta y \cos\left(\frac{\partial w}{\partial x} + \frac{\partial^2 w}{\partial x^2}\delta x\right) - N_x \delta y \cos\frac{\partial w}{\partial x} + \left(N_{yx} + \frac{\partial N_{yx}}{\partial y}\delta y\right)\delta x - N_{yx}\delta x = 0 \tag{A17}$$

For small deflection, we can assume $\partial w/\partial x$ and $\partial w/\partial x + (\partial^2 w)/(\partial x^2)\,\delta x$ are small and the cosines of these angles are therefore approximately equal to one. The equilibrium thus simplifies to

$$\frac{\partial N_x}{\partial x} + \frac{\partial N_{yx}}{\partial y} = 0 \tag{A18}$$

Similarly, for equilibrium in the y direction

$$\frac{\partial N_y}{\partial y} + \frac{\partial N_{yx}}{\partial x} = 0 \tag{A19}$$

Referring to Figure A.1c. The component of N_{xy} in the z direction is

$$\left(N_{xy} + \frac{\partial N_{xy}}{\partial x}\delta x\right)\delta y\left(\frac{\partial w}{\partial y} + \frac{\partial^2 w}{\partial x \partial y}\delta x\right) - N_{xy}\delta y\frac{\partial w}{\partial y} \tag{A20}$$

Neglecting higher order terms, this expression can be reduced to

$$N_{xy}\frac{\partial^2 w}{\partial x \partial y}\delta x\delta y + \frac{\partial N_{yx}}{\partial x}\frac{\partial w}{\partial y}\delta x\delta y \tag{A21}$$

Similarly, the contribution of N_{yx} is

$$N_{yx}\frac{\partial^2 w}{\partial x \partial y}\delta x\delta y + \frac{\partial N_{yx}}{\partial y}\frac{\partial w}{\partial y}\delta x\delta y \tag{A22}$$

From Figure A.1a, the component of N_x in the z direction is equal to

$$\left(N_x + \frac{\partial N_x}{\partial x}\delta x\right)\delta y\left(\frac{\partial w}{\partial x} + \frac{\partial^2 w}{\partial x^2}\delta x\right) - N_x\delta y\frac{\partial w}{\partial x} \tag{A23}$$

This expression can be simplified to

$$N_x\frac{\partial^2 w}{\partial x^2}\,\delta x\delta y + \frac{\partial N_x}{\partial x}\frac{\partial w}{\partial x}\delta x\delta y \tag{A24}$$

Similarly, the component of N_y in the z direction is equal to

$$N_y\frac{\partial^2 w}{\partial y^2}\,\delta x\delta y + \frac{\partial N_y}{\partial y}\frac{\partial w}{\partial y}\delta x\delta y \tag{A25}$$

The total force in the z direction is obtained by adding these expressions together, thus,

$$\begin{aligned} &N_x\frac{\partial^2 w}{\partial x^2}\,\delta x\delta y + \frac{\partial N_x}{\partial x}\frac{\partial w}{\partial x}\delta x\delta y + N_y\frac{\partial^2 w}{\partial y^2}\,\delta x\delta y + \frac{\partial N_y}{\partial y}\frac{\partial w}{\partial y}\delta x\delta y \\ &+\frac{\partial N_{yx}}{\partial y}\frac{\partial w}{\partial y}\delta x\delta y + 2N_{xy}\frac{\partial^2 w}{\partial x \partial y}\delta x\delta y + \frac{\partial N_{yx}}{\partial y}\frac{\partial w}{\partial y}\delta x\delta y \end{aligned} \tag{A26}$$

Since N_{xy} is equal to N_{yx} and using Equations (A18-A19), this expression can be reduced to

$$\left(N_x \frac{\partial^2 w}{\partial x^2} + N_y \frac{\partial^2 w}{\partial y^2} + 2N_{xy} \frac{\partial^2 w}{\partial x \partial y}\right) \delta x \delta y \tag{A27}$$

The equilibrium of the bending moment, twisting moment, and shears should also be considered. In addition to the in-plane forces shown in Figure A.1, an element of a slightly bent plate will have acting on it the moments and shears shown in Figure A.2.

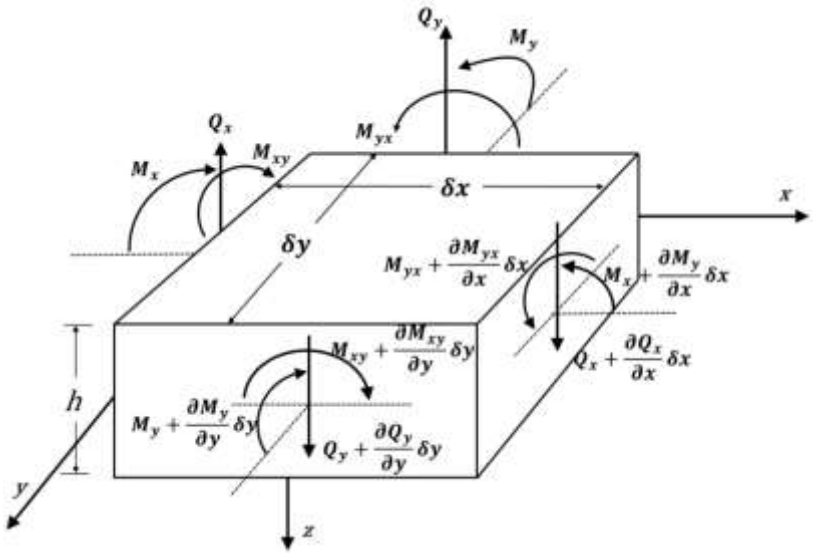

Figure 0.2 Plate element subjected to bending, twisting and transverse loads. (Adapted from (Megson 2012; Chajes 1974))

All forces and moments are considered positive when acting in the direction indicated. Components of the shear forces in the x and y direction are negligible, in the z direction, the component of shear force can be expressed as

$$\left(Q_x + \frac{\partial Q_x}{\partial x}\delta x\right)\delta y - Q_x \delta y + \left(Q_y + \frac{\partial Q_y}{\partial y}\delta y\right)\delta x - Q_y \delta x \tag{A28}$$

After simplification

$$\frac{\partial Q_x}{\partial x} + \frac{\partial Q_y}{\partial y} \tag{A29}$$

Taking moments about the x axis

$$M_{xy}\delta y - \left(M_{xy} + \frac{\partial M_{xy}}{\partial x}\delta x\right)\delta y - M_y \delta x + \left(M_y + \frac{\partial M_y}{\partial y}\delta y\right)\delta x$$
$$- \left(Q_y + \frac{\partial Q_y}{\partial y}\delta y\right)\delta x \delta y + Q_x \frac{\delta y^2}{2} - \left(Q_x + \frac{\partial Q_x}{\partial x}\delta x\right)\frac{\delta y^2}{2} = 0 \quad \text{(A30)}$$

Simplifying this equation and neglecting small quantities of a higher order gives

$$\frac{\partial M_{xy}}{\partial x} - \frac{\partial M_y}{\partial y} + Q_y = 0 \quad \text{(A31)}$$

Similarly taking moment about the y axis gives

$$\frac{\partial M_{xy}}{\partial y} - \frac{\partial M_x}{\partial x} + Q_x = 0 \quad \text{(A32)}$$

Differentiation of Equations (A31) and (A32) gives

$$\frac{\partial Q_x}{\partial x} = \frac{\partial^2 M_x}{\partial x^2} - \frac{\partial^2 M_{xy}}{\partial x \partial y} \quad \text{(A33)}$$

$$\frac{\partial Q_y}{\partial y} = \frac{\partial^2 M_y}{\partial y^2} - \frac{\partial^2 M_{xy}}{\partial x \partial y} \quad \text{(A34)}$$

Substituting Equations (A33), (A34) and (A29), and combining with Equation (A27), a single equation of equilibrium can be obtained, thus,

$$\frac{\partial^2 M_x}{\partial x^2} - 2\frac{\partial^2 M_{xy}}{\partial x \partial y} + \frac{\partial^2 M_y}{\partial y^2} + N_x \frac{\partial^2 w}{\partial x^2} + N_y \frac{\partial^2 w}{\partial y^2} + 2N_{xy}\frac{\partial^2 w}{\partial x \partial y} = 0 \quad \text{(A35)}$$

Substituting Equations (A14), (A15) and (A16) into Equation (A35) the differential equation of plate buckling can be obtained

$$D\left(\frac{\partial^4 w}{\partial x^4} + 2\frac{\partial^4 w}{\partial x^2 \partial y^2} + \frac{\partial^4 w}{\partial y^4}\right) = N_x \frac{\partial^2 w}{\partial x^2} + N_y \frac{\partial^2 w}{\partial y^2} + 2N_{xy}\frac{\partial^2 w}{\partial x \partial y} \quad \text{(A36)}$$

Appendix B

Derivation of the psotbuckling compatibility equations

Classical small deflection plate theory can lead to considerable overestimates of deflections and stresses in thin plates. The principal difference between small and large deflection theory is that small deflection theory assumes loads to be carried by bending action alone, whereas large deflection theory takes account of membrane forces that develop as a result of deflections. This key difference can be expressed in term of the strain-displacement equations. In large deflection theory, displacement comprise two components:

(1) The displacement due to bending

(2) Stretching of the middle surface of the plane due to out-of-plane deflections (i.e. the membrane displacement)

Considering an undeformed linear element AB on the middle surface along the x direction (shown in Figure A.3a), after bending, the deformed element A'B' is assumed to have changed length due to the two components described above. As a result of the in-plane displacement, the elongation of the element is

$$\frac{\partial u}{\partial x}dx \tag{B1}$$

The change in length of the element due to the w displacement is equal to the difference in length between the curved element A'B' and its projection on the horizontal plane.

The curved length is equal to

$$\int_0^L ds = \int_0^L \sqrt{1+\left(\frac{dw}{dx}\right)^2}\,dx \tag{B2}$$

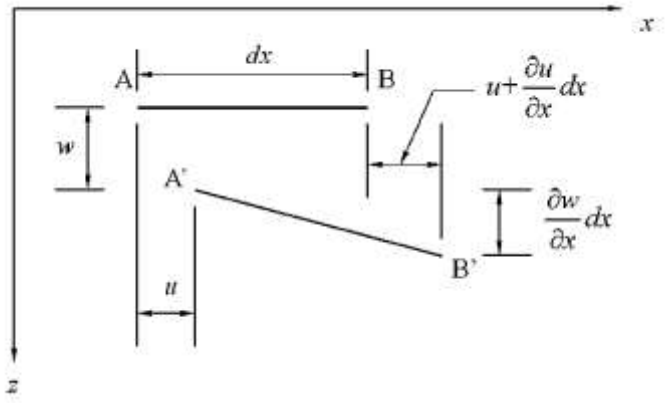

(a)

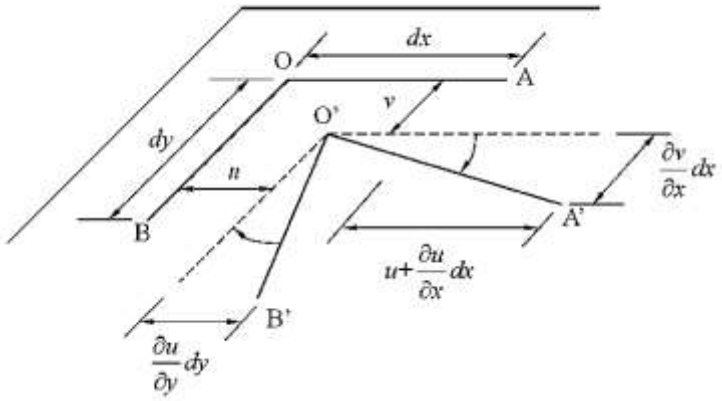

(b)

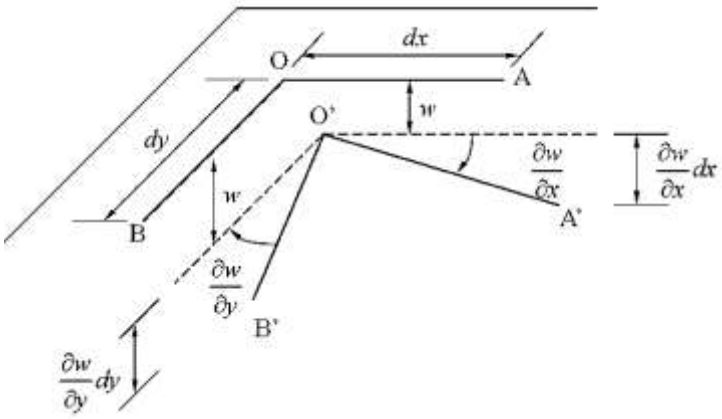

(c)

Figure 0.3 Strain in-plane under larger deflections: (a)axial strain, (b)shear strain due to in-plane displacement and (c)shear strain due to out-of-plane displacement (Adapted from (Chajes 1974))

The change in length of the element due to the out-of-displacement w is equal to

$$\frac{1}{2}\left(\frac{\partial w}{\partial x}\right)^2 dx \tag{B3}$$

Thus, the total strain in the x direction for an element on the middle surface is

$$\varepsilon_x = \frac{\partial u}{\partial x} + \frac{1}{2}\left(\frac{\partial w}{\partial x}\right)^2 \tag{B4}$$

Similarly, the total strain in the y direction for an element on the middle surface is

$$\varepsilon_y = \frac{\partial v}{\partial y} + \frac{1}{2}\left(\frac{\partial w}{\partial y}\right)^2 \tag{B5}$$

The shear strain can be represented by the change in angle between the two perpendicular lines, which is illustrated in Figures A.3b and A.3c. Similar to direct strain, the shear strain is comprised of components due to in-plane displacement and out-of-plane displacement, respectively. The shear strain due to the in-plane displacement u and v is

$$\frac{\partial u}{\partial y} + \frac{\partial v}{\partial x} \tag{B6}$$

The shear strain due to w is equal to

$$\gamma = \angle BOA - \angle B'O'A' \tag{B7}$$

Form the geometry, $B'A'$ can be expressed as

$$(B'A')^2 = (B'O')^2 + (O'A')^2 - 2(O'A')(B'O')\cos\left(\frac{\pi}{2} - \gamma\right)$$

Where

$$(O'A')^2 = (dx)^2 + \left(\frac{\partial w}{\partial x}dx\right)^2 \tag{B8}$$

$$(B'O')^2 = (dy)^2 + \left(\frac{\partial w}{\partial x}dy\right)^2 \tag{B9}$$

$$(B'A')^2 = (dx)^2 + (dy)^2 + \left(\frac{\partial w}{\partial x}dy - \frac{\partial w}{\partial x}dx\right)^2 \tag{B10}$$

Neglecting higher order terms gives

$$(O'A')(B'O') = dxdy \tag{B11}$$

For small angle $\cos\left(\frac{\pi}{2} - \gamma\right)$ is equal to γ, and the above equation can be reduced to

$$\gamma = \frac{\partial w}{\partial x}\frac{\partial w}{\partial y} \tag{B12}$$

Thus, the total shear strain is

$$\gamma_{xy} = \frac{\partial u}{\partial y} + \frac{\partial v}{\partial x} + \frac{\partial w}{\partial x}\frac{\partial w}{\partial y} \tag{B13}$$

Appendix C

Detailed calculations of Stein's power series method.

The details of transformation of von Karman equation by using power series.

$$N_x = \sum_{n=0,2}^{\infty} N_x^{(n)} \epsilon^n + \sum_{m=1,3}^{\infty} \sum_{n=1,3}^{\infty} N_x^{(mn)} \epsilon^{m+n} \tag{C1}$$

$$N_y = \sum_{n=0,2}^{\infty} N_y^{(n)} \epsilon^n + \sum_{m=1,3}^{\infty} \sum_{n=1,3}^{\infty} N_y^{(mn)} \epsilon^{m+n} \tag{C2}$$

$$N_{xy} = \sum_{n=0,2}^{\infty} N_{xy}^{(n)} \epsilon^n + \sum_{m=1,3}^{\infty} \sum_{n=1,3}^{\infty} N_{xy}^{(mn)} \epsilon^{m+n} \tag{C3}$$

where

$$N_x^{(n)} = \frac{Eh}{1-\nu^2}\left[\frac{\partial u^{(n)}}{\partial x} + \mu \frac{\partial v^{(n)}}{\partial y}\right] \tag{C4}$$

$$N_y^{(n)} = \frac{Eh}{1-\nu^2}\left[\frac{\partial v^{(n)}}{\partial y} + \mu \frac{\partial u^{(n)}}{\partial x}\right] \tag{C5}$$

$$N_{xy}^{(n)} = \frac{Eh}{2(1+\nu)}\left(\frac{\partial u^{(n)}}{\partial y} + \frac{\partial v^{(n)}}{\partial x}\right) \tag{C6}$$

$$N_x^{(mn)} = N_x^{(nm)} = \frac{Eh}{2(1-\nu^2)}\left(\frac{\partial w^{(m)}}{\partial x}\frac{\partial w^{(n)}}{\partial x} + \mu \frac{\partial w^{(m)}}{\partial y}\frac{\partial w^{(n)}}{\partial y}\right) \tag{C7}$$

$$N_y^{(mn)} = N_y^{(nm)} = \frac{Eh}{2(1-\nu^2)}\left(\frac{\partial w^{(m)}}{\partial y}\frac{\partial w^{(n)}}{\partial y} + \mu \frac{\partial w^{(m)}}{\partial x}\frac{\partial w^{(n)}}{\partial x}\right) \tag{C8}$$

$$N_{xy}^{(mn)} = \frac{Eh}{2(1+\nu)}\frac{\partial w^{(m)}}{\partial x}\frac{\partial w^{(n)}}{\partial y} \tag{C9}$$

Then, the von Karman large deflection equations are transformed to a series of homogeneous differential equations.

$$\begin{cases} \dfrac{\partial N_x^{(0)}}{\partial x}+\dfrac{\partial N_{xy}^{(0)}}{\partial y}=0 \\ \dfrac{\partial N_y^{(0)}}{\partial y}+\dfrac{\partial N_{xy}^{(0)}}{\partial x}=0 \\ D\nabla^4 w^1-\left(N_x^{(0)}\dfrac{\partial^2 w^{(1)}}{\partial x^2}+N_y^{(0)}\dfrac{\partial^2 w^{(1)}}{\partial y^2}+2N_{xy}^{(0)}\dfrac{\partial w^{(1)}}{\partial x}\dfrac{\partial w^{(1)}}{\partial y}\right)=0 \end{cases} \tag{C10}$$

$$\begin{cases} \dfrac{\partial N_x^{(2)}}{\partial x}+\dfrac{\partial N_{xy}^{(2)}}{\partial y}=-\left(\dfrac{\partial N_x^{(11)}}{\partial x}+\dfrac{\partial N_{xy}^{(11)}}{\partial y}\right) \\ \dfrac{\partial N_y^{(0)}}{\partial y}+\dfrac{\partial N_{xy}^{(0)}}{\partial x}=-\left(\dfrac{\partial N_y^{(11)}}{\partial y}+\dfrac{\partial N_{xy}^{(11)}}{\partial x}\right) \\ D\nabla^4 w^3-\left(N_x^{(0)}\dfrac{\partial^2 w^{(3)}}{\partial x^2}+N_y^{(0)}\dfrac{\partial^2 w^{(3)}}{\partial y^2}+2N_{xy}^{(0)}\dfrac{\partial w^{(3)}}{\partial x}\dfrac{\partial w^{(3)}}{\partial y}\right)= \\ \left(N_x^{(2)}+N_x^{(11)}\right)\dfrac{\partial^2 w^{(1)}}{\partial x^2}+ \\ \left(N_y^{(2)}+N_y^{(11)}\right)\dfrac{\partial^2 w^{(1)}}{\partial y^2}+\left(N_{xy}^{(2)}+N_{xy}^{(11)}\right)\dfrac{\partial w^{(1)}}{\partial x}\dfrac{\partial w^{(1)}}{\partial y} \end{cases} \tag{C11}$$

$$\begin{cases} \dfrac{\partial N_x^{(4)}}{\partial x}+\dfrac{\partial N_{xy}^{(4)}}{\partial y}=-\left(2\dfrac{\partial N_x^{(13)}}{\partial x}+\dfrac{\partial N_{xy}^{(13)}}{\partial y}+\dfrac{\partial N_{xy}^{(31)}}{\partial y}\right) \\ \dfrac{\partial N_y^{(4)}}{\partial y}+\dfrac{\partial N_{xy}^{(4)}}{\partial x}=-\left(2\dfrac{\partial N_y^{(13)}}{\partial y}+\dfrac{\partial N_{xy}^{(13)}}{\partial x}+\dfrac{\partial N_{xy}^{(31)}}{\partial x}\right) \\ D\nabla^4 w^5-\left(N_x^{(0)}\dfrac{\partial^2 w^{(5)}}{\partial x^2}+N_y^{(0)}\dfrac{\partial^2 w^{(5)}}{\partial y^2}+2N_{xy}^{(0)}\dfrac{\partial w^{(5)}}{\partial x}\dfrac{\partial w^{(5)}}{\partial y}\right)= \\ \left(N_x^{(2)}+N_x^{(11)}\right)\dfrac{\partial^2 w^{(3)}}{\partial x^2}+\left(N_y^{(2)}+N_y^{(11)}\right)\dfrac{\partial^2 w^{(3)}}{\partial y^2}+ \\ 2\left(N_{xy}^{(2)}+N_{xy}^{(11)}\right)\dfrac{\partial w^{(3)}}{\partial x}\dfrac{\partial w^{(3)}}{\partial y}+ \\ \left(N_x^{(4)}+2N_x^{(13)}\right)\dfrac{\partial^2 w^{(1)}}{\partial x^2}+\left(N_y^{(2)}+2N_y^{(13)}\right)\dfrac{\partial^2 w^{(1)}}{\partial y^2}+ \\ 2\left(N_{xy}^{(4)}+N_{xy}^{(13)}+N_{xy}^{(31)}\right)\dfrac{\partial w^{(1)}}{\partial x}\dfrac{\partial w^{(1)}}{\partial y} \end{cases} \tag{C12}$$

Appendix D

Detailed calculations of in-plane displacement, strain and stress resultants

The neutral surface strains and curvatures given by von Karman's large deflection theory are

$$\begin{bmatrix} \varepsilon_{xi} \\ \varepsilon_{yi} \\ \gamma_{xyi} \\ \kappa_{xi} \\ \kappa_{yi} \\ \kappa_{xyi} \end{bmatrix} = \begin{bmatrix} \frac{\partial u_i}{\partial x} + \frac{1}{2}\left(\frac{\partial w_i}{\partial x}\right)^2 \\ \frac{\partial v_i}{\partial y} + \frac{1}{2}\left(\frac{\partial w_i}{\partial y}\right)^2 \\ \frac{\partial u_i}{\partial y} + \frac{\partial v_i}{\partial x} + \frac{\partial w_i}{\partial x}\frac{\partial w_i}{\partial y} \\ -\frac{\partial^2 w_i}{\partial x^2} \\ -\frac{\partial^2 w_i}{\partial y^2} \\ -2\frac{\partial^2 w_i}{\partial x \partial y} \end{bmatrix} = \begin{bmatrix} \varepsilon_{xi0} & \varepsilon_{xic} & \varepsilon_{xis} & \varepsilon_{xiC} & \varepsilon_{xiS} \\ \varepsilon_{yi0} & \varepsilon_{yic} & \varepsilon_{yis} & \varepsilon_{yiC} & \varepsilon_{yiS} \\ \varepsilon_{xyi0} & \varepsilon_{xyic} & \varepsilon_{xyis} & \varepsilon_{xyiC} & \varepsilon_{xyiS} \\ \kappa_{xi0} & \kappa_{xic} & \kappa_{xis} & \kappa_{xiC} & \kappa_{xiS} \\ \kappa_{yi0} & \kappa_{yic} & \kappa_{yis} & \kappa_{yiC} & \kappa_{yiS} \\ \kappa_{xyi0} & \kappa_{xyic} & \kappa_{xyis} & \kappa_{xyiC} & \kappa_{xyiS} \end{bmatrix} \begin{bmatrix} 1 \\ \cos\frac{\pi x}{\lambda} \\ \sin\frac{\pi x}{\lambda} \\ \cos\frac{2\pi x}{\lambda} \\ \sin\frac{2\pi x}{\lambda} \end{bmatrix} \quad \text{(D1)}$$

Substituting from Equation (5.4-5.6) into Equation (D1) gives the following expressions:

$$\boldsymbol{\varepsilon}_i = \boldsymbol{\varepsilon}_0(\mathrm{w}_i, \psi_i) + \frac{1}{b}\boldsymbol{\varepsilon}_1 \mathbf{u}_i + \boldsymbol{\varepsilon}_2 \mathbf{u}_i' \quad \text{(D2)}$$

$$\boldsymbol{\kappa}_i = \boldsymbol{\kappa}_0(\mathrm{w}_i, \psi_i) \quad \text{(D3)}$$

where,

$$\boldsymbol{\varepsilon}_i = \left[\varepsilon_{xi0}\ \varepsilon_{xic}\ \varepsilon_{xis}\ \varepsilon_{xiC}\ \varepsilon_{xiS}\ \varepsilon_{yi0}\ \varepsilon_{yic}\ \varepsilon_{yis}\ \varepsilon_{yiC}\ \varepsilon_{yiS}\ \varepsilon_{xyi0}\ \varepsilon_{xyic}\ \varepsilon_{xyis}\ \varepsilon_{xyiC}\ \varepsilon_{xyiS}\right]^T \quad \text{(D4)}$$

$$\boldsymbol{\kappa}_i = \left[\kappa_{xi0}\ \kappa_{xic}\ \kappa_{xis}\ \kappa_{xiC}\ \kappa_{xiS}\ \kappa_{yi0}\ \kappa_{yic}\ \kappa_{yis}\ \kappa_{yiC}\ \kappa_{yiS}\ \kappa_{xyi0}\ \kappa_{xyic}\ \kappa_{xyis}\ \kappa_{xyiC}\ \kappa_{xyiS}\right]^T \quad \text{(D5)}$$

$$\boldsymbol{\varepsilon}_0(\mathrm{w}_i,\psi_i)=\begin{bmatrix}-\bar{\varepsilon}_x+\frac{\pi^2}{4\lambda^2}(w_{ic}^2+w_{is}^2)\\0\\0\\\frac{\pi^2}{4\lambda^2}(w_{is}^2-w_{ic}^2)\\-\frac{\pi^2}{2\lambda^2}w_{ic}w_{is}\\\frac{1}{4}(\psi_{ic}^2+\psi_{is}^2)\\0\\0\\\frac{1}{4}(\psi_{ic}^2-\psi_{is}^2)\\\frac{1}{2}\psi_{ic}\psi_{is}\\\frac{\pi}{2\lambda}(w_{is}\psi_{ic}-w_{ic}\psi_{is})\\0\\0\\\frac{\pi}{2\lambda}(w_{is}\psi_{ic}+w_{ic}\psi_{is})\\\frac{\pi}{2\lambda}(w_{is}\psi_{is}-w_{ic}\psi_{ic})\end{bmatrix}\quad\boldsymbol{\kappa}_0(\mathrm{w}_i,\psi_i)=\begin{bmatrix}0\\\frac{\pi^2}{\lambda^2}w_{ic}\\\frac{\pi^2}{\lambda^2}w_{is}\\0\\0\\0\\-\psi'_{ic}\\-\psi'_{is}\\0\\0\\0\\-\frac{2\pi}{\lambda}\psi_{is}\\\frac{2\pi}{\lambda}\psi_{ic}\\0\\0\end{bmatrix}\qquad\text{(D6), (D7)}$$

$$\boldsymbol{\varepsilon}_1=\begin{bmatrix}\mathbf{J}&\mathbf{O}\\\mathbf{O}&\mathbf{O}\\\mathbf{O}&\mathbf{J}\end{bmatrix},\quad\boldsymbol{\varepsilon}_2=\begin{bmatrix}\mathbf{O}&\mathbf{O}\\\mathbf{O}&\mathbf{I}\\\mathbf{I}&\mathbf{O}\end{bmatrix}\qquad\text{(D8), (D9)}$$

$$\mathbf{J}=\begin{bmatrix}0&0&0&0&0\\0&0&\omega_i&0&0\\0&-\omega_i&0&0&0\\0&0&0&0&2\omega_i\\0&0&0&-2\omega_i&0\end{bmatrix},\qquad\omega_i=\frac{\pi b_i}{\lambda}\qquad\text{(D10), (D11)}$$

$$\mathbf{O}=\begin{bmatrix}0&0&0&0&0\\0&0&0&0&0\\0&0&0&0&0\\0&0&0&0&0\\0&0&0&0&0\end{bmatrix},\qquad\mathbf{I}=\begin{bmatrix}1&0&0&0&0\\0&1&0&0&0\\0&0&1&0&0\\0&0&0&1&0\\0&0&0&0&1\end{bmatrix}\qquad\text{(D12), (D13)}$$

The extensional matrix (**A**) and coupling matrix (**B**) is multiplied by 5×5 identical matrix (**I**) to match the dimension of other terms.

$$\overline{\mathbf{A}}_i=\begin{bmatrix}A_{i_{11}}\mathbf{I}&A_{i_{12}}\mathbf{I}&A_{i_{16}}\mathbf{I}\\A_{i_{12}}\mathbf{I}&A_{i_{22}}\mathbf{I}&A_{i_{26}}\mathbf{I}\\A_{i_{16}}\mathbf{I}&A_{i_{26}}\mathbf{I}&A_{i_{66}}\mathbf{I}\end{bmatrix},\qquad\overline{\mathbf{B}}_i=\begin{bmatrix}B_{i_{11}}\mathbf{I}&B_{i_{12}}\mathbf{I}&B_{i_{16}}\mathbf{I}\\B_{i_{12}}\mathbf{I}&B_{22}\mathbf{I}&B_{i_{26}}\mathbf{I}\\B_{i_{16}}\mathbf{I}&B_{i_{26}}\mathbf{I}&B_{i_{66}}\mathbf{I}\end{bmatrix}\qquad\text{(D14), (D15)}$$

The derivatives of $\boldsymbol{\varepsilon}_0(\mathrm{w}_i,\psi_i)$, $\boldsymbol{\kappa}_0(\mathrm{w}_i,\psi_i)$ are calculated as:

$$\boldsymbol{\varepsilon}_0'(\mathrm{w}_i,\psi_i)=\begin{bmatrix}\frac{\pi^2}{2\lambda^2}(w_{ic}\psi_{ic}+w_{is}\psi_{is})\\0\\0\\\frac{\pi^2}{2\lambda^2}(w_{is}\psi_{is}+w_{ic}\psi_{ic})\\-\frac{\pi^2}{2\lambda^2}(w_{ic}\psi_{is}+w_{is}\psi_{ic})\\\frac{1}{2}\left(\psi_{ic}\psi'_{ic}+\psi_{is}\psi'_{is}\right)\\0\\0\\\frac{1}{2}\left(\psi_{ic}\psi'_{ic}-\psi_{is}\psi'_{is}\right)\\\frac{1}{2}\left(\psi_{is}\psi'_{ic}+\psi_{ic}\psi'_{is}\right)\\\frac{\pi}{2\lambda}\left(w_{is}\psi'_{ic}+w'_{is}\psi_{ic}-w_{ic}\psi'_{is}-w_{ic}\psi_{is}\right)\\0\\0\\\frac{\pi}{2\lambda}\left(w_{is}\psi'_{ic}+w'_{is}\psi_{ic}+w_{ic}\psi'_{is}+w_{ic}\psi_{is}\right)\\\frac{\pi}{2\lambda}\left(w_{is}\psi'_{is}+{\psi_{is}}^2-w_{ic}\psi'_{ic}-{\psi_{ic}}^2\right)\end{bmatrix} \tag{D16},$$

$$\boldsymbol{\kappa}_0'(\mathrm{w}_i,\psi_i)=\begin{bmatrix}0\\\frac{\pi^2}{\lambda^2}\psi_{ic}\\\frac{\pi^2}{\lambda^2}\psi_{is}\\0\\0\\0\\-\psi''_{ic}\\-\psi''_{is}\\0\\0\\0\\-\frac{2\pi}{\lambda}\psi'_{is}\\\frac{2\pi}{\lambda}\psi'_{ic}\\0\\0\end{bmatrix} \tag{D17}$$

The equilibrium equations can be further extended in the following expressions by rewriting the stress resultants in terms of their components.

$$N'_{yi0} = 0,$$

$$N'_{yic} + \frac{\pi}{\lambda} N_{xyis} = 0,$$

$$N'_{yis} - \frac{\pi}{\lambda} N_{xyic} = 0,$$

$$N'_{yiC} + \frac{2\pi}{\lambda} N_{xyiS} = 0,$$

$$N'_{yiS} - \frac{2\pi}{\lambda} N_{xyiC} = 0,$$

D18

$$N'_{xyi0} = 0,$$

$$N'_{xyic} + \frac{\pi}{\lambda} N_{xis} = 0,$$

$$N'_{xyis} - \frac{\pi}{\lambda} N_{xic} = 0,$$

$$N'_{xyiC} + \frac{2\pi}{\lambda} N_{xiS} = 0,$$

$$N'_{xyiS} - \frac{2\pi}{\lambda} N_{xiC} = 0$$

Appendix E

Coefficients in equivalent uniform stress resultants calculations

The parameters used to calculated the work done by the stress resultants.

$$\eta_{xi0} = -\lambda\bar{\varepsilon}_x - 2u_{ic} + \frac{\pi^2}{4\lambda}(w_{ic}^2 + w_{is}^2) \tag{E1}$$

$$\eta_{xic} = \frac{\pi}{2}u_{is} - \frac{8}{3}u_{iC} - \frac{2\pi}{3\lambda}w_{ic}w_{is} \tag{E2}$$

$$\eta_{xis} = -\frac{2\lambda}{\pi}\bar{\varepsilon}_x - \frac{\pi}{2}u_{ic} - \frac{4}{3}u_{iS} + \frac{\pi}{3\lambda}(w_{ic}^2 + w_{is}^2) \tag{E3}$$

$$\eta_{xiC} = \frac{2}{3}u_{ic} + \pi u_{iS} + \frac{\pi^2}{8\lambda}(w_{is}^2 - w_{ic}^2) \tag{E4}$$

$$\eta_{xiS} = \frac{4}{3}u_{is} - \pi u_{iC} - \frac{\pi^2}{4\lambda}w_{ic}w_{is} \tag{E5}$$

$$\eta_{yi0} = \lambda v'_{i0} + \frac{2\lambda}{\pi}v'_{is} + \frac{\lambda}{4}(\psi_{ic}^2 + \psi_{is}^2) \tag{E6}$$

$$\eta_{yic} = \frac{\lambda}{2}v'_{i0} + \frac{4\lambda}{3\pi}v'_{iS} + \frac{2\lambda}{3\pi}\psi_{ic}\psi_{is} \tag{E7}$$

$$\eta_{yis} = \frac{2\lambda}{\pi}v'_{i0} + \frac{\lambda}{2}v'_{is} - \frac{2\lambda}{3\pi}v'_{iC} + \frac{\lambda}{3\pi}(\psi_{ic}^2 + 2\psi_{is}^2) \tag{E8}$$

$$\eta_{yiC} - \frac{2\lambda}{3\pi}v'_{is} + \frac{\lambda}{2}v'_{iC} + \frac{\lambda}{8}(\psi_{ic}^2 - \psi_{is}^2) \tag{E9}$$

$$\eta_{yiS} = \frac{4\lambda}{3\pi}v'_{ic} + \frac{\lambda}{2}v'_{iS} + \frac{\lambda}{4}\psi_{ic}\psi_{is} \tag{E10}$$

$$\eta_{xyi0} = \lambda u'_{i0} + \frac{2\lambda}{\pi} u'_{is} - 2v_{ic} + \frac{\pi}{2}(w_{is}\psi_{ic} - w_{ic}\psi_{is}) \tag{E11}$$

$$\eta_{xyic} = \frac{\lambda}{2} u'_{ic} + \frac{4\lambda}{3\pi} u'_{iS} + \frac{\pi}{2} v_{is} - \frac{8}{3} v_{iC} + \frac{2}{3}(w_{is}\psi_{is} - w_{ic}\psi_{ic}) \tag{E12}$$

$$\eta_{xyis} = \frac{2\lambda}{\pi} u'_{i0} + \frac{\lambda}{2} u'_{is} - \frac{2\lambda}{3\pi} u'_{iC} - \frac{\pi}{2} v_{ic} - \frac{4}{3} v_{iS} - \frac{1}{3}(w_{is}\psi_{ic} + 7w_{ic}\psi_{is}) \tag{E13}$$

$$\eta_{xyiC} = -\frac{2\lambda}{3\pi} u'_{is} + \frac{\lambda}{2} u'_{iC} + \frac{2}{3} v_{ic} + \frac{\pi}{4} v_{iS} + \pi(w_{is}\psi_{ic} + w_{ic}\psi_{is}) \tag{E14}$$

$$\eta_{xyiS} = \frac{4\lambda}{3\pi} u'_{ic} + \frac{\lambda}{2} u'_{iS} + \frac{4}{3} v_{is} - \pi v_{iC} + \frac{\pi}{4}(w_{is}\psi_{is} - w_{ic}\psi_{ic}) \tag{E15}$$

Appendix F

Analytical derivation of postbuckling strain $\boldsymbol{\varepsilon_x}$ and $\boldsymbol{\varepsilon_y}$

The in-plane and out-of-plane displacements are assumed as

$$u = u_{max} \sin\frac{\pi y}{b} \sin\frac{2\pi x}{l} \tag{F1}$$

$$v = v_{max} \cos\frac{\pi y}{b} \cos\frac{2\pi x}{l} \tag{F2}$$

$$w = w_{max} \sin\frac{\pi y}{b} \sin\frac{\pi x}{l} \tag{F3}$$

Their corresponding derivatives are

$$\frac{\partial u}{\partial x} = \frac{2\pi}{l} u_{max} \sin\frac{\pi y}{b} \cos\frac{2\pi x}{l} \tag{F4}$$

$$\frac{\partial v}{\partial y} = -\frac{\pi}{b} v_{max} \sin\frac{\pi y}{b} \cos\frac{2\pi x}{l} \tag{F5}$$

$$\frac{\partial w}{\partial x} = \frac{\pi}{l} w_{max}\, sin\frac{\pi y}{b} cos\frac{\pi x}{l} \tag{F6}$$

$$\frac{\partial w}{\partial y} = \frac{\pi}{b} w_{max} \cos\frac{\pi y}{b} \sin\frac{\pi x}{l} \tag{F7}$$

According to large deflection theory, the middle surface strain can be expressed as

$$\begin{aligned}
\varepsilon_x &= \frac{2\pi}{l} u_{max} \cos\frac{2\pi x}{l} \left(\sin\frac{\pi y}{b}\right) + \frac{\pi^2}{2l^2} {w_{max}}^2 \cos^2\frac{\pi x}{l} \left(\sin^2\frac{\pi y}{b}\right) \\
&= \frac{2\pi}{l} u_{max} \cos\frac{2\pi x}{l} \left(\sin\frac{\pi y}{b}\right) + \frac{\pi^2}{4l^2} {w_{max}}^2 \left(1 + \cos\frac{2\pi x}{l}\right) \left(\sin^2\frac{\pi y}{b}\right) \\
&= \frac{\pi^2}{4l^2} {w_{max}}^2 \left(\sin^2\frac{\pi y}{b}\right) + \left[\frac{2\pi}{l} u_{max} \left(\sin\frac{\pi y}{b}\right) + \frac{\pi^2}{4l^2} {w_{max}}^2 \left(\sin^2\frac{\pi y}{b}\right)\right] \cos\frac{2\pi x}{l} \\
&= \frac{\pi^2}{8l^2} {w_{max}}^2 \left(1 - \cos\frac{2\pi y}{b}\right) + \left[\frac{2\pi}{l} u_{max} \left(\sin\frac{\pi y}{b}\right) + \frac{\pi^2}{4l^2} {w_{max}}^2 \left(\sin^2\frac{\pi y}{b}\right)\right] \cos\frac{2\pi x}{l}
\end{aligned} \tag{F8}$$

$$\varepsilon_y = -\frac{\pi}{b} v_{max} \cos\frac{2\pi x}{l} \left(\sin\frac{\pi y}{b}\right) + \frac{\pi^2}{2b^2} {w_{max}}^2 \sin^2\frac{\pi x}{l} \left(\cos^2\frac{\pi y}{b}\right) \tag{F9}$$

$$= -\frac{\pi}{b} v_{max} \cos\frac{2\pi x}{l} (\sin\frac{\pi y}{b}) + \frac{\pi^2}{4b^2} {w_{max}}^2 \left(1 - \cos\frac{2\pi x}{l}\right)\left(\cos^2\frac{\pi y}{b}\right)$$

$$= \frac{\pi^2}{4b^2} {w_{max}}^2 \left(\cos^2\frac{\pi y}{b}\right) - \left[\frac{\pi}{b} v_{max} \left(\sin\frac{\pi y}{b}\right) + \frac{\pi^2}{4b^2} {w_{max}}^2 \left(\cos^2\frac{\pi y}{b}\right)\right] \cos\frac{2\pi x}{l}$$

$$= \frac{\pi^2}{8b^2} {w_{max}}^2 \left(1 + \cos\frac{2\pi y}{b}\right) - \left[\frac{\pi}{b} v_{max} \left(\sin\frac{\pi y}{b}\right) + \frac{\pi^2}{4b^2} {w_{max}}^2 \left(\cos^2\frac{\pi y}{b}\right)\right] \cos\frac{2\pi x}{l}$$

Hence, the expression for middle surface strain can be rearranged as:

$$\varepsilon_x = \frac{\pi^2}{8l^2} {w_{max}}^2 - \frac{\pi^2}{8l^2} {w_{max}}^2 \cos\frac{2\pi y}{b} + \left[\frac{2\pi}{l} u_{max} \left(\sin\frac{\pi y}{b}\right) + \frac{\pi^2}{4l^2} {w_{max}}^2 \left(\sin^2\frac{\pi y}{b}\right)\right] \cos\frac{2\pi x}{l} \quad \text{(F10)}$$

$$\varepsilon_y = \frac{\pi^2}{8b^2} {w_{max}}^2 + \frac{\pi^2}{8b^2} {w_{max}}^2 \cos\frac{2\pi y}{b} - \left[\frac{\pi}{b} v_{max} \left(\sin\frac{\pi y}{b}\right) + \frac{\pi^2}{4b^2} {w_{max}}^2 \left(\cos^2\frac{\pi y}{b}\right)\right] \cos\frac{2\pi x}{l} \quad \text{(F11)}$$